Universität der Bundeswehr München
Fakultät für Luft- und Raumfahrttechnik
Institut für Thermodynamik

Reduced chemistry models for the numerical investigation of flow and heat transfer in methane combustion devices

M. Sc. Paola Breda

Vollständiger Abdruck der von der
Fakultät für Luft- und Raumfahrttechnik
der Universität der Bundeswehr München
zur Erlangung des akademischen Grades eines

Doktor-Ingenieurs (Dr.-Ing.)

genehmigten Dissertation

Vorsitzender:	Univ.-Prof. Dr.-Ing. habil. Markus Klein
1. Berichterstatter:	Prof. Dr. rer. nat. Michael Pfitzner
2. Berichterstatter:	Prof. Dr. rer. nat. habil. Ulrich Maas

Die Dissertation wurde am 03.02.2021 bei der Universität der Bundeswehr München eingereicht und durch die Fakultät für Luft- und Raumfahrttechnik am 03.06.2021 angenommen.

Tag der Prüfung: 22.06.2021

"We choose to go to the Moon in this decade and do the other things, not because they are easy, but because they are hard; because that goal will serve to organize and measure the best of our energies and skills, because that challenge is one that we are willing to accept, one we are unwilling to postpone, and one we intend to win, and the others, too."

John F. Kennedy Speech
Rice Stadium, Houston, TX
September 12, 1962

Abstract

Combustion technologies based on hydrocarbons will still play a relevant role in the long-term scenario, especially in the transportation sector. Numerical tools for the computation of turbulent reacting flows are of significant importance in the development phase of such technologies. Nevertheless, simulations of hydrocarbon combustion are not without difficulties. By increasing the dimensions of the chemical reaction differential equations, the stiffness of the chemical system increases, posing a limit to the available computational resources. An additional challenge is given by wall-confined turbulent flows at high Reynolds numbers, requiring wall treatment. Particular care is needed for the near-wall modelling if the prediction of thermal loads at the combustor wall is of interest, as key parameter to quantify thermomechanical limits.

The main contribution of this work is the investigation of suitable combustion models for LES applications of methane flames. Reduced chemistry mechanisms and tabulated chemistry databases are chosen to speed-up the computation. The turbulence-chemistry interaction (TCI) on the small scales is investigated for CH_4/air partially premixed flame configurations. Two transported PDF approaches are implemented to deal with reaction-diffusion manifolds (REDIM), respectively the Eulerian Stochastic Fields (ESF) and the Multiple Mapping Conditioning (MMC).

Wall heat flux predictions are investigated on a sub-scale rocket combustion chamber operated with gaseous CH_4/O_2. The best trade-off is sought in order to correctly represent the heat transfer at wall, while keeping the computation cheap. Flamelet-based chemistry databases including heat losses are used to model the effects of Flame/Wall Interaction (FWI). Additional validation of the reduced chemistry models is performed on an experimental configuration featuring near-wall reactions of CH_4 in a crossflow of hot combustion gases, where an autoignition delay is observed.

This work shows that the implemented models based on chemistry databases significantly reduce the requirements on computational power, providing a satisfactory accuracy in the results. Strong extinction/re-ignition effects can be well represented by the ESF-REDIM model, the table also showing potential for predicting autoignition delays. When using finite rate chemistry, the use of MMC is found to be advantageous compared to ESF, although satisfactory predictions are already obtained by neglecting the TCI model. Flamelet databases including enthalpy losses provide satisfactory wall heat flux predictions for a variation of chemical mechanisms and near-wall treatments, if the flame is not subjected to autoignition phenomena.

Kurzfassung

Verbrennungstechnologien basierend auf Kohlenwasserstoffen werden auch in Zukunft und längerfristig eine Rolle spielen, insbesondere im Verkehrswesen. Numerische Methoden für die Berechnung von turbulenten, reaktiven Strömungen haben einen hohen Stellenwert in der Entwicklungsphase derartiger Technologien. Aktuell ist die Simulation der Verbrennung von Kohlenwasserstoffen nach wie vor aufwändig. Durch die Erhöhung der Komplexität der Differentialgleichungen zur Beschreibung des Reaktionsmechanismus nimmt die Steifigkeit der Differentialgleichungen des chemischen Systems zu, was die Leistungsfähigkeit von heute verfügbaren Computer-Ressourcen übersteigen kann. Wandnahe turbulente Strömungen bei hohen Reynoldszahlen stellen eine weitere Herausforderung dar und verlangen eine gezielte Betrachtung der Grenzschicht. Die Bestimmung von Wärmelasten im Rahmen der thermomechanischen Auslegung von Verbrennungsmaschinen erfordert besondere Aufmerksamkeit der Modellierung wandnaher Phänomene, welche in diesem Zusammenhang ein Schlüsselelement darstellen.

Der wesentliche Beitrag dieser Arbeit ist die Untersuchung geeigneter Verbrennungsmodelle für LES-Simulationen von Methanflammen. Reduzierte Reaktionsmechanismen und Datenbanken tabellierter Chemie werden eingesetzt um die Berechnungen zu beschleunigen. Für partiell vorgemischte CH_4/Luft Flammen wird die Turbulenz-Chemie-Interaktion (TCI) auf kleinen Skalen untersucht. Zwei Transport PDF Ansätze wurden für das Reaction Diffusion Manifolds (REDIM) Modell implementiert: Die Eulerian Stochastic Fields (ESF) und die Multiple Mapping Conditioning (MMC) Methode.

Die Bestimmung von Wandwärmeströmen wird unter Verwendung einer Modellraketenbrennkammer, welche mit gasförmigen CH_4/O_2 betrieben wird, untersucht. Es wurde eine Optimierung auf kurze Berechnungszeiten bei gleichzeitig korrekter Bestimmung des Wandwärmestroms durchgeführt. Zur Modellierung der Flammen-Wand-Interaktion (FWI) werden flamelet-basierte Chemie-Datenbanken, welche Wärmeverluste berücksichtigen, eingesetzt. Zusätzliche Validierung dieser Datenbanken erfolgt unter Verwendung von Daten eines experimentellen Aufbaus zur Untersuchung der wandnahen Reaktionen von CH_4 in einer heißen Verbrennungsgas-Querströmung in der eine Selbstentzündung des eingebrachten Brennstoffes beobachtet wurde.

Diese Arbeit zeigt, dass die implementierten Modelle, basierend auf einer tabellierten Chemie-Datenbank, die benötige Rechenleistung signifikant reduzieren und dabei gleichzeitig eine zufriedenstellende Genauigkeit der Ergebnisse liefern können. Mittels des ESF/REDIM-Modells können starke Verlöschungs- und Wiederzündungs-Effekte gut repräsentiert werden, während die Tabelle gleichzeitig das Potential zur Vorhersage des Zeitverzugs von Selbstzündungen aufzeigt. Bei Verwendung von detaillierter Chemie zeigt sich das MMC-Modell vorteilhafter im Vergleich zum ESF-Modell. Dennoch, vielversprechende Ergebnisse werden bereits bei Vernachlässigung des TCI-Modells erreicht. Flamelet-Datenbanken mit Enthalpieverlusten zeigen für verschiedene Chemiemechanismen und Wandmodelle gute Vorhersagen von Wandwärmeströmen, solange Selbstzündungseffekte nicht zu berücksichtigen sind.

Acknowledgements

I would like to express my gratitude and appreciation to my supervisor, Prof. Dr. rer. nat. Michael Pfitzner, for welcoming me into his research group, despite my previous experience in the industry at the time. He displayed a level of trust that not everybody would have, under such circumstances. Without his guidance, advice and patience over these past years, this dissertation would not have taken form. During the more challenging moments, I also received great support and technical advice from my colleagues at the Institute of Thermodynamics; in particular, Rahand Dalshad, Lukas Fischer, Dr.-Ing. Maximilian Hansinger, Arne Lampmann, Prof. Dr.-Ing. habil. Tobias Sander, Elias Trautner (Master thesis student at the institute in 2019) and Dr. Davide Vimercati.

A strong cooperative network developed within the framework of this thesis. I would like to thank the following individuals and/or research groups, all of whom I hold in high esteem: Prof. Dr. rer. nat. habil. Ulrich Maas and Dr.-Ing. Chunkan Yu from the Institute of Technical Thermodynamics at KIT, Dr. Ruud Eggels from Rolls Royce Deutschland, Associate Prof. Matthew Cleary from the University of Sydney, Eshan Sharma from the Indian Institute of Technology Kanpur, Nikolaos Perakis from the Chair of Space Propulsion and Raffaele Olmeda from the Chair of Aerodynamics and Fluid Mechanics at TUM, Dr. Guido Saccone and Pasquale Natale from the Italian Aerospace Centre (CIRA), the NUMAP-FOAM School from Prof. Hrvoje Jasak and his research group at the Faculty of Mechanical Engineering and Naval Architecture in Zagreb.

Moral support from my beloved is, and will remain, my pillar of strength, especially through the most difficult times. The encouragement of my family and their reminders to always persevere in the face of adversity, helped me remain focused and motivated throughout these years. There is an Italian proverb which succinctly embodies the rollercoaster of emotions that this thesis presented: *Hai voluto la bicicletta adesso pedala*, translated as *"You bought the ticket, you take the ride"*. There is one person who knows how many times I had been tempted to disengage from this "ride". I feel I cannot thank Stefan enough for never letting me give up, and always doing so with kind, encouraging words. In retrospect, I did enjoy the "ride" after all.

Publications

In the framework of this work, several contributions were published in scientific journals or presented at international conferences. A complete list is provided hereby.

Peer-reviewed journal contributions

- Breda, P., Sharma, E., De, S., Cleary, M., and Pfitzner, M. Coupling the Multiple Mapping Conditioning Mixing Model with Reaction-diffusion Databases in LES of Methane/air Flames. *Combust. Sci. Tech.* (July 2021), DOI: https://doi.org/10.1080/00102202.2021.1954626

- Breda, P., and Pfitzner, M. Delayed Detached Eddy Simulations with Tabulated Chemistry for Thermal Loads Predictions. *J. Propuls. Power 37*, 1 (2021), 29–46, DOI: https://doi.org/10.2514/1.B37924

- Breda, P., Hansinger, M., and Pfitzner, M. Chemistry computation without a sub-grid PDF model in LES of turbulent non-premixed flames showing moderate local extinction. *P. Combust. Inst. 38*, 2 (2021), 2655–2663, DOI: https://doi.org/10.1016/j.proci.2020.06.161

- Breda, P., Yu, C., Maas, U., and Pfitzner, M. Validation of an Eulerian Stochastic Fields solver coupled with reaction-diffusion manifolds on LES of methane/air non-premixed flames. *Flow Turbul. Combust. 107* (2021), 441–477, DOI: https://doi.org/10.1007/s10494-020-00235-w

- Pfitzner, M., and Breda, P. An analytic probability density function for partially premixed flames with detailed chemistry. *Phys. Fluids 33*, 3 (2021), 035117, DOI: https://doi.org/10.1063/5.0038888

- Yu, C., Breda, P., Minuzzi, F., Pfitzner, M., and Maas, U. A novel model for incorporation of differential diffusion effects in PDF simulations of non-premixed turbulent flames based on Reaction-Diffusion Manifolds (REDIM). *Phys. Fluids 33*, 2 (2021), 025110, DOI: https://doi.org/10.1063/5.0039160

- Yu, C., Breda, P., Pfitzner, M., and Maas, U. Coupling of mixing models with manifold based simplified chemistry in PDF modeling of turbulent reacting flows. *P. Combust. Inst. 38*, 2 (2021), 2645–2653, DOI: https://doi.org/10.1016/j.proci.2020.06.132

- Zips, J., Traxinger, C., Breda, P., and Pfitzner, M. Assessment of Presumed / Transported Probability Density Function Methods for Rocket Combustion Simulations. *J. Propuls. Power 35*, 4 (2019), 1–18, DOI: https://doi.org/10.2514/1.B37331

Other contributions

- Breda, P., Fischer, L., Dalshad, R., and Pfitzner, M. Numerical investigation of autoignition length and wall heat flux for near-wall reaction of CH4. In *30. Deutscher Flammentag* (Sept. 2021)
- Breda, P., Trautner, E., Klein, M., Hansinger, M., and Pfitzner, M. CPU-based deployment of artificial neural networks for LES of reacting flows in OpenFOAM. In *13th International ERCOFTAC Symposium* (Sept. 2021)
- Breda, P., Pfitzner, M., Perakis, N., and Haidn, O. Generation of Non-adiabatic Flamelet Manifolds: Comparison of two Approaches Applied on a Single-element GCH4/GO2 Combustion Chamber. In *8th European Conference For Aeronautics and Space Science* (July 2019), DOI: https://doi.org/10.13009/EUCASS2019-121
- Breda, P., Hansinger, M., and Pfitzner, M. Low dimensional chemistry manifolds applied to premixed methane/air flames under atmospheric conditions. In *9th European Combustion Meeting* (Apr. 2019)
- Breda, P., Zips, J., and Pfitzner, M. A Non-Adiabatic Flamelet Approach for Non-Premixed O2/CH4 Combustion. In *Proceedings of the 3rd World Congress on Momentum, Heat and Mass Transfer* (Apr. 2018), DOI: https://doi.org/10.11159/csp18.109
- Olmeda, R., Breda, P., Stemmer, C., and Pfitzner, M. *Future Space-Transport-System Components under High Thermal and Mechanical Loads. Notes on Numerical Fluid Mechanics and Multidisciplinary Design.* Springer, Cham., 2021, ch. Large-Eddy Simulations for the Wall Heat Flux Prediction of a Film-Cooled Single-Element Combustion Chamber, pp. 223–234, DOI: https://doi.org/10.1007/978-3-030-53847-7_14
- Saccone, G., Natale, P., Battista, F., Breda, P., and Pfitzner, M. Methane / Oxygen Combustion Kinetic Scheme Optimization for Liquid Rocket Engine CFD Applications. In *Proceedings of the 4th World Congress on Momentum, Heat and Mass Transfer* (Apr. 2019), DOI: https://doi.org/10.11159/csp19.105

Contents

List of Figures

List of Tables

Nomenclature

Roman characters

$\dot{Q}$	Heat source term	W
$\dot{q}_w$	Wall heat flux	$W\,m^{-2}$
$\hat{d}^2_{p,q}$	Effective square distance between particles p, q	
$\mathcal{D}_{ij}$	Binary diffusion coefficient	$m^2\,s^{-1}$
$\mathcal{G}$	LES filter	
$\mathcal{H}$	Heaviside function	
$\mathcal{I}$	LES mesh index	
$\mathcal{K}$	Turbulent kinetic energy	$J\,kg^{-1}$
$\mathcal{M}$	Reduced chemistry space	
$\mathcal{P}$	PDF	
$\mathcal{Q}$	Stochastic variable	
$\mathcal{R}$	Perfect gas constant	$J\,mol^{-1}\,K^{-1}$
$\mathcal{T}$	Tangential space to $\mathcal{M}$	
$\mathcal{V}$	Second table parameter in β-PDF	
$\mathbf{C}$	Constant parametrization matrix	
$\mathbf{dW}$	Wiener process	$s^{1/2}$
$\mathbf{E}$	Element composition matrix	
$\mathbf{J}$	Jacobian matrix	
$\mathbf{P}_n$	Projection matrix normal to $\mathcal{T}$	
$\mathbf{P}_t$	Projection matrix on $\mathcal{T}$	
$\mathbf{S}$	Matrix of the stoichiometric vectors	
$\mathbf{u}$	Velocity vector	$m\,s^{-1}$
$\mathbf{V}^C$	Velocity correction on diffusion velocity	$m\,s^{-1}$
$\mathbf{V}_k$	Diffusion velocity of species k	$m\,s^{-1}$
a	Strain	s^{-1}
A_s	Sutherland coefficient	$Pa\,s$
c_k	Concentration of species k	$kmol\,m^{-3}$
c_p	Specific heat capacity at constant pressure	$J\,kg^{-1}\,K^{-1}$
c_v	Specific heat capacity at constant volume	$J\,kg^{-1}\,K^{-1}$
D_k	Mass diffusivity of species k	$m^2\,s^{-1}$
D_{th}	Thermal diffusivity	$m^2\,s^{-1}$
f	Mixture fraction	
h_a	Absolute enthalpy	$J\,kg^{-1}$
h_k^0	Standard enthalpy of formation of species k	$J\,kg^{-1}$
h_n	Normalized enthalpy	
h_s	Sensible enthalpy	$J\,kg^{-1}$
I	Momentum ratio	

k	Wave number	m^{-1}
L_{ig}	Autoignition length	m
Le	Lewis Number	
m	Mass	kg
m_s	Dimensions of reduced chemistry	
Ma	Mach number	
n_e	Number of elements	
N_f	Number of stochastic fields	
N_p	Number of particles	
n_r	Number of reactions	
n_s	Number of species	
p	Pressure	Pa
Pr	Prandtl Number	
R_j	Net rate of progress of reaction j	$kmol\,m^{-3}\,s^{-1}$
Re	Reynolds Number	
S_α^p	Mixing term on particle p	
S_{ij}	Strain rate tensor	s^{-1}
Sc	Schmidt Number	
T	Temperature	K
t	Time	s
T_s	Sutherland coefficient	K
u_τ	Friction velocity	$m\,s^{-1}$
W	Mean molecular weight	$kg\,kmol^{-1}$
W_k	Molecular weight of species k	$kg\,kmol^{-1}$
x^+, y^+, z^+	Non-dimensional wall units	
x_i	Physical coordinate in i-th direction	m
X_k	Mole fraction of species k	
Y_k	Mass fraction of species k	
y_τ	Viscous length scale	m
Z	MMC mixture fraction on particles	

Greek characters

$\boldsymbol{\Psi}$	Thermo-chemical state	
$\boldsymbol{\Psi}_\theta^+$	Pseudo-inverse matrix	
$\boldsymbol{\theta}$	REDIM generalized coordinates	
$\boldsymbol{\xi}$	Reduced physical coordinates	
χ	Scalar dissipation rate	s^{-1}
Δ	LES filter width	m
δ_{ij}	Kronecker delta	
$\dot{\omega}_k$	Source term of species k	$kg\,m^{-3}\,s^{-1}$
$\dot{\omega}_T$	Combustion heat release	$W\,m^{-3}$
ϵ	Energy dissipation rate	$J\,kg^{-1}\,s^{-1}$
Γ	Gamma function	
γ_{mix}	MMC mixing extent	
λ	Thermal conductivity	$W\,m^{-1}\,K^{-1}$
μ	Dynamic viscosity	$Pa\,s$

ν	Kinematic viscosity	$m^2\,s^{-1}$
ϕ_F	Equivalence ratio	
ϕ_k	Specific mole numbers of species k	$kmol\,kg^{-1}$
π_α	Sample space of ξ_α	
τ_w	Wall shear stress	Pa
τ_{ij}	Shear stress tensor	Pa
τ_L	MMC mixing time scale	s
ξ_α	PDF scalar quantities	
ζ_α^n	n-th realization of ξ_α	

Subscripts - Superscripts

$\bar{\ }$	Filtered field
$\tilde{\ }$	Favre-filtered field
$''2$	Variance
$''$	Standard deviation
ad	Adiabatic
c	Cold flow
h	Hot flow
p	Lagrangian particle
sgs	Sub-grid scale
st	Stoichiometric
w	Wall properties

Abbreviations

ANN	Artificial Neural Network
BC	Boundary Conditions
BI	Burning Index
BM	Base Mesh
CFD	Computational Fluid Dynamics
CFL	Courant-Friedrichs-Lewy
CMC	Conditional Moment Closure
CPU	Central Processing Unit
CSP	Computational Singular Perturbation
CSS	Carbon Capture and Storage
DAC	Dynamic Adaptive Chemistry
DD	Differential Diffusion
DME	Dimethyl Ether
DNN	Deep Neural Network
DNS	Direct Numerical Simulation
DRG	Direct Relation Graph
EMST	Euclidean Minimum Spanning Tree
EOS	Equation of State
ESF	Eulerian Stochastic Fields
FDF	Filtered Density Function
FGM	Flamelet Generated Manifold

FI	Flame Index
FM	FlameMaster
FP	Fokker-Plank
FPI	Flamelet Prolongation of ILDM
FPV	Flamelet Progress Variable
FWI	Flame/Wall Interaction
GPU	Graphics Processing Unit
GQL	Global Quasi-Linearisation
HCCI	Homogeneous Charge Compression Ignition
HMI	Homogeneous Mixing Ignition
HOQ	Head-On Quenching
HPC	High-Performance Computing
IDDES	Improved Delayed Detached Eddy Simulation
IEM	Interaction by Exchange with the Mean
ILDM	Intrinsic Low-Dimensional Manifold
ISAT	In-Situ Adaptive Tabulation
LES	Large Eddy Simulation
LOI	Level Of Importance
LUT	Look-Up Table
MGM	Multidimensional flamelet Generated Manifolds
MILD	Moderately/Intensively Low Oxygen Dilution
MMC	Multiple Mapping Conditioning
MR	Most Reactive
NA	Non-Adiabatic
NHFR	Net Heat Flux Reduction
NS	Navier-Stokes
ODE	Ordinary Differential Equation
OF	OpenFOAM
PCA	Principal Component Analysis
PCCI	Premixed Charge Compression Ignition
PDE	Partial Differential Equation
PDF	Probability Density Function
PE	Partial Equilibrium
PISO	Pressure-Implicit Split-Operator
PLIF	Planar Laser-Induced Fluorescence
PV	Progress Variable
QSS	Quasi-Steady State
RANS	Reynolds-Averaged Navier-Stokes
REDIM	Reaction-Diffusion Manifold
RIF	Representative Interactive Flamelets
RMS	Root Mean Square
ROF	Ratio Oxidizer Fuel
SA	Spalart-Allmaras
SDE	Stochastic Differential Equation
SM	Super Mesh
SPDE	Stochastic PDE

SPM	Stochastic Particle Method
SWQ	Side-Wall Quenching
TCI	Turbulence-Chemistry Interaction
TDAC	Tabulated DAC
TGLDM	Trajectory-Generated Low Dimensional Manifold
TNF	Turbulent Nonpremixed Flames
TPDF	Transported PDF
TVD	Total Variation Diminishing
WALE	Wall-Adapting Local Eddy-viscosity
WMLES	Wall-Modelled LES
WRLES	Wall-Resolved LES

1. Introduction

1.1. Motivation

It is without any doubt that the industrialized society as we know it will be forced soon to re-assess the role of combustion technologies in favour of renewable resources. The current goal in the European Union is in line with the Paris Agreement, which aims to contain the global temperature increase below 2° C, compared to pre-industrial levels. The European Commission announced its willingness to reach the climate neutral economy within 2050, i.e. net-zero CO_2 emissions from the transportation sector [1]. The use of fossil fuels in the industry however is the pillar of the world-wide economy, especially in the emergent markets. Combustion of hydrocarbons is still the driving energy source for ground, sea and air transportation, such as in internal combustion engines or gas turbines. Main stage rocket engines often rely on C_xH_y/O_2 combustion, belonging to the category of space access transportation. Power generation and metallurgic industry also rely mainly on combustion. An increased world fossil fuel consumption of 58 %[2] for coal, 25 % for crude oil and 53 % for natural gas was seen in the past two decades [249]. Based on the known fossil fuel reserves and the production level of 2015, barely 50 years of natural gas and oil and about 100 years of coal reserves are left. When compelling with the Paris Agreement however, about 60-80 % of such reserves must be kept in the ground to meet a 50 % probability to reach the global climate target [249]. It is therefore unlikely that fossil fuels will disappear from the scene in the short-term. Industry in this century must rely on the coexistence of renewable and fossil resources, improving the processes related to CO_2 containment and off-set [81]. While new technologies are constantly researched, the employment of renewable resources nowadays might be still less sustainable than fossil-fuels-based technologies involving Carbon Capture and Storage (CSS) [81]. Based on this preliminary assessment about the role of hydrocarbon fuels in the long-term scenario, this work justifies the investigation of turbulent reacting flows involving the simplest hydrocarbon, methane.

The rapid improvement in computer technologies and the deriving increase in computational power experienced in the past decades allowed the development of more detailed turbulent combustion models, required in the Computational Fluid Dynamics (CFD) branch of each research and development program. The preliminary design of thermal systems is an essential requirement of the industry, since the cost of experimental tests can be enormously reduced. However, the process must rely on valid CFD models for turbulent reactive flows. Computational modelling in thermal systems for commercial engineering enterprises includes but is not limited to the assessment of the heat loads and finite rate chemistry effects such as ignition, extinction or pollutant emissions (e.g. NOx) [81]. Access to experimental data for the validation of the software is a key point, to further validate the interaction between flow and chemistry.

The availability of High-Performance Computing (HPC) centres and pentascale supercom-

---

[1] https://ec.europa.eu/clima/news/commission-calls-climate-neutral-europe-2050_en

[2] comparison in TWh (tera-Watt per hour), from year 2000 to 2017

puters allowed the academic research to extend turbulence and combustion models originally conceived for the Reynolds-Averaged Navier Stokes equations (RANS) to Large Eddy Simulations (LES). Although Direct Numerical Simulations (DNS) can provide the best insight down to the smallest turbulent structures due to their model-free assumption, the computational power required by DNS is still unaffordable for the industry, since the computational time scales with the third power of the Reynolds number [52]. Instead, the use of LES has become more attractive in the industry, provided that a moderate computational cost can be guaranteed. Compared to RANS, LES have the advantage that the large scale turbulent structures are resolved on the computational grid, leading to a more accurate prediction of the unsteady flow. Modelling is only required for the small turbulent scales, which are filtered out in LES grids. When dealing with turbulent reacting flows however, chemical reactions can be affected by turbulent fluctuations localized at the molecular level, thus where the LES is unresolved. Therefore, it is particularly important that the numerical models can properly describe the Turbulence-Chemistry Interaction (TCI). When dealing with LES of reacting flows several challenges are foreseen, primarily dictated by the limitation of computational power.

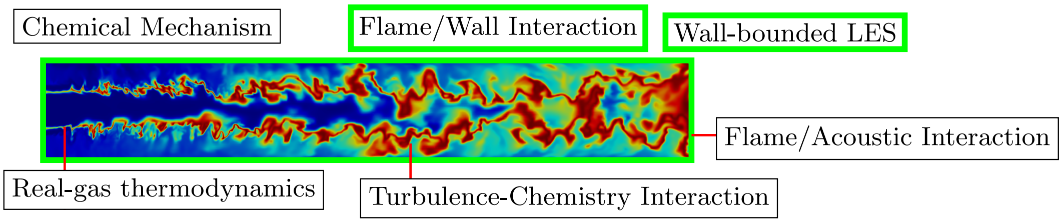

Figure 1.1.: Challenges encountered in a LES calculation of a CH_4/O_2 sub-scale rocket combustion chamber at 20 bar

Fig. 1.1 represents a typical flame configuration for high pressure CH_4/O_2 combustion, together with six critical challenges encountered in combustion modelling. The importance of the TCI modelling was already discussed. The computation of the advancement of the chemistry system of equations requires the highest share when estimating the computational resources. Usually, an accurate prediction of unsteady phenomena like extinction and re-ignition would require the use of a detailed chemistry mechanism. The reference mechanism for methane combustion in air, the GRI-3.0 [269], already contains 53 species and 325 reactions. By increasing the complexity of the fuel C_xH_y one can easily reach hundred of species and thousand of reactions [81]. When dealing with rocket combustion chamber applications, carbon-chemistry under high-pressure conditions further increases the stiffness of the chemical system. Agile computations with limited resources are only possible if the kinetic mechanism is reduced accordingly, if the chemistry routine is accelerated or, alternatively, if the thermo-chemical states are pre-tabulated in advance. A third challenge is encountered when attempting wall-resolved LES for high Reynolds numbers, where the computational cost is estimated to scale as $Re^{2.7}$ [52]. In this configuration the boundary layers at the wall are solved down to the viscous layer, and the computational grid usually features a normalized wall distance of $y^+ < 1$. The computational cost can be reduced to $Re^{0.53}$ if wall functions are employed, loosening the requirements on the grid spacing normal to the wall. An alternative method which reduces the computational cost proportionally to *log(Re)* [46] would be a hybrid LES/RANS turbulence model, where the boundary layers and detached flows are completely treated as RANS ([166] for a comparison). The implementation of wall-modelled LES leads to the fourth challenge, thus the description of the Flame/Wall Interaction (FWI) and the prediction of the wall heat flux. In fact, a wall-resolved LES would be more accurate if the prediction of the thermal loads is the target, since it resolves the flow down to the wall. On the other hand, secondary reactions might be present at the wall proximity, caused by the FWI [229] or by injection of a cooling film, which would ideally require specific wall functions to account for chemistry and strong temperature gradients at the wall proximity [45], in order to better describe the wall heat fluxes. Further complexity is added to the calculation if regions of fluid require a real gas thermodynamics approach, as observed for example for trans- or super-critical propellant injection or in the cooling channels of a rocket combustion chamber. Coupling mechanisms between acoustic waves and flames in a combustion system require the modelling of combustion instabilities.

The aim of this work is to tackle the above mentioned challenges encountered in LES of turbulent reactive flows based on CH_4 combustion, in order to drastically reduce their computational cost. Only the last two thematics are not assessed by this investigation. A detailed review of the recent developments available in the literature is now presented, in order to provide a context for the modelling developed in this work. Particular interest is shown for existing OpenFOAM implementations, being OpenFOAM [312] the CFD software used throughout this investigation.

1.2. State of art

1.2.1. Flame typologies

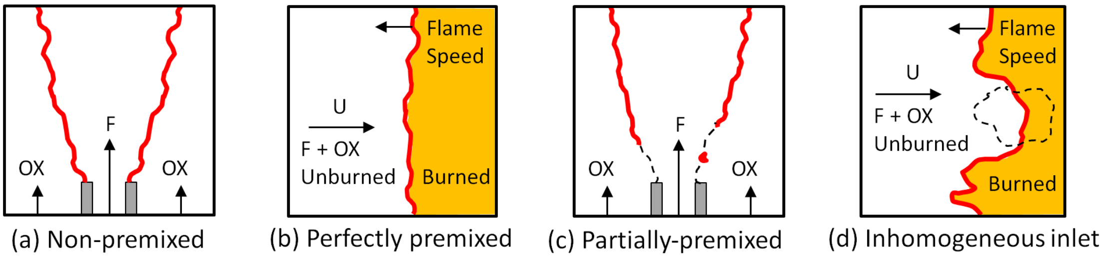

(a) Non-premixed (b) Perfectly premixed (c) Partially-premixed (d) Inhomogeneous inlet

Figure 1.2.: Typologies of flame

Ideally, flame regimes can be classified depending on the degree of mixing of the reactants. Fig. 1.2 reports four typical configurations. In non-premixed flames (a), the fuel and oxidizer are injected separately and the combustion process is driven by molecular diffusion. The flame (in red) is localized at the stoichiometric composition and it is anchored at the inlet tips. In perfectly premixed flames instead (b), a reaction zone propagates according to a characteristic flame speed into the unburned fuel/oxidizer mixture.

Mixed-modes however are typically encountered in industrial combustor devices, since partially premixed regimes enhance flame stabilization and contribute to reduce NOx and CO_2 pollutants [229]. In partially premixed flames (c), the inlet mixture composition lies outside the flammability limits so that the flame usually anchors downstream the injector wall (lifted flame), along the isoline of stoichiometric composition (black dashed line). The experimental setup of the Sandia series of flames D-E-F for CH_4/air combustion [10, 9] and the non-premixed swirl stabilized flames of Syndey [144, 192] provided experimental data for the validation of combustion models based on such partially premixed flames. The TNF workshops [8] also positively contributed to the experimental investigation of TCI in non-premixed flames and provided a valid database for the validation of numerical codes. Combustion technologies like Homogeneous Charge Compression Ignition (HCCI) in gasoline engines or Premixed Charge Compression Ignition (PCCI) in diesel engines operate within the Moderately or Intensively Low Oxygen Dilution (MILD) combustion regime, where a flame of type (c) is recognized. If the oxidizer is vitiated, meaning that its concentration gets reduced by mixing with hot gases, a reduction of the temperature peaks and therefore of NOx emissions is promoted. Autoignition would be the driving factor to stabilize the flame if the vitiated oxidizer has a sufficiently high temperature, because the mixture is already significantly reactive. Turbulent premixed flames in hot vitiated co-flows were investigated by Cabra [44, 43] and Dunn [77, 78]. The investigations show that the lift-off height is particularly sensitive to the coflow temperature [43].

Lifted flames are also observed in partially premixed regimes with inhomogeneous inlets (d), where the composition spans both flammable and non-flammable mixture regions. Localized fuel pockets (black dashed line) locally change the flame speed. Experimental data for the inhomogeneous regimes of hydrocarbon combustion are available for the Sandia modified piloted flames [196, 11], the bluff-body flames HM1-HM3 [65, 190, 191] and swirl-stabilized flames SMH1-SMH3 [1, 193]. When the inhomogeneous mixture fluctuates within the flammability limits, a stratified flame regime is observed, where the flame front propagates through a range of equivalence ratios and a local change in flame speed is observed. This configuration has been experimentally investigated by Drake [75], Yang [320] and Kuenne [160]. A multi-regime burner where inhomogeneous conditions are generated downstream instead (and not inside the nozzle as in [196]) was recently investigated in Darmstadt [38] and provides a challenging case for the validation of mixed combustion modes. A complete overview for partially premixed and stratified flame configurations is provided by Masri [189], to which the reader is pointed for further details.

1.2.2. Reduced chemistry models

The detailed reference mechanism for CH_4 combustion, the GRI-3.0 [269], contains species in quasi-steady states and reactions almost at the chemical equilibrium. Depending on the application, it usually requires chemistry time steps in the order of 10^{-12} for the resolution of the chemistry Ordinary Differential Equation (ODE). It was seen that up to 90 % of the CFD computation can be easily spent in the resolution of the finite rate kinetics [280], as the ODE system becomes stiff. This requires the use of implicit solvers [114].

One possibility to speed-up the ODE integration preserving the dimensionality of the original mechanism is using optimized routines to calculate the chemical reaction rates. The software *Cantera* [109] for example provides a faster integration routine than the standard CHEMKIN library. Zirwes et al [334] demonstrated the performance improvement when coupling the *Cantera* chemistry solver with the CFD software OpenFOAM, for methane combustion.

Alternatively, non-implicit solvers can be used to solve the ODE system, if stability is maintained. An overview of common implicit, semi-implicit and explicit solvers to solve stiff kinetic problems is provided in [280] for a 0D-ignition and a 1D laminar premixed flame problem.

However, a more popular strategy to speed-up the integration of the ODE is reducing the size of the ODE system itself, to remove its stiffness. This procedure can be done at run-time. For example, an explicit integration solver for DNS applications was proposed by Lu [174], where the stiffness of the system was removed at run-time by identifying Quasi-Steady State species (QSS) and Partial-Equilibrium (PE) reactions, generating sparse algebraic equations. The reduction of the mechanism on-the-fly was also proposed in the Dynamic Adaptive Chemistry (DAC) context [170, 329]. The In-Situ Adaptive Tabulation (ISAT) [236] instead aims to tabulate the accessed compositional states at run-time, while the new states are calculated from the finite rate chemistry. The ISAT was also coupled with DAC in the TDAC model of [62, 3].
Alternatively, the chemical mechanism can be reduced prior to the CFD simulation. One can use the Principal Component Analysis (PCA) [296] or a Direct Relation Graph (DRG) approach [172] to identify and remove redundant species/reactions. Analytically reduced mechanisms can be derived by removing the short time scales associated with the chemical stiffness, using for example the PE Approximation (PEA) on very fast reversible reactions or the QSS Approximation on fast species [110]. A time-scale analysis to identify QSS species can be performed via Computational Singular Perturbation (CSP) [163], the Intrinsinc Low-Dimensional Manifolds (ILDM) [182] or using the Level of Importance (LOI) technique [176]. Virtual chemistry optimization is adopted in [231, 47], where a reduced mechanism fulfilling global properties is built from scratch. A different approach employs Artificial Neural Networks (ANN) to represent a global-step reaction chemistry, as done for H_2/CO_2 [56, 261] and CH_4/air flames [20, 21, 167]. Porumbel et al [241] modelled the chemical source terms directly, while Chen et al [54] combined the ANN with the ISAT.

The numerical integration of the ODE's can be completely avoided if the thermo-chemical states are tabulated in a pre-processing step. The simplest tabulation technique, known as Look-Up Table (LUT) [55], performs a direct interpolation on a uniform grid. Conventional chemistry databases rely on a LUT routine when coupled with the CFD solver and are usually limited to 2 or 3 key parameters. Numerous flamelet-based [221] tabulation methods accounting for molecular transport were developed in the literature. The Flamelet Generated Manifold (FGM) [300] and the Flamelet-Prolongation of ILDM (FPI) [106] originally based on tabulations of unstrained premixed laminar flames were further extended beyond the flame flammability limits to cover non-premixed regimes [245, 90, 89]. Steady counterflow diffusion flames were used instead in the flamelet model [221] and in the Flamelet Progress Variable (FPV) approach [224]. Partially premixed combustion in FPV was accounted by means of the mixture fraction and a progress variable [27], Representative Interactive Flamelets (RIF) with two streams of mixture fraction [119, 87] and Multidimensional flamelet Generated Manifolds (MGM) [210]. Another model including molecular transport is the REaction DIffusion Manifold (REDIM) introduced by Bykov and Maas [40] which it is capable to cover the premixed, non-premixed and partially-premixed regimes. The use of the REDIM against FPV or FGM tables has the advantage that it involves projection of the diffusion term onto the slow manifold [40, 107, 282]. Although unsteady FPV databases were proposed by [225, 128], flamelet-based models suffer in regimes were strong extinction/re-ignition effects occur. Databases including autoignition phenomena usually track the ignition time via a progress variable describing the pool of reactants. Homogeneous reactors are usually chosen as flame archetype [98, 161, 157, 61, 26, 215, 133], also in combination with premixed flamelets [72]. One-dimensional mixing layer [157] or counter-flow diffusion flamelets [291, 84] can be also employed.

A major drawback of such tabulation techniques is the storage space required when more than three table parameters are involved. Smart optimizations like shared memory options or dynamic optimization of memory allocation exist, as recently proposed by Weise et al [310, 311]. Alternatively, one can replace the LUT with ANN trained on the flamelet database [149, 91, 130, 94, 116]. This was seen to reduce the memory footprint significantly [91], although performance gain compared to the interpolation routine was not always observed [116]. A discussion of ANN topologies and the inference architecture (GPU-based or CPU-based) for OpenFOAM solvers was recently reported in [295, 34].

1.2.3. Turbulence-Chemistry Interaction (TCI)

In the LES context it is important to take into account the effects of the sub-grid scale (sgs) fluctuations on the local filtered reaction rates, because the rate controlling processes like molecular transport and chemical reactions occur at the modelled scales [237]. This is the target of the TCI model.

Two approaches are used for TCI, depending on how the joint Probability Density Function (PDF) is calculated. A detailed review on this topic is provided by Haworth [120]. Reduced manifold models, like the flamelet approach [221] or the Conditional Moment Closure (CMC) [19, 155] are usually combined with a presumed PDF, as a function of the first two moments of one or more key quantities. This is the standard model for CFD simulations of rocket combustion chambers based on flamelet databases (e.g. [332, 185, 243, 31, 165, 217]). On the other hand, such an approach cannot be extended to the general case, since statistical independence is assumed between the PDF variables and the distribution shape is imposed. This limitation is lifted if the PDF is transported (TPDF), although a loss in computational speed is evident compared to presumed PDF computations [332]. While the chemistry source terms appear in closed form in TPDF, the mixing term requires modelling. Molecular mixing differs between combustion regimes and it is unlikely that a single approach will be able to satisfy all applications [229]. Moreover, due to the high dimensionality of the TPDF, the equation is impracticable to be solved in a deterministic way on computational grids [120]. The Lagrangian Monte Carlo particle TPDF method has been the dominant approach of the past decades to solve such equations in both LES and RANS context [140, 202, 234, 237]. Implementations of Lagrangian particles in RANS solvers are abundant in the literature, shown for example by the TPDF-RANS-ISAT solver of the research group of Pope (e.g. [318, 48]), the TPDF-RANS-REDIM solver stemming from the group of Maas [326, 197], or the TPDF-RANS-MMC solver adopted by several groups (e.g. [304, 285, 305, 325]) and based on the Multiple Mapping Conditioning (MMC) model. Nonetheless, the requirement of mass consistency between the ensemble of local particles and the Eulerian mesh [203, 246] poses a challenge in the LES context, since a large number of particles is required in order to achieve statistical convergence. Recently, a "sparse-Lagrangian" LES approach was proposed to overcome this limitation, based on the MMC model [58, 57, 59]. Its implementations for premixed and non-premixed regimes provided promising results (e.g [286, 96]). In fact,

enforcing locality in both composition and physical spaces allows to reduce significantly the overall number of particles compared to the number of mesh elements. Alternatively to the sparse Lagrangian MMC, the computational cost of Lagrangian particles LES can be also reduced using a conditional RANS-PDF method, which evaluates the composition joint-PDF on coarser meshes, as proposed in [25, 88].
Eulerian approaches were also investigated for TPDF in form of Eulerian Stochastic Fields (ESF) [251, 271, 297, 298], allowing in general an easier implementation of the modelled equations on the Eulerian mesh. Its implementation in the RANS context provided poor computational performance compared to the Lagrangian particle method [137] but this was not observed for LES. In fact, the number of stochastic fields required to approximate statistical convergence is considerably reduced, from $N_f = 40$ for RANS [137] to $N_f = 8$ for LES [141, 204]. Recent investigations on partially premixed flames configurations questioned the efficiency of the ESF solver compared to laminar chemistry computations neglecting the sgs-TCI modelling [118, 30, 164]. If enough HPC resources are not available when dealing with detailed chemistry ESF simulations, one could either neglect the sgs-TCI modelling on sufficiently refined meshes or make use of a tabulated chemistry. However, an extension of the first method to the general case should be avoided, since TCI modelling on the flame wrinkling is performed differently in premixed and non-premixed regimes. ESF solvers combined with pre-tabulated chemistry deriving from the FPV or the FGM combustion models were proposed for OpenFOAM applications by e.g. [6, 162] for premixed regimes and by [76, 187] for non-premixed regimes. A novel implementation of the "sparse-Lagrangian" MMC and the ESF solver coupled with the REDIM tabulated chemistry is proposed in this work instead.

1.2.4. Reacting film cooling

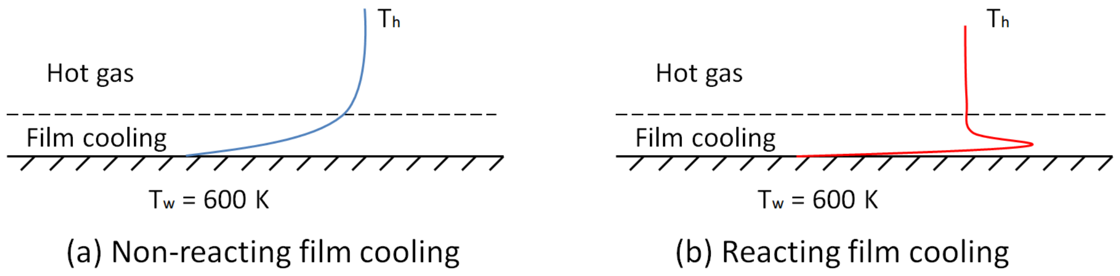

(a) Non-reacting film cooling

(b) Reacting film cooling

Figure 1.3.: Non-reacting and reacting film cooling

Thermal components for gas turbines and rocket combustion chambers are nowadays dimensioned to operate at hot gas temperatures above their thermal resistance limit, since higher temperatures can usually guarantee higher combustion efficiency. It is therefore necessary to prevent thermal damage of the structure by means of cooling techniques. Effusion cooling is typical of gas turbines applications, where the structure is usually protected by oxygen-rich cooling films, as sketched in Fig. 1.3-(a). Such devices operate at high fuel-air ratios, generating a significant heat release if species like CO and HC are emitted from the combustor in large quantities. When injecting coolant air into the hot fuel-rich mixture, secondary reactions can be triggered in the film, as depicted in Fig. 1.3-(b). This is not

ideal, since the chemical reactions near the wall would further increase the heat loads. Kirk [152] and Lukachko [175] estimated an increase in wall heat flux up to 25 % when a reactive boundary layer establishes. Investigation of secondary combustion in oxy-rich film cooling has been initiated in the past years at the Air Force Research Laboratory (AFRL) by Evans [85], using propane (C_3H_8) as fuel. Mixing between crossflows on the same test bench was numerically investigated by Polanka [230] using a 2-step mechanism for C_3H_8. The impact of variable geometry and allocation of the coolant holes was investigated in RANS calculations by Ghasemi [105]. De Lallo [70] and Bohan [22] modified the experimental setup of Evans [85], in order to investigate the effect of a second row of cooling holes on secondary combustion. PLIF data for OH emissions in the reacting zones were provided by [22]. This configuration was investigated in RANS simulations by Pohl [227, 226] to determine the impact of trench and ramp film cooling, and Frank [93] to validate tabulated frozen chemistry tables. The presence of only two thermocouple readings at the AFRL test bench allowed only the punctual calculation of the local wall heat flux.
Motivated by the need for further understanding secondary combustion, a novel test bench was developed at the Bundeswehr University of Munich by Dalshad [68]. The configuration is opposite to the test bench of Evans: cold fuel (CH_4, H_2 or C_3H_8) is injected into an oxygen-rich hot exhaust crossflow. PLIF measurements of OH allowed to locate the autoignition length of the fuel jets [68]. The wall heat fluxes could be reconstructed using the inverse heat transfer problem [66].

1.2.5. Flame-Wall Interaction (FWI)

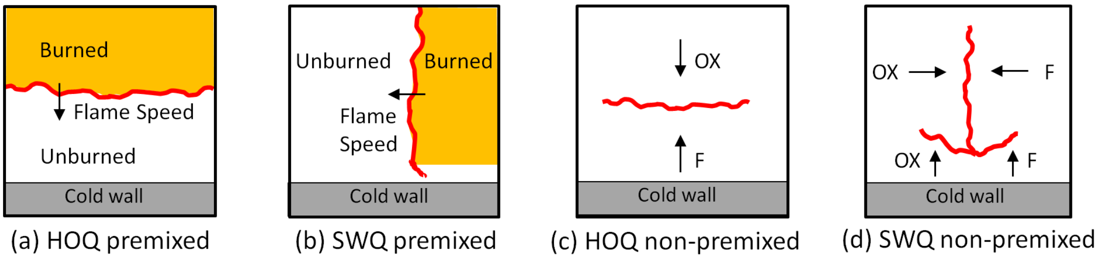

(a) HOQ premixed (b) SWQ premixed (c) HOQ non-premixed (d) SWQ non-premixed

Figure 1.4.: Typologies of Flame/Wall Interactions (FWI): Side-Wall Quenching (SWQ) and Head-On Quenching (HOQ) in premixed and non-premixed flames

In combustion devices like rocket engines, gas turbines or internal combustion engines the hot gases usually reach temperatures of 1500-2500 K, while the walls are cooled to 400-600 K [229]. The walls are heated by the flame, which is in turn subjected to enormous heat losses that can lead to local extinction (quenching). This interaction (FWI) is often the cause of local peaks in wall heat flux, due to the strong temperature gradients affecting the cooled flame. Therefore, FWI can have a negative impact on engine performance and components life. The complexity of the phenomenon increases in turbulent regimes, where the wall can modify the turbulent scales and near-wall effects, while turbulence can affect the flame wrinkling and strain. The experimental investigation of FWI is difficult, since the presence of maximum wall heat fluxes is intermittent [86, 139, 171]. Two quenching configurations could be identified in FWI of premixed laminar flames, as shown in Fig.1.4: in Head-On Quenching (HOQ) the flame front propagates perpendicularly to the wall, the flame thickness is reduced until quenching occurs at the wall proximity (a). In Side-Wall Quenching (SWQ) the flame propagates parallel to the wall and only the near-wall flame edge is subjected to quenching (b). HOQ premixed laminar configurations were investigated theoretically [314] and experimentally [86, 139], the SWQ configuration as well [303, 171]. A simple estimation of the maximum wall heat flux based on DNS of HOQ in laminar regime [228] could be extended to turbulent regimes [37, 2]. FWI using complex chemistry DNS for CH_4/air premixed flames was investigated in [240], demonstrating that global mechanisms based on single step reaction ([228, 37, 2]) are not suitable to describe FWI when the wall temperature exceeds 400 K. The previous studies on premixed regimes allowed an estimation of the maximum heat flux in the order of $0.5\,\mathrm{MW/m^2}$ for hydrocarbon flames ($5\,\mathrm{MW/m^2}$ for H_2/O_2 flames), alternatively comparable to 30% of the flame reference power [71, 308]. The study of FWI for diffusion flames is however scarce in the literature, because the identification of the flame topology near the wall is not as straightforward as for premixed flames. Since diffusion flames do not propagate, HOQ would lead to the stabilization of the flame at a certain distance from the wall, as shown in Fig.1.4-(c). If strain is introduced in the HOQ configuration, impinging of the flame against the wall is induced. The latter, named HOQS, was studied in the laminar DNS of [71] for hydrocarbon/air flames, revealing that heat fluxes larger than the those observed for a propagating premixed stoichiometric flame can be reached in such regimes. DNS of HOQ were investigated for fire applications using a single-step Ethylene/air mechanism by Wang [308]. Dabireau instead [63] focused on DNS of H_2/O_2 flames in HOQ. Diffusion and mixing were found to be affected stronger by FWI for H_2/O_2 diffusion flames, compared to hydrocarbon flames. SWQ in diffusion flames is difficult to capture, since the edge of the diffusion flame interacting with the wall can originate in a propagating triple flame [80], as illustrated in Fig.1.4-(d). The work of Wichman [313] describes such flames analytically.

Enthalpy losses generated by FWI must be modelled when reduced chemistry models are used, in order to correctly describe recombination reactions at the cooled walls. A numerical setup similar to Wang [308] was investigated for CH_4/O_2 combustion at 20 bar by Zips [331] to validate an equilibrium chemistry database. A further analysis using frozen chemistry and non-adiabatic tables identified the latter to better represent the FWI, provided that enthalpy losses are included in the database by means of a physical process [32, 31].
The test bench of the Technical University of Darmstadt investigates a SWQ burner configuration subjected to heat losses. A laminar methane [135, 136] or a dimethyl ether (DME) flame [158] at ambient condition can be stabilized by the hot exhaust gases. A detailed chemistry simulation of the sub-domain at the near-wall region [99] was able to match the CO predictions in good approximations for the CH_4/air configuration, while the same setup using FGM as tabulated chemistry showed an inaccurate CO prediction [121]. A further comparison of FGM and REDIM tables including enthalpy losses was performed for the methane [100] and DME configurations [277], showing again a systematic deficiency of the near-wall CO concentration predicted by the FGM. The versatility of REDIM tables to account for heterogeneous wall reactions [281] and detailed transport [283] in FWI configurations further confirms it as a valid alternative to the more commonly used flamelet databases (FGM, FPI, FPV).

1.2.6. CH_4 combustion for space applications

Another branch with growing attention for CH_4-based combustion technologies is the space industry. In fact, methane presents several advantages compared to the most commonly used fuel, H_2, when applied as liquid rocket propellant. For example, it requires smaller fuel tanks and feed systems, as well as a reduced operational cost [290]. It is also preferable to other oil-based hydrocarbons (e.g. RP-1) due to reduced soot deposition and coking under fuel-rich conditions. While the flame type in such combustion devices is relatively simple (non-premixed), the major challenge in the CFD is the representation of the wall heat fluxes and the non-ideal gas thermodynamics. Test campaigns were recently proposed worldwide in order to investigate methane combustion for space applications, as reported by Battista [13], Simontacchi [266], Tomita [294] and Tchou-Kien [292]. On the European level, the academic research has been active in the past decade. A recent effort in the framework of the Sonderforschungsbereich Transregio (SFB-TRR-40) promoted the generation of experimental data for gaseous CH_4/O_2 (and H_2/O_2) sub-scale combustion chambers. A capacitively cooled single-injector combustion chamber operated at a maximum pressure of 20 bar was developed at the Technical University of Munich [113, 51, 219, 316]. Injector-injector interactions could be further investigated by means of a second chamber operated up to 100 bar, consisting of 7 coaxial injectors [265]. Further understanding of supercritical injection and combustion of CH_4/O_2 was possible thanks to the Mascotte test facility of ONERA. An exemplary test case used for the validation of numerical codes based on real gas thermodynamics is the single-injector combustion chamber operated at the pressure of 50 bar [267].

Film cooling

Film cooling techniques for rocket combustion chambers use the fuel itself as cooling medium. Secondary reactions between hot gases and coolant however are here less probable, since cold fuel is injected into a fuel-rich mixture of combustion gases. Several configurations for film cooling were investigated at DLR. Suslov [288] investigated the interaction of the reacting flow with the film cooling (CH_4 at ambient conditions) close to the injector plate, in a CH_4/O_2 sub-scale combustion chamber operated at moderate pressure. Arnold instead [4, 5] investigated high pressure combustion of cryogenic LOX/GH2 with gaseous H_2 as film cooling. Numerical simulations from [288, 17] based on these chambers employed a pseudo-injector approach to avoid the prohibitive modelling of the multi-injector configurations, where composition products in chemical equilibrium were injected directly into the chamber. This assumption is usually justified for H_2 combustion but not for CH_4, since the C-chemistry cannot be considered infinitely fast. A single element GOX/Kerosene combustion chamber was developed and characterized by Kirchberger [151] at the Technical University of Munich (TUM). Recently, the single-injector GCH_4/GO_2 setup of Celano et al [51] was extended to provide an insight into film cooling [50, 49]. The film cooling effectiveness with tangential slot injection was investigated by varying the coolant fluid (CH_4 or Argon [49]), the combustion pressure (1 to 2 MPa), the slot geometry and the film blowing rate [50]. An increase in blowing rate did not necessarily correspond to an improvement in cooling performance, the latter reduced when using Argon as coolant due to its lower heat capacity. Numerous research groups already investigated a variety of combustion models for RANS [247, 186, 250, 165, 53, 244, 64, 218, 243, 309] and LES [201, 185, 333] based on the combustion chambers without film cooling. Only few numerical investigations have been recently published for the film-cooled configuration instead: the 1 MPa case with both cooling mediums for RANS [279] and the 2 MPa configuration with CH_4 as coolant for LES [213, 31].

Wall heat flux

In the design phase of the cooling system the prediction of mean wall heat fluxes is more important than the localization of the local peaks. In wall-resolved LES, the boundary layer is resolved across the burnt gas down to the viscous sub-layer, which allows a realistic prediction of the wall heat fluxes by means of the Fourier's law. Since high *Re* wall-resolved LES are computational expensive, hybrid RANS/LES or wall-stress modelled approaches are often the compelled choice [166]. In both approaches the small eddies in the inner boundary layer (about 20% of the turbulent boundary layer) are modelled, so that the inner layer models are used to estimate wall shear stresses and heat flux. Hybrid LES/RANS models (e.g. [15, 293, 212, 115, 264]) define the LES at a certain distance y from the wall, while the outer boundary layer is resolved by a RANS. When using hybrid methods where y is determined by the grid resolution [274, 212, 264] grid convergence is difficult to validate [166]. Nonetheless, accurate predictions of the wall heat fluxes were recently obtained in rocket combustion chambers using the Improved Delayed Detached Eddy Simulation (IDDES) model of Shur [264] in [31, 32, 126].
Wall-stress modelled LES instead are defined down to the wall, requiring an adequate wall-parallel cell resolution [166, 95]. To predict the wall heat flux in wall-modelled LES of rocket combustion chambers, the works of [201, 333, 185] used law-of-the-wall approaches, where an algebraic wall function is used to model the inner layer. Traditional law-of-the-wall formulations including heat transfer effects [257, 147] are based on nearly-isothermal assumptions: the temperature of the free flow T_g is close to the wall temperature T_w. Cabrit [46, 45] demonstrated that the conventional laws lose their validity in case $\frac{T_g}{T_w} > 3$, thus in combustion devices like rocket combustion chambers. A coupled law-of-the-wall accounting for strong temperature gradients and chemical effects was presented in [45]. Alternatively, the boundary layer equations can be solved via RANS using a local embedded grid (two-layer model), exploiting the thin equilibrium theory [42, 307, 145]. An improved version of [145] was applied to predict the wall heat fluxes in a RANS of a H_2/O_2 combustion chamber by Muto [207] combined with equilibrium chemistry tables to include chemical effects at the walls. An improved model to deal with CH_4/O_2 combustion was shown in [205]. Non-equilibrium thin boundary layers can also be solved according to the models of [7, 146]. Ma et al [177] introduced the resolution of a simplified 2D RANS equation to describe chemical effects at the wall in internal combustion engines. Radiation effects were accounted in the two-layer model of Zhang [328], where a reciprocal Monte Carlo approach was implemented to estimate the radiative power at the LES grid [327].

1.3. Scope of work

The scope of this thesis is providing a significant contribution to the investigation of reliable combustion models attractive for the industry, with focus on methane combustion (in air and O_2). Expensive LES of turbulent reacting flows are tackled by employing suitable reduced chemistry models capable of describing unsteady combustion regimes with extinction and re-ignition events. Fig. 1.5 shows the interconnectivity between the modelling blocks in a generic CFD solver. The solver communicates with the TCI module (blue box) to model the effects of chemistry on the sub-grid scale, and with the chemistry module to retrieve the thermo-chemical state at each time step. The latter can either exploit finite rate chemistry (gray box) or tabulated chemistry (orange box).

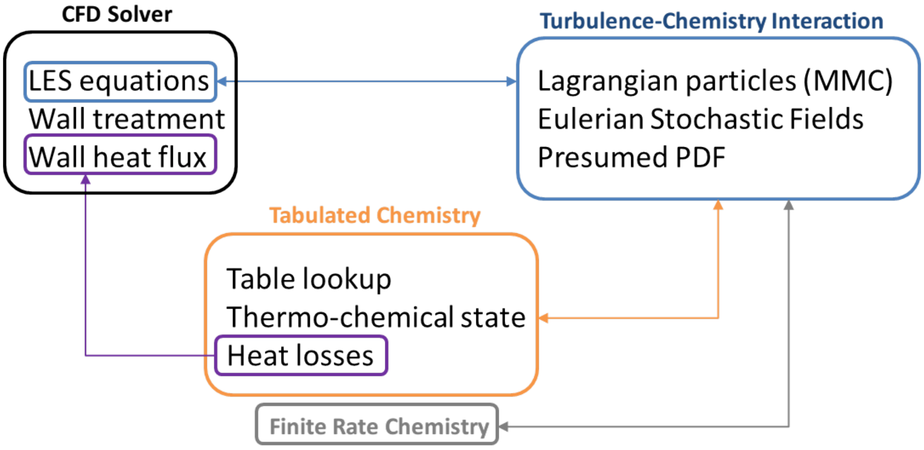

Figure 1.5.: Interconnectivity of the topics investigated in this work for LES of turbulent reacting flows

The effects of TCI and novel recent tabulated chemistry methods are thoroughly investigated for partially premixed CH_4/air flame configurations with homogeneous [10] and inhomogeneous inlets [11, 196]. In particular, two transported PDF methods are coupled with the promising tabulation technique of the REDIM, namely the Eulerian Stochastic Fields and the Multiple Mapping Conditioning (blue box). The investigation of FWI and the wall heat flux predictions are primarily conducted on CH_4/O_2 sub-scale rocket combustion chambers [113, 50], with a particular focus on the inclusion of FWI effects in flamelet-based databases and an efficient wall modelling (violet box). The experimental set-up recently developed at the Bundeswehr University of Munich [68] involving near-wall secondary reactions is selected as a benchmark for final validation using finite rate chemistry (gray box), as it can describe both autoignition delay and wall heat flux predictions. All implementations are developed in OpenFOAM [312].

1.4. Thesis outline

The fundamental equations for turbulent reacting flows and their modelling for LES computations are presented in Chapter 2, as well as the treatment required by wall-bounded flows. Chapter 3 presents a detailed discussion of the investigated chemistry models. An overview of novel reduced chemistry mechanisms for CH_4/O_2 combustion investigated in this work is provided, as well as a detailed description of the ILDM, REDIM and flamelet tabulation techniques. The complexity of the TCI modelling is introduced in Chapter 4, with focus on the transported PDF methods for ESF and MMC. A brief introduction to the presumed PDF assumption for flamelets is also provided. Finally, the test cases, the numerical setups and the results of this investigation are presented and discussed in Chapter 5. The conclusions are drawn in Chapter 6, together with an outlook for future investigations.

2. Turbulent reacting flows

2.1. The Navier-Stokes equations

Turbulent non-reactive flows (intended as fluid or gas) present unsteadiness and develop in the three dimensions. The Navier-Stokes (NS) equations govern the physical quantities involved in the process (mass, momentum and energy) resulting in a final system of five unknowns: the three velocity components u_i, the fluid density ρ and one of the energy parameters (pressure p, temperature T or enthalpy h). Transport equations for species conservation are additionally added in reacting flows.
The first equation implies the conservation of mass in the examined control volume, due to the absence of mass sources and sinks. The total mass of the system is conserved also in reacting flows, since combustion neither generates nor destroys mass. In compressible fluids, where the effects of pressure changes on the fluid density cannot be neglected, the continuity equation assumes the form:

$$\frac{\partial \rho}{\partial t} + \frac{\partial \rho u_i}{\partial x_i} = 0\,. \tag{2.1}$$

The conservation of linear momentum is derived from the Newton's second law, stating that the momentum ρu_i of a specific volume can only change due to a net external force. By neglecting the volume forces such as gravity, the following balance equation is obtained:

$$\frac{\partial \rho u_i}{\partial t} + \frac{\partial \rho u_i u_j}{\partial x_j} = -\frac{\partial p}{\partial x_i} + \frac{\partial \tau_{ij}}{\partial x_i}\,. \tag{2.2}$$

The RHS contains only the net contribution of the surface forces: the pressure gradient $\frac{\partial p}{\partial x_i}$ and the viscous stress tensor τ_{ij}. In order to model the viscous stresses, the fluid can be assumed to be Newtonian, where a linear relationship with the strain rate tensor exists. By writing the symmetric strain rate tensor S_{ij} as

$$S_{ij} = \frac{1}{2}\left(\frac{\partial u_i}{\partial x_j} + \frac{\partial u_j}{\partial x_i}\right) \tag{2.3}$$

the expression for the viscous stress tensor is linearly proportional to the strain rate tensor via the dynamic viscosity μ as:

$$\tau_{ij} = 2\mu\left(S_{ij} - \frac{1}{3}\frac{\partial u_k}{\partial x_k}\delta_{ij}\right)\,. \tag{2.4}$$

The dependency of the momentum equation on reacting flows is introduced via the properties μ and ρ, both strongly dependent on the fluid temperature.
The balance equation for energy is derived from the first law of the thermodynamics, stating that energy can be neither created nor destroyed during a process, but it can only be transformed. There are several possibilities to write this equation, depending on which scalar is chosen to describe the energy (for example specific enthalpy, internal energy or

temperature). In the OpenFOAM implementations used in this work the energy equation is mainly written for the mixture sensible enthalpy h_s. The NS energy equation is written accordingly as

$$\frac{\partial \rho h_s}{\partial t} + \frac{\partial \rho u_i h_s}{\partial x_i} = \frac{\partial p}{\partial t} + \frac{\partial u_i\, p}{\partial x_i} + \tau_{ij}\frac{\partial u_i}{\partial x_j} - \frac{\partial}{\partial x_i}\left(-\lambda \frac{\partial T}{\partial x_i} + \rho \sum_{k=1}^{n_s} (h_{s,k} Y_k\, V_{k,i}) \right) + \dot{\omega}_T + \dot{Q} \quad (2.5)$$

which requires further treatment on the RHS. The low Mach regimes (Ma < 0.3) encountered in this work allow to neglect the pressure fluctuations generated by the first two terms on the RHS, as well as the viscous heating term $\tau_{ij}\frac{\partial u_i}{\partial x_j}$. $\dot{Q}$ is a heat source term given for example by radiation, an electric spark or a laser, which is also not used in this work. Therefore, the only remaining terms derive from the following contributions:

- the heat diffusion expressed by the Fourier's law $\lambda \frac{\partial T}{\partial x_i}$, based on the thermal conductivity λ and the temperature gradient
- the diffusive enthalpy fluxes $\sum_{k=1}^{n_s}(h_{s,k} Y_k\, V_{k,i})$ including the sensible enthalpy $h_{s,k}$ and the i-th component of the diffusion velocity $\mathbf{V}_k$ of each species Y_k
- the heat released by combustion as $\dot{\omega}_T = -\sum_{k=1}^{n_s} \Delta h_k^0 \dot{\omega}_k$, containing the contribution of the species reaction rates $\dot{\omega}_k$ and their correspondent standard enthalpy of formation Δh_k^0

The complete discussion of this equation requires the definition of several thermo-chemistry properties, which are presented in the following paragraph.

2.1.1. Mixture properties: thermochemistry and transport

Each species involved in a reacting system can be characterized by the mass fraction $\mathrm{Y}_k = \frac{m_k}{m}$, with m_k the mass of species k present in a volume V and m the total mass of the gas. The sum of the mass fractions over the n_s species must fulfill the requirement of $\sum_{k=1}^{n_s} \mathrm{Y}_k = 1$. In anticipation to Section 3.3, several reacting systems describe the species in specific mole numbers $\phi_k = \frac{Y_k}{W_k}$ instead, where W_k is the molecular weight of species k. When including reacting species the dimensions of the Navier-Stokes system of equations is increased by additional n_s variables.

From the species properties, the mixture properties can be determined in the following way. By knowing (p, T) the mixture density is retrieved from the equation of state for ideal gases, as the ones investigated in this work:

$$\rho = \frac{p}{T}\frac{W}{\mathcal{R}}\,. \quad (2.6)$$

$\mathcal{R} = 8.315\,\mathrm{J/(mol\,K)}$ is the perfect gas constant and W the mean molecular weight of the mixture, calculated as $1/\sum_{k=1}^{n_s} Y_k/W_k$.

The enthalpy of each species k contains the contribution of the standard mass enthalpy of formation Δh_k^0, determined at temperature $\mathrm{T}_0 = 298.15\,\mathrm{K}$ and 1 atm, and the sensible enthalpy determined by the deviation from the standard conditions:

$$h_{s,k} = \int_{T_0}^{T} c_{p,k}(T)\, dT\,. \quad (2.7)$$

While the Δh_k^0 is a standard value pre-assigned in each numerical code, the calculation of $h_{s,k}$ requires the knowledge of the heat capacity at constant pressure $c_{p,k}$. The enthalpy calculation in OpenFOAM is performed in this work using the JANAF 7-coefficients polynomials [195] [1], resulting in a mixture sensible enthalpy of

$$h_s = \sum_{k=1}^{n_s} h_{s,k} Y_k = \int_{T_0}^{T} c_p \, dT \,. \tag{2.8}$$

The specific heat capacity of each species instead is calculated from the derived JANAF 5-coefficients polynomials (note that $\mathrm{dh}_s = \mathrm{c}_p \, \mathrm{dT}$), with the value for the mixture equal to

$$c_p = \sum_{k=1}^{n_s} c_{p,k} Y_k \,. \tag{2.9}$$

The calculation of the mixture temperature is done iteratively from Eq. (2.8).
The mixture viscosity depending on the local temperature T is calculated here from the Sutherland law [289] as

$$\mu = \frac{A_s \sqrt{T}}{1 + T_s/T} \tag{2.10}$$

with coefficients $\mathrm{A}_s = 1.67212 \cdot 10^{-6}\,\mathrm{Pa \cdot s}$ and $\mathrm{T}_s = 170.672\,\mathrm{K}$ [2]. By retrieving the heat capacity at constant volume as $\mathrm{c}_v = \mathrm{c}_p - \frac{\mathcal{R}}{W}$, the mixture thermal conductivity is calculated as

$$\lambda = \mu \, c_v \left(1.32 + \frac{1.77\,\mathcal{R}}{c_v \, W} \right) \tag{2.11}$$

according to the Eucken expression, as described in the book of Poling et al [232]. A limitation of this calculation is that the Sutherland coefficients A_s and T_s, originally derived for N_2, are equally assigned to all species. This assumption seems to be valid for hydrocarbon/air flames, where the properties of N_2 are dominating and the $\mathrm{c}_{p,N2}$ is very close to the mixture c_p. In combustion regimes of pure O_2, like the investigated rocket combustion chambers, this approximation could be weak. Fig. 2.1 reports a comparison of the two properties between the OpenFOAM transport (dashed lines) and the more detailed Wilke transport (cfr. [232]) implemented in the software Cantera (solid lines). A CH_4/O_2 counterflow diffusion flame calculated at 20 bar is used for comparison (introduced in Section 3.5). Although the difference appears remarkable, the effect on T (and major species) is minimal. The Sutherland transport is therefore retained for all simulations of this work.

2.1.2. Species transport

In reacting flows, each species k requires its Navier-Stokes transport equation, which is written as

$$\frac{\partial \rho Y_k}{\partial t} + \frac{\partial \rho u_i Y_k}{\partial x_i} + \frac{\partial \rho V_{k,i} Y_k}{\partial x_i} = \dot{\omega}_k \,. \tag{2.12}$$

---

[1] cfr. `janafThermo` thermodynamic class for OpenFOAM, e.g. https://cpp.openfoam.org/v3/a01208.html. Note that only 6 coefficients are used for h

[2] cfr. `sutherlandTransport` class for OpenFOAM, e.g. https://cpp.openfoam.org/v3/a02498.html

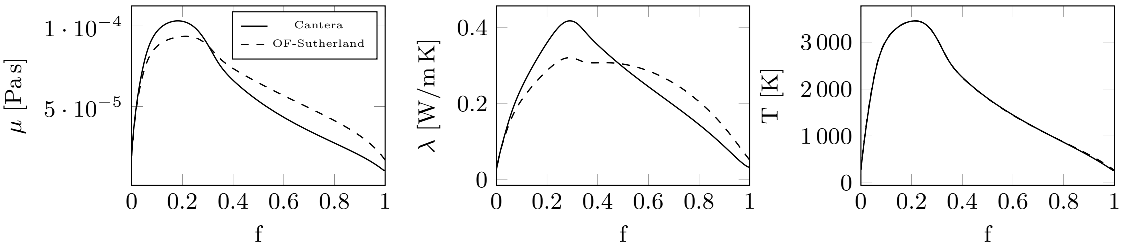

Figure 2.1.: Mixture transport properties μ and λ calculated with the Wilke model in Cantera (solid) and the Sutherland transport in OpenFOAM (dashed), for a CH_4/O_2 counterflow diffusion flame at 20 bar

If all n_s species equations are summed, one must obtain the continuity equation (2.1), implying two conditions: both the reaction rates and the diffusive fluxes sum to zero, thus $\sum_{k=1}^{n_s} \dot{\omega}_k{=}0$ and $\sum_{k=1}^{n_s} V_{k,i} Y_k{=}0$. The diffusive mass fluxes include the local diffusion velocity $\boldsymbol{V_k}$ previously encountered in Eq. (2.5). This is different from the convective transport determined by $\boldsymbol{u}$, since its general form includes the effects of the concentration gradients of all species except the investigated species k, temperature gradients and pressure gradients. The exact system for the $\boldsymbol{V_k}$ corresponds to a diffusion matrix of dimensions $n_s{\times}n_s$ which must be resolved at each time step and in each direction [315]. Since this operation is computational expensive, more simple approximations are conventionally used.

When using air as oxidizer, nitrogen is present in great amount, so that the diffusion flux $\boldsymbol{V_k} Y_k$ can be seen proportional to the concentration gradient of species k, i.e. $\nabla \mathrm{Y}_k$, leading to the Fick's law:

$$\boldsymbol{V_k}\, Y_k = -D_k \frac{\partial Y_k}{\partial x_i} - \frac{D_{k,th}}{\rho T} \frac{\partial T}{\partial x_i} \,. \tag{2.13}$$

D_k is the diffusion coefficient of species k in the mixture, which shall not be confused with the binary diffusion coefficient $\mathcal{D}_{ij}$ from the kinetic gas theory. A heat diffusivity coefficient is defined for the mixture as $\mathrm{D}_{th} = \lambda/(\rho\, \mathrm{c}_p)$. The second member of (2.13) represents the thermal diffusion due to temperature gradients (Soret effect).

Most numerical tools however rely on the Hirschfelder-Curtiss approximation [122], which is based on the gradient of mole fractions X_k. Considering the relation $\mathrm{X}_k = \frac{W}{W_k}\, \mathrm{Y}_k$ and the Hirschfelder approximation without the thermal diffusion term

$$\boldsymbol{V_k}\, X_k = -D_k \frac{\partial X_k}{\partial x_i} \tag{2.14}$$

the diffusion term on the LHS of Eq. (2.12) is re-written as

$$-\frac{\partial}{\partial x_i} \left(\rho D_k \frac{W_k}{W} \frac{\partial X_k}{\partial x_i} \right) \,. \tag{2.15}$$

The diffusion coefficients are calculated from $\mathcal{D}_{ij}$ as

$$D_k = \frac{1 - Y_k}{\sum_{j \neq k} X_j / \mathcal{D}_{ij}} \tag{2.16}$$

and are different from species to species, characterizing the so-called *differential diffusion* transport. This diffusion model is used in this work for the generation of REDIM chemistry

databases (presented in Section 3.4).
Three important quantities characterize mass and heat transport, thus the Lewis, Prandtl and Schmidt numbers:

$$Le_k = \frac{D_{th}}{D_k} \tag{2.17}$$

$$Pr = \frac{\mu/\rho}{D_{th}} \tag{2.18}$$

$$Sc_k = \frac{\mu/\rho}{D_k} \,. \tag{2.19}$$

Instead of using Eq. (2.16) to approximate the D_k, constant Lewis numbers Le_k can be assigned to each species in order to retrieve D_k from (2.17). A-priori sensitivity analysis has to be performed on the problem to estimate the Le_k.
In the Hirschfelder-Curtiss approximation however, the sum of the term (2.15) over all species is not zero, violating the requirement introduced for the original Eq. (2.12). A correction V_i^C is usually added to $\mathrm{V}_{k,i}$, the sum finally satisfying the constraint:

$$\frac{\partial}{\partial x_i}\left(\rho \sum_{k=1}^{n_s} D_k \frac{W_k}{W}\frac{\partial X_k}{\partial x_i} - \rho V_i^C\right) = 0\,. \tag{2.20}$$

To avoid this inconsistency, a further simplification can be applied on the diffusivities, using *unity Lewis numbers*, as it will be done through-out this work unless otherwise stated. Assuming $Le_k = Le = 1$ the species diffusivities are equal to the thermal diffusivity, which can be easily calculated at each time step from the mixture properties. The diffusive enthalpy fluxes introduced for the energy equation (2.5) are therefore null in this case. H_2/air or H_2/O_2 flames are examples where neglecting multi-component diffusion could lead to wrong predictions [117], since H_2 diffuses faster than any other species. Since this work is targeted to methane combustion, the assumption is retained to be valid. The effects of including differential diffusion in the chemistry databases for the calculation of the CH_4/air Sandia flames will be discussed in Chapter 5.

2.2. Turbulence modelling

The development of turbulence models features numerous challenges, mainly due to the fact that the turbulent motion is distributed across large and small scales. In a generic turbulent configuration the velocity field $\boldsymbol{u}$ is random in the 3D space, it is non-stationary and the motion appears as chaotic and rotational. Under such premises, the molecular transport is enhanced compared to a laminar configuration. The transition from a laminar to a turbulent configuration occurs when small flow perturbations cannot be further damped by the viscous forces. If the flow is characterized by a length scale $\mathcal{L}$, one of the key parameters to characterize turbulence is the Reynolds number $Re = \frac{U\mathcal{L}}{\nu}$, representing the ratio between the inertial and viscous forces. In the expression, U is a reference velocity and ν is the kinetic viscosity. The higher the Re, the more negligible is the viscous effect on the turbulent motion. A critical Re can be estimated from experimental configurations (e.g. channels, pipes or flows over a flat-plate) to locate the transition between laminar and turbulent regimes.

Eddies of size $l < l_0 \approx \mathcal{L}$ form within the turbulent flow. Seen from another perspective, thus in the spectral space, each eddy is characterized by a wave number $k = \frac{2\pi}{l}$ represented by a turbulent energy $\mathcal{E}(k)$. Integrating the turbulent energy $\mathcal{E}(k)$ over the spectral space leads to the definition of the turbulent kinetic energy $\mathcal{K}$. The latter can be also evaluated from the variances of the velocity components as

$$\mathcal{K} = \frac{1}{2}(\langle u''^2 \rangle + \langle v''^2 \rangle + \langle w''^2 \rangle) \tag{2.21}$$

where the symbol $\langle \cdot \rangle$ indicates from now on the average over time.
Turbulent eddies are unstable and are subjected to break-up towards smaller scales. In this process, known as energy cascade, the turbulent energy $\mathcal{E}(k)$ is transferred from the large eddies to the small ones (or alternatively, towards higher wave numbers k), until a point is reached where the energy is dissipated. This process is reproduced visually in Fig. 2.2 following the direction of the arrows from the right to the left:

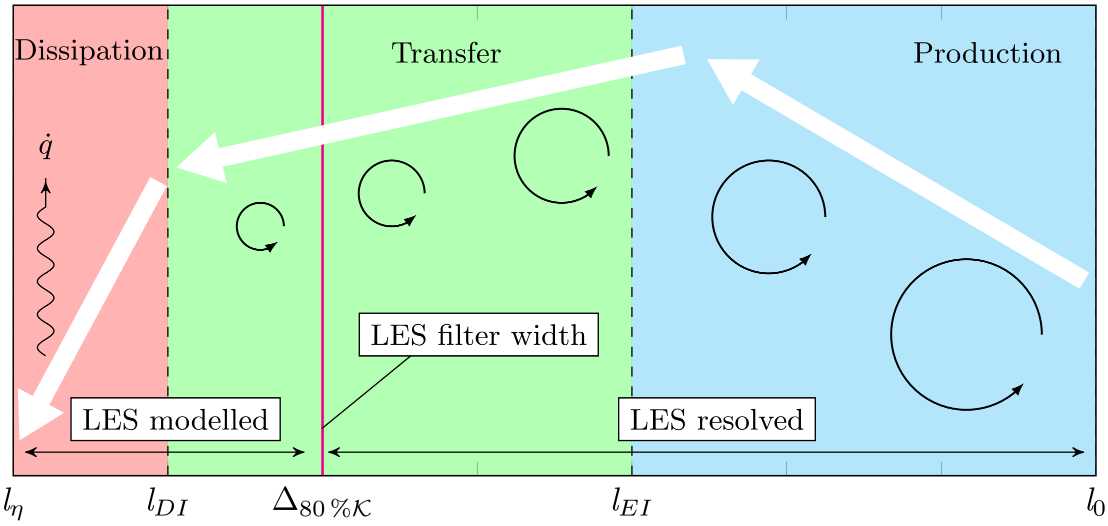

Figure 2.2.: Qualitative description of the energy cascade in turbulent flows from the large turbulent scales (l_0) to the smallest scales (l_η)

- Production of turbulent energy is dominant at larger scales, where fluctuations of the mean flow fields are stronger. Such fluctuations are generated for example by the inflow boundary conditions or the geometry of the investigated configuration and contribute to increase the turbulent kinetic energy of the flow. In this region (coloured in blue) the eddies are anisotropic and depend on the geometrical size of the problem. The main production is located at the shear layers. The rate of energy dissipation ϵ_0 for the scales l_0 can be estimated as $\frac{u_0^2}{\tau_0} = \frac{u_0^3}{l_0}$ where no viscous forces influence the process yet. The scale l_{EI} locates the peak in $\mathcal{E}(k)$ and sets the boundary to the inertial-driven region.

- According to the formulation of Kolmogorov, for $l < l_{EI}$ the eddies can be considered isotropic, thus any directional information transported by the large scales is lost. In the green region, the small eddies adapt quickly to maintain a dynamic equilibrium with the energy transfer rates derived from the large scales, so that the statistic motion can be described directly by the rate of dissipation ϵ. The inertial forces are dominant in this region. However, isotropy is not found in boundary layers.

- Dissipation of energy governs the remaining region (in red) for $l < l_{DI}$, where the turbulent energy is rapidly dissipated into heat by the fluid viscosity. The smallest scale at which the energy vanishes is the Kolmogorov length scale l_η, defined as $(\nu^3/\epsilon)^{1/4}$, at which the Reynolds number $Re_{l\eta}$ is unity.

For a detailed discussion of the energy cascade process and the integral lengths l_{EI}, l_{DI} the reader is pointed to chapter 6 of [237]. A relation between large and small turbulent structures can be defined for isotropic turbulence as

$$\frac{l_0}{l_\eta} = \frac{l_0}{(\nu^3/\epsilon_0)^{1/4}} = Re^{3/4} \tag{2.22}$$

showing how the Kolmogorov scale l_η strongly decreases by increasing the Reynolds number.

The application of Eq. (2.22) for direct CFD simulations would require a computational domain of at least dimension l_0, with a mesh resolution close to l_η, for a total number of grid points proportional to $Re^{3/4}$. Since Eq. (2.22) was derived for isotropic turbulence, a 3D case would require a number of grid points proportional to $Re^{9/4}$ instead. Considering time as a forth dimension for discretization, one obtains a proportion to Re^3. The resolution of the complete turbulence spectrum down to the Kolmogorov scale l_η represents the DNS approach. Since the Navier-Stokes equations presented in paragraph 2.1 are directly resolved on the computational grid, DNS can provide the highest fidelity computation. However, since the smallest turbulent scales must be resolved, the computational cost for high Reynolds numbers configurations is still prohibitive for industrial applications. The use of DNS is usually limited to academic investigations.

Opposite to DNS is the RANS approach, where the complete turbulence spectrum is modelled and the NS equations are solved for the average fields only. This dramatically alleviates the requirements on the computational cost, but introduces uncertainties due to the modelling.

The approach used in this work is LES, which lies between the DNS and RANS. Most of the turbulent scales are resolved on the grid, but the smallest eddies are subjected to a cut-off so that only the sub-grid fluctuations are modelled. The increased computational power in the past twenty years made this tool attractive for the industry, although simulations of turbulent reacting flows can be still computational demanding. One difficulty of LES, however, is the choice of the length scale l (or the cut-off wave length k) to delimit the small turbulent scales which shall be modelled. LES solutions are grid dependent, since the cut-off filter is usually the cell size Δ. However, Pope [238] introduced a measure for the turbulence resolution: the computational grid shall be sufficiently refined to guarantee that at least 80 % of the kinetic energy $\mathcal{K}$ is resolved. This delimiting line is qualitatively marked in Fig. 2.2 at location $\Delta_{80\%\mathcal{K}}$. All meshes used in the LES of this work satisfy the requirement of

$$\mathcal{I} = \frac{\mathcal{K}_{sgs}}{\mathcal{K}_{solved} + \mathcal{K}_{sgs}} < 0.2 \tag{2.23}$$

with $\mathcal{K}_{solved}$ the resolved turbulent kinetic energy and $\mathcal{K}_{sgs}$ the modelled one. One would find a DNS for $\mathcal{I} = 0$ and a RANS for $\mathcal{I} = 1$.
The computational advantages of LES against DNS are partially lost when modelling wall-bounded flows at high *Re*, unless wall treatments are considered, as explained in Section 2.4. The next paragraph introduces the LES model in detail.

2.3. Large Eddy Simulations

In LES, a spatial filter is applied to the NS equations, so that the large turbulent scales are directly resolved, and only the small turbulent scales require modelling. Compared to DNS, the constraint on the number of mesh points as a function of the Reynolds number is reduced to $Re^{2.7}$ [52].

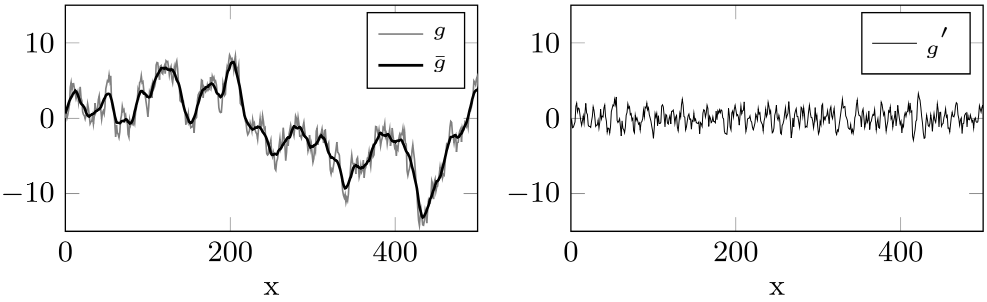

Figure 2.3.: LES spatial filtering of variable g leading to the resolved quantity $\bar{g}$. Only the sub-grid fluctuations g' require further modelling

A generic field g can be decomposed into $g = \bar{g} + g'$, the meaning of the decomposition depending on the modelling. While ensemble averages are used in RANS, in LES the variable is decomposed into a filtered part $\bar{g}$ which is calculated, and a small scale part g' which is modelled. Fig. 2.3 shows this decomposition on the physical space. Filtering the generic variable g means that a convolution product is applied in form of a low-pass filter $\mathcal{G}$, which satisfies the constraint

$$\int \mathcal{G}(\boldsymbol{x},\boldsymbol{y})\, d\boldsymbol{y} = 1\,. \tag{2.24}$$

The variables can be either filtered in spectral space using a cut-off frequency, or in physical space using a weighted average over a given volume. The latter approach is used in OpenFOAM, where $\mathcal{G}$ corresponds to averaging over a cubic box of size $\Delta = \sqrt[3]{V_{cell}}$. The filter function can be written as $\frac{1}{\Delta}\mathcal{H}(\frac{1}{2}\Delta - |x_i - y_i|)$ for each of the three spatial coordinates i, with $\mathcal{H}$ being the Heaviside function. The filtered variable is therefore written as

$$\bar{g}(\boldsymbol{x}, t) = \int g(\boldsymbol{x} - \boldsymbol{y}, t)\, \mathcal{G}(\boldsymbol{x},\boldsymbol{y})\, d\boldsymbol{y} \tag{2.25}$$

where each $\bar{g}(x_i)$ is the average of $g(y_i)$ within the interval $(x_i - \frac{1}{2}\Delta)$ and $(x_i + \frac{1}{2}\Delta)$.
When dealing with compressible fluids, a density-weighted filtering is further applied as $\tilde{g} = \overline{g\rho}/\bar{\rho}$, which leads the Favre decomposition

$$g = \frac{\overline{g\rho}}{\bar{\rho}} + g'' \tag{2.26}$$

allowing the transformation of Eq. (2.25) into

$$\tilde{g}(\boldsymbol{x},t) = \frac{\int \rho(\boldsymbol{x}-\boldsymbol{y},t)g(\boldsymbol{x}-\boldsymbol{y},t)\,\mathcal{G}(\boldsymbol{x},\boldsymbol{y})\,d\boldsymbol{y}}{\int \rho(\boldsymbol{x}-\boldsymbol{y},t)\,\mathcal{G}(\boldsymbol{x},\boldsymbol{y})\,d\boldsymbol{y}}\,. \tag{2.27}$$

2.3.1. Favre-filtered LES equations

Using Eq. (2.26) to filter the NS equations leads to the following transport equations for continuity, momentum, enthalpy and chemical species:

$$\frac{\partial\bar{\rho}}{\partial t} + \frac{\partial\bar{\rho}\tilde{u}_i}{\partial x_i} = 0 \tag{2.28}$$

$$\frac{\partial\tilde{\rho}u_i}{\partial t} + \frac{\partial\bar{\rho}\tilde{u}_i\tilde{u}_j}{\partial x_i} = -\frac{\partial\bar{p}}{\partial x_i} + \frac{\partial}{\partial x_i}\left(\bar{\tau}_{ij} - \bar{\rho}(\widetilde{u_i u_j} - \widetilde{u}_i\widetilde{u}_j)\right) \tag{2.29}$$

$$\frac{\partial\bar{\rho}\tilde{h}_s}{\partial t} + \frac{\partial\bar{\rho}\tilde{u}_i\tilde{h}_s}{\partial x_i} = \frac{\partial}{\partial x_i}\left(\overline{\lambda\frac{\partial T}{\partial x_i}} - \bar{\rho}\,(\widetilde{u_i h_s} - \tilde{u}_i\,\widetilde{h}_s)\right) + \bar{\dot{\omega}}_T \tag{2.30}$$

$$\frac{\partial\bar{\rho}\widetilde{Y}_k}{\partial t} + \frac{\partial\bar{\rho}\tilde{u}_i\widetilde{Y}_k}{\partial x_i} = \frac{\partial}{\partial x_i}\left(\overline{V_{ki}Y_k} - \bar{\rho}\,(\widetilde{u_i Y_k} - \tilde{u}_i\,\widetilde{Y}_k)\right) + \bar{\dot{\omega}}_k \tag{2.31}$$

The filtered stress tensor $\bar{\tau}_{ij}$ is written according to Eq. (2.4) using the filtered quantities. Due to the filtering, the equations present unclosed terms which require further modelling. A detailed discussion is provided for example by Sagaut [254] or Pope [237], but the terms are briefly introduced hereby:

- The unresolved Reynolds stresses $(\widetilde{u_i u_j} - \widetilde{u}_i\widetilde{u}_j)$ are approximated by the sub-grid scale turbulence model, which must correctly reproduce the energy dissipation process taking place in the red region of Fig. 2.2. The Boussinesq hypothesis allows to model this term as

  $$\bar{\rho}(\widetilde{u_i u_j} - \widetilde{u}_i\widetilde{u}_j) = \tau_{sgs,ij} = -2\nu_{sgs}\bar{\rho}\left(\widetilde{S}_{ij} - \frac{1}{3}\delta_{ij}\widetilde{S}_{kk}\right)\,. \tag{2.32}$$

  with ν_{sgs} requiring modelling. The *Smagorinsky* model [268] for ν_{sgs} is very popular because of its simple formulation. From a dimensional analysis, the sgs viscosity is seen to be proportional to the sgs length scales and the velocity scales. Smagorinsky chose the filter width and the resolved strain rate tensor to represent ν_{sgs} as

  $$\nu_{sgs} = (C_S\,\Delta)^2\sqrt{2\widetilde{S}_{ij}\widetilde{S}_{ij}}\,. \tag{2.33}$$

  Depending on the flow typology, the constant C_S can vary between 0.1 and 0.2, although a dynamic adaptation can be performed according to the model of Germano et al [104]. Here the constant value $C_S = 0.168$ was used, as implemented in the

OpenFOAM class [3]. A weakness of this model is that its parameters depend on the investigated configuration and the model itself is usually found to be too dissipative, especially near walls.
The Wall-Adapting Local Eddy-viscosity (*WALE*) model of Nicoud and Ducros [211] was conceived explicitly for wall-bounded LES and models the viscosity as

$$\nu_{sgs} = (C_w \Delta)^2 \frac{(s^d_{ij}\, s^d_{ij})^{2/3}}{(S_{ij}\, S_{ij})^{5/2} + (s^d_{ij}\, s^d_{ij})^{5/4}} \,. \tag{2.34}$$

The details regarding this model are reported in the original work [211].

- The filtered laminar diffusion fluxes of enthalpy $\overline{\lambda \frac{\partial T}{\partial x_i}}$ and species $\overline{V_{ki} Y_k}$ are modelled through a simple gradient approximation as $\lambda \frac{\partial \widetilde{T}}{\partial x_i}$ and $-\frac{\bar{\rho}\,\bar{\nu}}{Sc}\frac{\partial \widetilde{Y}_k}{\partial x_i}$, the latter exploiting the relations of (2.17)-(2.19) using the unity Lewis number assumption ($D_{th} = D_k = D$).

- The unresolved enthalpy and species fluxes ($\widetilde{u_i h_s} - \tilde{u}_i\, \widetilde{h}_s$) and ($\widetilde{u_i Y_k} - \tilde{u}_i\, \widetilde{Y}_k$) are also described using the gradient approximation

$$\widetilde{u_i h_s} - \tilde{u}_i\, \widetilde{h}_s = -D_{th,sgs}\frac{\partial \widetilde{h}_s}{\partial x_i} = -\frac{\nu_{sgs}\bar{c}_p}{Pr_{sgs}}\frac{\partial \widetilde{T}}{\partial x_i} \tag{2.35}$$

$$\widetilde{u_i Y_k} - \tilde{u}_i\, \widetilde{Y}_k = -D_{k,sgs}\frac{\partial \widetilde{Y}_k}{\partial x_i} = -\frac{\nu_{sgs}}{Sc_{sgs}}\frac{\partial \widetilde{Y}_k}{\partial x_i} \tag{2.36}$$

  with Sc_{sgs} and Pr_{sgs} being respectively the Schmidt and Prandtl numbers for the sub-grid scales. Here their value has been set to 0.7 according to previous investigations ran with this software (e.g. [330, 118]) unless otherwise stated.

- The closure of the filtered chemical reaction rates $\bar{\dot{\omega}}_k$ for Eq. (2.31) requires particular attention, since most of the turbulence-chemistry interaction occurs on the sub-grid scales which are modelled in LES. This topic will be addressed in detail in Chapter 4. The filtered heat released by combustion $\bar{\dot{\omega}}_T$ for the enthalpy equation (2.30) is calculated using the standard enthalpy of formation as $\bar{\dot{\omega}}_T = \sum_{k=1}^{n_s} \Delta h^0_k \bar{\dot{\omega}}_k$.

2.3.2. Statistical quantities

In order to compare LES with experimental data, statistical quantities must be extracted from the turbulent flow. Under the assumption that the filter size remains small compared to the spatial evolution of the means, the time averaged value of the resolved scales $\tilde{g}$ is calculated as

$$\langle g \rangle = \frac{1}{T}\int_{t=0}^{T} \tilde{g}(t)\, dt \tag{2.37}$$

while the variance of the quantity g is expressed as

---

[3] `https://caefn.com/openfoam/smagorinsky-sgs-model`: C_s is calculated from the OpenFOAM constants C_e and C_k

$$\langle g''^2 \rangle = \frac{1}{T} \int_{t=0}^{T} (\langle g \rangle - \tilde{g}(t))^2 \, dt \,. \tag{2.38}$$

The two expressions above are also known as the first and second moments of the turbulent field g. The choice of the time interval depends on the computational domain, with T usually set to guarantee an average over 5 to 10 flow-through times.

2.4. Wall-bounded turbulent flows

Turbulent structures in the proximity of walls are dominated by a rapid break-up of the eddies and the consequent heat dissipation within the boundary layer: the higher the *Re* in the core flow, the thinner the boundary layer. Since the small eddies are filtered by the cell size Δ, a sufficient mesh refinement in the wall normal direction is required in LES to guarantee that at least 80 % of $\mathcal{K}$ is resolved in this region. This configuration is known as *wall-resolved LES* (WRLES). In order to alleviate the computational cost of WRLES, one can apply the requirement of Eq.(2.23) only to the core flow, obtaining a *wall modelled LES* (WMLES), where the boundary layer is completely or partially modelled. According to the classification provided by Larsson et al [166], two types of WMLES exist, depending on the grid requirements in the wall-parallel direction: in *wall-stress modelled LES*, the LES must be defined down to the wall. In *hybrid LES/RANS* instead, only the core flow is treated as LES, while a RANS model is used at walls, allowing the use of a coarser grid spacing. The computational cost reduces to about $Re^{0.53}$ [52] in the first case and as a function of *log(Re)* [264] in the second case. Both WMLES were used in this work for the wall heat flux predictions of the sub-scale rocket combustion chamber [113].

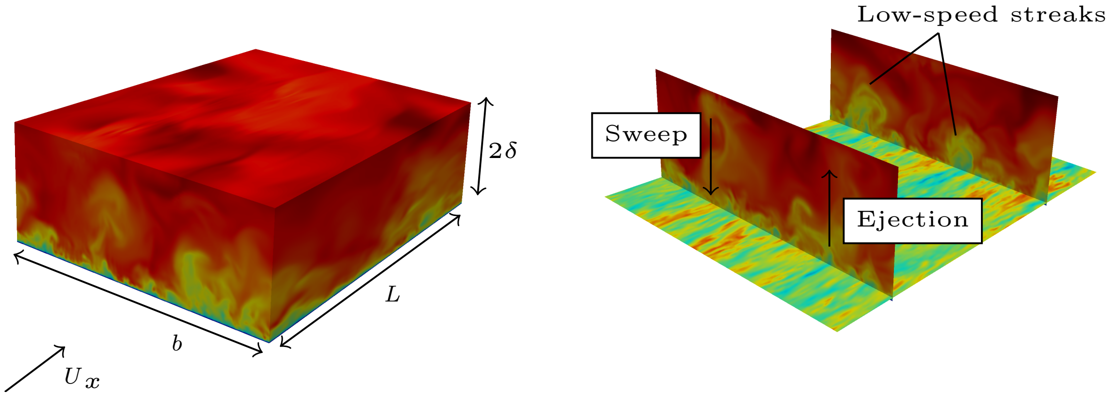

Figure 2.4.: Left: channel flow configuration qualitatively showing the axial velocity $\widetilde{U}_x$. No-slip conditions applied at the lower wall. Right: representation of the speed streaks developing near the wall

The variables required to describe the near-wall flows are presented for a fully-developed channel flow. Their definition and extension to pipe and flat-plate boundary flows can be found in [237]. For the next paragraphs it is useful to introduce a representative CFD configuration, shown in Fig. 2.4, whose characteristic length is set to be half of the channel height, here $\delta = 3\,\text{mm}$. The remaining dimensions are set to $L \times b = 16\delta \times 6\delta$, similarly to previous investigations [206, 153]. The fluid is bounded by walls at positions $y = 0$ and 2δ. A no-slip condition is applied at the bottom wall kept at temperature $T_{w,bottom} = 400\,\mathrm{K}$, while the upper wall has $T_{w,top} = 3000\,\mathrm{K}$ and slip boundary conditions. This allows to maintain a bulk temperature of 1500-1600 K in the core flow, whereas the bulk velocity U_b is set to 160 m/s. Cyclic boundary conditions are applied in the streamwise and spanwise directions. The near-wall turbulence is characterized by the so called flow streaks [237], represented on the right side of Fig. 2.4 by the axial velocity U_x. Ejection phenomena occur when a low-speed streak (blue/green color scale) migrates away from the wall, extending the region of cooled gases towards the core. Opposite is the sweep motion localized at the high-speed streaks, forcing the hot gases to approach the cooled wall. The latter causes the temperature gradient at wall to increase, leading to an increase in wall heat flux $\dot{q}_w$.

Momentum transfer due to turbulence is almost null close to the wall, because the fluctuations in the wall normal direction (U_y'') are blocked. The no-slip condition applied on the velocity at $y = 0$, thus $\mathrm{U}_y = 0$, induces a frictional shear at the wall, defined as

$$\tau_w = \rho_w \nu_w \left.\frac{dU_x}{dy}\right|_w \tag{2.39}$$

with ν_w the viscosity at wall and the friction velocity u_τ calculated as

$$u_\tau = \sqrt{\frac{|\tau_w|}{\rho_w}}\,. \tag{2.40}$$

The latter is used to normalize the mean velocity as $u^+ = \frac{U_x}{u_\tau}$. The influence of the viscous effects induced by the wall are captured by the viscous length scale $y_\tau = \frac{\nu_w}{u_\tau}$. This leads to the definition of the non-dimensional wall-distance $y^+ = \frac{y}{y_\tau}$, a fundamental indicator of the mesh refinement at wall. The streamwise and the spanwise non-dimensional distances x^+ and z^+ can be defined in the same way, based on y_τ. The ratio $x^+/z^+ \approx 3$ is an appropriate requirement for wall-bounded LES (see [95, 264]).
Similarly, the non-dimensional temperature in the wall-normal direction is written as

$$T^+ = \frac{T_w - T}{T_\tau} \tag{2.41}$$

where T_τ is directly calculated from the wall heat flux as $\frac{\dot{q}_w}{\rho_w\, c_{p,w}\, u_\tau}$ [229]. The non-dimensional velocity profile across the boundary layer is shown on the left side of Fig. 2.5, where four zones can be identified [257, 147]:

- $y^+ < 5$: *viscous layer*. The flow regime is quasi linear since only the molecular viscosity (ν) is responsible for heat dissipation, because in the LES equations $\nu_{sgs} \rightarrow 0$. Velocity and temperature boundary layers are expressed as $u^+ = y^+$ and $T^+ = Pr\, y^+$ respectively. A WRLES requires the first cell center at wall to be located within this range, in the optimal case at $y^+ = 1$.

- $5 < y^+ < 30$: *buffer layer*. Since the effects of viscosity and turbulent fluctuations are comparable in this layer, the first cell center is usually assigned outside this range ($y^+ < 5$ if the *Re* is small enough, or $y^+ > 30$ for high *Re*).

- $30 < y^+ < 50$: *log-layer within the inner boundary layer*. According to the boundary layer theory, a logarithmic law can describe u^+ and T^+ in the form of $\frac{1}{\mathcal{A}}\, ln(y^+) + \mathcal{B}$.

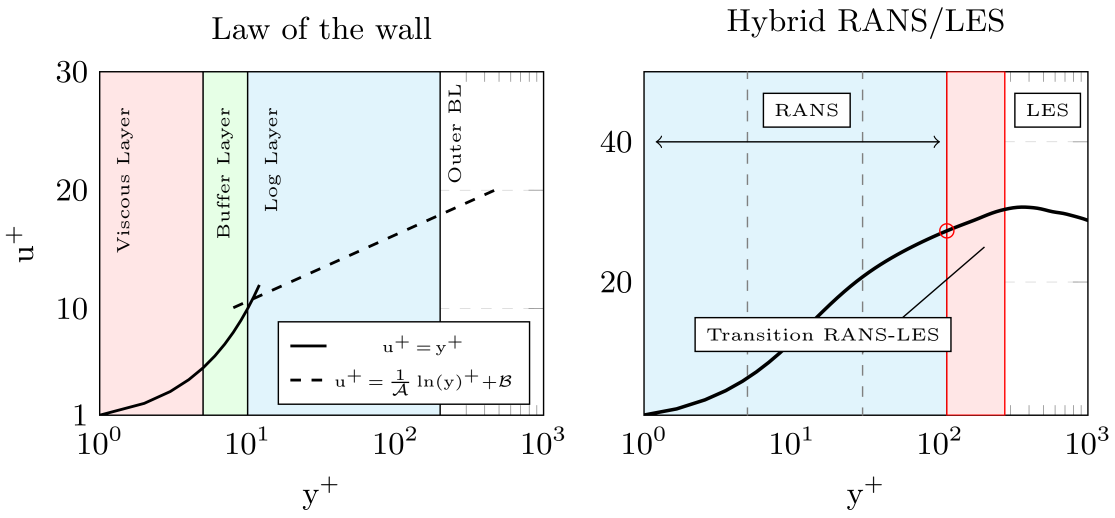

Figure 2.5.: Wall-modelled LES using the law of the wall (left) or a hybrid RANS/LES solver (right)

If the first cell center is located at $y^+ > 30$, one is using a wall model. Since the peak in turbulence production occurs in the lower buffer layer ($\mathrm{y}^+ < 20$), the exact location depending on the *Re* [237], not only Eq. (2.39) but also the wall heat flux $\dot{q}_w$ must be modelled by the wall function.

- $y^+ > 50$: *outer boundary layer.* In this layer the turbulent Reynolds stresses become dominant. An overlapping region between the inner and outer layer exists at high *Re* (cf. [237]) and its location marks the transition zone for the hybrid LES/RANS model explained in paragraph 2.4.4. The end of the inner layer is identified at $y/\delta = 0.1$.

Numerous wall functions exist in the literature [147], although most of them are derived from the investigation of non-reacting flows. The wall function from Spalding [275], already available in OpenFOAM in the class `nutUSpalding`, is used in this work as reference, since previously tested for the CH_4/O_2 combustion chambers (see [332, 333] for details). Although an accurate velocity profile can be obtained at wall, there is no coupling with the temperature profile T^+, so that a consistent evaluation of $\dot{q}_w$ is missing. In this case, the wall heat flux is approximated from $\lambda \nabla \widetilde{T}$.
Cabrit demonstrated that the standard laws (like `nutUSpalding`) can lose their validity if the temperature of the hot gases T_g is more than three times higher than the wall temperature T_w [46, 45]. Since values of $T_g/T_w > 5$ were observed for the investigated combustion chamber, the use of `nutUSpalding` shall be questioned. Two additional functions were implemented in OpenFOAM and reported hereby.

2.4.1. Nearly-isothermal wall function

The first implemented function, named `nearlyIsothermalWallFunction`, provides a log-law for T^+, but it assumes $T_g/T_w \approx 1$. Thus, its applicability is guaranteed where no significative heat transfer is present between the fluid and the walls. The expressions for the log layers are taken from Poinsot et al [229] and the following steps are applied at each time step and for each wall patch. The index $_1$ indicates the value at the first cell center from the wall:

1. u_τ is calculated from the following expression, using a Newton-Raphson iterator
$$\frac{u_1}{u_\tau} = 2.44\,ln\left(\frac{u_\tau\,y_1}{\nu_w}\right) + 5 \tag{2.42}$$
2. The y^+ is evaluated and, if its value is less than 10.8, the u_τ is recalculated to satisfy $u^+ = y^+$
3. For $y^+ > 13.2$ the reduced temperature is calculated as
$$T^+ = 2.075\,ln\left(\frac{u_\tau\,y_1}{\nu_w}\right) + 3.9 \tag{2.43}$$
otherwise it is retrieved as $T^+ = 0.7\,u^+$.
4. Finally, τ_w is calculated from Eq. (2.39) and $\dot{q}_w$ via T^+ from Eq. (2.41)

2.4.2. Coupled temperature-velocity wall function

The coupled u^+/T^+ law for LES presented by Cabrit [45] was validated for multicomponent reacting channel flows with significant heat transfer ($T_g/T_w > 3$) and low Mach numbers. Its complete formulation accounts for chemistry effects in the boundary layer (Appendix C of [45]), but a recent work of Maestro et al [185] showed that its simpler formulation, accounting only for the strong temperature gradients ∇T, is sufficient to correctly describe the $\dot{q}_w$ of the single-injector combustion chamber object of this study. Therefore, the same law shown in [185] was integrated in OpenFOAM and named `coupledTUWallFunction`. For each wall face, the following steps are applied at runtime:

1. The Van Wijngaarden-Dekker-Brent method [242] is used to find the root u_τ of the following equation
$$\frac{2\,T_w(Pr_{sgs}\,u_1 + K\,u_\tau)}{Pr_{sgs}(T_w - T_1)}\left(\sqrt{1 - \frac{K}{T_w}\frac{T_w - T_1}{Pr_{sgs}\,u_1 + K\,u_\tau}\,u_\tau} - \sqrt{\frac{T_1}{T_w}}\right) = \left(\frac{1}{\kappa}\,ln\,\frac{y_1\,u_\tau}{\nu_w} + C_{vd}\right)\,u_\tau \tag{2.44}$$
A detailed description of how to calculate the coefficient K is provided in the original paper [45]. The constants $\kappa = 0.41$ and $C_{vd} = 5.5$ are taken from the same paper. The expression is calculated for $Pr_{sgs} = Pr = 0.7$.
2. The y^+ is evaluated and if its value is less than 11.445, the u_τ is recalculated to satisfy $u^+ = y^+$
3. The T_τ is calculated according to
$$\frac{T_w - T_1}{T_\tau} = (Pr\,y^+)e^\Gamma + \left(Pr_{sgs}\frac{u_1}{u_\tau} + K\right)\,e^{\frac{1}{\Gamma}} \tag{2.45}$$
with Γ defined in [45]

Table 2.1.: Channel flow WMLES, $\widetilde{\dot{q}}_{w,avg}$ in [MW/m^2]

Wall Model	T$_g$ [K]	T$_w$ [K]	T$_g$/T$_w$	y$^+$	x$^+$	z$^+$	$\widetilde{\dot{q}}_{w,avg}$	Re$_b$
`nutUSpalding`	1717	400	4.29	93	116	35	-0.74	71925
`nearlyIso`	1823	400	4.56	83	145	44	-3.96	70837
`coupledTU`	1420	400	3.55	126	19	6	-0.74	79298

4. Finally, τ_w is calculated from Eq. (2.39) and $\dot{q}_w$ via T^+ from Eq. (2.41)

Differently from the default OpenFOAM class `nutWallFunction`[4], here the mixing-length model [145] is used to calculate the inner-layer eddy viscosity $\nu_w = \kappa\, u_\tau\, y_1\, D$, with D being the van-Driest damping function

$$D = [1 - exp(-y^+/17)]^2 \tag{2.46}$$

as reported by Kawai and Larsson [145].

2.4.3. Validation on channel flow

This paragraph aims to briefly show the difference between the implemented laws and the Spalding law, using the CFD domain described in Fig. 2.4. The final mesh consists of about 3 million cells with gridding N$_x$×N$_y$×N$_z$ = 254×61×204. The first cells at wall are located at position y^+ varying between 70 and 130. The LES criterion on x^+/z^+ is satisfied, as reported in Table 2.1. The species are not transported and the temperature is considered a passive scalar.

For the range of temperature gradients expected in rocket combustion chambers ($T_g/T_w > 1$, Table 2.1), no DNS data or experimental measurements are available from the literature. As a consequence, a qualitative representation of the velocity and temperature profiles is provided similarly to Cabrit [46]. The velocity profile u^+ is re-scaled according to Huang and Coleman [124], using the Van Driest transformed velocity to account for flow compressibility (labelled as u^+_{VD} in the plots). The main findings are summarized in Fig. 2.6. The canonical function `nutUSpalding` (in blue) can approximate the momentum layer following the log behaviour also without the van Driest correction, while the thermal layer is out of range compared to the other T^+-based functions. The comparison of T^+ in the log-layer is here performed using the Kader's law [143]. An opposite behaviour is seen for the `nearlyIso` law (red), which is matching the Kader's law very well (since isothermal) but it misses the attaching point to the u^+, unless the van Driest correction is applied. As mentioned before, this law is already outside its T_g/T_w validity. When looking at `coupledTU` (green), the profiles present a steeper gradient across the boundary layer compared to the log-law. The velocity profiles seem to depart from the log-law behaviour (dashed line) as for `nutUSpalding`, but the corrected u^+_{VD} does not collapse to the log law. Four LES calculations from Cabrit (cases 38-41 of Table 4.2 in [46]) ran with the same coupled law for $T_g/T_w = 2$, 3, 4, 5 are added for comparison. The reader should notice that Cabrit imposed $T_w = 320$ K and a maximum T$_g$ = 1600 K in his calculations. Cabrit's computations are shown here because comparable with the boundary conditions of Table 2.1 and because they are useful to justify the steeper gradient reported by the green curves. Overall, an increase in T_g/T_w corresponds to higher values of u^+ when using the `coupledTU`. The u^+ calculated in OpenFOAM

---

[4] http://www.tfd.chalmers.se/ hani/kurser/OS_CFD_2016/FangqingLiu/openfoamFinal.pdf

is in good agreement with the results of Cabrit. The T^+ instead appears to overestimate the calculations of [46]. However, the behaviour of the thermal boundary layer is qualitatively reproduced by `coupledTU`, contrarily to `nearlyIso`. The fact that `nutUSpalding` provided an estimation of the wall heat flux very close to `coupledTU` (in MW/m^2 in Table 2.1) is due to the bulk temperature T_g, about 300 K lower for the `coupledTU` simulation.
To summarize, the `nearlyIso` function does not reproduce correctly the effects of a strong temperature gradient at wall. For this reason, only `nutUSpalding` and `coupledTU` are applied to the WMLES of the CH_4/O_2 combustion chamber in Chapter 5. Different wall heat flux predictions are expected from these laws, in accordance to what observed in Fig. 2.6.

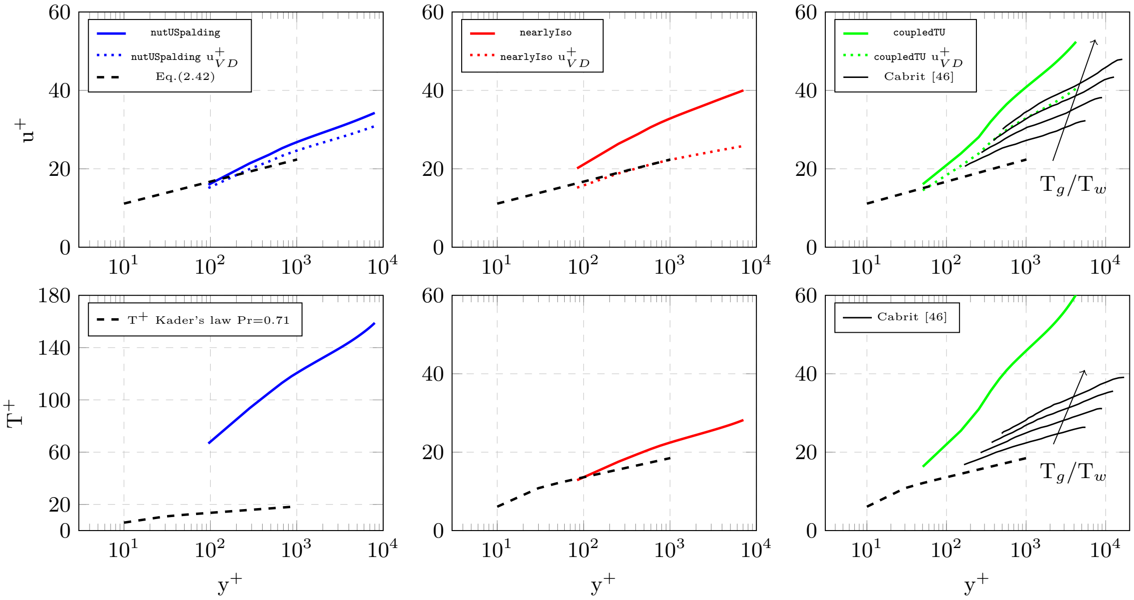

Figure 2.6.: Top: classical and van Driest scaling for u^+, using the wall functions of Table 2.1. Bottom: classical scaling for T^+ using the log-law of Kader [143] for isothermal flows. Additional profiles calculated for varying T_g/T_w are taken from Cabrit [46]

2.4.4. Hybrid LES/RANS

The Improved Delayed Detached Eddy Simulation model (IDDES) of Shur et al [264] is proposed in this work as an alternative to the *law of the wall* models. This model allows to treat the near-wall region as RANS (about 20 % of the turbulent boundary layer) and it is available in OpenFOAM in the class `SpalartAllmarasIDDES`. An example of transition behaviour from RANS to LES is provided on the right side of Fig. 2.5. When the RANS is active, the Spalart-Allmaras (SA) equation is used to transport the artificial viscosity $\tilde{\nu}$

$$
\begin{aligned}
\frac{\partial \tilde{\nu}}{\partial t} &= C_{b1}(1 - f_{t2})\tilde{S}\tilde{\nu} + \frac{1}{\sigma}\left(\frac{\partial}{\partial x_i}\left((\overline{\nu} + \tilde{\nu})\frac{\partial \tilde{\nu}}{\partial x_i}\right) + C_{b2}\frac{\partial^2 \tilde{\nu}}{\partial x_i^2}\right) \\
&- \left(C_{w1}\, f_w - \frac{C_{b1}}{k^2} f_{t2}\right)\left(\frac{\tilde{\nu}}{\tilde{d}}\right)^2 + f_{t1}\Delta U^2
\end{aligned}
\tag{2.47}
$$

from which the eddy viscosity is calculated as $\nu_{sgs} = \bar{\rho}\tilde{\nu}\ \mathrm{f}_{v1}$. A detailed description of the functions and constants of Eq. (2.47) can be found in the original paper of Spalart [272]. The equation is valid throughout the boundary layer, provided that the first y^+ is contained within the viscous layer.
A detailed description of the transition method is provided by Spalart at al [273] and Shur at al [264]. The CFD application for the CH_4/O_2 combustion chamber was recently discussed by Breda and Pfitnzer [31]. Even if strong sensitivity to grid resolution and numerics is experienced by WMLES in general [166], it is harder to demonstrate grid-independence for IDDES, since the transition interface between RANS and LES depends on the computational grid. The discussion of this topic was addressed in [31] and is partially presented in Chapter 5 for a direct comparison with WMLES.

3. Reduced chemistry models

3.1. Chemical kinetics

Reacting flow simulations usually approach the integration of the chemistry system using an operator-split technique [214], where the chemistry process is governed by the following system

$$\begin{aligned} \frac{dY_k}{dt} &= \frac{\dot{\omega}_k \, W_k}{\rho} \qquad k \;=\; 1, \ldots, n_s - 1 \\ \frac{dT}{dt} &= -\frac{1}{c_p} \sum_{k=1}^{n_s} (h_k \, \dot{\omega}_k) \, . \end{aligned} \tag{3.1}$$

Variations in species concentration in Eq. (3.1) are usually calculated for n$_s$-1 species, since one is retrieved as Y$_{n_s}$ = 1-$\sum_{k=1}^{n_s-1} Y_k$ to guarantee mass conservation. For air-fed combustion the inert species is usually N$_2$. The equation of state for an ideal gas closes the thermodynamic system as

$$p \;=\; \rho \frac{\mathcal{R}}{W} T \;=\; \mathcal{R} \, T \sum_{k=1}^{n_s} c_k \tag{3.2}$$

with c$_k$ = ρ Y$_k$/W$_k$ being the molar concentration of species k. Using the constant pressure (volume) assumption during a reaction sub-step allows to retrieve ρ (p). The production rates in Eq. (3.1) are non-linear functions of p, T and c_k and cause the stiffness of the ODE system. This can be demonstrated as follows. A single elementary reaction j involving the reaction of species $\mathcal{X}_k$ can be written as

$$\sum_{k=1}^{n_s} s^{'}_{k,j} \, \mathcal{X}_k \rightleftharpoons \sum_{k=1}^{n_s} s^{''}_{k,j} \, \mathcal{X}_k \tag{3.3}$$

for a total of n$_r$ reactions, where the overall stoichiometric coefficient for species k in reaction j is calculated as $s_{k,j} \;=\; s^{''}_{k,j} - s^{'}_{k,j}$. Each reaction is then characterized by a net rate-of-progress, determined by the difference between the forward and backward reactions as

$$R_j \;=\; k_{f,j} \prod_{k=1}^{n_s} c_k^{s^{'}_{k,j}} - k_{b,j} \prod_{k=1}^{n_s} c_k^{s^{''}_{k,j}} \tag{3.4}$$

with $k_{f,j}$ and $k_{b,j}$ respectively the forward and backward constants of reaction. The forward reaction rate constant is given by the three-parameter Arrhenius form

$$k_{f,j} \;=\; A_j \, T^{\beta_j} \exp\left(-\frac{E_{a,j}}{\mathcal{R} \, T}\right) \tag{3.5}$$

consisting of the pre-exponential factor A_j, the temperature exponent β_j and the activation energy $E_{a,j}$. If the reaction is reversible, the $k_{b,j}$ is not zero and it is retrieved from the equilibrium constant K_c as $k_{b,j} = k_{f,j}/K_c$. The evaluation of $k_{f,j}$ already hinders the computation: Zirwes et al [334] estimated that about 20 % of the total simulation time of a DNS was spent in evaluating the exponential function of Eq. (3.5), using a 53 species mechanism (GRI-3.0) for CH_4 combustion. However, the final bottleneck can be understood from the expression of the net molar production rates, which is written as

$$\dot{\omega_k} = W_k \sum_{j=1}^{n_r} C_j \, s_{k,j} \, R_j \tag{3.6}$$

where C_j is an effective mixture concentration in case of a third-body reaction and/or pressure effects. By increasing the dimensions of the mechanism (n_r and n_s), the ODE increases in stiffness, since the chemistry time scales span a broader range. Its resolution would require the use of an implicit solver, as explained in detail by Hairer [114]. This would lead to an approximate cost scaling between $\mathrm{n}_s \times \mathrm{n}_r$ (evaluation of the Jacobian matrix) and n_s^3 (cost of implicit integration). Recalling that in CFD simulations of reactive flows this ODE must be integrated at every time step in each cell, the full integration of system (3.1) requires a tremendous computational power. As a consequence, only reduced chemistry mechanisms and tabulated chemistry methods are used in this work to characterize CH_4 combustion.

3.2. Reduced chemistry mechanisms

Two typologies of reduced reaction mechanisms are used in this work, whenever a finite rate chemistry calculation is attempted. All mechanisms are summarized in Table 3.1.

The first type is based on reduced chemistry mechanisms targeted for CH_4/O_2 combustion, as currently object of research of Saccone et al [253, 252, 209]. The *lprb* mechanism presented in [253] was generated starting from the skeletal mechanism Lu30 [172] (derived from GRI-3.0 [269]). A reaction path analysis was performed in Cantera, followed by the sensitivity analysis described in [252]. The *lprb* was targeted for atmospheric pressure and $\mathrm{T} = 2000\,\mathrm{K}$. An improved version of the *mprb* mechanism, originally presented in [253], is currently under investigation and targets fuel-rich combustion at moderate pressure. A third mechanisms, *hprb*, was optimized for high pressure combustion (52 bar) and temperatures ranging between 1000 and 1200 K. It derives from a detailed mechanism for CH_4/O_2 ignition at high pressure, the RAMEC [222]. Satisfactory results could be reproduced by all mechanisms using the autoignition problem and a 1D counterflow diffusion flame computation, compared to the reference mechanisms (Lu30 and GRI3.0) [253]. The CPU speed-up compared to the reference GRI-3.0 [1] is shown on the left hand side of Fig. 3.1. A quantitative comparison of the flame structure with the Lu30 computation is provided in paragraph 3.5.

The second type of reaction mechanisms exploited in this work is based on an analytically reduction method (CSP) which allows to treat a certain number of species in QSS algebraically, avoiding the calculation of the Arrhenius coefficients (Eq. (3.5)). Such mechanisms are labelled as Lu19 and Lu13 in Table 3.1. An OpenFOAM accelerated routine was provided by Zirwes et al [334]. There, the mechanisms are pre-compiled to optimize the

---

[1] based on the calculation of a flamelet on single core in OpenFOAM

Table 3.1.: Reduced chemistry mechanisms for CH_4/air-O_2 combustion used in this work

Name	Species	Reactions	Reduction Method	Parent
Lu30 [172]	30	184	Directed Relation Graph (DRG)	GRI-3.0
lprb [253]	16	47	Reac. Path + Sensitivity Analysis	Lu30
mprb	19	51	Reac. Path + Sensitivity Analysis	Lu30
hprb	19	48	Reac. Path + Sensitivity Analysis	RAMEC [222]
Lu19 [173]	19	184	CSP + ODE Acceleration [334]	Lu30
Lu13 [173]	13	73	CSP + ODE Acceleration [334]	Lu17 [256]

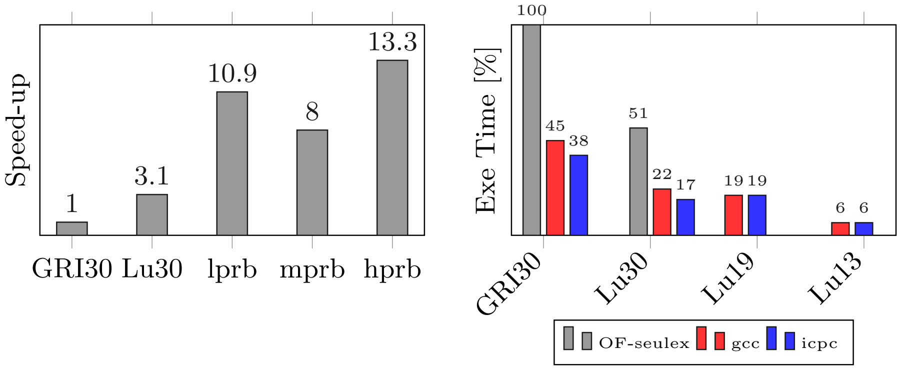

Figure 3.1.: CPU time acceleration for a flamelet calculation in OpenFOAM, using the mechanisms of Table 3.1. Right hand side in red and blue: accelerated chemistry routine from Zirwes et al [334]

calculation of the Arrhenius coefficients. Moreover, the ODE solver exploits the Sundials CVODE libraries embedded in Cantera. A quick comparison with a default OpenFOAM ODE integrator (e.g. type `seulex` [114]) is shown on the right hand side of Fig. 3.1, again for a single flamelet computation. To get a better idea of the performance gain obtained by the accelerated chemistry, the computations are normalized on the GRI-3.0 calculation (gray bar) using the original OpenFOAM chemistry solver, which took approximately 75519 s to complete (21 hours). Fig. 3.1 shows the relative execution times of the mechanisms using the original integrator in gray and the imported module from [334] in red. The GRI-3.0 computation itself is reduced of about 55 % (about 10 hours instead of 21). Compiling the above accelerated chemistry with Intel `icpc` (blue) instead of the standard `gcc` (red) allows to reduce the flamelet computation of another 7 % with GRI-3.0 and 5 % with Lu30. The latter however does not seem to play a significant role for the analytically reduced mechanisms Lu19 and Lu13, possibly due to the reduced amount of species and reactions involved. While the mechanisms belonging to the 'Lu' family were originally optimized for CH_4/air combustion at atmospheric condition, several studies (e.g. [332, 31]) showed that such mechanisms behave well also for CH_4/O_2 combustion at moderate pressure.

Understanding the range of time scales involved in a turbulent reacting flow computation allows the development of tabulated chemistry models. Fig. 3.2 shows typical time scales covered by the chemistry ($\tau_{chemistry}$) and the turbulent flow (τ_{flow}). Although an overlapping zone exists, the chemistry scales span a broader range, depending on the chemistry involved. Mathematically reduced chemistry models are based on the decoupling between the fast $\tau_{chemistry}$ typical of QSS species and PE reactions (qualitatively marked in red) and the slow chemistry scales typical of major species reactions, autoignition induction or NOx production (in cyan). Flamelet-based manifolds instead are based on the fast chemistry assumption, resulting in a poor prediction of ignition/extinction effects. Both tabulation methods will be introduced in the next paragraphs.

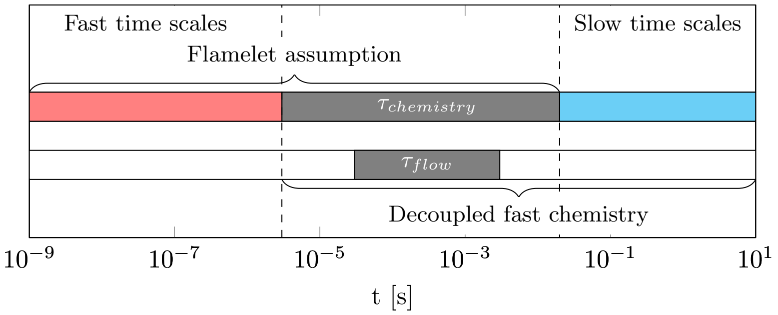

Figure 3.2.: Time scales governing a reacting turbulent flow

3.3. Low-dimensional surface attractors

DNS of turbulent reactive flows showed that only a minimal fraction of the composition space is accessed during a simulation (see e.g. [184]). In fact, most of the chemistry processes are faster than the physical processes (cf. Fig. 3.2) reducing the dimensionality of the accessed composition space when turbulence and mixing occur. The theory behind the construction of mathematically reduced chemistry models based on this observation is discussed first. Further details on this approach are available in the works of Maas [182] and Eggels [82].

Homogeneous isobaric reactors characterized by a detailed chemistry mechanism of n_s species and n_r reactions can be cast in a system of ODE as:

$$\frac{d\boldsymbol{\Psi}}{dt} = \frac{d}{dt}\begin{bmatrix} h \\ p \\ \phi_k \end{bmatrix} = \begin{bmatrix} 0 \\ 0 \\ \dot{\omega}_k/\rho \end{bmatrix} = \boldsymbol{\Omega}(\boldsymbol{\Psi})\,. \tag{3.7}$$

The vector of the thermo-chemical state is represented by the (n_s+2) variables as $\boldsymbol{\Psi} = [h, p, \phi_1, \ldots, \phi_{n_s}]^T$. If pressure and enthalpy are constant, the vector of the source terms is written for the reactive scalars as $\dot{\boldsymbol{\omega}} = \boldsymbol{S}\,\boldsymbol{r}$, with $\boldsymbol{S} = [\boldsymbol{s_1}|\ldots|\boldsymbol{s_{n_r}}]$ the $n_s \times n_r$ dimensional matrix of the n_r stoichiometric vectors $\boldsymbol{s_k}$, and $\boldsymbol{r}$ the n_r-dimensional vector of the reaction rates. While $\boldsymbol{S}$ determines in which direction of the composition space $\boldsymbol{\phi}$ is changing, $\boldsymbol{r}$ determines how fast the chemistry is evolving. Another n_e constants are added to the conserved scalars, thus the specific element mole numbers $\boldsymbol{\chi} = \boldsymbol{E}\ \boldsymbol{\phi}$, where $\boldsymbol{E}$ is the element composition matrix of dimensions $n_e \times n_s$. For a CH_4/air system, it is $n_e = 4$ to account for atoms C, O, H, N. The constraint on the conservation of the element mole numbers determines an important property of the composition space, thus $\boldsymbol{e_j} \cdot \boldsymbol{s_k} = 0$. It means that the n_e-dimensional element subspace is orthogonal to the (n_s-n_e)-dimensional reaction subspace.

When researching low-dimensional surface attractors, the ILDMs, one is looking for the direction in which the reaction rates $\boldsymbol{r}$ of system (3.7) are most rapidly decreasing. Dynamically perturbing the Jacobian $\boldsymbol{J} = \partial\boldsymbol{\Omega}/\partial\boldsymbol{\Psi}$ leads to the resolution of an eigenvalue problem for system (3.7). The Jacobian can be re-written using the right and left eigenvectors as $\boldsymbol{J} = \boldsymbol{V^R}\boldsymbol{\Lambda}\boldsymbol{V^L}$, where $\boldsymbol{\Lambda} = diag\{\lambda_1, \dots, \lambda_{n_s+2}\}$. An orthonormal basis (Shur basis) of $\boldsymbol{J}$ can be used alternatively [182]. A variant of the ILDM, known as GQL, uses the eigenspaces of a quasi-linearization matrix [39] as basis instead. Null eigenvalues (in their real part $Re(\lambda_i)$) are given by the conserved variables (pressure, enthalpy, elements), while the remaining states usually show $Re(\lambda_i) << 0$ [181]. A detailed analysis of the eigenvalues is also discussed for H_2/air systems in [82].
After perturbing the Jacobian, the null eigenvalues of $(h,\, p)$ are removed from the system for convenience. The remaining eigenvalues are re-ordered by decreasing negative real part $Re(\lambda_i)$, determining the slow and fast chemistry subspaces for the composition space $\boldsymbol{\phi}$

$$\boldsymbol{J_\phi} = [\boldsymbol{V}_s^R \boldsymbol{V}_f^R] \begin{bmatrix} \boldsymbol{\Lambda}_s & 0 \\ 0 & \boldsymbol{\Lambda}_f \end{bmatrix} \begin{bmatrix} \boldsymbol{V}_s^L \\ \boldsymbol{V}_f^L \end{bmatrix} \tag{3.8}$$

with $\boldsymbol{V}_s^L$ having dimension $\mathrm{m}_s \times \mathrm{n}_s$, $\boldsymbol{V}_f^L$ with $\mathrm{m}_f \times \mathrm{n}_s$ and $\boldsymbol{\Lambda}_s$ with $\mathrm{m}_s \times \mathrm{m}_s$. The system state can be confined to a m_s-dimensional space corresponding to the slow chemistry, with $\mathrm{m}_s << \mathrm{n}_s$. Using the slow and fast subspaces, the compositional space can be written using the new basis:

$$\frac{d}{dt} \begin{bmatrix} \boldsymbol{\phi}_s \\ \boldsymbol{\phi}_f \end{bmatrix} = \begin{bmatrix} \boldsymbol{V}_s^L \\ \boldsymbol{V}_f^L \end{bmatrix} \boldsymbol{\omega} = \begin{bmatrix} \boldsymbol{V}_s^L \boldsymbol{\omega} \\ \boldsymbol{V}_f^L \boldsymbol{\omega} \end{bmatrix} = \begin{bmatrix} \boldsymbol{V}_s^L \boldsymbol{\omega} \\ 0 \end{bmatrix}. \tag{3.9}$$

The second block of equations characterizes the ILDM subspace and represents a steady state assumption for the (n_s-m_s) fast species $\boldsymbol{\phi}_f$. Through this constraint the manifold can be considered in equilibrium compared to the fast scales, which relax rapidly towards the slow compositional space. The full composition space $\boldsymbol{\Psi}$ can be therefore represented by a significantly reduced amount of coordinates m_s. In this work, 2D and 3D-ILDM databases were constructed using the software ChemR [82], with $\{\phi_{CO2}, \phi_{H2O}\}^T$ to identify the slow sub-space (and eventually the mixture fraction f for non-premixed regimes).
It is worth mentioning that the ILDM approach presents an advantage against QSSA and PEA methods, because no prior knowledge of the QSS species and PE reactions is needed. However, the steady state approximation might not completely satisfy the constraint $\boldsymbol{e_j} \cdot \boldsymbol{s_k} = 0$, causing marginal movements off the manifold (ILDM not invariant). For this reason, another approach is found in the literature [69, 208], where a modified Fraser algorithm starting from a non-invariant ILDM generates a solution where any movement off the manifold caused by the chemistry is absent.

The first column of Fig. 3.3 shows several reaction paths calculated using a 2D-ILDM built for a lean CH_4/air mixture, using the Smooke chemistry [270]. A divergence from the finite rate chemistry route (Cantera, red dotted line) is usually observed in the transition region and at the equilibrium (cfr. final temperatures). The decoupling of the fast scales instead is justified by looking at the bottom figure: about half of the reaction path is covered within the first 0.1 ms, while only a short distance in the composition space is covered between 0.5 ms and 10 ms by approaching the equilibrium. While a 1D-ILDM would still describe well the equilibrium region, higher dimensions are required far from the equilibrium. Such observations derive from several investigations [259, 258, 82, 29]. At least one additional

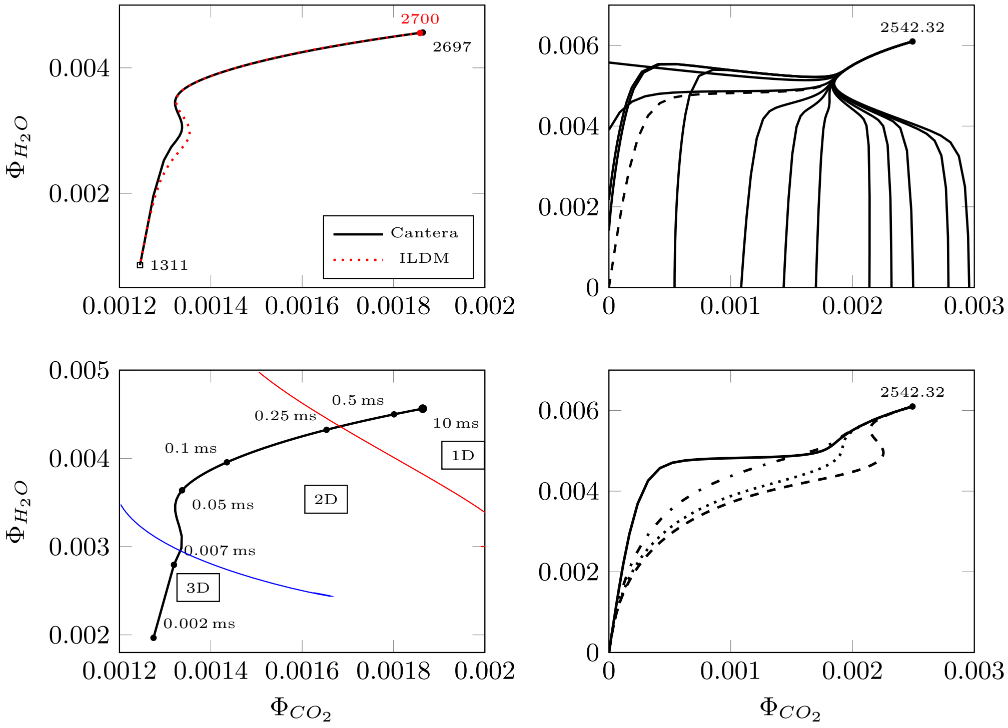

Figure 3.3.: 2D ILDM for CH_4/air fuel-lean mixtures. ILDM trajectories (1st column) and TGLDM (2nd column)

reactive progress variable is necessary in order to capture the correct flame speed in CH_4 premixed flames. On the contrary, CO_2-H_2/air and H_2/O_2 systems suffer less from this limitation [181, 183, 83], due to the fact that the hydrogen chemistry time scales are faster than the C-chemistry scales and span a shorter range.

An alternative method to ILDM is given by the Trajectory-Generated Low Dimensional Manifold (TGLDM)[239], where instead of analysing the eingenvectors of the chemical system, each trajectory is integrated from the boundary value to the equilibrium. This manifold typology is shown on the second column of Fig. 3.3. Note that the crossing of trajectories visible in the 2D view is due to the calculation involving the full chemical mechanism. The TGLDM was tested for laminar premixed combustion of CO_2-H_2/air [239] and CH_4/air [306]. At least one difficulty arises: the calculation of the trajectory starting from a CH_4/air mixture, characteristic of the autoignition problem (dashed line), for cold unburned gases. In fact, at low temperatures the reaction rates are so slow that the ignition time of a mixture at 400 K becomes extremely long. A Stochastic Particle Method (SPM) was used for example in [306] on TGLDMs to by-pass this problem. However, due to the stochastic nature of the SPM a different trajectory towards the equilibrium was obtained at each integration, requiring the definition of an average trajectory. Alternatively, one could mix the initial composition with a fraction of the equilibrium composition before starting the reaction calculation. However, different reaction paths were observed again, as shown on the bottom right plot of Fig. 3.3. In the end, the generation of TGLDMs was considered to be too expensive compared to the generation of ILDMs [306] and it was not followed in this work. The unburned mixture composition for the investigated test cases is expected to vary between 1000 K and 1500 K, so that the autoignition problem for $T_u < 1000$ K shall not be encountered.

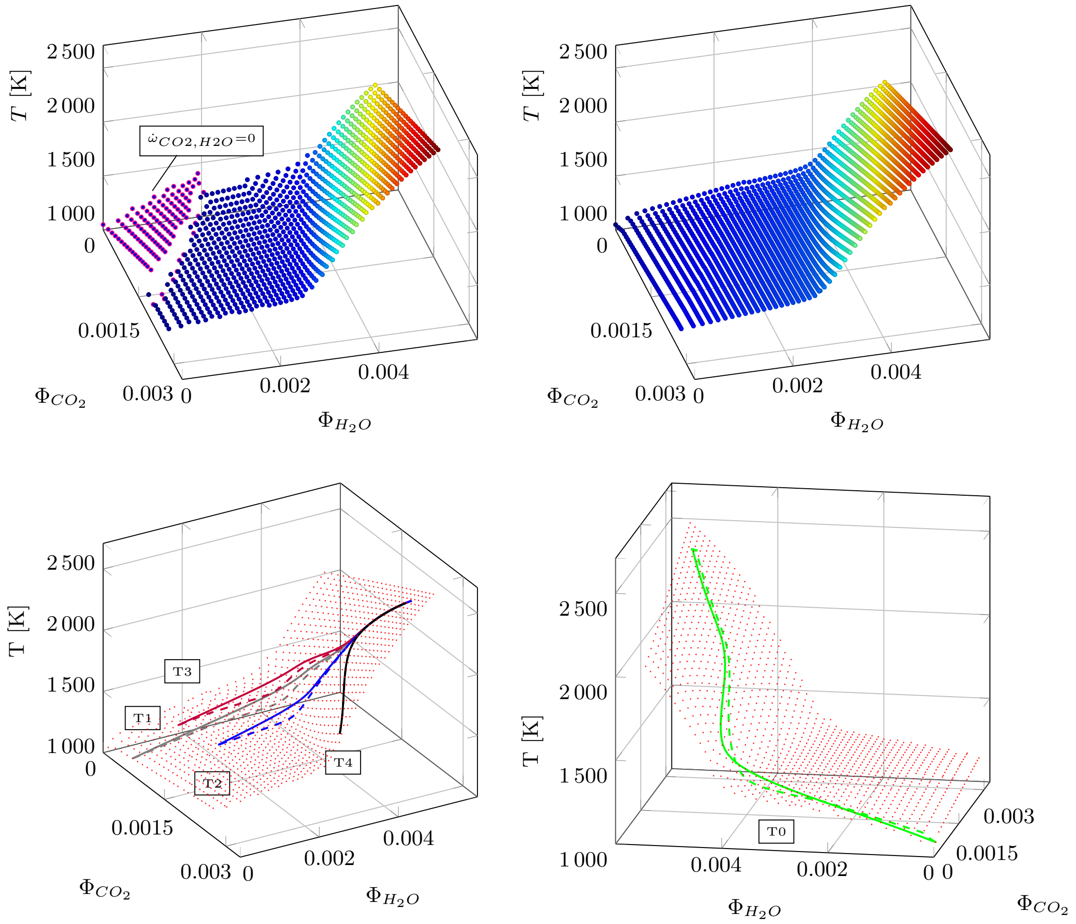

Figure 3.4.: 2D-ILDM for $T_u = 1000$ K, equivalence ratio 0.8. Top: ChemR assumption for low T region (left) against smooth surface extrapolation (right). Bottom: selected reactor trajectories

The existence of ILDMs in the low temperature region is not trivial and derives from the fact that overlapping eigenvectors characteristic of slow reaction rates cannot be easily decoupled. The top left plot of Fig. 3.4 shows a 2D-ILDM created for a fuel-lean mixture of CH_4/air at 1000 K. The discontinuity in the low temperature region derives from the treatment of the unsolved manifold points in ChemR [83], which assumes zero reaction rates for the chosen variables (H_2O and CO_2). The manifold dimension $m_s = 2$ is assigned a priori. Since it is not guaranteed that a m_s-dimensional manifold exists everywhere in the state space, additional slow eigenvectors might be required in domains of low mixture reactivity to find a solution for the perturbed system. Therefore, assigning a unique ILDM dimensionality a priori can be a disadvantage. Ren and Pope [248] analysed the geometry of

Table 3.2.: Autoignition delay (t_{ig}) and equilibrium temperature (T_e) for CH_4/air at $T_u = 1000\,K$ and equivalence ratio 0.8. Cantera reactor vs ILDM integration

Case	Cantera		ILDM	
	t_{ig} [s]	T_e [K]	t_{ig} [s]	T_e [K]
T0	0.03605	2442.45	0.00145	2436.98
T1	0.01045	2438.15	0.01515	2436.98
T2	0.00435	2438.98	0.01065	2436.98
T3	0.00135	2437.52	0.00805	2436.98
T4	$5{\cdot}10^{-5}$	2437.52	0.00015	2436.98

attracting manifolds in the composition space, concluding that sufficient negative λ_i exists in the low T region to guarantee the existence of an ILDM. Several techniques were proposed, such as an adaptive local increase of the ILDM dimensions [41, 125], assumptions on QSS species and PE reactions [83], a hybrid model with flamelet-based trajectories covering the unresolved ILDM points [106]. A smooth extrapolation of an ILDM surface towards the unburned states was presented as part of this work in [29], based on the assumption that linear surfaces can be used in this region, because the diffusion process has a stronger effect here [41]. This method can be easily applied to 2D manifolds, since it only requires the extrapolation of species Y_k towards the origin (ϕ_{CO2}, ϕ_{H2O}) = (0, 0) and an equilibrium calculation for each modified composition with constant (h, p) from the original ILDM. The non-null source terms ($\dot{\omega}_{CO2}$, $\dot{\omega}_{H2O}$) are retrieved from one integration step of a reactor calculation. The modified manifold is shown on the top right of Fig. 3.4. The bottom plots of Fig. 3.4 show 5 reactor trajectories calculated with finite rate chemistry in Cantera (solid lines) compared to an integration using the 2D-ILDM (dashed lines). All trajectories converge to the same trace in the chemistry-dominant region at high temperatures, while the finite rate chemistry calculations starting in the low-T region (T1-T3) evolve outside the manifold in the region of maximum steepness. The latter is usually observed if the manifold is not inertial: the constraint $\boldsymbol{e_j} \cdot \boldsymbol{s_k} = 0$ is not exactly realized and reaction vectors exist outside the tangential plane of the manifold. Trajectory T0 represents a CH_4/air mixture and describes autoignition for the non-perturbed reacting system. A change in curvature along the trajectory results in a different ignition time between the finite rate and the ILDM calculations, as reported in Table 3.2 for T0-T4. However, the differences are contained within the same order of magnitude, suggesting that the ILDM can qualitatively capture the investigated combustion regimes. The discussion of the ILDM behaviour for premixed flame configurations is left to a previous work of the author [29]. The validation for a 2D laminar diffusion flame instead is reported in Appendix A.1.1, followed by the application of ILDM for Sandia Flame D in Section 5.1.4.

The lack of existence of the manifold in the regions at lower temperatures is not the only difficulty derived from the ILDM theory. Complex eigenvalues in the Jacobian are common and the constraint of Eq. (3.9) does not exclude the presence of the so called 'ghost' manifolds. These two issues are not investigated in this work. Real and imaginary parts are treated in the ChemR solver to create a modified real basis [83] and improved techniques for the generation of ILDM were proposed by Borok et al [23, 24] to avoid 'ghost' manifolds. The most successful solution to recover the low temperature region however is including diffusion-convection into the manifold, using flamelet-based models or reaction-diffusion manifolds (REDIM). The applicability and limitations of the former models have been well understood by the community in the past decades. Hereby, the advanced formulation of ILDM, the REDIM, is retained for investigation.

3.4. Reaction-Diffusion Manifolds

A reaction-diffusion system is characterized by a system of Partial Differential Equations (PDE) and can be written in the same way as Eq. (3.7) by adding the convection and diffusion terms [40]:

$$\frac{d\boldsymbol{\Psi}}{dt} = \boldsymbol{\Omega}(\boldsymbol{\Psi}) - \boldsymbol{u} \cdot \nabla\boldsymbol{\Psi} + \frac{1}{\rho}\nabla \cdot (\boldsymbol{D}\,\nabla\boldsymbol{\Psi}) = \boldsymbol{\Omega}(\boldsymbol{\Psi}) + \boldsymbol{L}(\boldsymbol{\Psi})\,. \tag{3.10}$$

Mass and thermal diffusivities are included in the transport matrix $\boldsymbol{D}$. This is the start equation from which the REDIM database is derived. A general transport model can be assumed, based on the conventional unity Lewis numbers or a detailed transport assumption [180, 283]. In the first case the transport matrix $\boldsymbol{D}$ would be diagonal, in the second case it would be full.

While the ILDMs of this work are calculated directly on physical coordinates $\boldsymbol{\xi}$, i.e. using variables belonging to $\boldsymbol{\Psi}$, the introduction of generalized coordinates proposed by Bauer et al [14] allows to store the computed points on a uniform equidistant grid. Such generalized coordinates are defined as $\boldsymbol{\theta}$ in the REDIM theory [41]. It is important to understand that $\boldsymbol{\theta}$ does not carry a physical meaning and it only represents the mapping of the non-uniform grid of $\boldsymbol{\xi}$. Therefore, the tangential space of the REDIM is spanned by the matrix of the partial derivatives of the state $\boldsymbol{\Psi}$ with respect to the generalized coordinates $\boldsymbol{\theta}$, written as $\boldsymbol{\Psi_\theta}$. Eq. (3.10) can be projected into its tangential and normal subspaces respectively via the projection matrix $\boldsymbol{P_t} = \boldsymbol{\Psi_\theta}\,\boldsymbol{\Psi_\theta^+}$ and $\boldsymbol{P_n} = (\boldsymbol{I} - \boldsymbol{\Psi_\theta}\,\boldsymbol{\Psi_\theta^+})$. The thermo-chemical state is a function $\boldsymbol{\Psi} = \boldsymbol{\Psi}(\boldsymbol{\theta})$. The REDIM is generated by researching the stationary solution for the projected equation into the normal subspace, so that composition changes off manifold are avoided (consult [41] for details):

$$\frac{d\boldsymbol{\Psi}(\boldsymbol{\theta})}{dt} = \boldsymbol{P_n}\{\boldsymbol{\Omega}(\boldsymbol{\Psi}(\boldsymbol{\theta})) + \frac{1}{\rho}\nabla \cdot [\boldsymbol{D}\,\boldsymbol{\Psi_\theta}\,\nabla\boldsymbol{\theta}]\} = 0. \tag{3.11}$$

A pseudo-inverse matrix of $\boldsymbol{\Psi_\theta}$ is represented by $\boldsymbol{\Psi_\theta^+} = (\boldsymbol{\Psi_\theta^T}\boldsymbol{\Psi_\theta})^{-1}\boldsymbol{\Psi_\theta^T}$ and it has the property of $\boldsymbol{\Psi_\theta^+}\boldsymbol{\Psi_\theta} = \boldsymbol{I}$ [108]. The projection of Eq. (3.10) into Eq. (3.11) [40] shows that only the diffusion term is maintained, thus convection is already included into the tangential direction of the REDIM.

One challenge of this model is the assumption made on the physical gradients when generating the manifold. If $\nabla\theta = 0$ diffusion is absent and Eq. (3.11) falls back to the slow invariant manifold equation of [208]. Assuming constant $\nabla\theta$ could lead to inaccuracies when generating 1D or 2D-REDIMs. The optimal solution would be retrieving the gradients from DNS data based on the flame type of the study, as performed for example by Strassacker et al [282, 283]. Several investigations however showed that the REDIM is robust to a variation of gradient assessment. In particular, an approximate gradient taken from a strained counterflow diffusion flame was seen to provide accurate results, in the strain region far from extinction [197].

The REDIMs of this work were generated using the software HOMREA from the Karlsruhe Institute of Technology (KIT) in its recent version (e.g. [197, 323]). Contrary to the

ILDM database which is based on reactor trajectories, the generation of REDIMs is flexible and its boundaries can be set according to the investigated flame types, i.e. premixed, non-premixed or partially premixed configurations. The REDIM can be also generated to include heat losses, starting from a premixed configuration. It was shown in [100] that a good approximation for a SWQ configuration could be derived from a gradient estimation based on HOQ.

3.4.1. Projection strategies

CFD simulations usually include physical transport (diffusion and mixing) which cannot be directly represented by ILDMs, since they do not contain any information about the physical process $\boldsymbol{L}(\boldsymbol{\Psi})$ (cfr. Eq. (3.7) and (3.10)). A physical process $\boldsymbol{L}(\boldsymbol{\Psi})$ perturbing a state of the manifold $\mathcal{M}$ is shown in Fig. 3.5a for an ILDM database. By decomposing this process into the slow and fast subspaces one obtains a system similar to Eq. (3.9). If the physical scales (τ_{flow} of Fig. 3.2) have the same order of magnitude of the slow $\tau_{chemistry}$, thus $\boldsymbol{V_f^L}\boldsymbol{L}(\boldsymbol{\Psi}) \approx 0$, the fast chemistry would relax the perturbation to the manifold and the slow $\boldsymbol{V_s^L}\boldsymbol{L}(\boldsymbol{\Psi})$ would interact with the reaction term in the tangential space $\mathcal{T}$ [181]. A projection matrix accounting for physical perturbations in the direction of slow chemistry can be therefore stored for each state as $\boldsymbol{P_t} = \boldsymbol{V_s^R}\boldsymbol{V_s^L}$, allowing to restrict the evolution of the full system on the tangential manifold as:

$$\frac{d\boldsymbol{\Psi}}{dt} = \boldsymbol{\Omega}(\boldsymbol{\Psi}) - \boldsymbol{u}\cdot\nabla\boldsymbol{\Psi} + \frac{1}{\rho}\boldsymbol{P_t}\nabla\cdot(\boldsymbol{D}\,\nabla\boldsymbol{\Psi})\,. \tag{3.12}$$

In the ILDM framework the source term belongs completely to the tangential space. The convective term does not pull the states off the manifold either. The tangential space of the ILDM is spanned by the eigenvector basis limited to the slow time scales, thus matrix $\boldsymbol{V_s^R}$, so that $\boldsymbol{\Psi_\xi}$ in the gradient terms can be written as a linear combination of the spanning eigenvectors. This leads to

$$\boldsymbol{P_t}\,\boldsymbol{u}\cdot\nabla\boldsymbol{\Psi} = \boldsymbol{P_t}\,\boldsymbol{V_s^R}\,\boldsymbol{u}\cdot\nabla\boldsymbol{\xi} = \boldsymbol{u}\,\boldsymbol{V_s^R}(\boldsymbol{V_s^L}\boldsymbol{V_s^R})\cdot\nabla\boldsymbol{\xi} = \boldsymbol{u}\cdot\nabla\boldsymbol{\Psi}. \tag{3.13}$$

Alternatively to storing the projection matrix $\boldsymbol{P_t}$ in the database, Eggels [83] projected directly the diffusion gradients of 1D flat flame equations as $\mathrm{d}\phi_i/\mathrm{dx} = \mathrm{d}\phi_i/\mathrm{d}\theta_j \cdot \mathrm{d}\theta_j/\mathrm{dx}$. Although the storage of the projection matrix $\boldsymbol{P_t}$ is avoided, extending this coordinate transformation to multi-dimensional gradients is not straightforward. A third possibility would be neglecting matrix $\boldsymbol{P_t}$ in Eq. (3.12) for a targeted choice of the variables: the fast chemical processes should relax in the directions of constant $\boldsymbol{\xi}$, as demonstrated in [324] for the REDIM approach.

The lack of description of the diffusion process is the main disadvantage of the ILDM formulation, with increasing effect when dealing with turbulent mixing in reacting flows [16]. A recent investigation of Strassacker et al [282] demonstrated the advantage of using a REDIM-based tabulation compared to ILDMs and flamelet-based models. When applied to laminar regimes, the REDIM shows invariance with respect to the choice of $\boldsymbol{\theta}$ and the projection matrix. In fact, in REDIM databases generated by Eq. (3.11) the diffusion and reaction terms are balanced for each state. The resulting movement remains in the tangential plane, as shown in Fig. 3.5b. The evolution of the full state tangent to the manifold has the same form of Eq. (3.12), with the only difference in the projection matrix $\boldsymbol{P_t} = \boldsymbol{\Psi_\theta}\,\boldsymbol{\Psi_\theta^+}$.

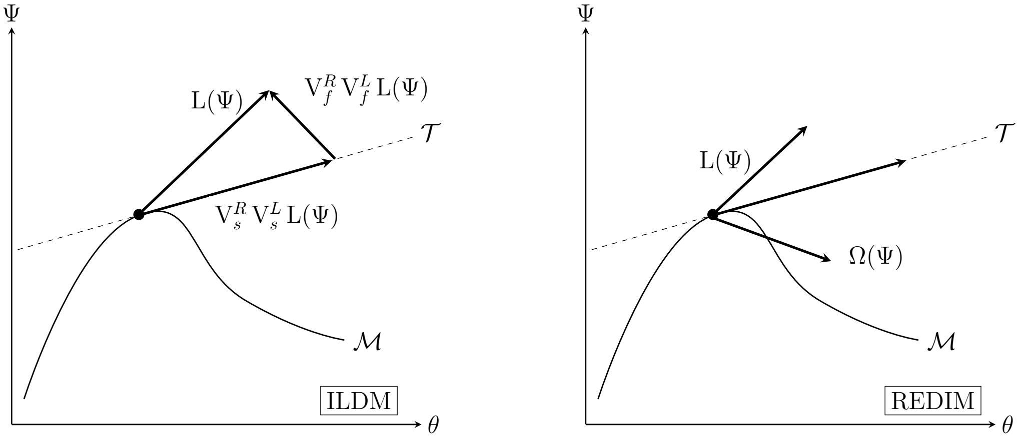

(a) ILDM: projection of a diffusion process (b) REDIM: projection of a diffusion process

Figure 3.5.: Reaction-diffusion balance in ILDM and REDIM for a laminar reacting flow

3.4.2. Reduced system of equations

Eq. (3.12) confines the movement of $\boldsymbol{\Psi}$ tangentially to the manifold, but the system is still redundant, since the tangential space $\mathcal{T}$ is described by only m_s progress variables. The most common technique to reduce the coordinate vector is based on a constant parametrization matrix of the thermo-chemical state $\boldsymbol{\Psi}$. For example, let ϕ_{N2} and a composed reaction progress variable $\phi_{CO2} + \phi_{H2O}$ describe a 2D manifold ($\mathrm{m}_s = 2$). The physical coordinates are extracted as

$$\begin{pmatrix} \phi_{N2} \\ \phi_{CO2} + \phi_{CO2} \end{pmatrix} = \boldsymbol{\xi} = \boldsymbol{C}\,\boldsymbol{\Psi} = \begin{bmatrix} 0 & 0 & 1 & 0 & 0 & \dots & 0 \\ 0 & 0 & 0 & 1 & 1 & \dots & 0 \end{bmatrix} \begin{pmatrix} h & p & \phi_{N2} & \phi_{CO2} & \phi_{H2O} & \dots \end{pmatrix}^T . \tag{3.14}$$

When applying this transformation to Eq. (3.12) one obtains:

$$\frac{d\boldsymbol{\xi}}{dt} = \boldsymbol{C}\boldsymbol{\Omega}(\boldsymbol{\Psi}) - \boldsymbol{u} \cdot \nabla\boldsymbol{\xi} + \frac{1}{\rho}\boldsymbol{C}\boldsymbol{P_t}\nabla \cdot (\boldsymbol{D}\,\nabla\boldsymbol{\Psi}) \tag{3.15}$$

which is now m_s-dimensional. The projection direction of $\mathbf{CP}_t$ is represented by the red line of Fig. 3.6a. It is common practice to exploit this parametrization, since it is simple to implement. Nonetheless, if the manifolds are not invariant[2] and the projection $\boldsymbol{P}_t$ is neglected, as it is usually done for flamelet-based manifolds, systematic errors could be relevant [282]. The results reported in Appendix A.1.2 for a 2D bunsen flame confirm these findings, although the REDIM results are less sensitive to the choice of the progress variable than an FPV method. If the REDIM is applied to turbulent flows, the use of $\boldsymbol{C}$ also generates a certain dependence of the solution on the choice of the progress variables, as confirmed in a recent work of Yu et al [323]. However, Fig. 3.6a qualitatively shows that if the ξ coordinates are chosen so that the fast perturbation $\boldsymbol{P}_t\,\Delta\Psi$ evolves in the direction of constant ξ (blue line), the projection operator of Eq. (3.14) can be neglected. One way

---

[2] In the REDIM framework, the slow manifold is considered invariant if the parametrization coordinates $\boldsymbol{\theta}$ are used. If the physical coordinates $\boldsymbol{\xi}$ are used, as it usually happens for FPV, the manifold is not invariant

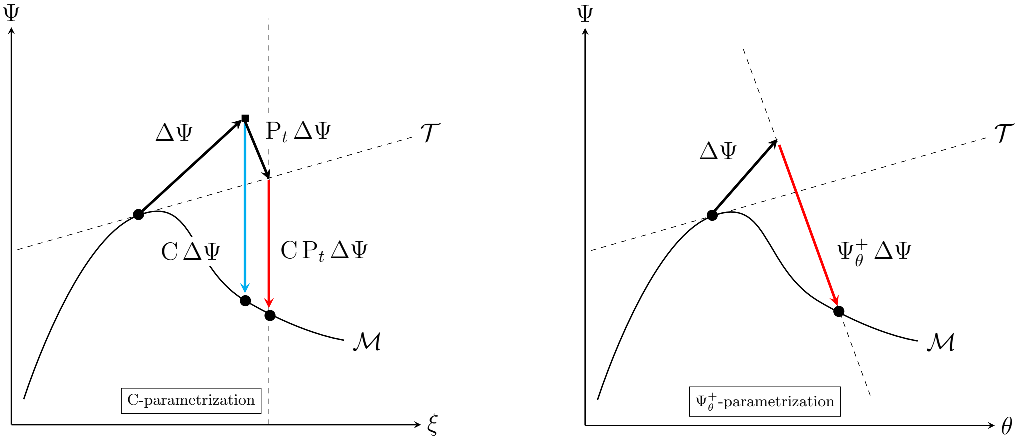

(a) Constant matrix $\boldsymbol{C}$ (b) General matrix $\boldsymbol{\Psi}_{\theta}^{+}$

Figure 3.6.: Type of projections of an off-manifold state

to chose the $\boldsymbol{\xi}$ accordingly would be performing a priori analysis on the chemical system to identify the progress variables which represent the slow movements with greater accuracy, using for example the GQL method [324].

The second parametrization strategy is applied to manifolds based on generalized coordinates and it exploits the modified Moore-Penrose pseudo-inverse matrix. By writing

$$\boldsymbol{\theta} = \boldsymbol{\Psi}_{\boldsymbol{\theta}}^{+}\,\boldsymbol{\Psi} \tag{3.16}$$

the projected equation becomes

$$\frac{d\boldsymbol{\theta}}{dt} = \boldsymbol{\Psi}_{\boldsymbol{\theta}}^{+}\boldsymbol{\Omega}(\boldsymbol{\Psi}) - \boldsymbol{u}\cdot\nabla\boldsymbol{\theta} + \frac{1}{\rho}\boldsymbol{\Psi}_{\boldsymbol{\theta}}^{+}\nabla\cdot\left(\boldsymbol{D}\,\boldsymbol{\Psi}_{\boldsymbol{\theta}}\,\nabla\boldsymbol{\theta}\right). \tag{3.17}$$

Here the matrix $\boldsymbol{P_t}$ is absent, since the movement in the reaction-diffusion space is already confined to the tangential space during the construction of the manifold (cfr. Fig. 3.5b). The fast process is then projected back in the direction normal to the tangential subspace, as qualitatively shown in Fig. 3.6b. The pseudo-inverse matrix can be also written for the physical variables $\boldsymbol{\Psi}_{\boldsymbol{\xi}}^{+}$, as derived in [282]. The projection in $\boldsymbol{\Psi}_{\boldsymbol{\theta}}^{+}$ has been extensively used for TPDF-RANS based on REDIM tabulated chemistry (e.g. [324, 323, 197]), restricted to a 2D computational domain. This variant was also validated for laminar flame computations during this work, however an extension to a 3D-LES domain exploiting stochastic fields or Lagrangian particle methods for the representation of the TCI was avoided, to reduce the number of interpolation calls in the code. Only the $\boldsymbol{C}$ matrix was used in this work for turbulent reacting LES, with a proper choice of reaction progress variables as presented in [35]. Its use is justified because only smaller displacements of the composition state from the manifold surface are expected, due to the smaller filter volume and the smaller time steps required in the LES.

3.5. Flamelet-based manifolds

Turbulent diffusion flames not subjected to processes like flame extinction and re-ignition can be seen as an ensemble of laminar diffusion flames, called flamelets. Such assumption holds in the region highlighted in red in Fig. 3.2, where $\tau_{chemistry} \ll \tau_{flow}$. This means that the flame structure reacts immediately to a sudden flow perturbation. A counterflow diffusion flame can be used as prototype to describe the combustion process and Fig. 3.7 shows the schematics of the model. The oxidizer jet enters the domain in counter direction to the fuel stream. The chemical reactions are located at stoichiometry (f_{st} in the figure).

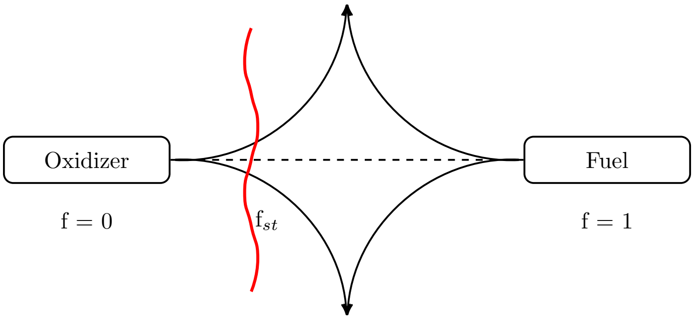

Figure 3.7.: Schematic view of a counterflow diffusion flame

If equal diffusivities and unity Lewis numbers are assumed, it is possible to describe the flamelet structure along a single scalar coordinate, the mixture fraction f, such that the transport equations for the k-th species Y_k and the absolute enthalpy can be written as

$$\rho \frac{\partial Y_k}{\partial t} - \frac{\chi \rho}{2} \frac{\partial^2 Y_k}{\partial f^2} = \dot{\omega}_k \tag{3.18}$$

$$\rho \frac{\partial h_a}{\partial t} - \frac{\chi \rho}{2} \frac{\partial^2 h_a}{\partial f^2} = 0 \tag{3.19}$$

Eq. (3.18)-(3.19) are derived from a change of coordinates, where only the terms normal to the flame front are kept, thus along the direction of the gradient of f. The mixture fraction acts as a passive scalar, from which species composition and temperature depend. It basically represents how much fuel is contained or mixed with the oxidizer in the total stream [229] and it can be derived from the knowledge of the inflow $\dot{m}$. Alternatively, it can be calculated from the element mass fractions Z_e (with $e =$ C, H, O) as proposed by Bilger [18]:

$$f = \frac{2(Z_C - Z_{C,0})/W_C + 0.5(Z_H - Z_{H,0})/W_H - 2(Z_O - Z_{O,0})/W_O}{2(Z_{C,1} - Z_{C,0})/W_C + 0.5(Z_{H,1} - Z_{H,0})/W_H - 2(Z_{O,1} - Z_{O,0})/W_O} \,. \tag{3.20}$$

In order to describe non-equilibrium effects on the flame, the scalar dissipation rate χ is introduced. Its instantaneous value depends on the thermal diffusivity D and the mixture fraction gradient

$$\chi = 2D \, |\nabla f|^2 \,. \tag{3.21}$$

This variable is essential as it gives a measure of the flow time scale τ_{flow} within the flame front (via ∇f) and it directly represents the flame strain rate [229]. Departing from the chemical equilibrium ($\chi = 0$), an increase in strain rate first promotes combustion, since the diffusion of fresh products is able to quickly remove the heat from the flame front. At higher χ the flame is subjected to quenching, as more heat is removed from the flame front than chemical reactions can provide. During the calculation of a flamelet, Eq. (3.21) is typically approximated by an analytical error function scaled on the stoichiometric value of mixture fraction f_{st} [221]. If enthalpy losses affect the flame, different expressions for χ can lead to different recombination effects as shown in the work of Breda and Pfitzner [31].

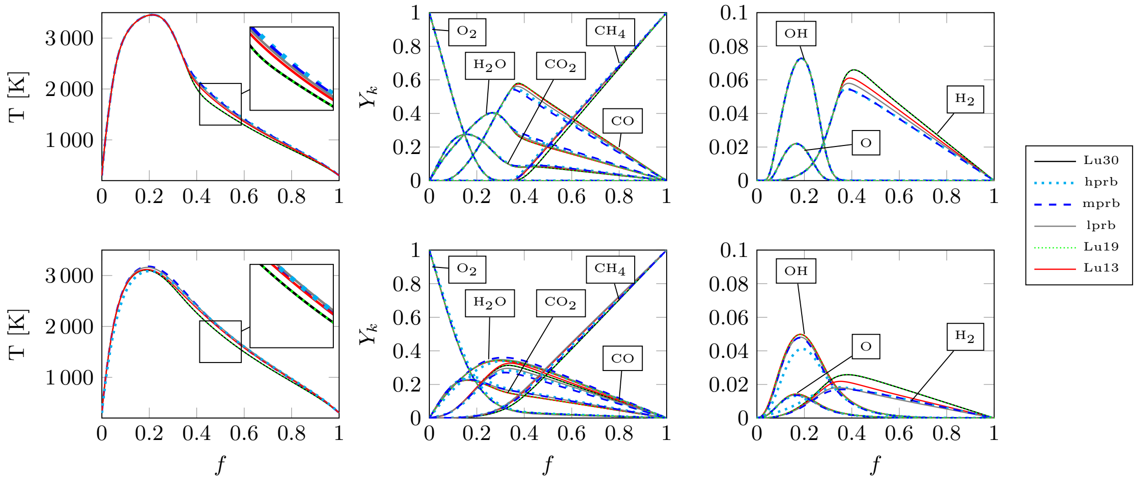

Figure 3.8.: Flamelet structure for CH_4/O_2 flamelets at 20 bar using the chemistry mechanisms of Table 3.1, $\chi_{st} = 1\,s^{-1}$ (top) and $10^4\,s^{-1}$ (bottom)

An example of flamelet structure is shown in Fig. 3.8 for the chemical mechanisms of Table 3.1. The boundary conditions are taken from the rocket combustion chamber simulation with CH_4 as fuel and O_2 as oxidizer injected in a 20 bar environment, localizing the flame front at $f_{st} = 0.2$. The first row shows the structure obtained when assigning $\chi = \chi_{st} = 1\,s^{-1}$ in Eq. (3.18)-(3.19). One can see that the choice of the chemical mechanisms influences the predictions on the fuel-rich side of the flame, for $0.4 < f < 0.8$. In fact, the number of species and reactions involved in the carbon chemistry is significantly different among the mechanisms. All mechanisms present close agreement of temperature peaks at stoichiometry ($f_{st} = 0.2$). Overall, Lu19 provides the best match with Lu30. Both show a lower concentration of CH_4 across the flame, indicating the presence of more fuel-splitting reactions. Since these reactions are endothermic, they absorb energy from the system resulting in a slightly lower temperature profile. Except from Lu19 and Lu30, the remaining mechanisms show higher temperatures on the fuel-rich side. Most of the difference is seen in species CO and H_2.

The bottom row of Fig. 3.8 shows the flame structure for $\chi_{st} = 10^4\,s^{-1}$. Quenching for this configuration occurs at $\chi_q \sim 3{\cdot}10^5\,s^{-1}$, but the effects of strain are already visible. The temperature peak at f_{st} is reduced by about 400 K and the profiles do not perfectly match anymore. Higher temperatures are foreseen for fuel-rich mixtures, due to the shift of chemical reactions towards recombination (cfr. CO_2, H_2O). The radicals OH, O and species

H_2 are reduced, while slightly different profiles are observed also for OH with this strain. Overall, the Lu19 still shows an excellent agreement with the Lu30.

Adiabatic Flamelet manifolds The flamelet structure presented in Fig. 3.8 corresponds to an adiabatic profile, where no enthalpy losses are contemplated. Such flamelet databases can be used for simulations of stable burning regimes, where none or very little extinction/re-ignition is present. The table parameters for such databases are usually (f, χ_{st}). An adiabatic flamelet database was used only in Appendix A.1.1 for a comparison with the ILDM chemistry on a laminar flame configuration.

PV-based manifolds In regimes of stronger extinction/re-ignition or in partially premixed mode a reaction progress variable (PV) can be chosen as table key parameter instead of χ_{st}, in order to track the progress of reaction, provided that this variable is uniquely defined in f [129, 84]. Usually, a linear combination of n_{PV} species is chosen, to comply with the requirement of monotonicity. One can write it for mass fractions as $\sum_{i=1}^{n_{PV}} \alpha_i Y_i$ [224, 129], for specific mole numbers as $\sum_{i=1}^{n_{PV}} \alpha_i \phi_i$ [300, 326] or normalize one of the previous expressions on its value at the equilibrium as $\frac{PV}{PV^{eq}}$ [61, 72, 98, 161, 215] for autoignition problems. The table parameters are here (f, PV). PV-based tables are not limited to diffusion flame structures, but can be constructed for free-flames to describe premixed combustion, or from reactors to describe autoignition. Only two PV-databases are used in this work, in Appendix A.1.2 and in Section 5.1.4, to support the use of the REDIM tabulation method.

3.5.1. Partially-premixed databases

The investigated test cases of the Sandia flames and the experiment of Dalshad [68] are characterized by a partially-premixed flame structure. Referring to Fig. 3.7, this means that the composition at either the oxidizer or the fuel inlets (or both) has been premixed. The top row of Fig. 3.9 shows partially premixed flame configurations when CH_4 is premixed with air at the fuel inlet. The upper and lower flammability limits for a CH_4/air mixture are marked respectively by the gray and blue dashed lines. The effect of increasing the flame strain in terms of χ is also reported in the plots for completeness. If the CH_4/air mixture is injected at or close to stoichiometry (equivalent ratio $\phi_F = 1$ in the plot), the flame front is located immediately at the fuel inlet, showing a steep temperature increase typical of premixed profiles. By increasing ϕ_F (thus the fuel percentage on the right side) the steepness of the temperature gradient is reduced, until the profile of a counterflow diffusion flame is obtained when the injected mixture is outside its flammability limits ($\phi_F > 5$). The latter configuration is encountered in the Sandia flames [10, 11] and the correspondent REDIM databases were constructed using such counterflow flames as boundary conditions and for the gradient estimation. An example of a low strained flamelet for the Sandia test case is shown in blue on the bottom left plot. Details regarding the construction of the REDIM for the Sandia flames can be found in [326, 197, 278] and their description is not intended in this work.

The experiment of Dalshad et al [68] aimed to investigate secondary reactions of methane would require a more complex database, since the autoignition delay has to be modelled. The second row of Fig. 3.9 illustrates what happens in this case. The oxidizer is not pure air at ambient conditions, but consists of an oxygen-rich hot exhaust mixture, while pure

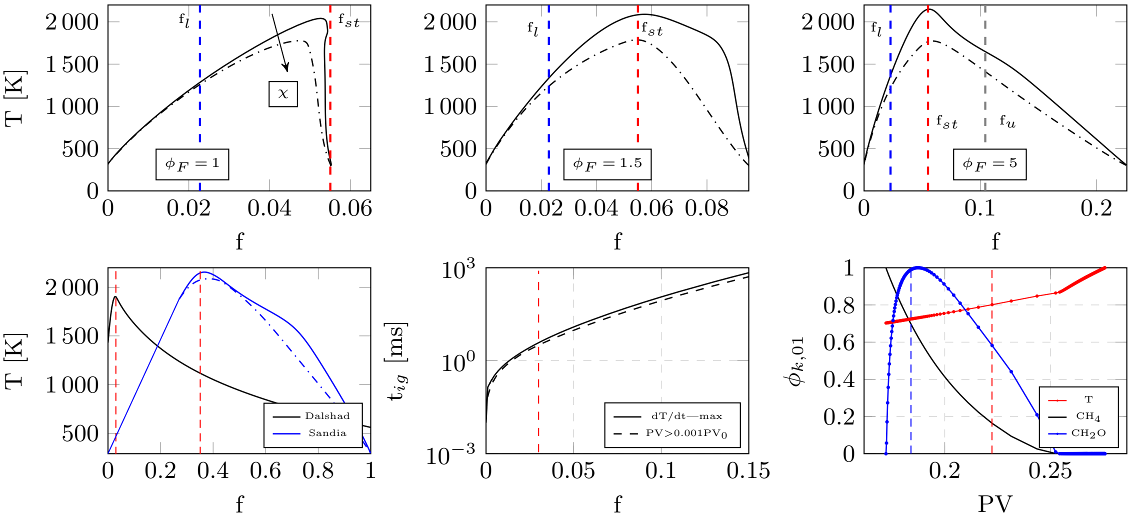

Figure 3.9.: Top row: exemplary partially premixed flamelets obtained for a premixed CH_4/air mixture at the fuel inlet varying between $\phi_F = 1$, 1.5 and 5, including the effect of χ. Bottom row: partially premixed flame configurations investigated in this work, with a zoom on the autoignition problem characteristic of [68]

CH_4 is injected at ambient temperature. A representative flamelet profile at $\chi_{st} = 1\,s^{-1}$ is shown on the bottom left figure, in black. One can see that in this configuration the stoichiometric f (red dashed line) is very close to the oxidizer stream. The work of Mastorakos et al [194] showed that autoignition occurs around the most reactive value of the mixture fraction f_{MR}, which does not correspond to f_{st}, whenever fuel and oxidizer are injected with a different temperature. Thus, ignition occurs in the stream with higher temperature, the oxidizer in this experiment. The second plot on the bottom row shows that the most reactive mixture is located very close to the oxidizer stream boundary ($f_{MR} = 0.00022$) in this configuration.

Chemistry databases based on the homogeneous mixing ignition model (HMI) can be used to analyse the thermo-chemical states [157]. Each linear composition between the fuel and oxidizer stream is evolved as a single reactor. The trajectory of each independently evolving reactor can be tracked in the composition space by a progress variable. The literature suggests several combinations such as $Y_{CO2}+Y_{CO}$ [72, 215] or $Y_{CO2}+Y_{CO}+Y_{CH2O}$ [61] or simply the radical Y_{CH2O} [133, 26] for hydrocarbon combustion, as derived from the study on vitiated flames [43, 142]. The importance of CH_2O is better described on the bottom right plot of Fig. 3.9. The normalized fields T, CH_4 and CH_2O are plotted over a selected progress variable PV at each point of a reactor built close to stoichiometric conditions of Dalshad's test case ($f = 0.02336$, $T_u = 1524\,K$). Two autoignition criteria are compared, chosen from a preliminary investigation of possible autoignition criteria as reported in Appendix A.1.3. One criterion is based on the maximum temperature gradient (localized by the vertical dashed red line on the bottom right plot of Fig. 3.9), the other one on the relative increase of +1% of the progress variable $PV = Y_c/Y_c^{eq}$ (vertical dashed blue line). The temperature increases slowly while the CH_2O is built, remaining nearly constant before ignition occurs. After the mixture ignites (+1% PV_0), within several time steps a sudden increase in temperature is observed, since the reaction rates rapidly speed-up. Here it is the region where the conventional ignition delay time based on $\nabla \mathrm{T}_{max}$ is found. Afterwards the mixture shifts quickly towards the equilibrium value, with the radical pool consumed within a few steps. The plot shows that the mixture ignites later if the autoignition criterion is based on the maximum temperature gradient.

The assumption of infinitely fast mixing behind the HMI model was justified by [157] when applied to CH_4. However, a couple of disadvantages are foreseen when applied to the test case of Dalshad. First, the chemistry might not be the only influencing factor on the autoignition delay observed for this configuration, since the reactants are injected through a variety of momentum ratios. For instance, Sakellarakis [255] showed that heat conduction can be a significant factor for triggering autoignition in mixture compositions located outside the range of the most reactive composition. A reaction-diffusion database (such as the REDIM) might be preferred to capture the correct behaviour. Secondly, the sgs flame structure for HMI manifolds is typically approximated by a presumed PDF approach, as in the flamelet formulation [98, 72]. The variance PV''^2 is added as table parameter and additional modelling for its transport equation is required (see Section 4.2.1). It would be useful to remove the assumption on the presumed PDF and use the ESF approach instead, which can as well describe autoignition based on tabulated chemistry [61]. The CFD computation of the autoignition test case would therefore consider the ESF-REDIM approach for validation.

3.5.2. Non-adiabatic flamelets

In combustion devices thermal damage at walls is avoided by means of cooling techniques. This is particularly critical for rocket combustion chambers, where strong temperature gradients occur within 1 mm from the wall surface. Although the REDIM could be successfully tested and validated for non-adiabatic premixed flame configurations featuring air as oxidizer [281, 283, 277], a validation for high pressure CH_4/O_2 combustion has not been reported yet by the time of writing. A conventional flamelet database can be exploited for the investigated sub-scale combustion chambers instead, because combustion occurs within a stable regime. The database would require the inclusion of non-adiabatic effects to correctly describe the near-wall chemistry.

In the recent years several non-adiabatic combustion models were presented to the community and applied to rocket applications. Their development was certainly enhanced by the regional cooperation offered in the framework of the SFB program TRR-40. An overview over the past five years is presented in Table 3.3. Previous works aimed to include radiation effects [60, 123, 188, 127] or a convective sink term in the flamelet equation to induce SWQ [168, 93]. Two methodologies were found promising: the use of a permeable inert wall on the fuel-rich side of the flamelet [317] and the introduction of an extra time scale for the frozen chemistry near the wall [243]. The first method is followed here, as originally implemented in the in-house OpenFOAM routine by Frank [93] and extended towards the low enthalpy states by Zips [330]. A comparison with the method of Perakis [220] was provided in [32].

The generation of the Non-Adiabatic (NA) flamelet database in OpenFOAM has been thoroughly explained in previous works (e.g. [332, 330, 31]) but it will briefly recalled in this paragraph. Fig. 3.10 shows an example of enthalpy, temperature, majors products and flame heat release obtained for $\chi_{st} = 1\,\mathrm{s}^{-1}$. The flamelets previously shown in Fig. 3.8 correspond to the solid black profiles, thus the adiabatic solution. The non-adiabatic flamelet calcula-

Table 3.3.: Recent research in non-adiabatic flamelet modelling for rocket combustion chambers

Group	Method
Wu et al. [317]	permeable wall
Ma et al. [178, 179]	permeable wall
Perakis et al. [220]	imposed target enthalpy, from Kim [150]
Rahn et al. [244]	target enthalpy with modified source term
Rahn et al. [243]	improving [244] with an additional frozen time scale
Perakis et al. [217]	improving [220] with [243]

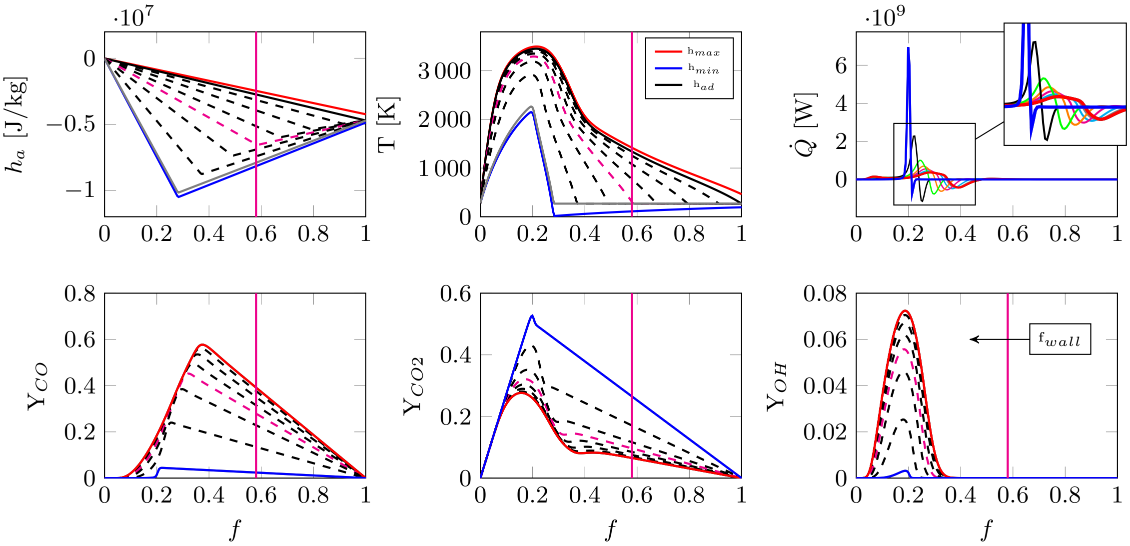

Figure 3.10.: Non-Adiabatic flamelet manifold constructed using the permeable wall assumption [317] for $\chi_{st} = 1\,\mathrm{s}^{-1}$. f_{wall} moves leftwards

tion is initiated by introducing a chemically inert wall in proximity of the fuel inlet, which allows only molecular transport on its right side. A representative non-adiabatic flamelet and its assigned f_{wall} position are shown in magenta. After each flamelet calculation, the wall is shifted on the left towards the flame front, as visually reproduced in the OH plot. Since only diffusion is allowed for $f_{wall} < f < 1$, the species show a linear behaviour. Thus, a thermal boundary condition is applied at f^+_{wall} and f^-_{wall}, so that $\mathrm{Y}_i(f)$ is continuous and differentiable in f_{wall}. The temperature can either be forced to be constant within this range (thus $\mathrm{T}_{f_{wall}} = \mathrm{T}_{f=1}$) or it can be linearly interpolated between $\mathrm{T}_{f_{wall}}$ and $\mathrm{T}_{f=1}$, ensuring $\mathrm{T}_{f^+_{wall}} = \mathrm{T}_{f^-_{wall}}$. With this procedure, all the black dashed profiles are obtained. The calculation stops where a flamelet solution cannot be found anymore because of quenching, at $f_{wall} \approx 0.28$ for this configuration, represented by the gray profile in the h and T plots. The upper and lower enthalpy boundaries of the manifold (h_{max} and h_{min}) were further extended using the conventional frozen chemistry approach as explained in [332], resulting in a reduction of $h_{0.28}$ towards h_{min} (solid blue line) and an increase of h_{ad} towards h_{max} (solid red line). Since in this procedure the chemistry is kept unaltered, the boundaries of the composition space are not modified. One can see that the transition from the red to the blue profile results in a reduction of radicals CO and OH, but an increase in CO_2 (and H_2O, not shown). The chemistry is shifted towards recombination reactions due to the approaching cold wall, but since they are exothermic the heat release $\dot{Q}$ increases as well (top right plot). This causes the flame to choke, since the reaction products are not quickly removed.

The enthalpy space is normalized between 0 and 1 using the max and min profiles, in order to facilitate the interpolation routine. The normalized enthalpy is therefore calculated as

$$h_n = \frac{h_a - h_{min}}{h_{max} - h_{min}} \,. \tag{3.22}$$

The table parameters become (f, h_n). In order to cover all the flamelets states at low and high χ encountered in a turbulent simulation, one should account for a third parameter, the χ_{st} indeed. This has been done for example in the parallel work of Zips et al [332], when simulating the GOX/GCH_4 7-injector sub-scale combustion chamber [265]. In the work of Breda and Pfitzner [31] it is shown that a multi-χ_{st} database converges to a single-χ_{st} database from approximately 30 mm downstream the faceplate, for the investigated single-injector combustion chamber of this work. As a consequence, a NA-database at fixed $\chi_{st} = 1\,s^{-1}$ is retained suitable to represent the wall heat flux in this configuration.

Table 3.4.: Non-adiabatic flamelet solvers based on the permeable-wall assumption [178]

	OpenFOAM (OF)	FlameMaster (FM)
Chemistry input	CHEMKIN, OF-specific	FM-specific (binary)
Analytically reduced mechanisms	yes	no
Diffusion model	Le = 1	Le = 1, Le = const, differential diffusion
Generate start solution	+	-
Chemistry import	+	-
Computational time	-	+
Parallelization required	yes	no

NA-Flamelet Generation Tool The previous in-house OpenFOAM solver for the generation of flamelets showed poor performance compared to 1D-combustion software like Cantera [109] or FlameMaster[3], as quantified by Breda et al [32]. A certain speed-up of the OpenFOAM routine could be achieved in this work by changing the compiler to Intel `icpc`, whenever using the accelerated chemistry mechanisms of Table 3.1, according to the observations of Zirwes et al [334]. They reported a speed-up of 15-20% on the accelerated GRI-3.0 mechanism, when using Intel `icpc` rather than the standard GNU `gcc`. The reduction in computational time obtained in this work is graphically presented on the right side of in Fig. 3.1, using an adiabatic flamelet calculation as a reference. The simulation is advanced on a single core of type Intel(R) Xeon(R) CPU E5-1620 v3, until 0.1 s of the CFD time is reached.

A more efficient solver was implemented in cooperation with the TUM [213] within the framework of this work. It is based on FlameMaster (v. 4.0) and exploits the 30 species

---

[3] https://www.itv.rwth-aachen.de/downloads/flamemaster

chemistry [31, 213]. The computational speed-up obtained in this case is enormous. A single-core computation would take about 25 hours with FlameMaster and 60 days with the `icpc`-improved OpenFOAM to generate a complete flamelet database with grid points $(f,\ h_n,\ \chi_{st}) = (201,\ 50,\ 5)$, using Lu30. Multi-core parallelization is absolutely required in OpenFOAM to achieve acceptable wall-clock times. A minor drawback characterizes the FlameMaster routine: analytically reduced mechanisms (Lu19, Lu13) are not easy to import. Table 3.4 provides an overview on the features of both flamelet solvers. A '+' indicates an advantage, a '−' sign a disadvantage.

The non-adiabatic flamelet manifolds of this work were created on an equally distributed grid with 50 points in h_n and 201 points in f. A maximum table size of 52 MB was obtained for the Lu30 configuration. A qualitative comparison between the memory storage required by REDIM, flamelet and ILDM tabulations is provided in Table A.1.

4. Turbulence-Chemistry Interaction

4.1. Flame fluctuations in turbulent flows

The modelling of the filtered chemical source term introduced in Section 2.3.1 for Eq. (2.31) is discussed in this chapter. The challenge given by this term is its strong non-linearity to the flow properties as shown by the Arrhenius Eq. (3.5), which makes filtering a difficult task. It is useful to discuss this point first.

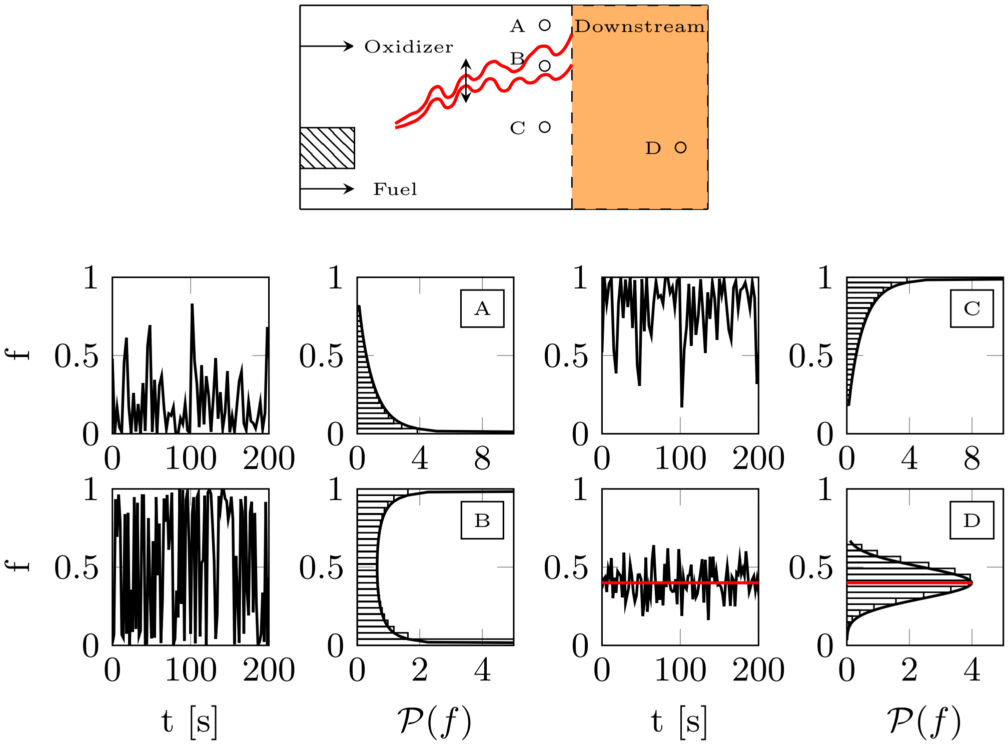

Figure 4.1.: Flame fluctuations due to turbulence and PDF reconstruction at locations A (fuel-lean), B (flame flutter), C (fuel-rich), D (burning solution)

Let us take a typical lifted flame configuration, as shown on the top of Fig. 4.1. The oxidizer and the fuel are injected separately into the domain and the flame tip anchors after the mixing zone close to the injector. The flame front (red line) extends further downstream following the iso-lines of stoichiometric composition and its position fluctuates in time. By sampling the local value of mixture fraction at three different locations across the flame brush (A, B, C in the figure), fluctuations would be visible in time. The recorded signal would be similar to the one shown on the bottom plots. In A it would primarily localize the oxidizer (mean close to 0), in C the fuel (mean close to 1), while in B the strong fluctuation due to the flapping motion of the flame front would generate a double-peak distribution. By defining the range of f in sub-intervals, called bins, and counting the number of occurrences for each bin over the time t, one obtains the shape of a Probability Density Function (PDF) of f, which is labelled as $\mathcal{P}(f)$ in the plots. Fig. 4.1 also shows the PDF shapes at the investigated locations. By selecting point D downstream in the burning region, one would obtain a Gaussian distribution centred on a burned mixture composition. The mean of f can be obtained from the knowledge of the N sampled occurrences f_i

$$\widetilde{f} = \frac{1}{N} \sum_{i=1}^{N} f_i \,. \tag{4.1}$$

Let us assume that at point D the distribution is centred on $\widetilde{f} = 0.4$ (red line). Recalling from the flamelet assumption presented in Section 3.5 that a non-linear function $T(f)$ exists, one could approximate the filtered temperature $\widetilde{T}$ with the value of the instantaneous T at $\widetilde{f} = 0.4$, obtaining in this example 1850 K. The mean of T retrieved as $\widetilde{T} = \frac{1}{N}\sum_{i=1}^{N} T_i$ instead, would give 1800 K. The reason behind this mismatch is simple: at point D the shapes of $\mathcal{P}(T)$ and $\mathcal{P}(f)$ are affected by turbulence, which generates a greater number of occurrences off-mean. This contributes to flatten the PDF profile (and therefore its maximum) compared to a laminar profile distribution. This leads to the important observation that in general $T(\widetilde{f}) \neq \widetilde{T}(\widetilde{f})$.

The reader should note that in this example the statistical evolution of a fixed point in space was recorded over time, in order to introduce the concept of a statistical distribution. However, the PDF method for LES implies a space filtering within the computational cell, while keeping the time step fixed.

4.2. Probability Density Function

PDF methods for turbulent combustion modelling allow to account for the effect of turbulent fluctuations on velocity and/or the composition state. Many implementations exist and a recent overview (from 2010) is provided by Haworth [120]. The models used in this work do not include a PDF for the velocity.

In LES, the PDF serves to model the turbulence-chemistry interaction at the small scales, where the chemical reactions take place through molecular transport. Because the subgrid scales are not resolved by the LES, the thermo-chemical state of a cell is determined by the statistical quantities (moments) generated by the PDF. The scalar quantities of interest $\alpha = 1, \ldots, n$ are represented by ξ_α, while their sample spaces are denoted as π_α. The fine-grained (one-point marginal) $\mathcal{F}_\alpha$ of each scalar α is described as $\mathcal{F}_\alpha(\boldsymbol{\pi} : \boldsymbol{x},t) = \delta(\pi_\alpha - \xi_\alpha(\boldsymbol{x},t))$. The joint-PDF over all sets of scalars is the product of the marginal probabilities $\mathcal{P}(\boldsymbol{\pi} : \boldsymbol{x},t) = \prod_{\alpha=1}^{n} \delta(\pi_\alpha - \xi_\alpha(\boldsymbol{x},t))$. Using the Favre filter from Eq. (2.27), one gets the probability of $\boldsymbol{\xi} = \boldsymbol{\pi}$ localized on the filtered volume:

$$\widetilde{\mathcal{P}}(\boldsymbol{\pi} : \boldsymbol{x},t) = \frac{1}{\bar{\rho}} \int \rho(\boldsymbol{x} - \boldsymbol{y},t) \prod_{\alpha=1}^{n} \delta(\pi_\alpha - \xi_\alpha(\boldsymbol{x},t))\, \mathcal{G}(\boldsymbol{x},\boldsymbol{y})\, d\boldsymbol{y} \,. \tag{4.2}$$

The PDF derived from Eq. (4.2) is known as Filtered Density Function (FDF) in the LES context, as originally suggested by Pope [235] and later on adopted in the review of Haworth [120]. For simplicity, the term PDF is kept in this work, with the only reminder that a convolution with the LES filter kernel is applied. The starting point to treat the filtered source term of Eq. (2.31) is writing the expression based on the statistics of the full thermo-chemical state $\boldsymbol{\Psi}$ using the so-called joint-composition PDF:

$$\bar{\dot{\omega}}_k = \int\int\cdots\int \dot{\omega}_k(\Psi_1,\Psi_2 \ldots,\Psi_{n_s+2})p(\Psi_1,\Psi_2 \ldots,\Psi_{n_s+2})\, d\Psi_1\, d\Psi_2 \,\ldots\, d\Psi_{n_s+2} \tag{4.3}$$

Note that in this expression it is $p = \int \mathcal{P}(\boldsymbol{\pi} : \boldsymbol{x},t)\,\mathcal{G}(\boldsymbol{x},\boldsymbol{y})\,d\boldsymbol{y}$, slightly different from $\widetilde{\mathcal{P}}$ because the Favre-average is not applied. While this expression can handle complex chemical mechanisms and no assumption on the local flame structure is required, the estimate of the joint-composition PDF is challenging and its computational cost is high [112, 234]. The assumption of statistical independence reducing the joint-PDF to multiple marginal PDFs as $p(\Psi_1)p(\Psi_2),\ldots,p(\Psi_{n_s+2})$ is in general not justified, since composition and temperature are closely related in flames (see for example the flamelet formulation). Two major possibilities exists to estimate $\bar{\dot{\omega}}_k$. In presumed PDF models the shape of the distribution is given a-priori and the statistical moments (e.g. the mean and variance) of a selected quantity are calculated from transport equations. Such models are usually associated with flamelet databases, since the chemistry is already described by a reduced number of variables (the table key parameters). In transported PDF methods instead, a transport equation is written for the joint-PDF and the statistical moments are derived from the ensemble of its possible realizations. Although the chemical source term appears in close form, further modelling is required for the turbulent molecular mixing. Both methods are used in this work to investigate TCI.

4.2.1. Presumed β−PDF method

It was seen in section 3.5 that in steady flame regimes the flamelet manifolds are usually described by two parameters: the mixture fraction and either a reaction progress variable PV, the enthalpy loss h_n or the scalar dissipation rate χ. The second table parameter is hereby labelled as $\mathcal{V}$ to keep the PDF generic. The flame structure described by Y_k and T is generalized in the flamelet approach as $\boldsymbol{\Psi}(f,\, \mathcal{V})$. The TCI is therefore restored by the joint-PDF $\widetilde{\mathcal{P}}(f,\mathcal{V})$ and closes any thermo-chemical quantity as

$$\widetilde{g} = \int\int g(f,\mathcal{V})\,\widetilde{\mathcal{P}}(f,\mathcal{V})\,df\,d\mathcal{V}\,. \tag{4.4}$$

Using the Bayes' theorem, the joint-PDF can be written as $\widetilde{\mathcal{P}}(f,\mathcal{V}) = \widetilde{\mathcal{P}}(f)\widetilde{\mathcal{P}}(\mathcal{V}|f)$, with the marginal PDF $\widetilde{\mathcal{P}}(\mathcal{V}|f)$ describing the fluctuation of the second table parameter conditioned on f. Assuming statistically independence of the variables f and $\mathcal{V}$, it is $\widetilde{\mathcal{P}}(\mathcal{V}|f) = \widetilde{\mathcal{P}}(\mathcal{V})$. During this work the $\widetilde{\mathcal{P}}(\mathcal{V})$ was approximated by a Dirac function as $\delta(\mathcal{V} - \widetilde{\mathcal{V}})$.
The closure of the thermo-chemical quantities is provided by $\widetilde{\mathcal{P}}(f)$, which is assigned as a β distribution [221]. Because conditional fluctuations of the reactive scalars are not considered, this method is a first order closure. The β-PDF reads

$$\widetilde{\mathcal{P}}(f) = f^{\alpha-1}(1-f)^{\beta-1}\frac{\Gamma(\alpha+\beta)}{\Gamma(\alpha)\Gamma(\beta)}, \quad \alpha = \widetilde{f}(\gamma-1), \quad \beta = (1-\widetilde{f})(\gamma-1), \quad \gamma = \frac{\widetilde{f}(1-\widetilde{f})}{\widetilde{f''^2}} \tag{4.5}$$

where $\widetilde{f''^2}$ is the sub-grid mixture fraction variance. Its value is pre-tabulated and normalized between 0 and 1 via γ, which becomes the fourth parameter for the flamelet tables. The required statistical moments are transported at run-time and are used to retrieve the filtered scalar quantities from the table. The convolution of the fields with the β-PDF is applied in a pre-processing step. The additional transport equations for this combustion model are

$$\frac{\partial \bar{\rho}\tilde{f}}{\partial t} + \frac{\partial \bar{\rho}\tilde{u}_i\tilde{f}}{\partial x_i} = \frac{\partial}{\partial x_i}\left(\left(\frac{\bar{\mu}}{Sc} + \frac{\mu_{sgs}}{Sc_{sgs}}\right)\frac{\partial \tilde{f}}{\partial x_i}\right) \tag{4.6}$$

$$\frac{\partial \bar{\rho}\widetilde{f''^2}}{\partial t} + \frac{\partial \bar{\rho}\tilde{u}_i\widetilde{f''^2}}{\partial x_i} = \frac{\partial}{\partial x_i}\left(\left(\frac{\bar{\mu}}{Sc} + \frac{\mu_{sgs}}{Sc_{sgs}}\right)\frac{\partial \widetilde{f''^2}}{\partial x_i}\right) - 2\,\bar{\rho}\tilde{\chi} + 2\left(\frac{\bar{\mu}}{Sc} + \frac{\mu_{sgs}}{Sc_{sgs}}\right)\left(\frac{\partial \tilde{f}}{\partial x_i}\right)^2 . \tag{4.7}$$

The last equation proposed by Kemenov [148] contains the instantaneous scalar dissipation rate $\widetilde{\chi}$. It is approximated analytically according to Domingo [73]

$$\tilde{\chi} = \frac{\tilde{\mu}}{\bar{\rho}\;Sc}\left(\frac{\partial \tilde{f}}{\partial x_i}\right)^2 + \frac{C_\chi\;\mu_{sgs}}{2\;\bar{\rho}\;Sc_{sgs}}\frac{\widetilde{f''^2}}{\Delta^2} \tag{4.8}$$

with $\mathrm{C}_\chi = 2$ and Δ being the grid filter.

4.2.2. Transported PDF methods

Numerous combustion models are derived using the one-point one-time PDF approach because no further assumption is required to describe the flame statistics. For LES, the pioneer work of Dopazo [74] introduced a modelled equation for the joint composition PDF, which was further elaborated by Pope [234, 235] (for a detailed treatment comprehending the RANS context, consult [120, 92, 237]). The formulation of the $\widetilde{\mathcal{P}}$ equation was later on derived from Gao [101] and Jaberi [134]. The equation, derived for unity Lewis numbers, reads

$$\begin{gathered}\frac{\partial \bar{\rho}\widetilde{\mathcal{P}}}{\partial t} + \frac{\partial \bar{\rho}\tilde{u}_j\widetilde{\mathcal{P}}}{\partial x_j} + \sum_{\alpha=1}^{n}\frac{\partial}{\partial \pi_\alpha}(\bar{\rho}\dot{\omega}_\alpha\widetilde{\mathcal{P}}) = \\ \frac{\partial}{\partial x_j}\left[\bar{\rho}\left(\frac{\bar{\nu}}{Sc} + \frac{\nu_{sgs}}{Sc_{sgs}}\right)\frac{\partial \widetilde{\mathcal{P}}}{\partial x_j}\right] - \sum_{\alpha=1}^{n}\sum_{\beta=1}^{n}\frac{\partial^2}{\partial \pi_\alpha \partial \pi_\beta}\left(\bar{\rho}\,\overline{\frac{\bar{\nu}}{Sc}\frac{\partial \xi_\alpha}{\partial x_i}\frac{\partial \xi_\beta}{\partial x_i}\bigg|_{\boldsymbol{\xi}=\boldsymbol{\pi}}}\;\widetilde{\mathcal{P}}\right) .\end{gathered} \tag{4.9}$$

The first line of Eq. (4.9) contains the temporal evolution of $\widetilde{\mathcal{P}}$, the convective transport term and the variation due to chemical reactions. The latter shows the advantage of using a transported PDF, because the chemical source terms appear in closed form. When using tabulated chemistry, this allows to directly look-up $\dot{\omega}_\alpha$ from the database. On the RHS of the equation, the scalar conditioned velocity fluctuations on the sub-grid level have been modelled using the gradient flux hypothesis. The last term represents the molecular mixing (or micro-mixing) and requires further modelling, because the one-point PDF alone does not contain any information about the scalar gradients and the length scales.

The deterministic solution of Eq. (4.9) for finite-volume solvers would require a high computational power due to its dimensionality (n_s+5). This equation is usually solved statistically, using the Monte-Carlo approach. The trick consists in replacing Eq. (4.9) with a statistically equivalent system, using a Stochastic Partial Differential Equation (SPDE). The latter can be written as a generalized diffusion process by means of the *Fokker-Plank* (FP) equation. While the details of the derivation can be found in the book of Gardiner [102], it is important to understand the concept that the SPDE written for the PDF of a stochastic variable $\mathcal{Q}$(x,t) (considering the FP equation in one dimension, for simplicity), is equivalent to writing a Stochastic Differential Equation (SDE) for the n-th stochastic realization $\mathcal{Q}^n$(x,t) as

$$d\mathcal{Q}^n(x,t) = A^n(x,t)\,dt + B^n(x,t)\,dW^n \tag{4.10}$$

by using the Itô formalism. The terms A^n and B^n represent respectively the drift and diffusion coefficients. Eq. (4.10) is integrated in time to determine the evolution of $\mathcal{Q}^n(x,t)$. The Wiener process dW^n corresponds to a normal distributed random walk with 0 mean and variance 1, generally modelled as $N(0,1)\sqrt{dt}$. With the Itô formalism, the Wiener process can be evaluated at the beginning of each time step t$_k$. The Stratonovich integration instead leads to a different form of Eq. (4.10) and requires the evaluation at the mid-point of the time step (t$_{k+1/2}$) (consult [102] for further details). Two approaches derived from the Itô formalism were considered in this work: the Lagrangian particles method and the Eulerian Stochastic Fields.

The Lagrangian particles method

One approach to implement Eq. (4.10) in a turbulent combustion problem is using the Lagrangian particles method introduced by Pope [233] in the eighties. The ensemble of N_p stochastic particles evolving according to Eq. (4.10) generates the statistical moments required to describe the sgs-TCI. The $\mathcal{Q}^n$(x,t) stochastic realization corresponds to evolving the particle x^p in the physical space as

$$d\boldsymbol{x}^p = \boldsymbol{A}^p\,dt + \boldsymbol{B}^p\,\boldsymbol{dW}^p \tag{4.11}$$

with $\mathrm{A}_i = \widetilde{u}_i + \frac{1}{\rho}\frac{\partial}{\partial x_i}(\rho(D + D_{sgs}))$ and $\mathrm{B}_i = \sqrt{2(D + D_{sgs})}$ used in this work[1]. Then, the particle evolves in the compositional space according to the mixing process S^p_α, followed by the reacting process $\dot{\omega}^p_\alpha$:

$$d\xi^p_\alpha = (S^p_\alpha + \dot{\omega}^p_\alpha)\,dt\,. \tag{4.12}$$

It is again to notice that the source term $\dot{\omega}^p_\alpha$ appears in closed form.

Although the Lagrangian approach is the most followed in the literature, it shows some disadvantages. First, the spatial distribution of the particles must be consistent with the fluid mass distribution within the computational cell. This requires a coupling with the grid-based Eulerian solver, usually performed via a density feedback [203, 246] to ensure physical consistency. Also, statistical convergence in LES requires a high number of particles per cell (N_p) compared to RANS, that could easily reach a total of millions of particles, leading to an increased computational cost. This issue is avoided if the *sparse* Lagrangian

---

[1] Based on the `mmcFoam-5.0` libraries. Further details are reported by Galindo et al [97]

approach for LES is used, based on the Multiple Mapping Conditioning (MMC) model [59], as presented later in this section. A third disadvantage, common to all transported PDF methods, is the computational effort required by a detailed chemistry simulation. The ISAT storage-retrieval algorithm was used for example by the Pope group [48, 318] to speed-up the chemistry. This work exploits a more common reduction technique based on tabulated chemistry (see e.g. [6, 162, 187, 326]).

The Eulerian Stochastic Fields (ESF)

The ESF approach for LES found recent interest in the academic community because it is easy to implement: the statistics is directly evaluated on the computational grid. For each of the scalar fields of the joint-PDF, a composition of N_f stochastic fields exists, with ζ_α^n being the n-th realization of the scalar having index α. A statistically equivalent SPDE to Eq. (4.9) was derived by Valiño [297] using the Itô integration and by Sabel'nikov [251] using the Stratonovich integral. Hereby the second implementation of Valiño from 2016 [298] was used, which reads

$$\begin{aligned} &d\bar{\rho}\zeta_\alpha^n + \frac{\partial(\bar{\rho}\tilde{u}_i\zeta_\alpha^n)}{\partial x_j}dt - \frac{\partial}{\partial x_j}\left(\left(\frac{\bar{\mu}}{Sc}+\frac{\mu_{sgs}}{Sc_{sgs}}\right)\frac{\partial \zeta_\alpha^n}{\partial x_j}\right)dt = \\ &\bar{\rho}\left(\frac{2\mu_{sgs}}{\bar{\rho}Sc_{sgs}}\right)^{1/2}\frac{\partial \zeta_\alpha^n}{\partial x_j}dW_j^n - \frac{\bar{\rho}}{2\tau_{sgs}}(\zeta_\alpha^n-\widetilde{\xi}_\alpha)\,dt - \bar{\rho}\dot{\omega}_\alpha^n(\zeta^n)\,dt\,. \end{aligned} \tag{4.13}$$

While the laminar diffusivity was originally included in the stochastic term of Eq. (4.13) (first on the RHS) [297], only the sub-grid contribution is considered in [298]. This prevents unphysical fluctuations of the scalar gradients due to the stochastic term in purely laminar regions of the flow. The Wiener term is approximated as $\mathrm{d}W_j^n = \gamma_j\sqrt{dt}$, with $\gamma_j = \{-1, 1\}$ being a random dichotomic vector with zero mean [297]. Because a limited number of stochastic fields is sufficient for LES to reach statistical convergence of the first two moments (usually $N_f = 8$), γ_j can substitute $N(0,1)$ as a weak first order approximation generating a zero mean. The second term on the RHS is the micro-mixing term, approximated in ESF by the Interaction by Exchange with the Mean (IEM) [301]. It will be explained in detail in the next section. The filtered $\widetilde{\xi}_\alpha$ required by the IEM model are computed from the average over the fields as $\widetilde{\xi}_\alpha = \frac{1}{N_f}\sum_{n=1}^{N_f}\zeta_\alpha^n$. By setting $\mathrm{C}_d = 2$ according to previous LES applications [141, 204], the sub-grid time scale τ_{sgs} is approximated using the sub-grid viscosity according to Valiño [298]:

$$\frac{1}{\tau_{sgs}} = C_d\frac{\nu_{sgs}}{\Delta^2}\,. \tag{4.14}$$

The source terms $\dot{\omega}_\alpha^n$ are either direct solutions of the chemistry ODE system for the n-th field or interpolated from a thermo-chemical database.

4.2.3. The micro-mixing term

The discussion of the micro-mixing model requires a separate paragraph. The evolution of the PDF should include the change in local composition due to molecular mixing, ideally evolving in time toward a Gaussian (point D in Fig. 4.1). If the initial distribution of the reactants at the sub-grid level is not modified (the β-PDF shown by point B), reactions will not trigger. The two mixing models used in this work are listed in Table 4.1, as well as the main requirements that shall be satisfied by the models [237]. Other mixing models exists (see e.g. [138, 287]) but they are exempted from this investigation.

Table 4.1.: Mixing models used in this work for transported PDF methods

Requirements/Model	IEM [301, 74]	MMC [156, 57]
Conservation of $\widetilde{\xi}_\alpha$	yes	yes
Decay of $\widetilde{\xi''^2_\alpha}$	yes	yes
Boundedness of scalars ξ_α	yes	yes
joint-PDF of inert scalars should relax to a joint-Gaussian	no	yes
Localness in composition space	no	yes

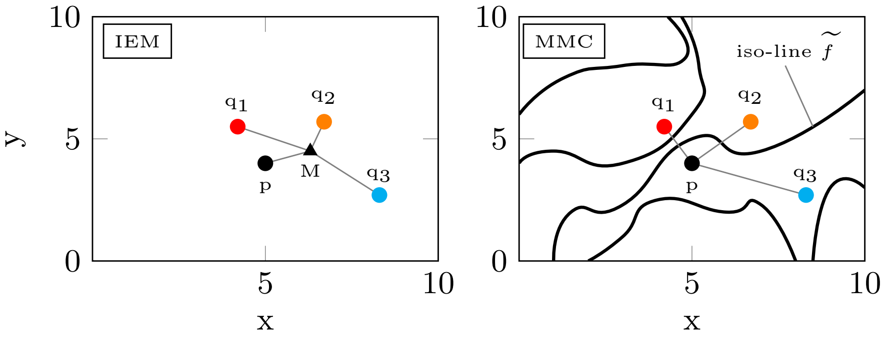

Figure 4.2.: Schematic illustration of the IEM and MMC mixing models using the Lagrangian particle method

IEM The principle of IEM is shown on the left side of Fig. 4.2, adopting the Lagrangian particle method for convenience. The x-y domain can be representative of a computational cell, in which the four particles (circles) are contained. The scalar average of the four particles is shown by the triangle and labelled as M. The scalar value of each particle relaxes towards the mean value, in the directions shown by the gray connection lines. Using the IEM model, the last term of Eq. (4.9) can be written as

$$\frac{\bar{\rho}}{\tau_{sgs}} \sum_{\alpha=1}^{n} \frac{\partial}{\partial \pi_\alpha} \left[\left(\pi_\alpha - \widetilde{\xi}_\alpha \right) \widetilde{\mathcal{P}} \right] \tag{4.15}$$

as found in the ESF formulation. Although Table 4.1 lists two unfulfilled requirements for the IEM model, it was seen to suffice when combined to *dense* Lagrangian particle and ESF models for LES [58, 198, 134]. There, the sgs mixing has small influence on the resolved flow and composition scales and a well-resolved grid already includes some kind of localness. A poor performance is seen instead on coarser grids (e.g. for RANS applications [198]) and when the distance between particles becomes very large (*sparse* Langrangian LES [58]).

Multiple Mapping Conditioning (MMC) The MMC plays the role of a mixing model that incorporates the conditioning closure existing for reduced manifolds (e.g. flamelets).

Thus, it is based on the observation that not all the thermo-chemical space is accessed. The turbulent fluctuations of a generic major scalar $\widetilde{\xi_\alpha''^2}$ are fully or partially confined to a reference space where the PDF is known or prescribed. Usually the (Eulerian) filtered mixture fraction $\widetilde{f}$ is selected as reference variable for non-premixed regimes [58] (for premixed regimes using a reaction progress variable $\widetilde{c}$, see for example Straub et al [286]). Such variable should emulate as close a possible the key major species of the real Lagrangian particles. In other words, two mixture fractions exist in MMC: the real field calculated for the Lagrangian particles via the SDE system, and the Eulerian $\widetilde{f}$ which mimics closely the actual variable. Although a deterministic version of MMC exists [156], only its (stochastic) generalized version was investigated in this work [154, 57].
In MMC each selected particle pair (p, q) interacts with each other instead of with a mean scalar, as depicted on the right side of Fig. 4.2. The idea of mixing between two random particles was already introduced in the modified Curl model [138], leading however to localized unphysical mixing. The MMC solves this problem by specifically selecting the particles to mix, which are near in the reference space. Iso-countours of $\widetilde{f}$ are shown in Fig. 4.2. Localness in physical space is achieved if particles (p, q_1) are mixed, however two levels of $\widetilde{f}$ (the reference space) are crossed. What happens if the flame front is located between p ad q_1? Burned and fresh gases will be mixed across the flame front causing non-localization in composition space. On the other hand, localness in $\widetilde{f}$ would be achieved by mixing (p, q_3). The MMC model would select the mixing pair (p, q_2) because the distance in both physical and reference space is minimized. This property allows to reduce the ratio *particles/cell* required by a standard Lagrangian particle LES (*dense*) from a value of dozens to less than one. The computational time is massively reduced.

It is useful to introduce some aspects of MMC, in order to understand the numerical models adopted in this work. The selection of the pairs to be mixed is based on the minimization of the effective square distance in physical and reference space [59]

$$\hat{d}^2_{p,q} = \sum_{i=0}^{3} \left(\frac{dx_i^{p,q}}{r_m/\sqrt{3}} \right)^2 + \left(\frac{df^{p,q}}{f_m} \right)^2 \tag{4.16}$$

where r_m (f_m) is the characteristic physical (reference) separation scale. Their correlation is derived from the fractal theory applied to turbulence [276]. The minimization method and particle sorting is based on the `kd-tree` algorithm as explained in [97]. Once each pair (p, q) is selected for mixing, the particles are mixed according to

$$\begin{aligned} \xi_\alpha^p(t+\Delta t) &= \xi_\alpha^p(t) + \gamma_{mix}[\bar{\xi}_\alpha^{p,q}(t) - \xi_\alpha^p(t)] \\ \xi_\alpha^q(t+\Delta t) &= \xi_\alpha^q(t) + \gamma_{mix}[\bar{\xi}_\alpha^{p,q}(t) - \xi_\alpha^q(t)]\,. \end{aligned} \tag{4.17}$$

The two-particle mean $\bar{\xi}_\alpha^{p,q}$ is calculated from the knowledge of the particle masses as $(\mathrm{m}^p\xi^p + \mathrm{m}^q\xi^q)/(\mathrm{m}^p + \mathrm{m}^q)$, while the extent of mixing $\gamma_{mix} = 1\text{-exp}(\text{-}\Delta t/\tau_L)$ requires the knowledge of a mixing time scale τ_L. The latter is calculated using the anisotropic approach for the reference variable gradients as proposed by Vo et al [302] for the *sparse* Lagrangian approach. After mixing, the additional source terms $\dot{\omega}_k$ are calculated for each particles using an ODE chemistry solver available in OpenFOAM.
The coupling problem between the Langrangian particles and the Eulerian solver follows the concept of the equivalent enthalpy of Muradoglu et al [203], with additional Eulerian transport equations solved for the main species. This module is not reported here since it

was not modified by this implementation. Detailed information about the density-feedback in MMC is available in [58, 97].

4.3. Neglecting sub-grid TCI

The models introduced in the previous paragraph derive from the necessity of modelling the effects of flow fluctuations on the chemistry within the sub-grid scales, which are not resolved by the LES. For the chemical source term this translates into $\overline{\dot{\omega}}_k \neq \dot{\omega}_k(\widetilde{T},\widetilde{Y}_k)$, as explained in the example at the beginning of this chapter. However, recent LES investigations on CH_4/air partially-premixed flame configurations [30, 118, 204], oxy-fuel flames [117] and multi-regimes burners [164] showed that neglecting the TCI on the sub-grid scales when using finite rate chemistry on sufficiently fine grids was enough to approximate the available experimental data, with the advantage of reducing the computational cost. In other words, the identity $\overline{\dot{\omega}}_k \neq \dot{\omega}_k(\widetilde{T},\widetilde{Y}_k)$ was considered valid.

Obviously, necessary and sufficient criteria to justify this assumption over a wide range of flame configurations and operating conditions are hard to find. These will be different for non-premixed, partially premixed and fully premixed combustion. For instance, premixed combustion cases require a highly refined computational grid in order to resolve the flame front sufficiently to ensure the correct flame propagation. It is also unclear what would be the subgrid requirements for lifted methane-air flames in vitiated coflow (e.g. the experiment of Cabra et al [43]), where autoignition is the driving mechanism for flame stabilization. The model employed to compute the sub-grid mixture fraction variance could already affect the lift-off height of the flame [148]. Nonetheless, this model was considered in this work for partially premixed flame configurations and a novel autoignition investigation, justified by the fulfilment of the LES grid requirement of Eq. (2.23). In fact, if $\dot{\omega}_k(T,Y_k)$ can be approximated well by its first order Taylor expansion in (T,Y_k), then $\overline{\dot{\omega}}_k = \dot{\omega}_k(\widetilde{T},\widetilde{Y}_k)$.

4.4. Tabulated chemistry/TCI solver implementations

The following information can be useful to the reader if the code structure and the numerical implementation are of interest. However, it is not fundamental for the understanding of the next chapter. A detailed description of the implemented OpenFOAM routines based on tabulated chemistry is summarized in Appendix C. After a brief discussion of the pressure-based solver, the library `ESFredimFoam-6` is first introduced. This library contains the coupling of the ESF model with the REDIM tabulated chemistry, as depicted schematically in Fig. C.2. Afterwards, the second library based on `mmcFoam-5.0` is discussed, where the MMC was coupled to REDIM as shown in Fig. C.3. Finally, a brief description of the flamelet solver is provided in C.4.

An overview of the flame configurations and combustion models applied to the simulations of Chapter 5 is also reported for completeness in Appendix B.

5. Results

This chapter presents the results and discussion for the four investigated test cases using the combustion models introduced in the previous sections. For each test case, a trade-off between model accuracy compared to the available experimental data and computational performance is provided.

5.1. CH_4/air partially premixed flames with homogeneous inlet

The first investigation is based on the CH_4/air flames D-E-F from the Sandia series featuring homogeneous inlets and an increasing Reynolds number [10]. The latest experimental data were provided by Schneider et al [260]. Such flames are well known in the community and are often taken as benchmark for the validation of TCI models. Hereby the target is to assess the influence of the TCI models (no-TCI, ESF and MMC) and the tabulated chemistry (REDIM with simplified and detailed transport) on the predictions, as well as the computational performance.
An homogeneous partially premixed mixture of CH_4-Air in volume percentage 25/75 is injected at 294 K into the domain through a pipe of diameter D = 7.2 mm, with a bulk velocity $u_b = 49.6$ m/s (74.4, 99.2 m/s) for configuration D (E, F). The cold jet is stabilized by a burned lean mixture at 11.4 m/s (17.1, 22.8 m/s) and 1880 K (1860 K for flame F). Under such conditions the stoichiometric mixture fraction is $f_{st} = 0.351$, at the pilot inlet $f_p = 0.271$ and at the fuel inlet $f_f = 1$. An air coflow at 291 K embeds the pilot with a velocity of 0.9 m/s in all configurations. An overview of the boundary conditions is provided in Table 5.1. The inlet composition does not change between the flames.

Table 5.1.: Sandia flames: boundary conditions at inlets

Inlet	u_b [m/s]: D	E	F	T [K]	Y_{O2}	Y_{CH4}	Y_{H2O}	Y_{CO2}	Y_{N2}
Pilot	11.4	17.1	22.8	1880 (F: 1860)	0.056	0	0.092	0.11	0.73
Fuel	49.6	74.4	99.2	294	0.197	0.156	0	0	0.647
Coflow	0.9	0.9	0.9	291	0.233	0	0	0	0.756

Flame F is particularly challenging for the TCI models because it features a strong degree of local extinction. This flame is illustrated in Fig. 5.1, with a snapshot of the temperature field in the background. The iso-contour of $\widetilde{f}_{st}$ is coloured with a gray scale representing the $\widetilde{OH}$ field. This is a clear indicator of flame extinction, shown by the black regions in the figure (thus, absence of radical OH). The axial locations x = 54, 108, 216, 324 mm correspond to the non-dimensional values of x/D = 7.5, 15, 30 and 45 where experimental data are available.

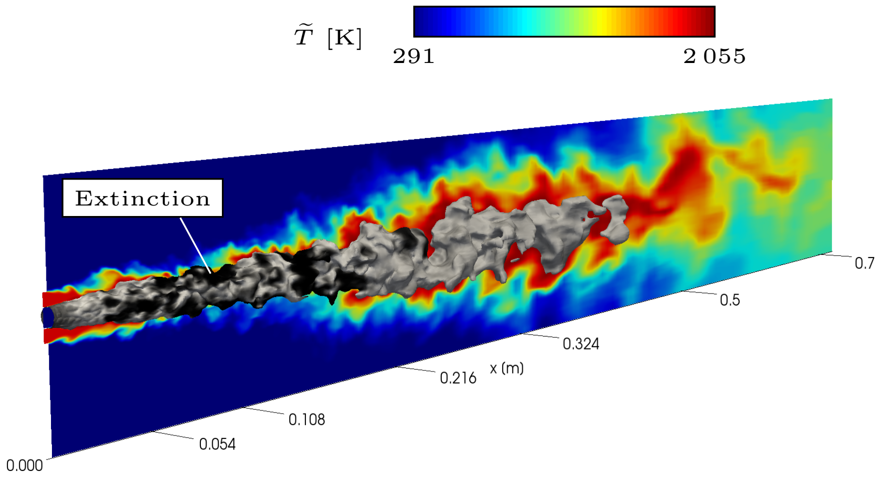

Figure 5.1.: Sandia Flame F, characterized by strong extinction (black spots located at $\widetilde{OH} = 0$). The iso-contour is shown for $\widetilde{f}_{st} = 0.351$, $\widetilde{T}$ is the background field

5.1.1. Numerical setup

Two 3D axial-symmetric meshes were investigated in this work. This first one consists of about $2.3{\cdot}10^6$ volume cells and is selected as reference (labelled as R). Mesh dependency was investigated in previous publications [30, 35], to which an interested reader is pointed. The computational domain extends to 100 D in axial direction and to about 13.9 D in radial direction.

The second mesh is targeted for the MMC investigation and was kindly provided by Eshan Sharma (Indian Institute of Technology Kanpur) for a joint investigation. It consists of two levels of meshing: the base mesh (BM) with $2.2{\cdot}10^6$ cells for the Eulerian part of the solver (cf. Fig. C.3) and the *super* mesh SM with $0.19{\cdot}10^6$ cells for the Lagrangian solver [1]. Here the computational domain is limited to 35 D in axial direction and 12.5 D in radial direction.

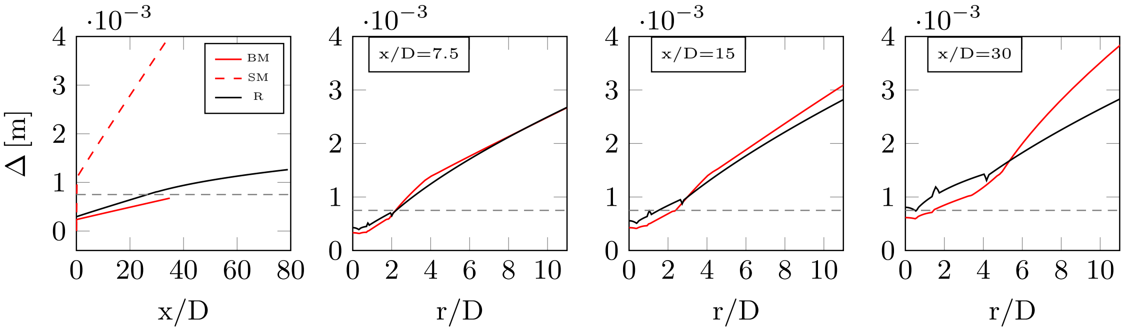

Figure 5.2.: Axial and radial development of the LES filter width Δ on the reference mesh R (black), and the MMC-targeted meshes BM and SM (red)

Fig. 5.2 reports the cell size Δ along the axis and at the investigated sections x/D = 7.5, 15, 30. The gray dashed line shows the resolution of 0.75 mm derived from the experiment [9].

---

[1] The MMC group refers to these meshes respectively as LES-mesh and superMesh

BM provides a better refinement than R around the centreline, but less refinement radially for r/D$>$6 (cf. section x/D$=$30). The coarse mesh SM for the Lagrangian particles is shown only in the first plot, with an axial development of the cell size from 1 to 4 mm moving downstream.
Turbulence is generated at the fuel inlet by means of a separate pipe LES, while a velocity block profile is applied for both pilot and coflow. The WALE turbulence model is used for these flames. The CFD fields are averaged over 5-10 flow-through times. The mixture fraction is calculated using the conservation of elements C, O, H as provided by Bilger in Eq.(3.20). This is advantageous for the simulations based on the REDIM including differential diffusion, because its value is directly retrieved from the element conservation. In fact, the use of Eq. (4.6) is strictly valid only under the unity Lewis number assumption.

ESF Solver The ESF solvers use an implicit Euler time integration scheme and a Total Variation Diminishing (TVD) scheme of type van Leer for the scalar fluxes. A second order scheme from OpenFOAM (`filteredLinear`) is used instead for the velocity field, because less dissipative. A total number of 8 stochastic fields are transported, according to previous investigations [30, 118]. This is the base solver used for the TCI investigation of this paragraph.

MMC Solver The sparse Lagrangian MMC solver uses 1 particle for 6 Eulerian LES cells (1L/6E), where the particle number control is associated with the mesh SM. The number of particles per BM-cell is $N_p = 20$, limited between 17 and 30. The parameter f_m is set to 0.03 [103] while r_i is calculated as explained by Cleary and Klimenko [58]. Note that these settings derive from the previous investigation conducted at the IIT Kanpur and are not modified in this work. The density coupling is performed via a Kernel estimator [97].

5.1.2. Micro-mixing in ESF

Molecular mixing on the sub-grid scale is modelled by the IEM model, where the mixing constant $C_d = 2$ is assigned in this work (cf. Eq. (4.14)). Previous investigations showed that LES are rather insensitive to the choice of C_d (e.g. Jones et al [141] for ESF), because the energetic motions are resolved. This statement is supported in this work by Fig. 5.3.

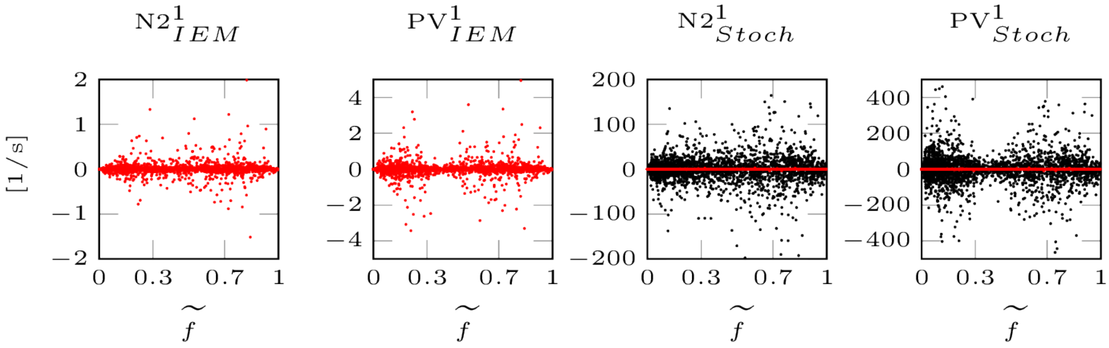

Figure 5.3.: Flame D: scatter data for the IEM (red) and stochastic terms (black) at section x/D$=$15. REDIM variables N2 and PV are sampled from the stochastic field $n = 1$. Note the difference in scale

The figure shows the scatter data for the micro-mixing (red) and the stochastic terms (black) of Eq. (4.13), sampled without the multiplicative term $\overline{\rho}$. Flame D was sampled at the representative section x/D = 15 using mesh R. The remaining sections showed similar results and are therefore not reported. The joint-PDF is built for tabulated chemistry using the REDIM variables $\xi_\alpha^n = \{N_2^n, PV^n\}$ and the field at $n = 1$ is selected for the representation. If one overlaps the two clouds of data, one can clearly see that the magnitude of the IEM term is about factor 100 less than the magnitude of the stochastic contribution, for both transported fields. As a consequence, a variation of C_d is not expected to shift considerably the weight of the IEM term towards the stochastic contribution, and it is therefore not further investigated.

5.1.3. Absence of TCI

Assuming that the micro-mixing term does not significantly influence the ESF computations, the focus is now switched to the chemistry. In fact, finite rate ESF simulations require a considerable computational power, if the entire chemistry system has to be solved for the N_f transported stochastic fields on each cell. The first solution proposed in this work to overcome this issue is neglecting the sub-grid TCI modelling, if the grid resolution satisfies the LES criterion given in Eq. (2.23). Selected results presented hereby were previously published in [30]. The need of this investigation stems from previous observations [118, 204] comparing finite rate chemistry ESF with laminar chemistry computations (i.e. ESF switched off): no significant differences were observed when removing the sgs-TCI interaction provided by the ESF.

Finite rate chemistry simulations of Flame E using the Lu19 chemistry are shown in Table 5.2. The number of transported stochastic fields is varied as $N_f = 2$, 4 and 8. A laminar computation is also run, where the unfiltered source term $\dot{\omega}_k$ is directly used in the species transport equation (2.31). Note that this laminar simulation could be also achieved by switching off the stochastic term in the ESF equation, while transporting only one stochastic field ($N_f = 1$). However, because the two solvers differ in the implementation, an exact match is not achieved. Table 5.2 summarizes the configurations. The computational speed-up of the laminar computation compared to the reference ESF with 8 stochastic fields is about factor 5 (same CPU architecture of [35]).

Table 5.2.: Finite rate chemistry: no-TCI vs ESF

Case	sgs-TCI	N_f	Composition	Speed-up
Lam-Lu19	none	(1)	$\widetilde{Y}_k$ from Eq. (2.31) with $\overline{\dot{\omega}}_k \approx \dot{\omega}_k$	4.63
ESF2-Lu19	ESF	2	$\widetilde{Y}_k = (\sum Y_k^n)/N_f$ after solving Eq. (4.13)	3.20
ESF4-Lu19	ESF	4		1.87
ESF8-Lu19	ESF	8		1

The chemical mechanism investigated here is based on 19-species. The comparison among different chemical mechanisms is reported in a previous publication of the author [30]. It was seen there that a stronger deviation of the mean profiles in both physical and composition space is expected when the chemical mechanism is changed. Since the chemistry is left unaltered in this paragraph, more interesting is the discussion of the resolved fluctuations, because they are a result of the sgs-TCI model. This is shown in Fig. 5.4. In

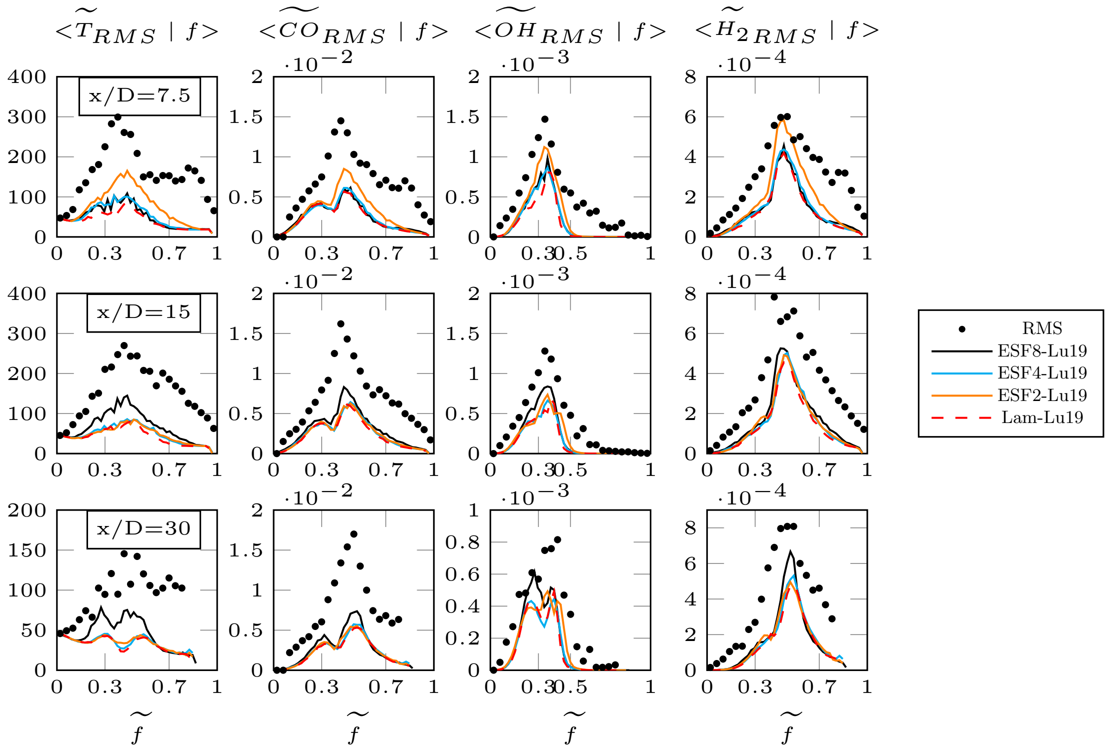

Figure 5.4.: Flame E: Conditional fluctuations of T and major species at x/D = 7.5, 15 and 30. Comparison ESF against laminar chemistry (no-TCI)

section x/D = 7.5 the ESF2-Lu19 calculation reports stronger fluctuations than the other simulations, with a fair prediction of OH and H$_2$. In sections x/D = 15 and 30 instead, the ESF8-Lu19 provides slightly better results. It should be remarked that the configuration with N$_f$ = 2 tends to be noisy, because the Wiener term is applied on a single pair of stochastic fields. This was already observed by the author for the tabulated chemistry configuration in [35]. The better predictions upstream could be here a coincidence. While the RMS seems to be better represented downstream for N$_f$ > 2, there is no strong evidence that a larger number of fields provides a significantly better result compared to Lam-Lu19. This statement is supported by a recent work of Hansinger et al [118], using a maximum of N$_f$ = 64 in a more challenging flame configuration. Surely the effect of ESF would become stronger by decreasing the mesh refinement (expected at x/D > 30 for mesh R, according to Fig. 5.2), because the TCI is able to represent the micro-mixing processing which would be otherwise filtered out. The range of applicability of ESF on coarser meshes for non-premixed flame configurations however is limited by the minimum grid refinement required by a well-resolved LES, thus the criterion on the sgs turbulent kinetic energy given in Eq. (2.23). The idea behind this reasoning is the following: if the mesh satisfies the requirements for LES, then the ESF application would be justified. According to the results of this paragraph, the laminar chemistry computation can still provide satisfactory results. Therefore, a laminar chemistry simulation can be attempted first, leading to significant reduction in computational time. The LES requirement for mesh R is evaluated directly for all flames using the laminar chemistry. The results are shown in Fig. 5.5. The modelled $\widetilde{k}_{sgs}$ is less then 10 %

in all sections, with a stronger dependence on the inlet boundary conditions up to about x/D = 15.

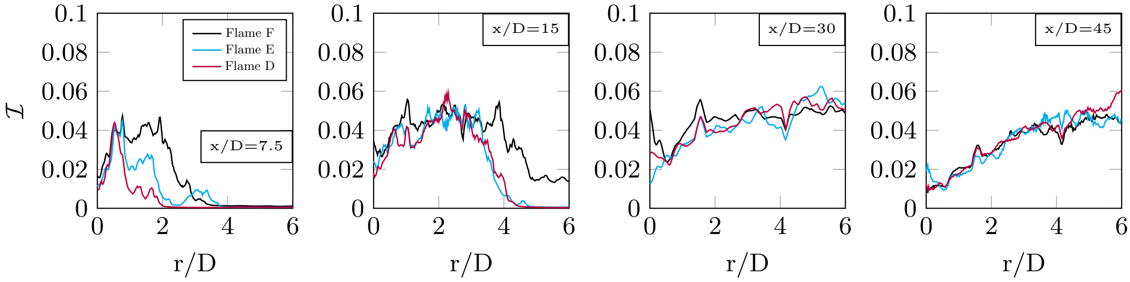

Figure 5.5.: Flame D-E-F: Mesh requirement $\mathcal{I} < 0.2$ satisfied for all sections using a laminar chemistry computation

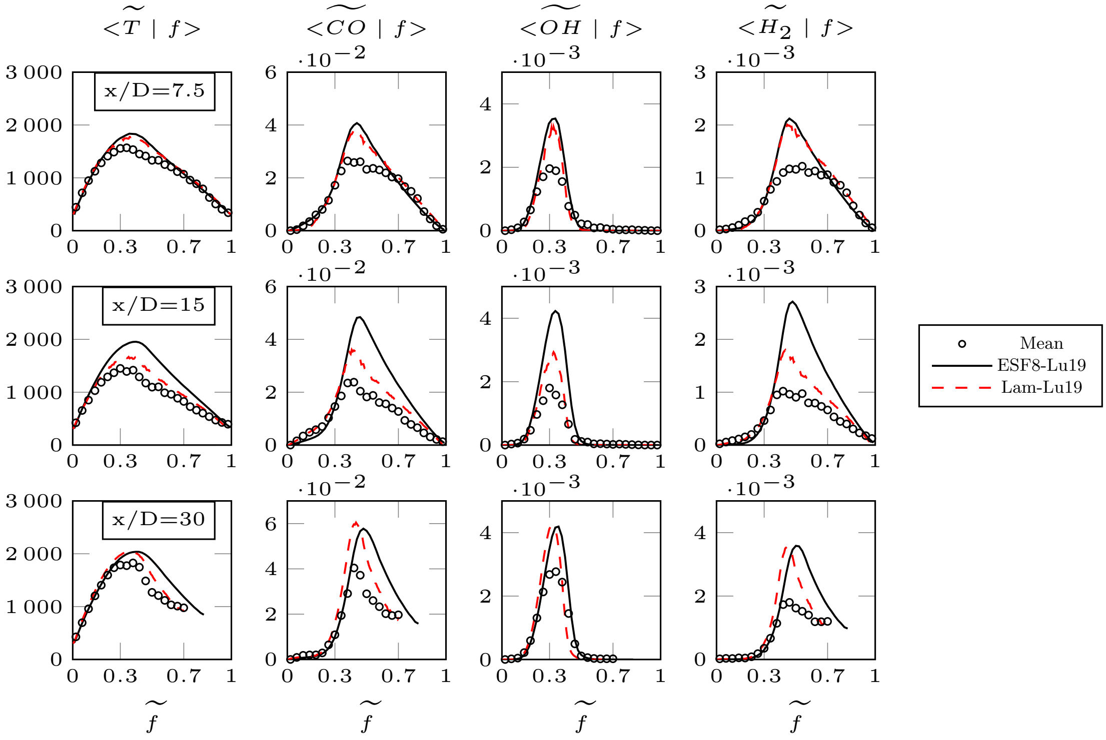

Figure 5.6.: Flame F: Conditional means of T and major species at x/D = 7.5, 15 and 30. Comparison ESF against laminar chemistry (no-TCI)

If one compares the 8ESF-Lu19 with the Lam-Lu19 setup on flame F (Fig. 5.6), one can see that both simulations lack to predict the correct degree of extinction/re-ignition, especially at x/D = 15. The fact that the laminar case provides a better prediction could be a coincidence, generated by the numerical schemes. This observation leads the way to further investigations:

- The finite rate ESF solver itself does not seem to correctly predict strong extinction/re-ignition events in this implementation. A dual benefit could derive if tabulated chemistry is used: a dramatic reduction of the computational cost and additional information about the composition space accessed in proximity of a reaction-diffusion surface attractor. Paragraph 5.1.4 summarizes the results of this investigation.

- Despite the chemistry model, the poor extinction/re-ignition representation of ESF could be due to the TCI model itself. A comparison with a second TCI model is beneficial to assess advantages and disadvantages of this solver. ESF is compared with MMC in Paragraph 5.1.5.
- The results obtained from the laminar chemistry computation are satisfactory instead. One could try to further increase the computational speed-up using accelerated chemistry solvers. The short manuscript of Breda et al [30] covered this topic. In [30], the TDAC module implemented in OpenFOAM by Contino et al [62] was found to be a promising candidate to speed up the laminar chemistry computation of factor 2 on a variety of flame regimes, provided that an optimization of the tabulation parameters is performed.

5.1.4. REDIM-based ESF

The choice of tabulated chemistry

Two low-dimensional attractor strategies were presented in Chapter 3, namely the ILDM and the REDIM. In a preliminary step, both tabulated chemistries were coupled with the ESF solver and compared in the simulation of flame D, which shows a low degree of extinction. The chemistry tables are described in Table 5.3. The non-premixed nature of the flame requires a second reactive progress variable in ILDM, extending its dimensions to 3. Its memory allocation is therefore higher than REDIM. The interpolation time is also higher, since the 3D-ILDM is based on a non-uniform grid and has a clustering of grid points around stoichiometry. The tables are not based on the same chemistry (Smooke for ILDM and GRI-3.0 for REDIM), but this should have a minor effect at least on flame D. The passive progress variable is N_2 for REDIM and f for ILDM.

Table 5.3.: Tabulated chemistry: ILDM vs REDIM

Case	Variables	Grid	Chemistry	Memory [MB]
ESF-ILDM	$\phi_{CO2} \times \phi_{H2O} \times f$	90×90×170^a	Smooke [270]	476 MB
ESF-REDIM	$Y_{N2} \times Y_{CO2}$	200×200^b	GRI-3.0	80 MB

^{a} non-uniform grid with expansion ratio $\delta_r = \{0.8, 0.8, 1.08\}$

^{b} uniform equidistant grid

Fig. 5.7 shows the unconditional means of mixture fraction, temperature and the major species. At x/D = 7.5 there is a good agreement between the two manifolds, except for CO and OH. This is because the ILDM lacks of information from the diffusion term in the composition space. It can be visually explained with the scatter data of Fig. 5.8. The surface is the 2D-REDIM coloured by CO (left) and H_2O (right). Scatter data from x/D = 7.5 are reported by the white points for REDIM and by the red points for ILDM. For CO (and therefore the radicals), one can see that the ILDM tabulation on the fuel-rich side is covering chemical states far away from the reaction-diffusion attractor. In this region the ILDM would require additional dimensions to correctly separate the slow chemistry from the fast

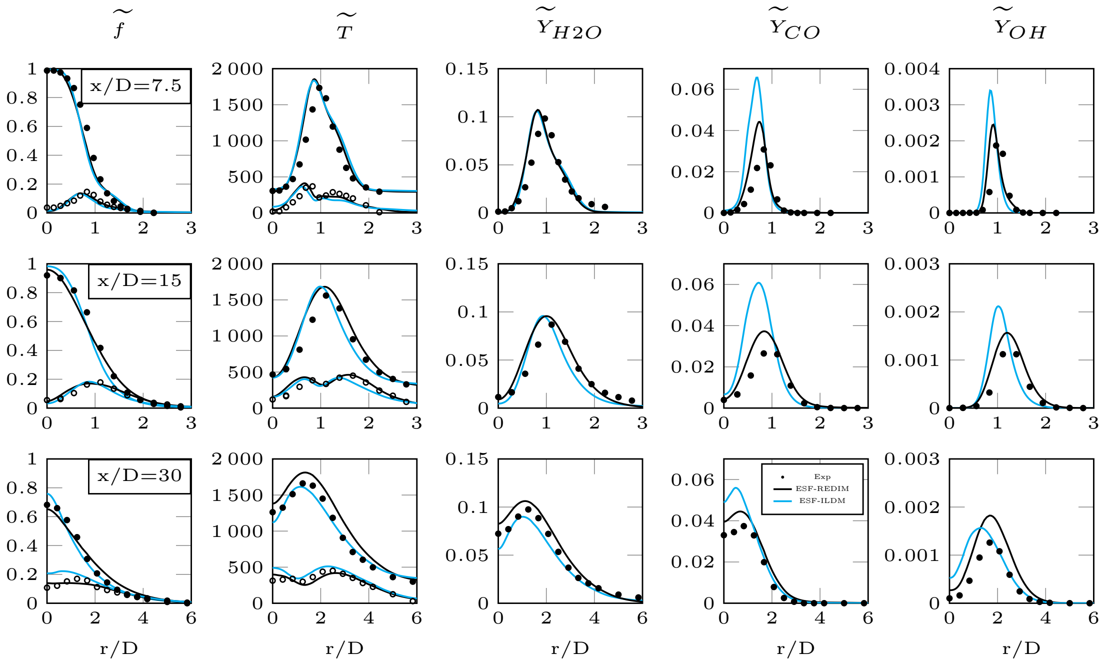

Figure 5.7.: Flame D: Unconditional T and major species at x/D = 7.5, 15 and 30. Comparing 3D-ILDM with 2D-REDIM

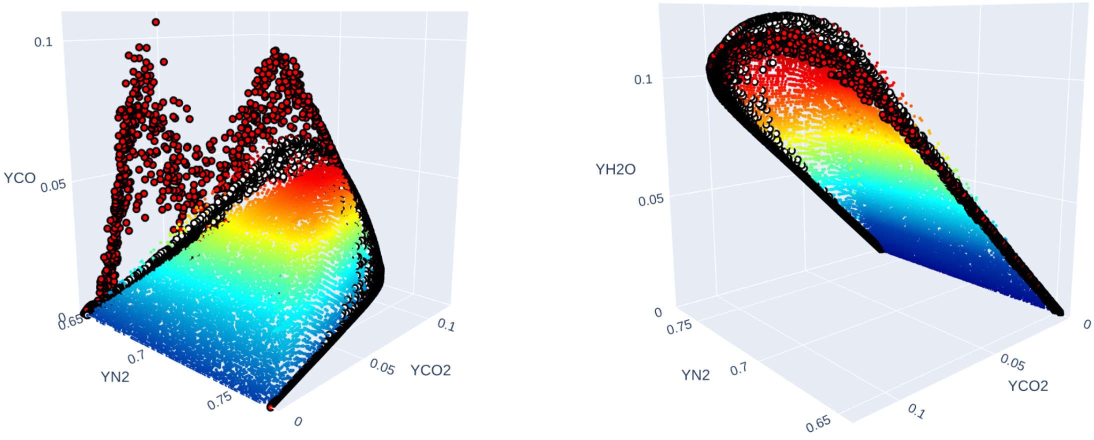

Figure 5.8.: 2D-REDIM surface coloured by CO (left) and H_2O (right). Scatter data sampled at x/D = 7.5 for REDIM (white dots) and ILDM (red dots)

one. Different is the case of H_2O, because it is already a variable of the ILDM. The two clusters of data appear shifted for H_2O. This could be due to the chemistry used to build the table (16 species for ILDM, 53 species for REDIM). A more accurate implementation of ESF-ILDM would require the projection of the diffusion terms of the ESF equations onto the ILDM manifold, with a similar approach used by Eggels [83] for 1D-laminar flames. This is obviously an expensive routine. For the reasons explained, the ILDM was discarded from the investigations involving severe extinction regimes.

A 2D-REDIM based on the unity Lewis number assumption represents the solution of a flamelet database (like FGM or FPV), if its gradients are estimated from counterflow diffusion flames or free flames. As previously explained in Chapter 3, its advantage against FPV is that the reaction and diffusion terms are already balanced, so that a laminar flame is entirely described by the low-dimensional REDIM surface. The situation is different in turbulent reactive flows. The composition space accessed by flame D can be in general well approximated by any reaction-diffusion manifold (FPV, FGM, REDIM, . . .) created for these boundary conditions, because the thermo-kinetic states correspond to a burning solution. Testing on the extreme case, flame F, reveals important limitations instead. Let us compare a premixed-based FPV database (thus the original formulation of van Oijen) with a non-premixed-based REDIM. The features of both tables are summarized in Table 5.4. The configuration of the β-PDF-FPV for OpenFOAM was widely discussed in previous publications, to which the reader is pointed for details (e.g. [93, 116]).

Table 5.4.: Tabulated chemistry: FPV vs REDIM

Case	Variables	Grid	PV	sgs-TCI
β-PDF-FPV	$\widetilde{f} \times \widetilde{f''^2} \times$PV	501×10×501	$\phi_{CO2}+\phi_{H2O}+\phi_{CO}$	β-PDF
ESF-REDIM	$Y_{N2}\times$PV	200×200	$Y_{CO2}+Y_{H2O}+Y_{CO}+Y_{H2}$	ESF

In both computations the off-manifold states are projected back to the surface using the constant parametrization matrix **C** (see Ch. 3), which however generates a certain dependence on the choice of the reactive progress variable PV [323]. The expression of $PV = Y_{CO2}+Y_{H2O}+Y_{CO}+Y_{H2}$ for REDIM was used for flame F in this work.
Fig. 5.9 shows a comparison of the conditional means of temperature and major species calculated for flame F. The β-PDF-FPV represents T and OH well in section x/D = 7.5 and fairly good in the remaining sections. However, CO and H_2 are completely overestimated, also compared to the REDIM. In general, the over prediction of CO signalizes that a second reacting progress variable is required for a better approximation of the slow chemistry. This was confirmed by Yu et al [323] by adding OH as third progress variable in the REDIM. The same can be done with FPV, obtaining a 4D-table. Ihme and Pitsch [129] showed that the FPV predictions for the Sandia flames can be improved if the variance $\widetilde{PV''^2}$ is included as table parameter, thus modelling the marginal PDF for the reactive scalar (leading again to a 4D-FPV table). The REDIM seems to require less dimensions (smaller tables) and less modelling on the TCI side (no assumption on the PDF shape) in order to provide better results than the FPV method. The scope of the next paragraphs is to show the potential of REDIM to accurately describe flame F.

REDIMs with unity Lewis numbers

The detailed investigation of 2D-REDIM configurations for Sandia flames D and E, as well as the dependency on the number of stochastic fields was presented in a previous paper of the author [35]. The results of [35] are here only briefly summarized and used as start point for the next discussion. The ESF-REDIM solver was validated primarily using a 2D-REDIM with $\{Y_{N2},\ Y_{CO2}+0.5\,Y_{H2O}\}$ as reduced coordinates. The solver was able to

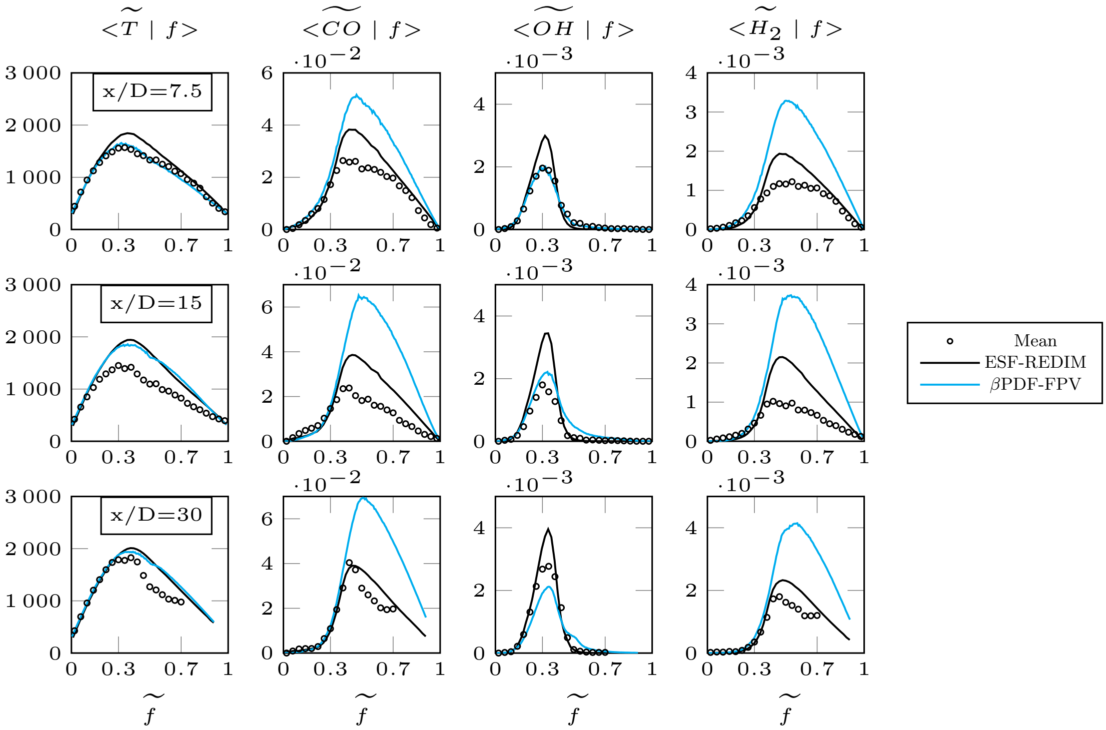

Figure 5.9.: Flame F: tabulated chemistry computation, FPV vs 2D-REDIM. Conditional means of temperature and major species

correctly capture the flame behaviour in the investigated sections, although local extinction was underestimated by the ESF close to the injector plate. The H_2 concentrations were strongly influenced by the REDIM transport model instead.
These premises are the basis for the evaluation of the ESF-REDIM solver on flame F. As anticipated in the last section of [35], using the same 2D-REDIM configuration for flame F lead to a strong underestimation of the extinction events. This configuration is labelled as F1-Le1 in Table 5.5, and it is marked in black in the conditional plots of Fig. 5.10-5.11.

Table 5.5.: REDIM tables for flame F built for unity Lewis numbers

Case	χ	Dim	Model χ	PV
F1-Le1	504	2D	-	$Y_{CO2}+Y_{H2O}+Y_{CO}+Y_{H2}$
F2-Le1	73, 145, 218, 291, 363, 504	3D	$D(\nabla\widetilde{f})^2+C_\chi D_{sgs}\widetilde{f''^2}/2\Delta^2$ [73]	$Y_{CO2}+Y_{H2O}+Y_{CO}+Y_{H2}$
F3-Le1	73, 145, 218, 291, 363, 504	3D	$(D+D_{sgs})(\nabla\widetilde{f})^2$	$Y_{CO2}+Y_{H2O}+Y_{CO}+Y_{H2}$
F4-Le1	73, 145, 218, 291, 363, 504	3D	$D(\nabla\widetilde{f})^2+C_\chi D_{sgs}\widetilde{f''^2}/2\Delta^2$ [73]	$\phi_{CO2}+\phi_{H2O}+\phi_{H2}$

Looking at the conditional means, it is clearly visible that this configuration is more stable in sections x/D = 7.5 and 15: higher temperatures than the experiment are seen, especially

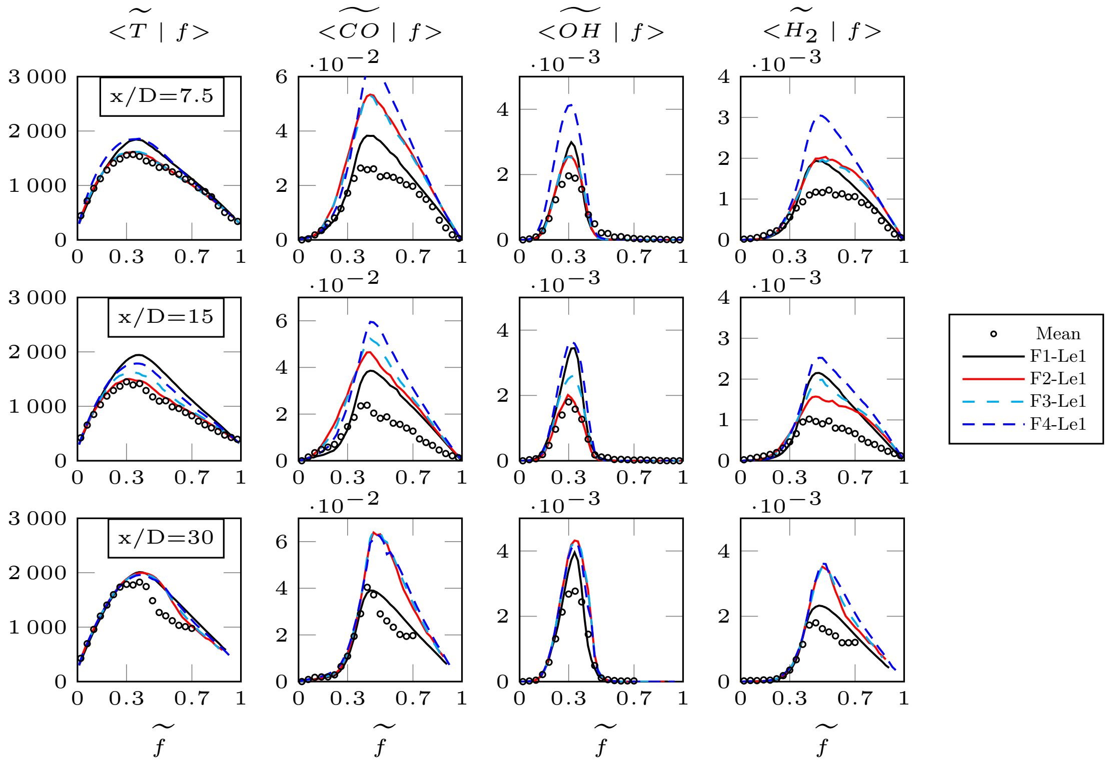

Figure 5.10.: Flame F: Conditional means of temperature and major species for the test cases of Table 5.5

at section 15 where most of the extinction/re-ignition events are expected. On the other hand, CO and H_2 show overall a good prediction, especially downstream at section 30. When looking at the conditional fluctuations instead, the profiles are strongly underpredicted compared to the experiment, especially at section x/D = 30.

The 2D-REDIM table for F1-Le1 was built from a gradient estimate $\gamma(\boldsymbol{\theta})$, deriving from a detailed solution of a steady counterflow flame[2]. One possibility to improve the predictions for flame F is using several 2D-REDIMs, each of it featuring a different gradient estimate $\gamma(\boldsymbol{\theta})$. In this way the thermo-chemical state is capable to describe the extinction region based on higher scalar dissipation rates, and to cover the stable solutions otherwise. This configuration is referred as 3D-REDIM hereby, where the scalar dissipation rate χ becomes the third table parameter. Table 5.5 reports the investigated 3D-REDIM configurations. Six tables built for different $\gamma(\boldsymbol{\theta})$ are used. The ESF-REDIM solver requires now a model for $\widetilde{\chi}$, which has to be calculated for each cell before performing table interpolation. Simulations F2-Le1 and F3-Le1 compare two different χ models. The expression of Domingo at al [73] contains the sub-grid contribution, which requires the knowledge of variance $\widetilde{f''^2}$, calculated here as $\Delta^2(\nabla\widetilde{f})^2$. The value $C_\chi = 2$ is taken for the multiplicative constant. The second model instead is based on the gradient transport assumption. Simulations F2-Le1 and F4-

---

[2] One can re−write the term in square brackets of Eq. (3.11) containing the gradient $\nabla\boldsymbol{\theta}$ as a function of the scalar dissipation rate: $(\boldsymbol{D}\,\boldsymbol{\Psi}_{\boldsymbol{\theta}} \cdot \gamma(\boldsymbol{\theta}))_{\theta} \cdot \gamma(\boldsymbol{\theta})$. The gradient estimate is therefore expressed as $\gamma(\boldsymbol{\theta}) = \nabla\boldsymbol{\theta} = \begin{bmatrix}\nabla\theta_1 & \nabla\theta_2 & \dots & \nabla\theta_{ms}\end{bmatrix}^T$

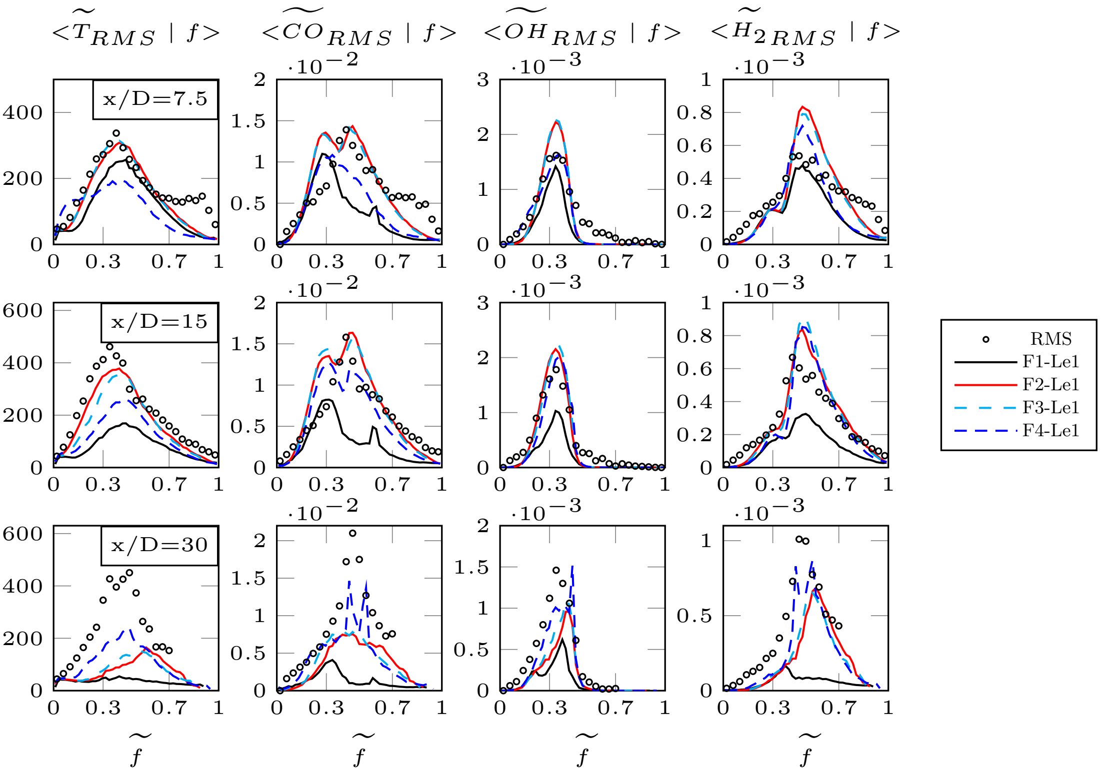

Figure 5.11.: Flame F: Conditional fluctuations of temperature and major species for the test cases of Table 5.5

Le1 aim to compare a different choice of PV: $Y_{CO2}+Y_{H2O}+Y_{CO}+Y_{H2}$ proposed by Ihme and Pitsch [128] and $\phi_{CO2}+\phi_{H2O}+\phi_{H2}$ proposed by van Oijen and de Goey [299].

Fig. 5.10-5.11 include the results for the 3D-REDIM configurations. The comparison of the means for F2-Le1 and F3-Le1 shows that the model for χ plays a significant role in the prediction of the extinguished states at section x/D = 15. The sub-grid contribution for $\widetilde{\chi}$ plays the major role here. F2-Le1 predicts very well the mean temperatures and OH concentrations in this section, although CO and H_2 are overpredicted. The conditional RMS show a similar behaviour, with a very good prediction in sections 7.5 and 15. Section 30 is recovered, compared to the case F1-Le1. By comparing the progress variables, one can see that F4-Le1 tends to predict too less extinction events in the first two sections, approaching the solution of F1-Le1 for T, OH and H_2. This explains the poorer RMS predictions at the same sections, but interestingly there is an improvement at x/D = 30 compared to F2-Le1. These results show that the simulations of flame F are stronger influenced by the choice of the progress variable and at least three dimensions are required in the table. Overall the best setup is provided by configuration F2-Le1, which is retained for further comparison.

It is interesting to compare the accessed composition space of $\widetilde{T}$ and $\widetilde{OH}$ for F2-Le1 at location x/D = 15, with the REDIM at the lowest and highest χ, respectively 73 and 504 s^{-1}. This is reported in Fig. 5.12 by the white points, with the physical coordinates expressed in specific mole numbers to retain the original shape of the REDIM. At low temperatures the composition space is primarily accessed on the REDIM at lower χ (in yellow). Fuel-lean compositions at higher temperatures are closer to the other surface instead (in red).

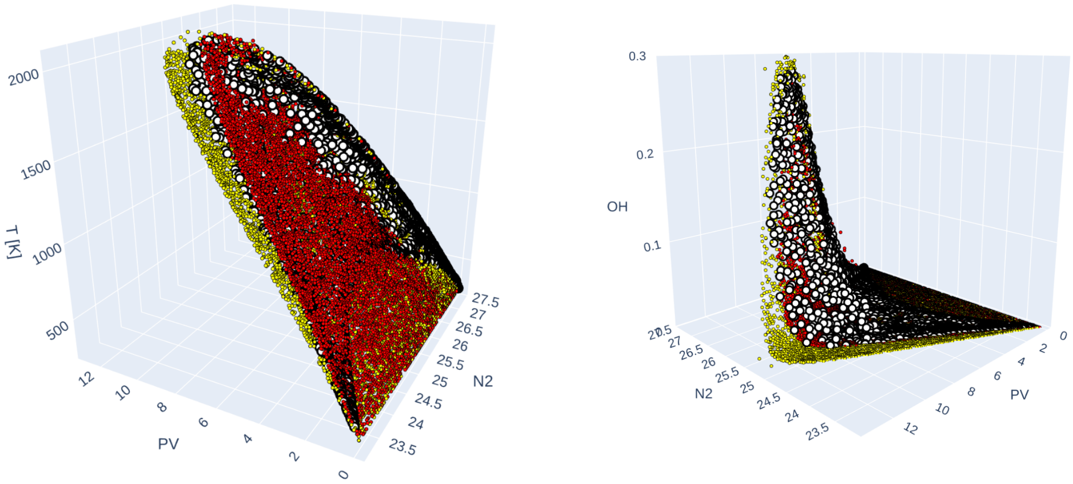

Figure 5.12.: Flame F: scatter data (white points) for $\widetilde{T}$ (left) and $\widetilde{OH}$ (right) at x/D = 15 using configuration F2-Le1. Yellow points: 2D-REDIM built for $\chi = 73\,\mathrm{s}^{-1}$. Red points: 2D-REDIM built for $\chi = 504\,\mathrm{s}^{-1}$

REDIMs with detailed transport

In this paragraph a detailed transport model to account for differential diffusion in the matrix $\boldsymbol{D}$ of Eq. (3.11) is considered. The detailed transport model used for the generation of the REDIM is based on the Hirschfelder-Curtiss approximation reported by Eq. (2.14)[122], including the Soret effect [79]. Table 5.6 summarizes the new configurations for differential diffusion (DD).

Table 5.6.: REDIM tables for flame F built for detailed transport

Case	χ	Dim	Model χ	PV
F1-DD	137	2D	-	$Y_{CO2}+Y_{H2O}+Y_{CO}+Y_{H2}$
F2-DD	370	2D	-	$Y_{CO2}+Y_{H2O}+Y_{CO}+Y_{H2}$
F3-DD	370	2D	-	$Y_{CO2}+Y_{H2O}+Y_{CO}$
F4-DD	137, 370	3D	$(D+D_{sgs})(\nabla\widetilde{f})^2$	$Y_{CO2}+Y_{H2O}+Y_{CO}$

The gradient estimate of these manifolds derives from a detailed solution of a steady counterflow flame calculated with detailed transport. A series of tests was run first with a single 2D-REDIM to investigate the effect of the progress variable and χ (simulations F1-DD, F2-DD and F3-DD). A 3D-REDIM simulation based on two χ databases is labelled as F4-DD. Note that the last one requires again a model for $\widetilde{\chi}$. The expression with the gradient assumption of $\nabla\widetilde{f}$ is chosen in this case, where $\widetilde{f}$ is calculated algebraically using the Bilger formula. The element conservation included in the Bilger formula allows to treat the mixture fraction for detailed transport, otherwise the use of a transport equation for $\widetilde{f}$ and $\widetilde{f''^2}$ would require further modelling to include differential diffusion terms.
Let us investigate the behaviour of the conditional means, shown in Fig. 5.13. Compared to the cases with unity Lewis numbers one can see a significant improvement of the H$_2$ pre-

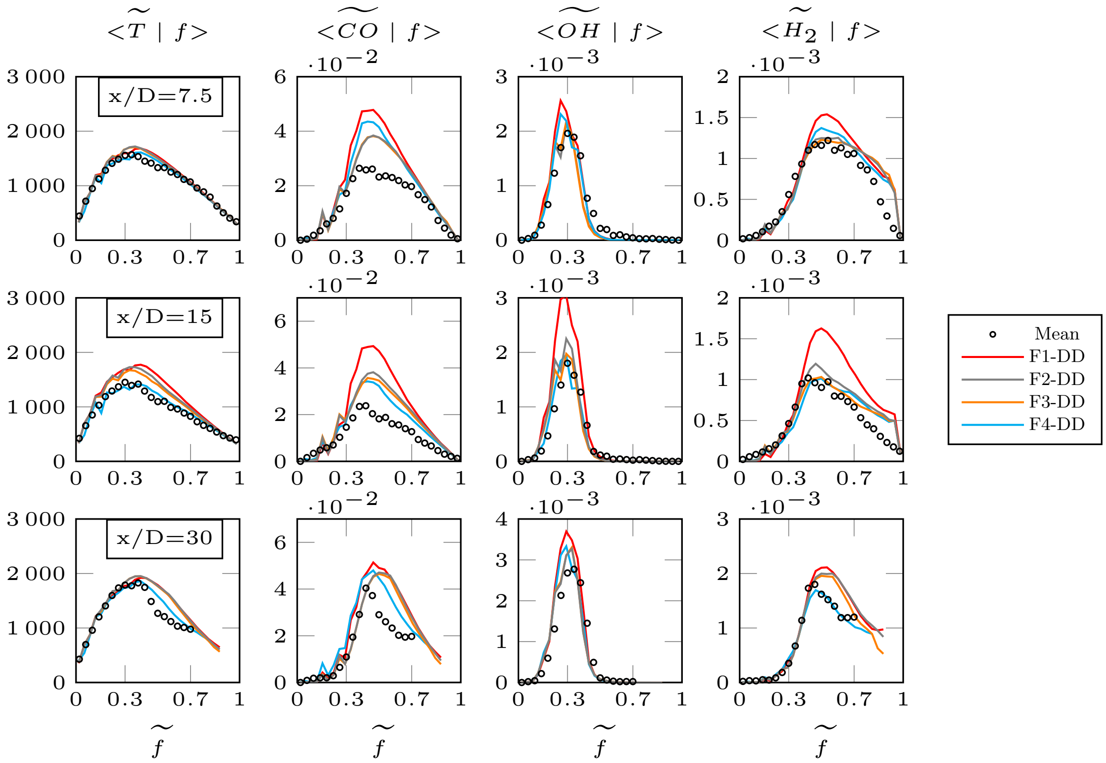

Figure 5.13.: Flame F: Conditional means of temperature and major species for the test cases of Table 5.6

dictions in all sections. The predictions are in good agreement with the experiment if the 2D-REDIM at higher χ is used in the simulation ($370\,s^{-1}$), without a strong dependence on the choice of the progress variable. The extinction events at section x/D = 15 are very well captured through all species, CO showing a certain overprediction. It is interesting to note the fact that a single REDIM table with high χ can already provide a satisfactory estimation for this flame (e.g. F2-DD or F3-DD). When looking at the conditional RMS however (Fig. 5.14), one can clearly see that a multi-χ database improves the predictions. In case F4-DD the T and CO fluctuations are slightly overpredicted compared to the experiment, meaning that a little stronger extinction occurs at sections x/D = 7.5 and 15. However, OH is very well captured by this simulation, as well as H_2. One can conclude that a 2D-REDIM with differential diffusion would be sufficient to represent the conditional means of flame F, but the extension to a 3D database would definitely improve the RMS values.

There are two important phenomena that have to be captured in this flame: the correct degree of extinction/re-ignition and the effect of differential diffusion, which plays a determinant role for H_2 in all Sandia flames (for D and E please see reference [35]). It is worth showing the scatter plots of H_2 in Fig. 5.15 for four selected simulations presented in the previous discussion. The red vertical line corresponds to the stoichiometric $f_{st} = 0.351$. At x/D = 7.5 and 15 the scatter data of F1-Le1 show a stronger clustering around $f \approx 0.4$, corresponding to a more stable solution. F2-Le1 instead contains a stronger scattering of H_2 on the fuel rich side, which better represents the extinction events. The DD simulations repro-

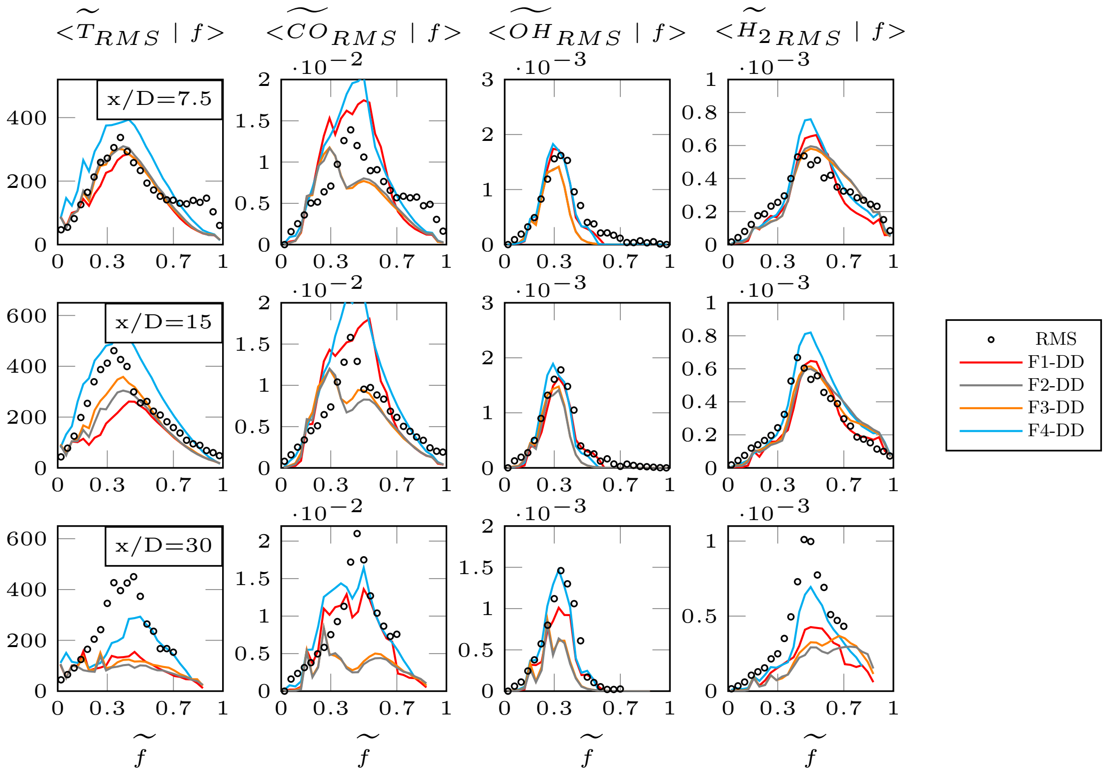

Figure 5.14.: Flame F: Conditional fluctuations of temperature and major species for the test cases of Table 5.6

duce well the scatter data distributions of the experiment in the first section. In $x/D = 15$ the extinction is a little too strong for the DD manifolds compared to the experiment, but the cloud shape is preserved. When looking at section 30 instead, one can see that the F2-Le1 simulation better represents the experiment. This brings us to the conclusion that the unity Lewis number assumption holds downstream in the flame, but differential diffusion is required upstream in order to correctly capture the H-chemistry. Extinction events are well captured by both 3D-REDIMs, with satisfactory results deriving from the simplified transport model.

A final look is given to the same four simulations for the unconditional values of $\widetilde{f}$, $\widetilde{T}$ and major species, to complete the picture. The comparison is shown in Fig. 5.16. The first thing to notice is that F4-DD shows a strongly diffusive behaviour on the fuel-lean side of the flame for all scalars, compared to the other simulations. This configuration has $Y_{CO2}+Y_{H2O}+Y_{CO}$ as progress variable, thus it does not contain Y_{H2}. F4-DD is shown here on purpose to underline the importance of species H_2 when tracking the progress of reaction on the fuel-lean side of this flame. However, the detailed transport contained in the database is responsible of shifting the peaks of the DD simulations towards the right and to increase the diffusivity of the profiles for $r/D > 2$. The REDIM modelling plays a dominant role in section $x/D = 15$, where a stronger divergence of the profiles is observed. The 3D-REDIMs capture well the degree of extinction here, although different predictions are obtained on the fuel-line side of the flame ($r/D > 2$). The CO predictions are strongly overpredicted by F2-Le1. While the introduction of differential diffusion seems to mitigate

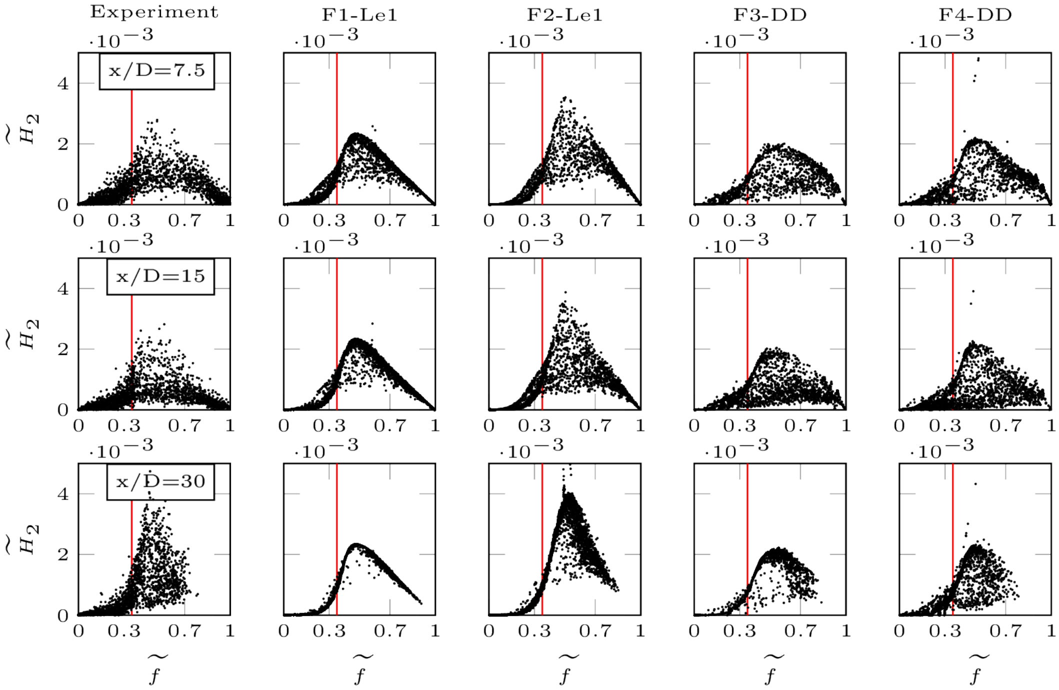

Figure 5.15.: Flame F: scatter plots of $\widetilde{H}_2$ for selected cases of Tables 5.5-5.6

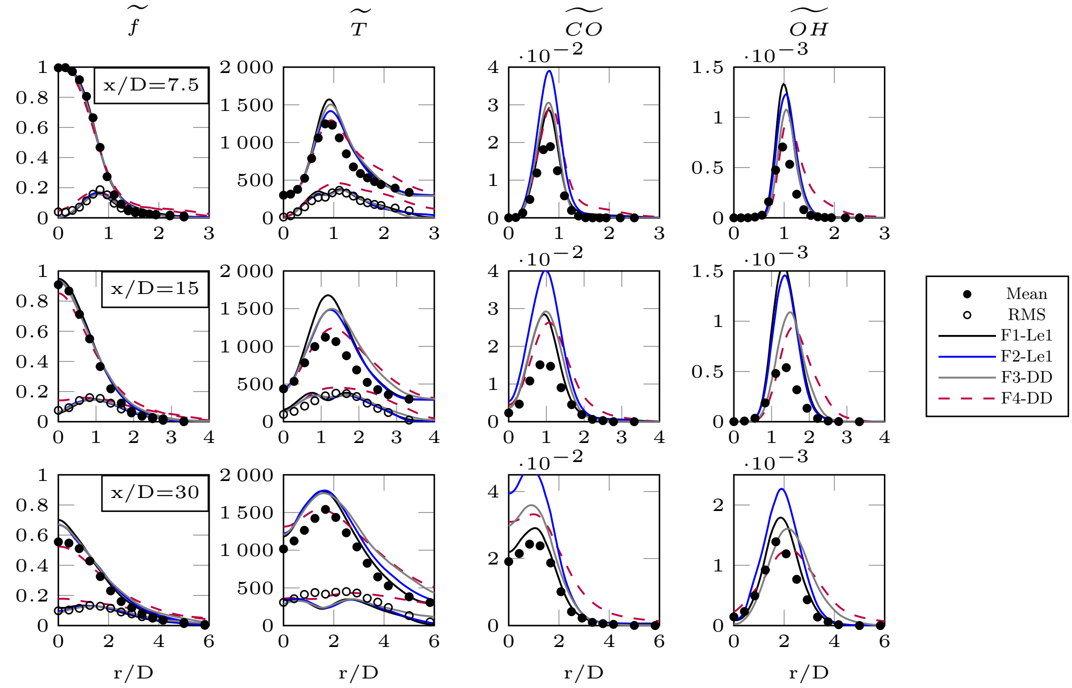

Figure 5.16.: Flame F: unconditional mixture fraction, temperature and major species for selected cases of Tables 5.5-5.6

the effect on CO, an additional table parameter would be beneficial for F2-Le1, in order to correctly capture the slow carbon chemistry (see e.g. [323]).

Computational time

In the previous paragraph it was shown that the ESF predictions for flame F were significantly improved by substituting the finite chemistry integration with a tabulated chemistry, the REDIM. It is now time to show what is the computational speed-up achieved by the ESF-REDIM solver. All setups are run for 500 time steps with fixed $\Delta t = 2{\cdot}10^{-7}$ s. The numerical schemes and solver settings are identical for all cases. The chemical mechanism for finite rate chemistry and table interpolation is the skeletal Lu30. Each simulation is run on 120 cores of type Intel-Xeon E5-2670 for a total of three times, to leverage the network performances. The ESF setup is run for 2, 4 and 8 fields, for both finite rate and tabulated chemistry. The ESF-REDIM solver uses a 3D-REDIM with 6 values of χ. Fig. 5.17 reports the results of this investigation.

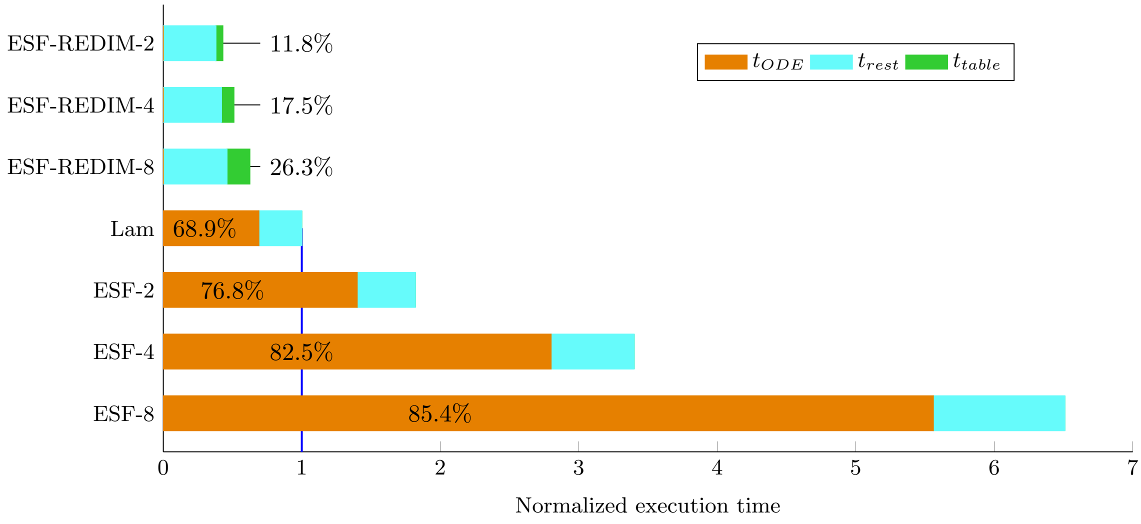

Figure 5.17.: Computational times over 500 time steps of $\Delta t = 2{\cdot}10^{-7}$ s, normalized on the laminar chemistry computation. Orange: ODE integration share. Green: table interpolation share. Cyan: remaining transport equations

The execution time (or wall clock-time) was normalized on the laminar chemistry computation (*Lam* in the figure). The orange stacked bars report the share time required to integrate the chemistry ODE, while the cyan bars represent the time share required to solve the remaining equations. It can be seen that t_{ODE} increases by increasing the number of stochastic fields. The ODE integration requires from 70 to 85 % of the total execution time. The standard ESF solver with 8 transported fields is about 6.5 times slower than the laminar chemistry computation. The ESF-REDIM computations are quicker than the laminar computation, as expected. By increasing the number of stochastic fields, the interpolation time t_{table} increases consequently, as shown by the green stacked bars. However, the interpolation time is still about 26 % of the total execution time in the case of 8 fields, meaning that the solution of the remaining transport equations requires the major share.
It is interesting to compare the influence of the REDIM dimensionality on the computational time. For this purpose the ESF-REDIM simulations are also run using a single χ

table (labelled χ_1) and compared to the previous runs with 6 χ tables (namely χ_6). This comparison is shown in Fig. 5.18.

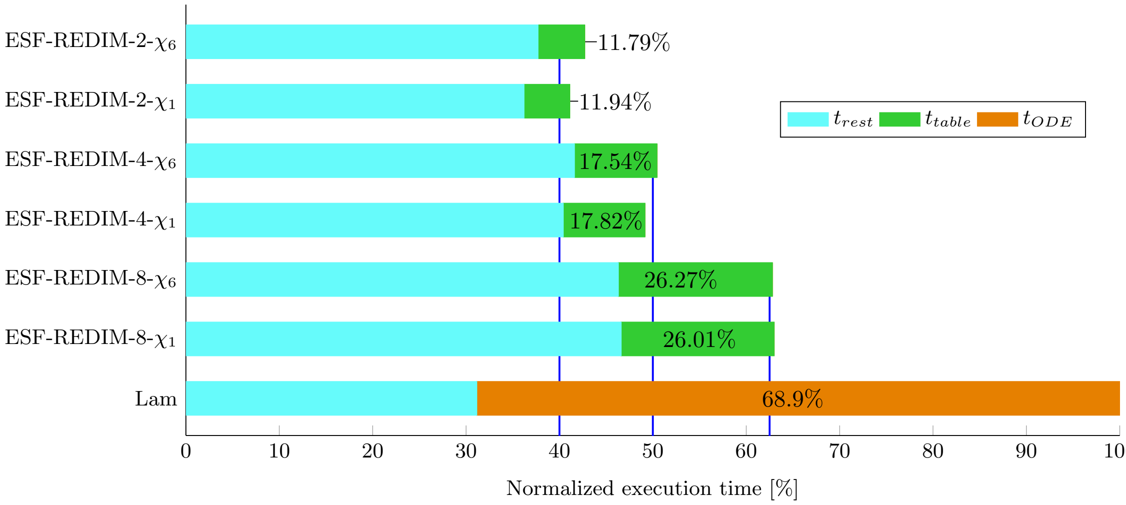

Figure 5.18.: Computational times of ESF-REDIM normalized on the laminar chemistry computation. Orange: ODE integration share. Green: table interpolation share. Cyan: solution of the remaining transport equations

The reference case is again the laminar computation. A minimal improvement of less than 1 % is observed for t_{table}, if a 2D-REDIM database is used. The interpolation routine can manage well the third dimensionality of the database, adding only a minimal cost. Usually 5 to 10 values of χ are sufficient to describe the burning regime of the investigated flames, so that χ_6 can be taken as a good reference setup in this work. The vertical blue lines mark the computational time using 8 fields (62 % of *Lam*), 4 fields (50 % of *Lam*) and 2 fields (40 % of *Lam*). The trend shown by t_{table} suggests that a computation with 64 fields and tabulated chemistry would require approximately the same resources of the reference case, losing the advantage of this solver. One could certainly improve the interpolation routine, but it should be remarked that the use of more that 8 stochastic fields in LES is very rare in the literature, so that this advantage is preserved for the common user case.

5.1.5. Influence of the sgs-TCI model

The previous section showed that the novel ESF solver based on the REDIM chemistry can represent well the extinction events of flame F, at a reduced computational cost. However, the ESF method does not work extremely well upstream, where stronger mixing is present. This can be a limitation of the ESF, since the only implemented model for micro mixing is the IEM, one of the simplest mixing models. Additionally, it was shown in paragraph 5.1.2 that the mixing term in the SPDE provides only a minor contribution compared to the stochastic term. In this paragraph, the ESF method is compared to another Monte Carlo approach, the MMC sparse Lagrangian particle method.
Before doing so, the current ESF-REDIM solver is compared with previous computations available in the literature and based on the particle method, as shown in Table 5.7. The reader should note that the selected cases for comparison are RANS-based, where the influence of the micro mixing model is stronger. The reference case is *PR-ISAT* (Particle-RANS

using ISAT chemistry) from Cao and Pope [48], where the Euclidean Minimum Spanning Tree (EMST) was chosen as mixing model. The latter was shown to deliver better results when applied to RANS [198]. The second simulation selected for comparison is a RANS solver coupled with REDIM reduced chemistry [321]. Similarly to *PR-ISAT*, the constant C_ϕ was set to 1.5 for the EMST model. This case is labelled as *PR-EMST*. Finally, the same simulation was run using the IEM model with $C_\phi = 2$ (*PR-IEM*), allowing a direct comparison with the ESF-REDIM.

Table 5.7.: LES-ESF vs RANS-TPDF

Name	Solver	Mixing model	C_ϕ	Chemistry
PR-ISAT [48]	RANS-Lagrangian	EMST	1.5	ISAT
PR-EMST [321]	RANS-Lagrangian	EMST	1.5	REDIM
PR-IEM	RANS-Lagrangian	IEM	2	REDIM
ESF-REDIM	ESF	IEM	2	REDIM

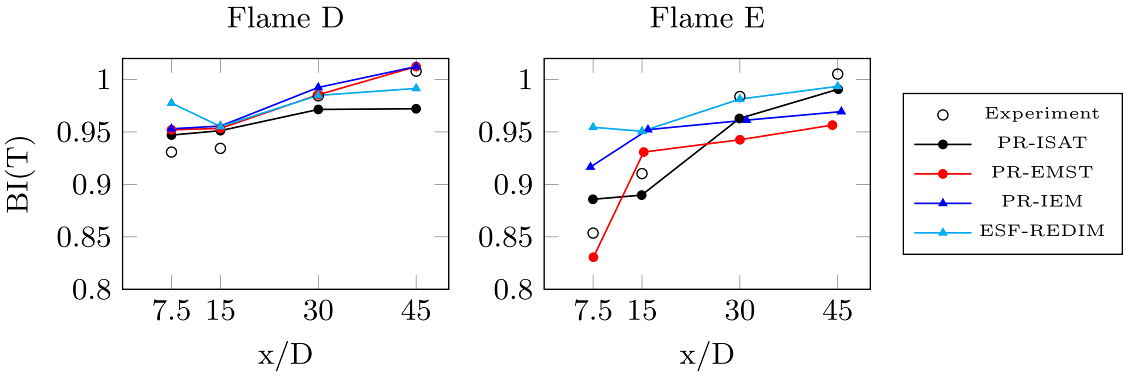

Figure 5.19.: Flames D and E: Burning Index (BI) calculated from temperatures for the setups of Table 5.7

It is sufficient to perform a quantitative comparison for flames D and E, in order to understand the importance of the mixing model. For this purpose, the flame Burning Index (BI) based on temperature is evaluated for each flame according to [48, 318]. The BI is defined as the ratio between the conditional mean temperature (conditioned on $0.3 < f < 0.4$) and a reference value of $T = 2023\,K$, obtained from a laminar flame calculation with strain $a = 100\,s^{-1}$:

$$BI = \frac{1}{N} \sum_{i=1}^{N} \frac{T_i - 291}{2023 - 291} . \tag{5.1}$$

A burning flame is represented by BI = 1, while BI = 0 corresponds to a complete flame extinction. This index is shown for both flames in Fig. 5.19. A first observation is that the simulation results show stronger deviations for flame E, featuring a moderate degree of extinction. In fact, the mixing model is there essential to describe the unstable events correctly. For both flames D and E, the ESF simulation provides a too stable flame at x/D = 7.5, as previously observed. *PR-ISAT* and *PR-EMST* provide the most accurate predictions for flame E because exploiting a more accurate mixing model (EMST). A comparison of ESF-REDIM with *PR-IEM* confirms the tendency of IEM to predict less extinction states across all sections.

Based on these observations, it is definitely worth to compare a particle-based solver with the ESF-REDIM in the LES framework. Because Lagrangian particle solvers for LES are computationally expensive, the MMC model was chosen as best candidate in this context. In fact, for how it is conceived, MMC allows the use of a significantly reduced amount of particles to describe the PDF statistics.

MMC-REDIM

Table 5.8 reports the numerical investigations conducted on mesh BM. The MMC simulations also require the use of the coarser mesh SM for the Lagrangian/Eulerian density coupling. The effect of the choice of the inlet boundary conditions on the axial development of the fluid speed and scalars is also investigated in this configuration. In one case, a precursor pipe LES is applied as in the previous paragraphs. In the second case, artificial boundary conditions based on the experimental velocity profiles at the inlets are applied using the OpenFOAM library of Kroger and Kornev [159]. The finite rate calculation MMC-FR and the 2D-REDIM used in cases ER and MR are based on the Lu30 chemistry, with unity Lewis numbers. For the sake of simplicity, the REDIM progress variables are set to (Y_{N2}, Y_{CO2}). The reader is reminded that all numerical settings of the MMC configurations are taken from the test case of the IIT Kanpur and a parameter study for MMC is not the object of this work. Due to the different treatment of the MMC and ESF solvers, the numerical schemes are not exactly the same (cf. Appendix C.2).

Table 5.8.: MMC and ESF configurations

Case	sgs-TCI	Chemistry	Turbulent Inlet
MMC-FR	MMC	Finite rate	LES Precursor
MR	MMC	REDIM	LES Precursor
ER	ESF	REDIM	LES Precursor
MR-S	MMC	REDIM	Artificial turbulence
ER-S	ESF	REDIM	Artificial turbulence

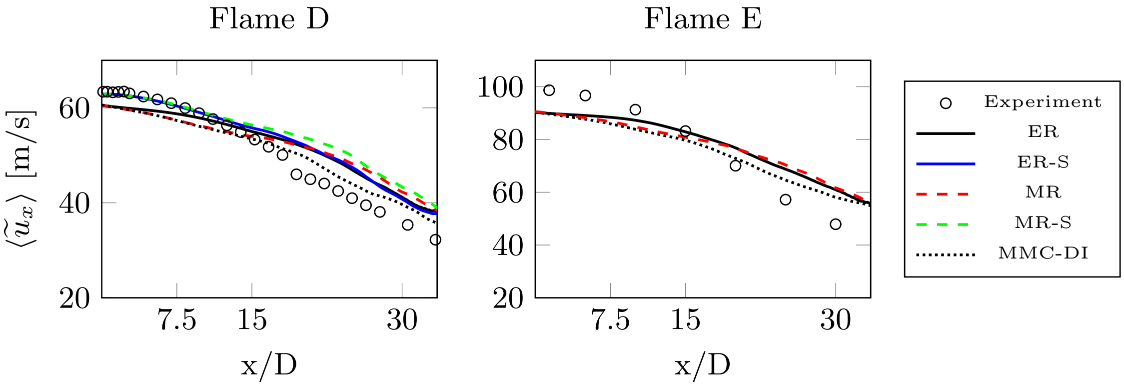

Figure 5.20.: Axial profiles of the mean centreline streamwise velocity for flames D and E, for the simulations of Table 5.8 [33]

A first analysis of the axial development of scalars and velocity is conducted for Flame D using the two different jet boundary conditions. The left side of Fig. 5.20 reports the investigation. One can see that the artificial inlet based on the experimental velocity profiles allows both MMC and ESF solvers to catch the velocity decay for x/D < 15 (MR-S and ER-S). Using a precursor LES data instead leads to an underprediction of the velocity in the same region. In any case, all computations predict a lower jet decay in the second half of the domain, with the MMC-FR computation better approaching the experimental distribution. One can see for flame E (right) that the difference between the inlet Boundary Conditions (BC) and the experimental data becomes stronger, but both solvers are affected similarly as in flame D. The reader should note that the overprediction of the mean velocity for x/D > 20 was already observed in numerous studies for flame D (e.g. Kemenov et al [148]) employing different methods to define the inflow conditions. Because the experimental data could also include unverified uncertainties, we refrain from achieving a perfect match here. The precursor LES remains the preferred turbulent inlet BC, to be consistent with the results obtained in the previous paragraphs.

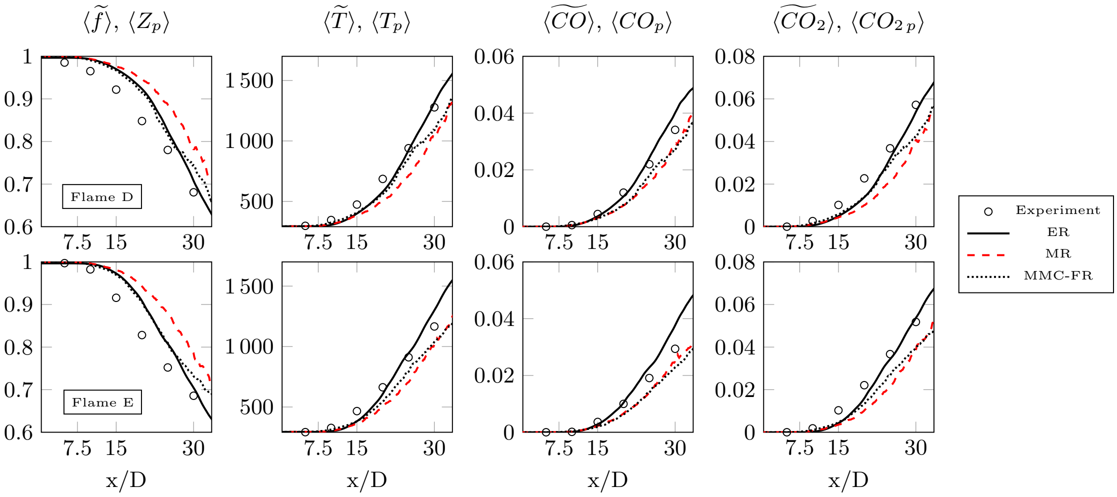

Figure 5.21.: Development of axial scalar quantities for flames D and E [33]

On the other hand, what appears to be better predicted at x/D > 20 is the behaviour of the scalars, shown in Fig. 5.21 for both flames. It can be also seen that the ER computations better match the experimental results, with MMC showing a too low mixture fraction decay (thus lower temperatures and reaction products in the jet core). To understand the reason of this underprediction, it should be reminded that the averaged scalars shown in Fig. 5.21 for MMC derive from the particle statistics denoted as $field_p$, thus $\langle\widetilde{T}\rangle$ should be close but not exactly equal to $\langle T_p\rangle$. The former is an equivalent field transported on the Eulerian mesh and required for the density feedback, in order to provide mass consistency between the particles and the Eulerian cell volumes. More details on the MMC solver are provided in App. C.4, as well as the equivalent fields chosen for this configuration. More interesting is the comparison of mixture fraction and temperature for MMC-FR and MR, as shown in Fig. 5.22. While $\widetilde{T}$ is an equivalent field for the density coupling, $\widetilde{f}$ represents the reference space where particles are mixed. The particle statistics instead is given by Z_p and T_p. One can see that at sections 15 and 30 there is a stronger mismatch of such quantities, being the values of (Z_p, T_p) underpredicted compared to ($\widetilde{f}$, $\widetilde{T}$). The mean mass inconsistency is about 1.14 % for MMC-FR and 0.25 % for MR. A lower peak of temperature is observed for MMC-FR at x/D = 15 compared to the experiment (i.e. stronger extinction), with both MMC-FR and MR predicting a longer fuel core in x/D = 30. Interestingly, the tabulated chemistry MMC (case MR) provides good results for section 15 compared to MMC-FR.

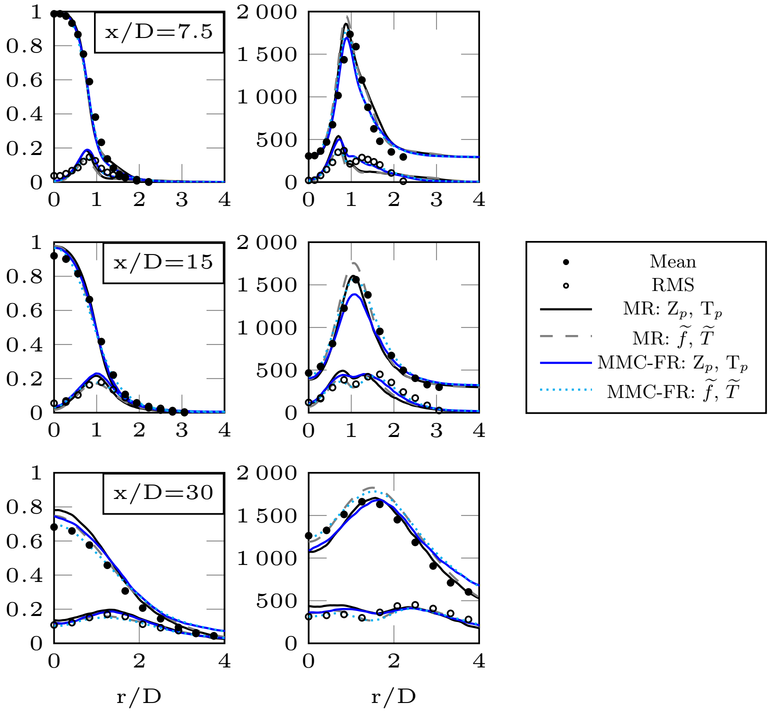

Figure 5.22.: Flame D: Particle statistics (Z_p, T_p), equivalent field $\widetilde{T}$ and reference variable $\widetilde{f}$ for MMC-FR and MR (cf. Table 5.8)

Because this inconsistency is seen in the finite rate MMC computation as well, it cannot be entirely attributed to the switch to tabulated chemistry. Numerical diffusion and the density feedback based on the kernel estimation could be responsible for this mismatch. However, the fact that MR provides a more stable solution at x/D = 15 compared to MMC-FR is due to the accessed composition space, i.e. the REDIM surface where the mixed states are projected.

Having a look at the conditional means and fluctuations of Flame D in Fig. 5.23-5.24, it is evident that the finite rate MMC simulation (MMC-FR) is in excellent agreement with the experimental data. This is due to the mixing model, which considers the proximity of the particles in the physical space and in the reference space. The fact that the tabulated chemistry MR is not as good as MMC-FR is due to the accessed composition space, which is in this case the 2D-REDIM. It is definitely expected that ER and MR provide the same distribution, because the thermo-chemical states off manifold are projected back to the same REDIM. As seen in the previous paragraph, a more accurate choice of PV or the inclusion of differential diffusion into the table would improve the conditional means. For what concerns the conditional RMS instead, it was seen before that the tabulated chemistry provides

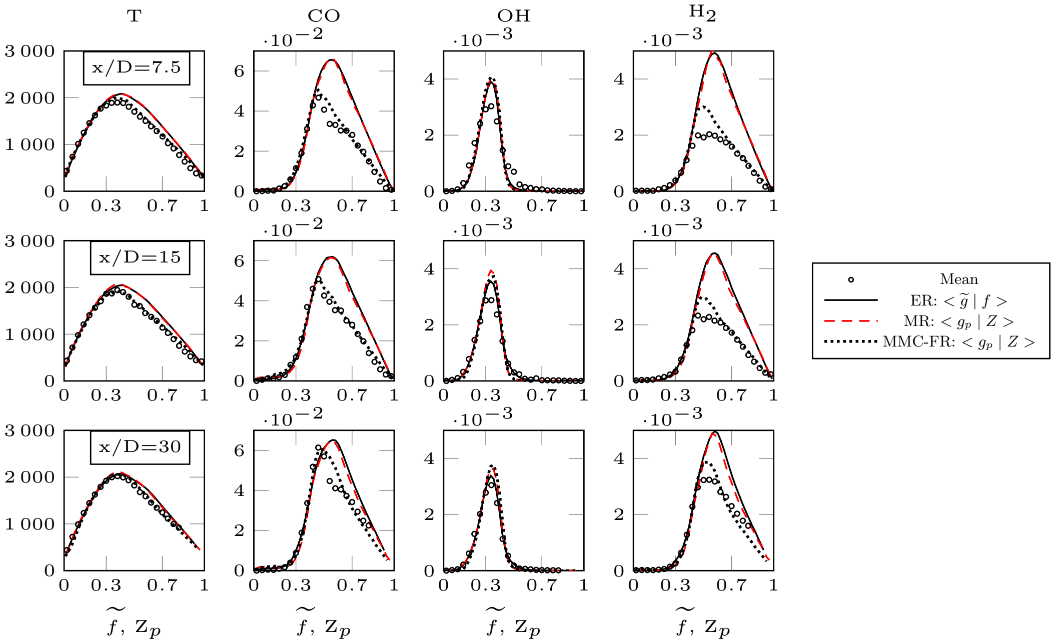

Figure 5.23.: Flame D: conditional means of temperature and major species [33]

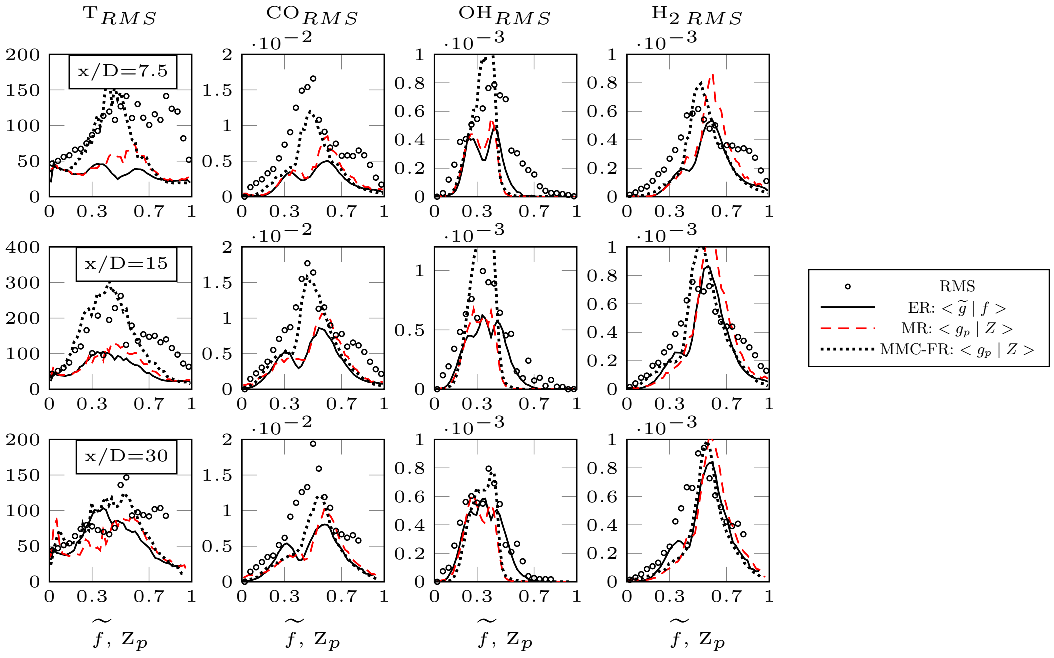

Figure 5.24.: Flame D: conditional RMS of temperature and major species [33]

less fluctuations that a finite rate ESF simulation. The excellent agreement of the MMC fluctuations at sections x/D = 7.5 and 15 confirms the superiority of MMC in predicting extinction/re-ignition events compared to the ESF solver.

A complementary check is done for the scatter data of temperature and CO, provided in

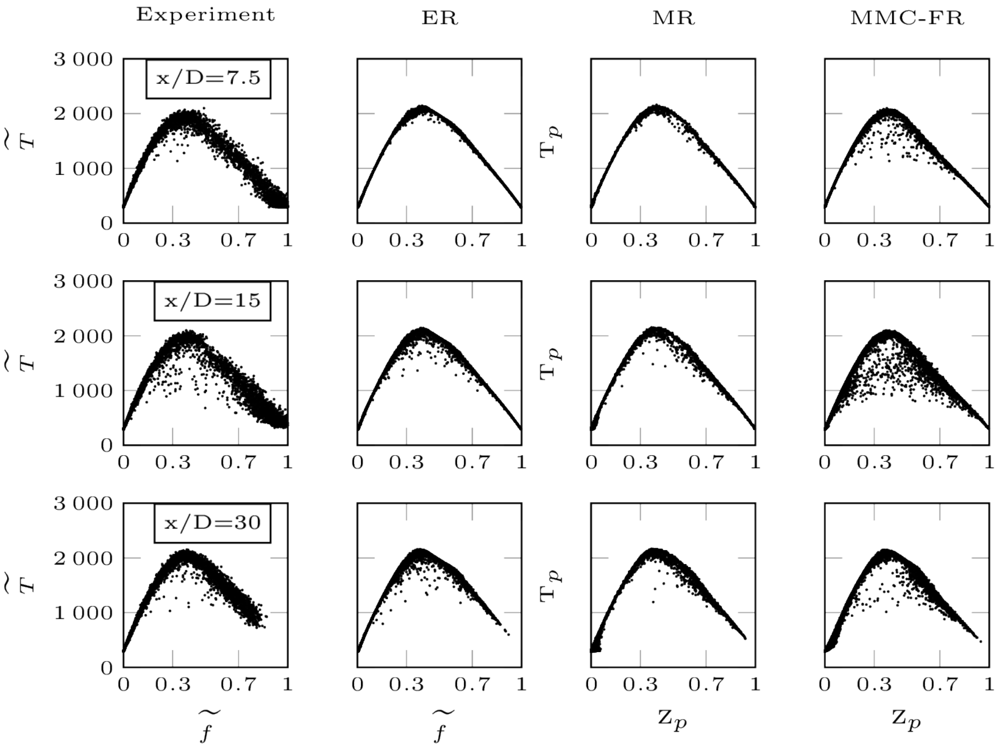

Figure 5.25.: Flame D: scatter data of $\widetilde{T}$ for ESF solver and T_p for MMC solvers [33]

Fig. 5.25-5.26. Flame D is overall a very stable flame, but the MMC-FR simulation shows more extinction events in section 15. ER and MR instead show a similar scatter, confirming the correct coupling of the MMC solver with REDIM. It is interesting to notice a cluster of data at $Z_p \approx 0$ for MMC-FR at section 30, which is absent in the experiment and ER. This local cloud justifies the importance of a correct projection strategy. This is better explained in the 3D representation of Fig. 5.27, with the REDIM surface coloured by the temperature field. The zoomed region on the right side shows thermo-chemical states off manifold retrieved from the MMC-FR computation (white points). In that region turbulent mixing is the principal agent acting on the particle. If a burning solution of MMC-FR is used to initialize the MR computation, these states off-manifold are immediately projected back to the REDIM surface (red points). However, they are projected back into a region away from the oxidizer boundary and towards the reaction zone, explaining the local consumption of CO_2 towards CO at $Z_p \approx 0$. If the simulation is restarted from time zero, those thermo-chemical states will be accessed in the same way due to the micro-mixing model. A possible solution to overcome this issue in MR would be to apply a more accurate projection method for REDIM [323], which however would require a significant interpolation time for LES (the investigation of [323] was based on 2D-RANS).

The conditional means and RMS for flame E are shown in Fig. 5.28-5.29. A similar behaviour to flame D is observed: the MMC-FR simulation better captures the composition distribution, although it shows stronger extinction than the experiment at section x/D = 15. Both REDIM-based simulations instead show an excess of CO and H_2 across the domain.

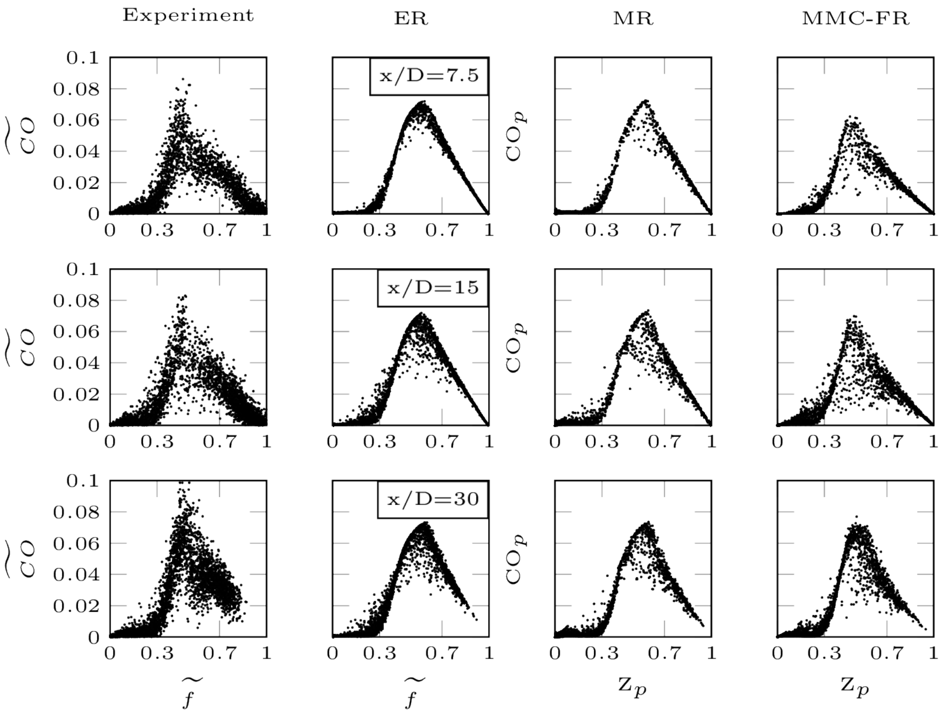

Figure 5.26.: Flame D: scatter data of $\widetilde{CO}$ for ESF solver and CO_p for MMC solvers [33]

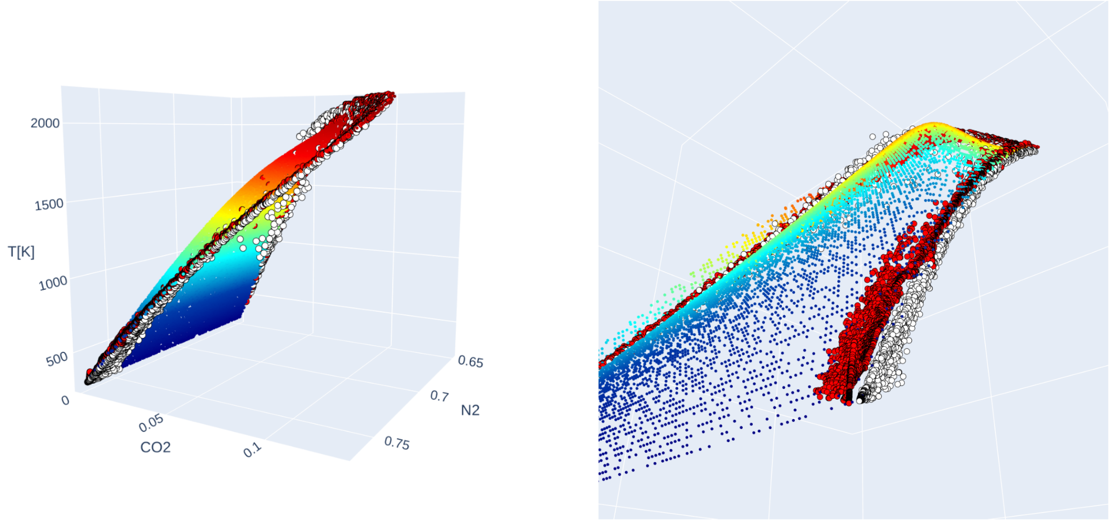

Figure 5.27.: 2D-REDIM surface coloured by T. Scatter data sampled at x/D = 30 from MMC-FR (white dots) and MR (red dots)

However, this can be corrected respectively by using a different PV and by introducing detailed transport in the REDIM table. MR shows again similar results to ER, validating the MMC-REDIM implementation. The RMS of H$_2$ are well represented by all simulations and overall the MMC-FR is in excellent agreement with the experimental data. The tabulated

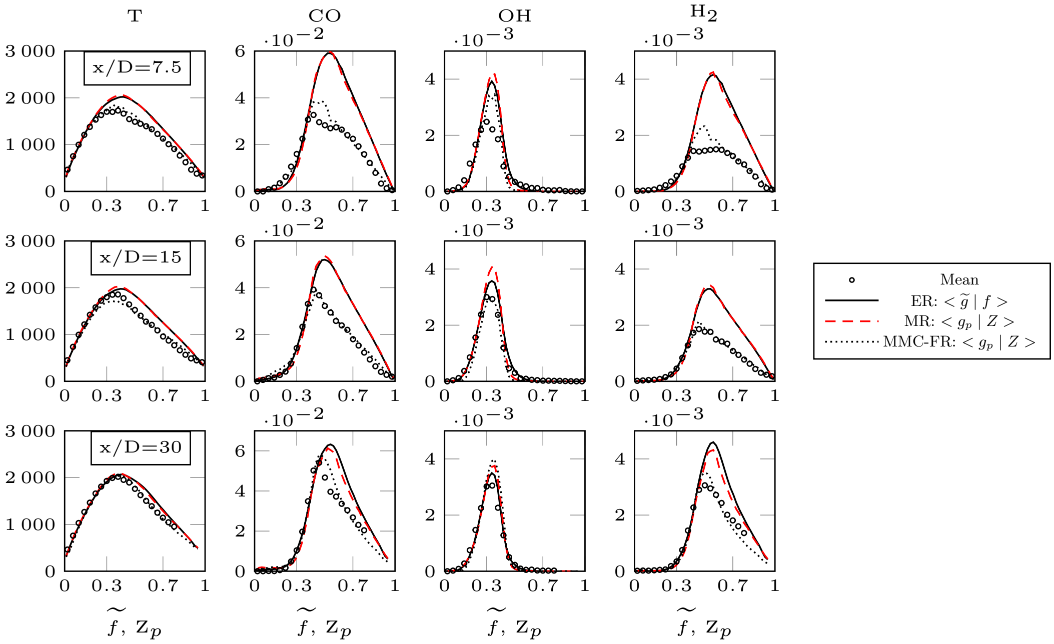

Figure 5.28.: Flame E: conditional means of temperature and major species [33]

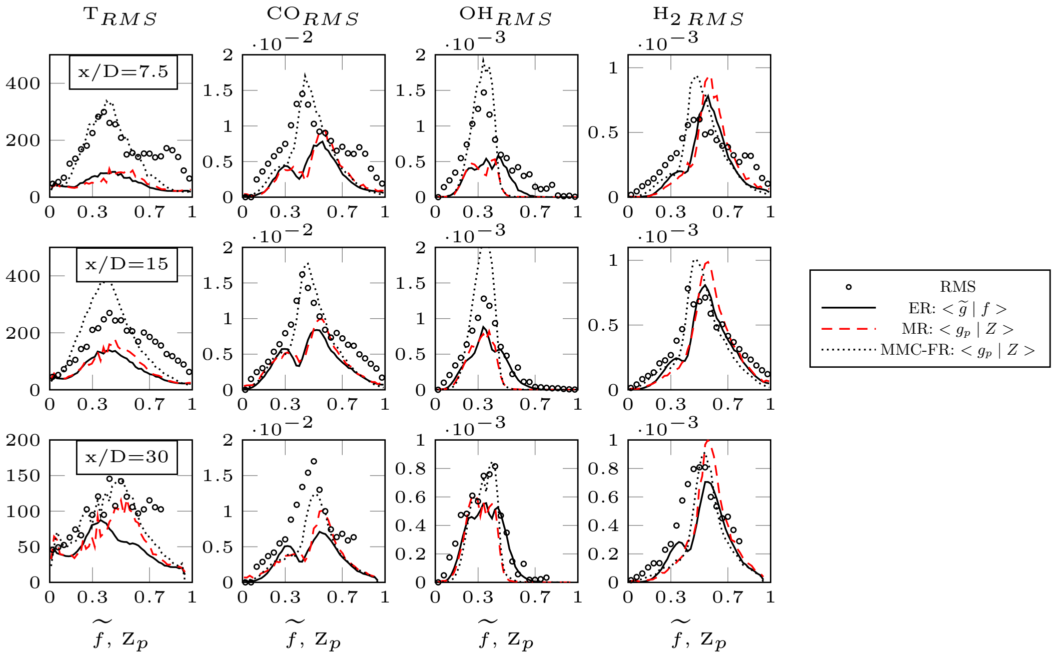

Figure 5.29.: Flame E: conditional RMS of temperature and major species [33]

chemistry overpredicts the temperature and main species composition in sections 7.5 and 15. The scatter plots for T and CO in Fig. 5.30-5.31 confirm the observations derived from the conditional quantities.

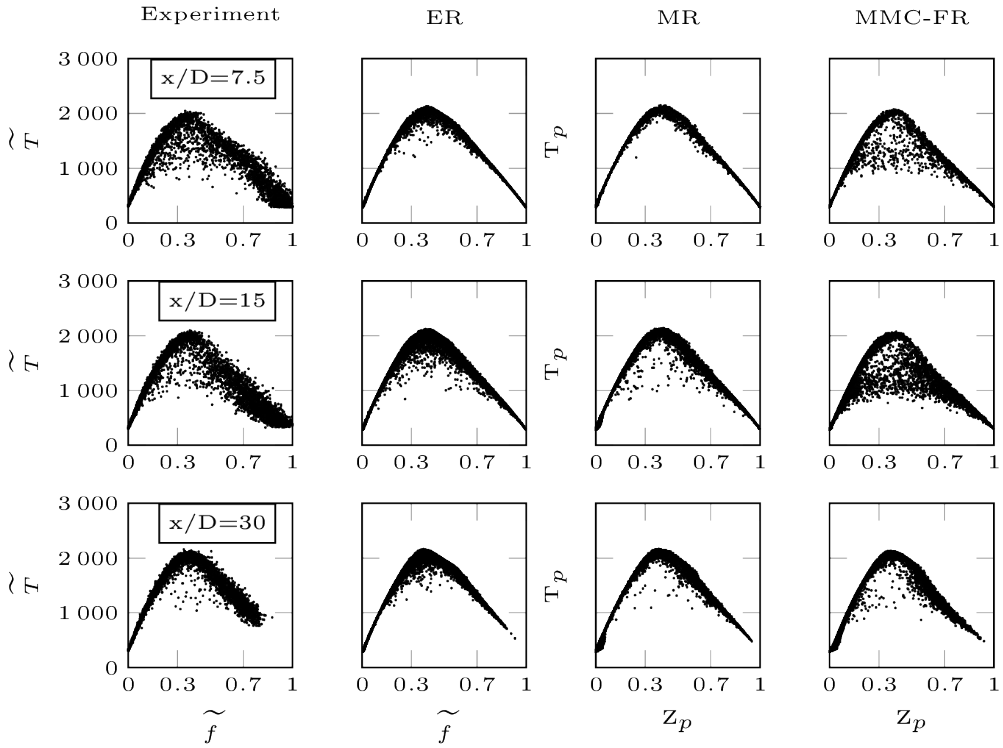

Figure 5.30.: Flame E: scatter data of $\widetilde{T}$ for ESF solver and T_p for MMC solvers [33]

It is now clear that the composition space and the extinction events at the upstream sections can be better represented by the MMC model. Note that the extension of the calculation to flame F would require a reactive progress variable defined as linear composition of the major products. Further modelling is needed in the MMC solver to deal with the mixing of the composed progress variable. A final trade-off between MMC and ESF is presented in the next paragraph, based on the computational time.

Computational time

The ESF and MMC are first compared for a finite rate chemistry computation using the Lu30 reaction mechanism on Flame D. The reader might recall that the finite rate simulations of ESF exploit the accelerated chemistry solver for Lu30. According to Fig. 3.1 (on the right), the Lu30 accelerated chemistry (in red) is at least two times faster the original OpenFOAM chemistry solver (in gray). Because the MMC libraries do not exploit this accelerated chemistry, it is fair to compare both solvers using a default OpenFOAM chemistry integrator, i.e. the `seulex`. The base setup is run for 500 time steps with fixed $\Delta t = 2{\cdot}10^{-7}$ s, on 120 cores of type Intel-Xeon E5-2670 for a total of three times, to leverage the network performances. Fig. 5.32 summarizes the results.

The total execution times were normalized on the laminar chemistry computation (Lam). An ESF simulation with four stochastic fields (ESF-4) is sufficient to show the gap with the MMC solver, the latter being faster than the laminar computation itself. The first thing to notice is that the chemistry share (in orange) is higher than the values previously observed in Fig. 5.17. This is because the computation was run with a non-accelerated chemistry solver.

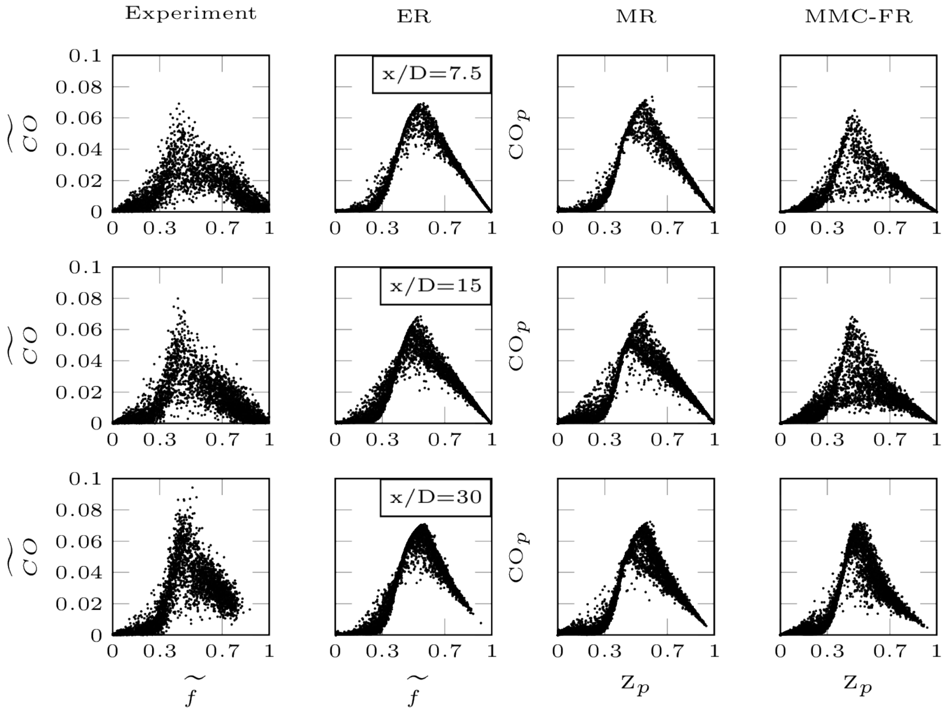

Figure 5.31.: Flame E: scatter data of $\widetilde{CO}$ for ESF solver and CO_p for MMC solvers [33]

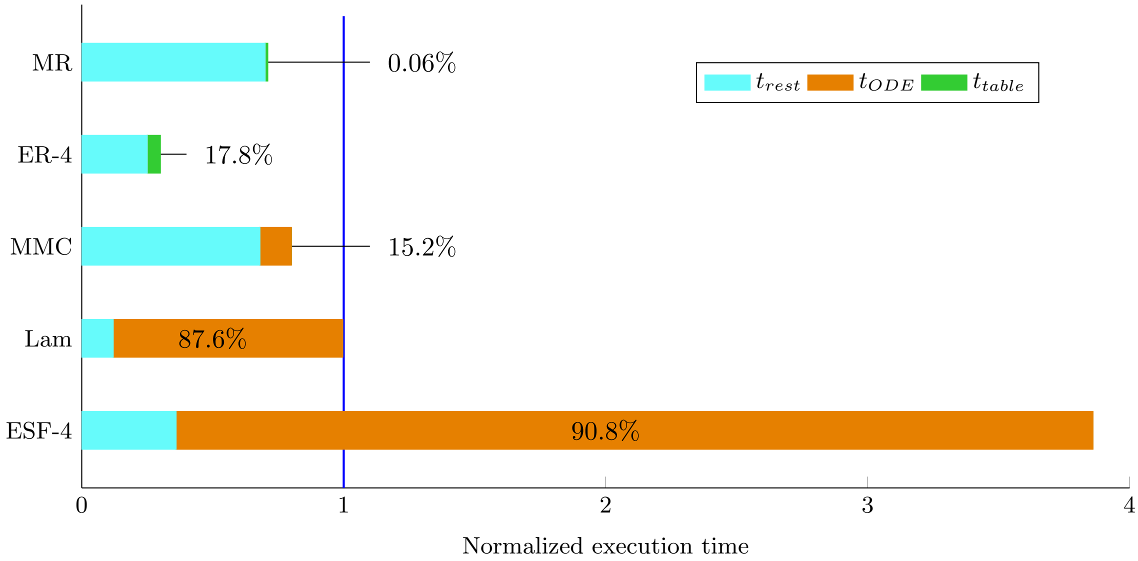

Figure 5.32.: Computational times of ESF-based and MMC-based solvers, normalized on the laminar chemistry computation. Orange: ODE integration share. Green: table interpolation share. Cyan: solution of the remaining transport equations [33]

Secondly, the chemistry share of MMC takes only about 15 % of the total time. Although the computational time of MMC for Flame E increased of 1.2 %, a similar chemistry share was observed (not shown). The bottleneck of the MMC computation seems to be given by the particle module (move particles, search particle pairs to mix, particle control) and the density feedback (consistence between particles and Eulerian mesh).

Let us now discuss what happens when both solvers are coupled with the REDIM chemistry. It was seen before that the ER-4 shows a significant speed-up compared to Lam, with about 18 % share required for table interpolation. This advantage is somehow lost in MR, although still faster than MMC. To draw a conclusion, the MMC definitely outperforms the ESF for both accuracy (see previous paragraphs) and computational efficiency, when using finite rate chemistry and for small scale computations. The use of tabulated chemistry for MMC does not seem as advantageous as for ESF at least in the investigated configurations, because the bottleneck is not given by the chemistry share. This investigation shall be extended to more challenging flame configurations and more complex chemical mechanisms, where the advantage of tabulated chemistry against ODE integration would be more evident.

5.2. CH_4/air partially premixed flames with inhomogeneous inlet

In this paragraph the validity of the ESF-REDIM solver on a flame configuration featuring inhomogeneous inlets is briefly investigated. The test cases provided by Barlow [11] and Meares [196] are more challenging because a premixed flame mode is observed close to the inlet, while a diffusion flame regime is observed further downstream. The setup FJ200-5GP-Lr75-57 was selected here in order to compare the results with the finite rate ESF simulations of Hansinger et al [118].

5.2.1. Numerical setup

The burner configuration is similar to the Sandia flames, but it consists of two concentric tubes surrounded by a pilot. The inner tube is retractable with a diameter of 4 mm, while the outer tube provides the reference diameter for this flame (D = 7.5 mm). This configuration allows to define the degree of homogeneity between the fuel and the oxidizer in the main pipe. Thus, a full pipe recession ($L_r = 300$ mm) corresponds to a fully premixed mixture, absence of recession ($L_r = 0$) corresponds to a non-premixed configuration. In configuration FJ200-5GP-Lr75-57 there is a recess of 75 mm, generating a partially premixed mixture composition within the flammability limits. The value 57 indicates the jet bulk velocity of the methane/air mixture, in m/s. The 5-gas pilot (5GP) of this configuration contains C_2H_2, H_2, CO_2 and air, in quantities which match the stoichiometric condition of a CH_4/air burned mixture. The pilot inflow enters the domain with a bulk velocity of 26.6 m/s and it is surrounded by a cold co-flow flowing at 15 m/s.
The numerical setup and mesh convergence study were presented in the work of Hansinger et al [118] and the precursor LES/DNS data for the turbulent inlet were provided by Zirwes et al [335]. The reader is referred to both papers for further details. Here the fine mesh with 4.6 million cells is used for the investigations reported in Table 5.9. The fuel and oxidizer inlet boundary conditions are reported in Appendix B. The reference case is the ESF simulation of Hansinger et al [118] with 8 stochastic fields and the Lu19 chemistry.

Table 5.9.: ESF configurations tested for FJ200-5GP-Lr75-57

Case	Chemistry	PV	# ESF
ESF8	Lu19	-	8
ER4-PV1	2D-REDIM	Y_{CO2}	4
ER8-PV1	2D-REDIM	Y_{CO2}	8
ER8-PV2	2D-REDIM	$Y_{CO2}+Y_{CO}+Y_{H2O}+Y_{H2}$	8

The validity of this REDIM was previously assessed by Shrotriya et al [263, 262] on the same flame configuration where it was coupled with a presumed PDF model. The upper boundary of the investigated 2D-REDIM table was generated from a detailed chemistry computation of a counterflow diffusion flame with low strain rate, featuring pure CH_4 on one side and 79/21 of mol% for air on the oxidizer side. As lower table boundary a pure mixing line between fuel and oxidizer at 300 K was chosen. An additional flame solution with intermediate strain was provided as gradient estimate to initialize the REDIM calculation. ER4-PV1 and ER8-PV1 aim to show the dependency on the number of stochastic fields using the progress variable Y_{CO2}, which is the same variable used in [263, 262]. ER8-PV2 compares a second progress variable, namely $Y_{CO2}+Y_{CO}+Y_{H2O}+Y_{H2}$, previously used for Sandia Flame F.

5.2.2. REDIM-based ESF

Fig. 5.33 represents the instantaneous temperature and mixture fraction fields obtained for configuration ER8-PV1 of Table 5.9. The cold jet with inhomogeneous methane/air enters the domain at the centreline and it is surrounded by the hot pilot. The white dashed lines represent the sections investigated in this paragraph.

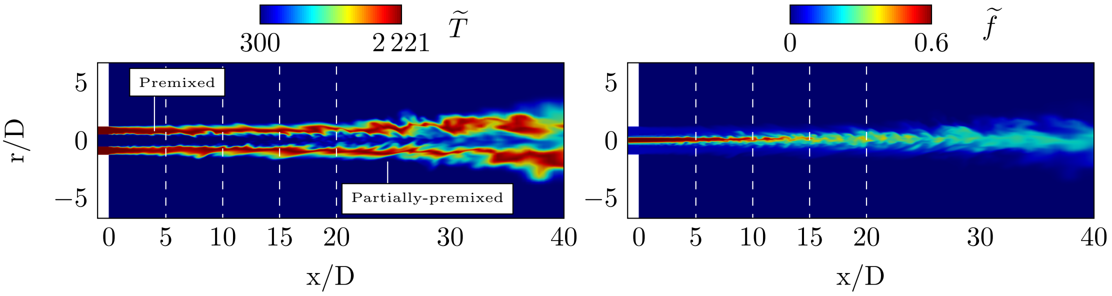

Figure 5.33.: Flame Lr75-57: instantaneous values of $\widetilde{T}$ and $\widetilde{f}$ for configuration ER8-PV1 of Table 5.9

In partially premixed regimes with inhomogeneous fuel distribution it is not a trivial task to identify the premixed-dominated zone from the non-premixed zone. Zirwes et al [336] performed a post-processing analysis on flame Lr75-57, starting from a quasi-DNS computation. It was shown that, for $x/D < 10$, about 90 % of the flame heat release is originated by the premixed regions. Further downstream, the contribution from the non-premixed regions assumes equivalent importance instead. In the same work, it was concluded that regime markers based on the alignment of the gradients ∇Y_{O_2} and ∇Y_{CH_4} (e.g. the flame index from Yamashita et al [319] or Fiorina et al [89]) may lead to wrong results in the reaction zone where CH_4 is completely consumed.
The identification of a multiple flame regime is shown here by means of the scatter plots for temperature in Fig. 5.34. The red line corresponds to the stoichiometric $f_{st} = 0.055$. The experimental data in section $x/D = 5$ indicate the presence of stratified combustion, where the thermo-chemical states evolve rapidly from the unburned to the burned state, in proximity of f_{st}. This behaviour is enhanced in ER8-PV1, where the transition path line follows the vertical line of f_{st}. However, ER8-PV1 also reports the presence of high temperature samples in the fuel rich region, which are absent in the experiment and ESF8. Moving downstream to $x/D > 5$ also the experiment shows hotter fuel-rich samples, indicating the presence of the non-premixed regime. The diffusion of ER8-PV1 on the fuel-rich side remains strong, although this simulation can predict local extinction phenomena in $x/D = 15$ and 20 better than ESF8. ER8-PV2 shows similar results.

Selected time averaged flow quantities are reported in Fig. 5.35 for the investigated cases. The reference case is ESF8 (in cyan). In the core jet, the mixture fraction is overpredicted in all sections by ESF8, but the ER simulations can represent well the mixture fraction decay for $x/D > 10$. When calculating f using Eq.(3.20), the Bilger formula, the values of

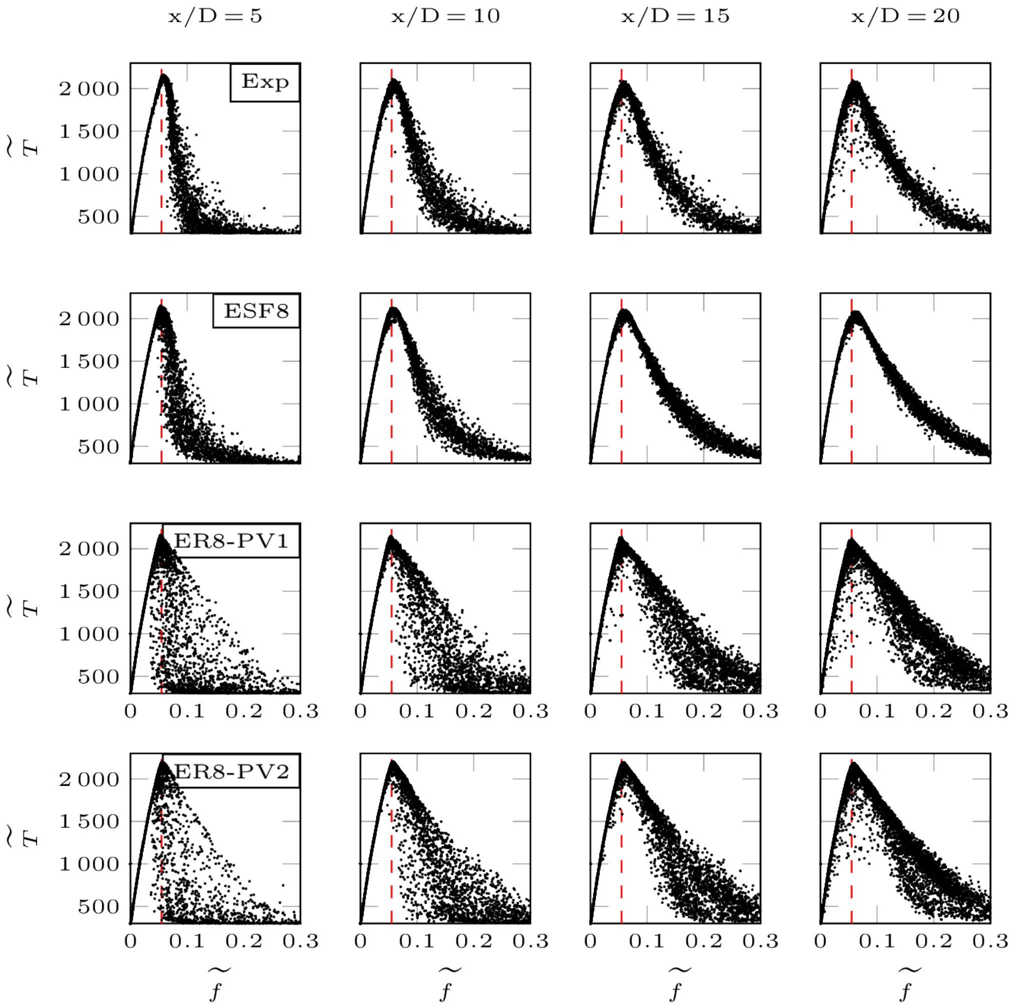

Figure 5.34.: Flame Lr75-57: scatter plots of temperature over mixture fraction at sections x/D = 5, 10, 15, 20. Comparison between experiment, ESF8, ER8-PV1 and ER8-PV2 from Table 5.9

Y_k are required, which are retrieved differently in the two solvers: in ESF8 the composition is calculated directly from the ensemble of the transported stochastic fields, in ER the values are retrieved from the table. This could explain the difference observed between the two solvers. By looking at the temperatures, there is a good agreement for $x/D < 10$ in all simulations except for ER4-PV1. This is the only simulation transporting 4 stochastic fields instead of 8. This configuration with tabulated chemistry seems to require the standard 8 stochastic fields to be correctly represented, as also shown for the other quantities. Note that this difference was not observed when investigating the Sandia flames D-E (cf. Supplementary Material of [30]). Overall the ER simulations are closer to the experimental temperatures than ESF8, although the fuel-lean region is overpredicted from all simulations for $x/D > 15$. The same observations apply to the major species CO_2, CO and H_2O. Species CO_2 and H_2O are overpredicted by the REDIM simulations in sections $x/D = 15$ and 20. The CO predictions for the REDIM-based simulations are under-estimating the experiment

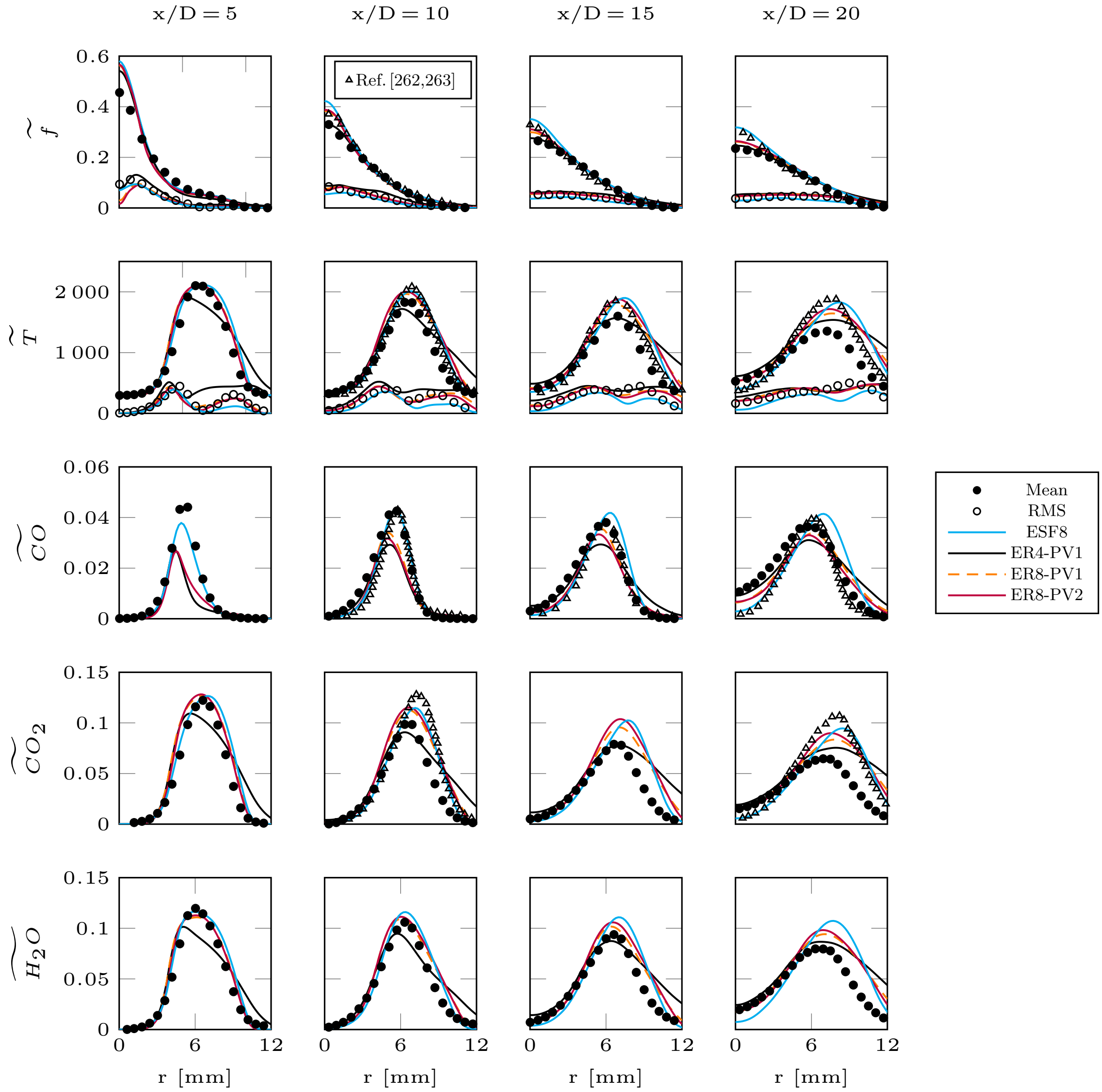

Figure 5.35.: Lr75-57: mean and RMS values for mixture fraction, temperature and major species at sections x/D = 5, 10, 15, 20

in all sections, although a fairly good representation is given for x/D > 10 by ER8-PV1. Changing PV from ER8-PV1 to ER8-PV2 has a minor effect on the peak production of the major species: with PV2, a stronger consumption of CO is observed. The conditional means shown in Fig. 5.36 show a similar behaviour discussed for the unconditional values.

It is useful to compare the computations with the results obtained by Shrotriya et al [262, 263], where the REDIM was coupled with a presumed PDF approach (a clipped Gaussian for CO_2 and a top-hat distribution for N_2). The available profiles for *f*, T, CO and CO_2 are added to Fig. 5.35 and are marked by triangles. In [263], the same REDIM with parameters (Y_{N2}, Y_{CO2}) was used, but the variances of the reduced variables were transported to account for TCI via a presumed PDF model, leading to a 4-dimensional table. One can see that this model overestimates the mean *f* in the core flow and the maximum

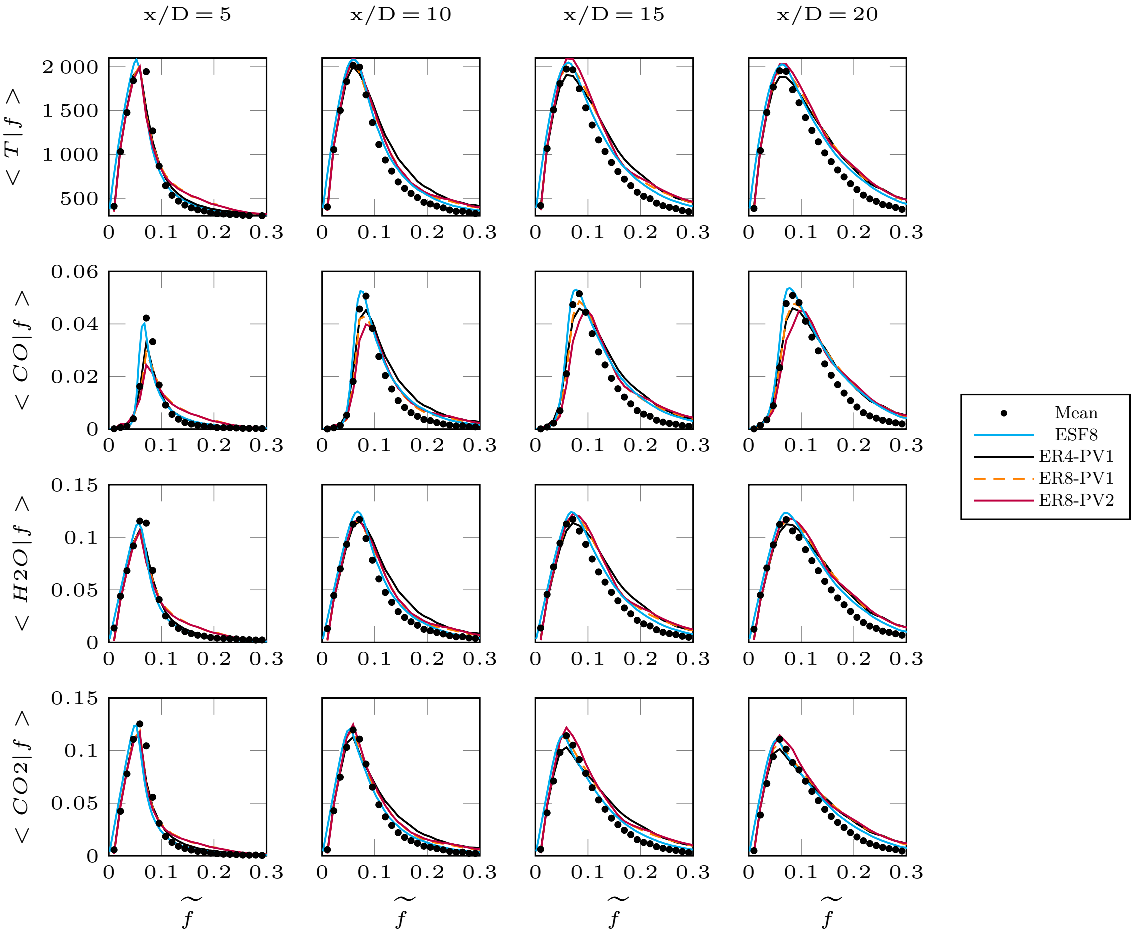

Figure 5.36.: Lr75-57: Conditional means of temperature and major species at sections x/D = 5, 10, 15, 20

T for x/D = 10, 15 and 20, while the RMS of the same fields are overall underpredicted (not shown). On the contrary, the RMS of f and T in this work are correctly represented. In the simulation of [263] a very good prediction is provided for CO, while CO_2 is largely overestimated and its maximum is shifted towards the fuel-rich side of the flame. The boundary conditions applied at the pilot inlet are the same of this work, thus the burned products of a stoichiometric premixed CH_4/air flame. Hansinger et al [118] and Zirwes et al [336] showed how the mixture fraction and a normalized reaction progress variable c are strongly correlated for this flame configuration. The assumption of statistical independence between the REDIM variables, as assumed in the model of [263], could lead to a different development of major products downstream the injector nozzle. Because a transported PDF model is expected to provide better accuracy than a presumed PDF for this flame, the better results obtained for CO in [263] could be here a coincidence.

Overall it can be confirmed that the ESF-REDIM solver can capture the transition between flame regimes given by the stratified flame composition with satisfactory agreement. An improved database could account for a second reaction progress variable to improve the CO predictions. The standard PV = Y_{CO2} seems to be sufficient to describe this flame structure.

5.3. Wall heat-flux prediction for CH_4/O_2 combustion

FWI modelling was primarily investigated using the sub-scale single-element combustion chamber of [113, 51] and its extension with film cooling [50]. The investigated combustion model is the NA-Flamelets-β-PDF for WMLES and hybrid RANS/LES solvers.

Among the variety of operational points investigated in the experiment, the nominal pressure of 20 bar and the mixture ratio ROF = 2.6 were selected. Gaseous CH_4 and O_2 are injected separately into the chamber via a single co-axial element, whose dimensions are reported in Fig. 5.37 (right). The combustion chamber has a square cross-section of $12{\times}12\,\mathrm{mm}^2$. The chamber reaches a total length of 290 mm at the nozzle throat, which has a contraction ratio of 2.5. Since the chamber walls are capacitively cooled, the test bench can be operated for the limited amount of time of about 3 s. The chamber walls are equipped with static pressure transducers and thermocouples, which record the pressure evolution and the temperature at wall. The thermocouple readings are used in post-processing for the inverse heat-transfer problem, in order to reconstruct the wall heat flux [216]. Optical access is included for the measurement of the OH chemiluminescence [316]. The quartz window is protected by a non-reactant coolant, gaseous N_2, which does not significantly influence the near-injector flow. A visual representation of the flame in the chamber is given in Fig. 5.37 (left), showing the flame temperature at the stoichiometric contour of $f_{st} = 0.2$ developing within the first 150 mm from the injector plate. The vertical cut shows the instantaneous $\widetilde{f}$ with a value of 1 at the CH_4 inlets (co-axial injector and film slot) and a value of 0 in the core flow.

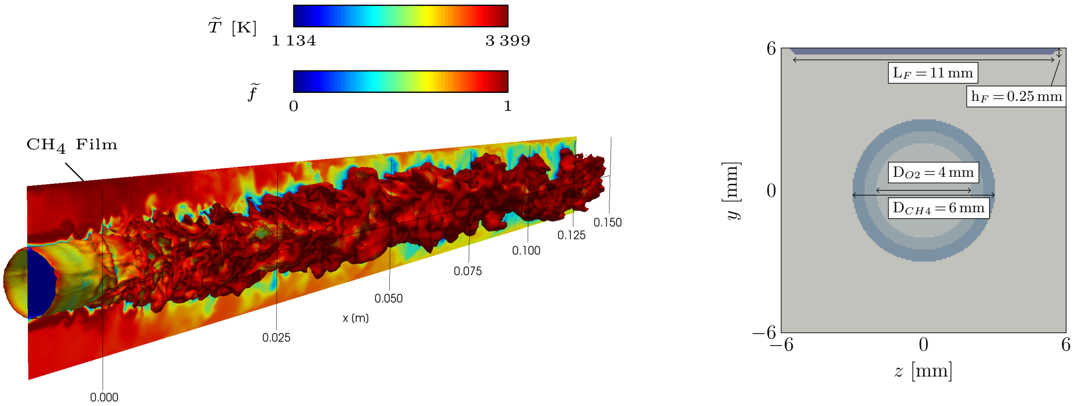

Figure 5.37.: Single-injector combustion chamber: $\widetilde{T}$ field at the iso-contour of $\widetilde{f}_{st} = 0.2$, with $\widetilde{f}$ shown in the axial cut (left). Injector geometry (right) with the film slot applied to mesh M3 (Table 5.11)

For the film cooling investigation, the configuration with gaseous CH_4 as coolant and a width-to-height ratio of the injection slot of 11 mm/0.25 mm is chosen [50, 49]. The correspondent inflow boundary conditions for both cases are summarized in Table 5.10. Note that the original coolant temperature for this configuration would be $T_c = 251\,\mathrm{K}$ [49], corresponding to a higher pressure compared to the p_c at the faceplate (20.35 bar vs 20.12 bar). The coolant temperature provided by the experiment is associated with a pressure higher than 20 bar as encountered in the feeding line. Because the computational domain in OpenFOAM includes only a patch of the injector and the cooling slot on the faceplate, the temperature was recalculated using the NIST database[3] to match a mean chamber pressure of 20 bar. This results in $\bar{T}_c = 217\,\mathrm{K}$ as reported in the table.

Table 5.10.: Inflow boundary conditions

Case	T_{CH4} [K]	T_{O2} [K]	$\bar{T}_c$ [K]	$\dot{m}_{CH4}$ [g/s]	$\dot{m}_c$ [g/s]	$\dot{m}_{O2}$ [g/s]
without film - W	269	278	-	17	0	45
with film - F	269	278	217	17	4.37	45

5.3.1. Numerical setup

The meshes investigated for this case are listed in Table 5.11. The first three meshes were used for the investigation of grid dependency of the IDDES solver in [31] and have $y^+_{mean} < 1$ at the wall. While meshes M1-M2 cover the entire domain before the nozzle section, M3-M4 are limited to the first half of the chamber ($x_{max} = 150\,\mathrm{mm}$). Mesh M3 includes a refinement on the top wall and the film slot patch at the faceplate, in order to investigate the configuration with film cooling. M4 is targeted for WMLES and has $y^+_{mean} \approx 33$.
The injector elements (oxygen, methane, post-tip) and the film slot for M3 are patched to the faceplate as shown in Fig. 5.37. The minimum requirement of 5 cells for the post-tip resolution is satisfied for all meshes. Local refinement is applied along the shear layers using hanging nodes. The temperature at the walls is interpolated from the temperature readings available from the experiment [113]. The faceplate and the post-tip are treated as adiabatic walls instead. A fixed pressure value is assigned at the outlet from the last pressure transducer reading in M1-M2, while the value is interpolated at $x = 150\,\mathrm{mm}$ for M3-M4. Turbulent inlet boundary conditions are achieved at the methane and oxygen inlet by means of digital filters [131]. The time averaged fields are evaluated over 5 flow-through times.

Table 5.11.: Investigated meshes

Mesh	Cell volumes [10^6]	x_{max} [mm]	y^+_{mean}	y^+_{max}	Solver
M1	53	272.5	0.0814	31	IDDES
M2	30	272.5	0.0002	0.91	IDDES
M3	9	150	0.19	8	IDDES
M4	7	150	33	100-130	WMLES

A PISO algorithm is used in OpenFOAM for the momentum/pressure coupling. First order Euler implicit time stepping was combined with second order TVD-VanLeer schemes for the advective terms, with the exception of the velocity field using a standard 2^{nd} order unboundend scheme, since this is less dissipative. The time step is adjusted to comply with a maximum CFL number of 0.4.

5.3.2. IDDES with tabulated chemistry

The results presented in this section are mostly taken from a previous publication (Breda and Pfitzner [31]), but the major achievements will be summarized hereby.

---

[3] https://webbook.nist.gov/chemistry/fluid/

Wall heat flux prediction

Let us first compare the pressure and wall heat flux predictions on the configuration without film cooling, using the NA-flamelet manifold introduced in Section 3.5.2 and built for the Lu30 chemistry, . This corresponds to the first three profiles listed in the legend of Fig. 5.38. The experimental data show a pressure peak within the first 50 mm downstream, caused by the impinging of the jet at wall. A recirculation zone is formed in this region. The pressure gradually reduces further downstream, reaching almost a plateau before entering the nozzle. All cases can qualitatively capture the pressure profile, converging to the value imposed by the boundary condition. The profile of W-M3-Lu30-NA is 'shifted' upwards in order to match the pressure constraint at x = 150 mm, while the pressure value at the same location is calculated from the PISO equations in W-M1-Lu30-NA and W-M2-Lu30-NA. Because the combustion chamber has a squared cross-section, the wall heat flux has been circumferentially averaged in the CFD simulations. The most recent reconstructed heat flux from the inverse conjugate heat transfer problem [216] is shown in the right plot. The steep rise within the first 50 mm locates the recirculation zone where the hot gases impact at wall. The experimental profile reaches a plateau of about 5 MW/m^2 at the end of the domain. While no significant pressure variation was observed between W-M1-Lu30-NA and W-M2-Lu30-NA, a deviation in $\dot{q}_w$ is present in the second half of the chamber. The first peak at x = 10 mm is well captured by W-M3-Lu30-NA, because the pressure is fitted at x = 150 mm instead of 272.5 mm. All profiles show a drop in $\dot{q}_w$ after the reattachment of the recirculation zone, followed by a very good match until about 150 mm. From here, W-M2-Lu30-NA departs towards higher values of $\dot{q}_w$, while W-M1-Lu30-NA approaches a constant value of 4.3 MW/m^2. Overall, the profiles are contained within the error bars until almost the end of the domain.

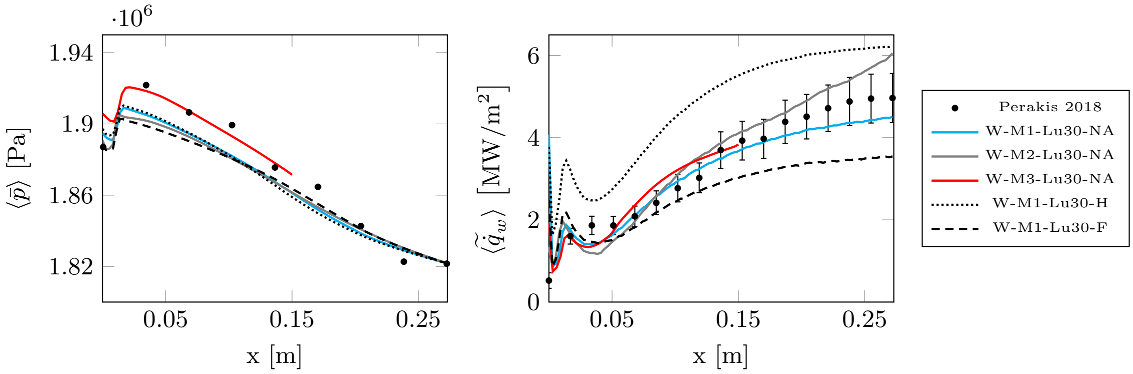

Figure 5.38.: Axial pressure and wall heat flux distribution for Lu30-based flamelet manifolds on meshes M1-M2-M3 without film cooling

Enthalpy losses in the flamelet database

Fig. 5.38 also reports the calculations performed with two databases including enthalpy losses, but calculated differently from NA. The first database used for W-M1-Lu30-H (dotted) was provided by Perakis [220], where the flame structure is calculated after an enthalpy profile has been imposed. The second database used for W-M1-Lu30-F (dashed) exploits the common assumption of frozen chemistry at the wall proximity. The profiles obtained from

$\dot{q}_w$ show results at the extremes: W-M1-Lu30-H overpredicts the wall heat flux across the entire domain, while W-M1-Lu30-F underpredicts the heat flux starting 75 mm downstream. In the first case the model includes too much recombination at wall, shifting the chemistry almost to the equilibrium. This behaviour is shown in the scatter plots of Fig. 5.39, where the CO_2 concentration for the fuel-rich mixture at wall (the blue cloud) of W-M1-Lu30-H is almost doubled compared to W-M1-Lu30-NA. The data are coloured by the value of enthalpy loss $\widetilde{h}_n$. Note that the database used for W-M1-Lu30-H could be improved using the enthalpy profiles of W-M1-Lu30-NA as imposed solution, as shown in [32, 217]. In W-M1-Lu30-F instead, recombination reactions at the wall are completely neglected, reducing $\dot{q}_w$ because of the missing heat release from the exothermic reactions at wall. The scatter plot for W-M1-Lu30-F does not show the CO_2 recombination on the fuel-rich side at the wall.
This paragraph shows that, if the enthalpy profiles are not directly derived from a physical process (H) or do not include recombinations effects (F) or informations on the local τ_{chem} [243], an erroneous wall heat flux can result.

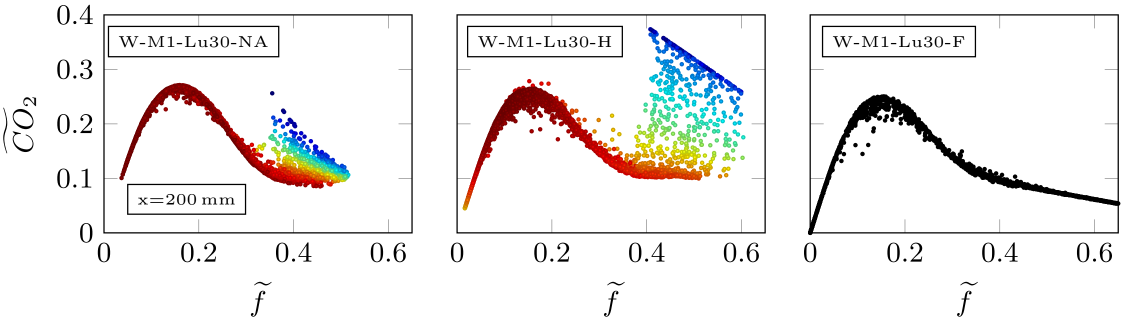

Figure 5.39.: Scatter plots of $\widetilde{CO_2}$ at x = 200 mm using mesh M1 and flamelet databases with different enthalpy loss methods. W-M1-Lu30-NA using database from Perakis et al. [220]

RANS/LES transition

The IDDES solver used in this work uses a DDES [273] as wall model for the inner boundary layer, located at $y^+ < 100$, while the outer boundary layer and the core flow are modelled by LES. The DDES-branch uses a RANS model, the Spalart-Allmaras equation. The left side of Fig. 5.40 shows a snapshot of the axial velocity (compressed of factor 4 along x and stretched of factor 2 along y), including the transition line between the RANS and the LES solver (in red). The transition point depends on the wall-parallel grid refinement and it is adapted through the domain as shown for mesh M2 (a detailed discussion can be found in [31]). A detailed comparison of the IDDES activation functions provided in [31] for meshes M1-M2-M3 showed that transition is initialized correctly by the model, despite noticeable differences in the number of transition cells and turbulent content. The model reacts therefore robustly to the mesh refinements applied in this work.
The IDDES solver however should avoid a transition from LES to RANS in the core flow, whenever the turbulent content is significantly reduced due to an increase in mesh refinement. This is performed by the low-Reynolds correction function Ψ, introduced by Spalart et al [273] into the turbulent length scale $\widetilde{d}$ of Eq. (2.47). Its instantaneous value is reported

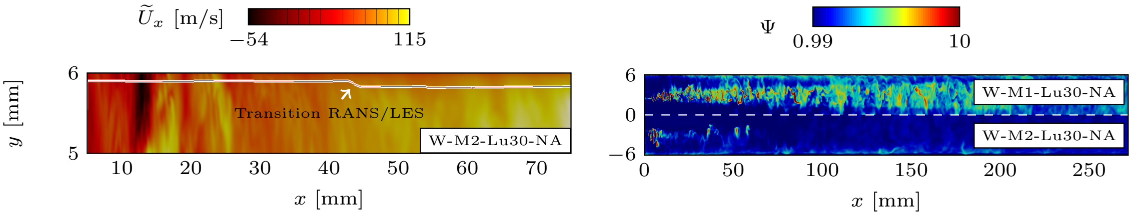

Figure 5.40.: Left: Axial cut of $\widetilde{U}_x$ 1 mm from the upper wall and RANS/LES transition line. Right: Low-*Re* correction function for meshes M1 (top) and M2 (bottom)

on the right of Fig. 5.40 for meshes M1 (top) and M2 (bottom). It is clear that values in the core flow are higher for mesh M1 (most refined with 53 million cells), where the values of ν_{sgs} are lower because of the reduced LES filter width Δ. ν_{sgs} is also decreasing while approaching the walls, but the transition from LES to RANS is avoided in the core flow due to the contribution of Ψ into $\widetilde{d}$.

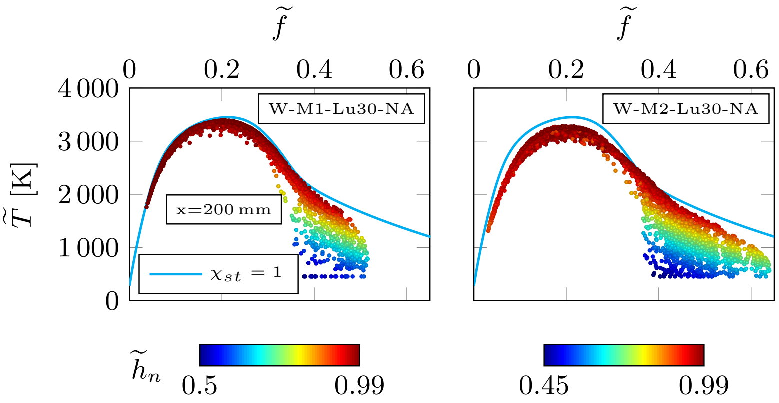

Figure 5.41.: Scatter plots of $\widetilde{T}$ at x = 200 mm for M1 and M2 without film cooling. Data coloured by enthalpy losses

On the other hand, less refined meshes like M2 and M3 have a higher turbulent content ν_{sgs} in the core flow, which is passed to the LES solver as a Smagorinsky-like dissipation [264]. The higher turbulent content increases the effect of $\widetilde{f''^2}$ in the core flow, contributing to reduce the peak temperatures and species concentrations, as shown from the temperature scatter data at x = 200 mm in Fig. 5.41. A flamelet profile for $\chi_{st} = 1\,\mathrm{s}^{-1}$ is superimposed and the scatter data are coloured by normalized enthalpy. Although the same NA flamelet database was used for the two simulations, more fuel-rich states are found at the wall proximity for W-M2-Lu30-NA and for higher enthalpy losses (cf. the mixture fraction values reached by the cold states in Fig. 5.41 for both simulations). These states correspond to a higher degree of recombination, generating the higher wall heat flux prediction observed in Fig. 5.38.

5.3.3. Configuration with film cooling

The $\dot{q}_w$ predictions confirmed the validity of the NA-flamelet combustion model combined with IDDES. What happens if the same setup is applied to a configuration with film cooling [50]? Can the wall heat flux be represented as well as before? The film cooling efficiency is discussed in this paragraph for the Lu30 chemistry using mesh M3. The results obtained for W-M3-Lu30-NA (-NA is dropped hereby) shown in Fig. 5.38 are now compared with F-M3-Lu30, where the film injection is activated. The coolant mass flow rate $\dot{m}_c$ is taken from the experimental data and corresponds to about 30 % of $\dot{m}_{CH4}$. The inflow velocity is calculated accordingly and corresponds to 80 m/s. The pressure distribution for this configuration [50] was recently provided by the Technical University of Munich, so that the boundary conditions on the pressure field differ from the ones previously used in [213, 31]. There, the pressure distribution was taken from the original combustion chamber [113].

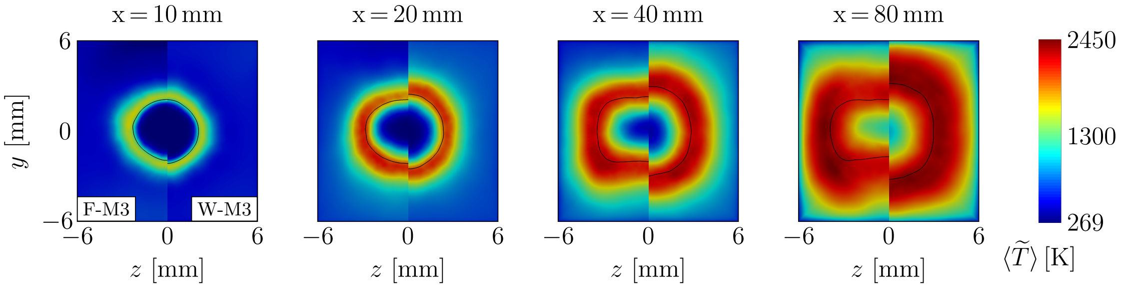

Figure 5.42.: Radial flame expansion at cross sections x = 10, 20, 40, 80 mm with (F-M3) and without film cooling (W-M3)

Fig. 5.42 reports the mean temperature field at selected cross sections to compare the flame radial expansion in the case with (F-M3) and without film cooling (the previous label W-M3-Lu30-NA becomes W-M3 in the figure for the sake of clarity). In both cases the flame shape gradually shifts from circular, close to the injector plate, to squared further downstream, because constrained within the squared chamber. This means that the heat load distribution at wall is concentrated at the center line, lowering at the corners where the fuel-rich mixture is confined. The isoline for $f_{st} = 0.2$ is shown in the figures to locate the flame front. In F-M3, the hot gases do not expand uniformly in the squared chamber (left side of each figure) and the circular shape evolves earlier to a rectangular shape, visible already 40 mm downstream. The film coolant applied at the top wall starts pushing the flame front downwards, so that the cold O_2 core is forced to expand more at its sides (cf. x = 40 mm). Therefore, the flame becomes thinner in the vertical direction compared to the case without film cooling. This results in a faster consumption of the core, visible at x = 80 mm. There is a side effect derived by the flame expansion in F-M3: although the thermal boundary layer is protecting the upper and lower walls from the hot gases, the latter are closer to the side walls than in configuration W-M3. This seems to affect the circumferential averaged $\dot{q}_w$ negatively for F-M3, leading to an increase of $\dot{q}_w$ in the second section, rather than a decrease.
Fig. 5.43 shows the circumferentially averaged wall heat flux, together with the experimental values (F-Exp) reconstructed from the inverse wall heat flux problem by Perakis et al [216]. The dotted line shows the calculated heat flux without film cooling (the same of Fig. 5.38).

Due to the cooling film injected parallel to the upper wall, F-M3-Lu30 reports a lower $\dot{q}_w$ peak within the first 50 mm. This peak is not captured by the experimental data instead, which show however a steeper gradient at this location. Further downstream, both profiles are in good agreement with the experimental data, meaning that the cooling efficiency is significantly reduced. For the reason explained before, F-M3-L30 reports higher $\dot{q}_w$ values in the second half of the domain. A change in combustion chamber geometry to have a circular cross section and its consequently CFD simulation could help to clarify if this effect is primarily due to the squared cross section.

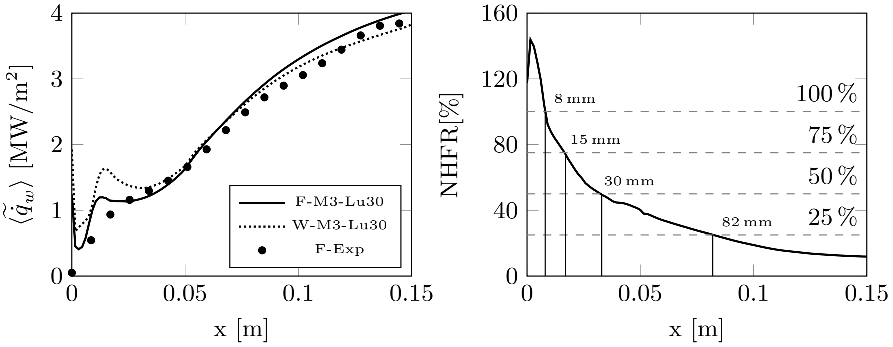

Figure 5.43.: Left: M3-Lu30 with (F) and without (W) film cooling. Right: Net Heat Flux Reduction (NHFR) distribution for M3-Lu30

Film cooling efficiency

To assess the effectiveness of film cooling on the upper wall, the Net Heat Flux Reduction (NHFR) proposed by Bartz [12] is used in this work. It is calculated as

$$NHFR(x) = 1 - \frac{\dot{q}_{wu,F}(x)}{\dot{q}_{wu,W}(x)} \left(\frac{p_W(x)}{p_F(x)} \right)^{0.8} \tag{5.2}$$

where p is the axial pressure distribution in the two cases, W and F. In the NHFR, the $\dot{q}_{wu}$ is integrated at the upper wall only, i.e. where the film injection slot is located. The right side of Fig. 5.43 shows the NHFR axial evolution. The efficiency exceeds 100 % in the first 8 mm because the heat is transferred from the wall to the colder CH_4. Once the film has heated up, a drop of 25 % efficiency is observed within the first 15 mm downstream, reducing to 50 % at 30 mm and 75 % at 82 mm. At the mid chamber length (x = 150 mm) the NHFR has dropped to about 10 %, justifying why the reduced axial domain of M3 is sufficient to capture the region of most cooling effectiveness.

Validation of novel CH_4-chemistry mechanisms

Proceeding a step further from the previous paragraph, the reduced chemical mechanisms listed in Table 3.1 targeted for CH_4/O_2 combustion (*lprb*, *mprb* and *hprb*) are now validated on the F-M3 configuration. Because finite rate simulations would be too expensive, the chemical mechanisms are used for the generation of the NA-flamelet databases instead.
Fig. 5.44 shows the axial pressure and $\dot{q}_w$ distribution for the investigated NA-databases, with the additional F-M3-Lu30 simulation as reference. The pressure profile is shifted

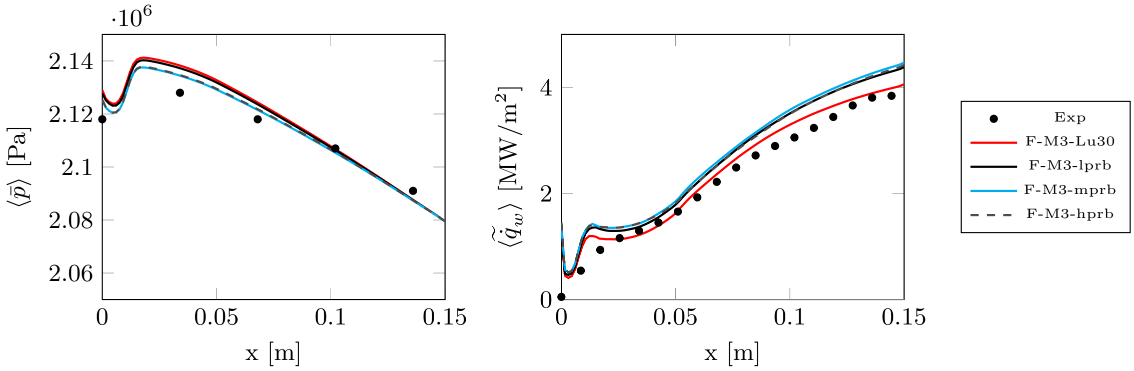

Figure 5.44.: Axial pressure and wall heat flux distribution for the film cooling test case F-M3 with reduced chemistries *lprb*, *mprb* and *hprb*

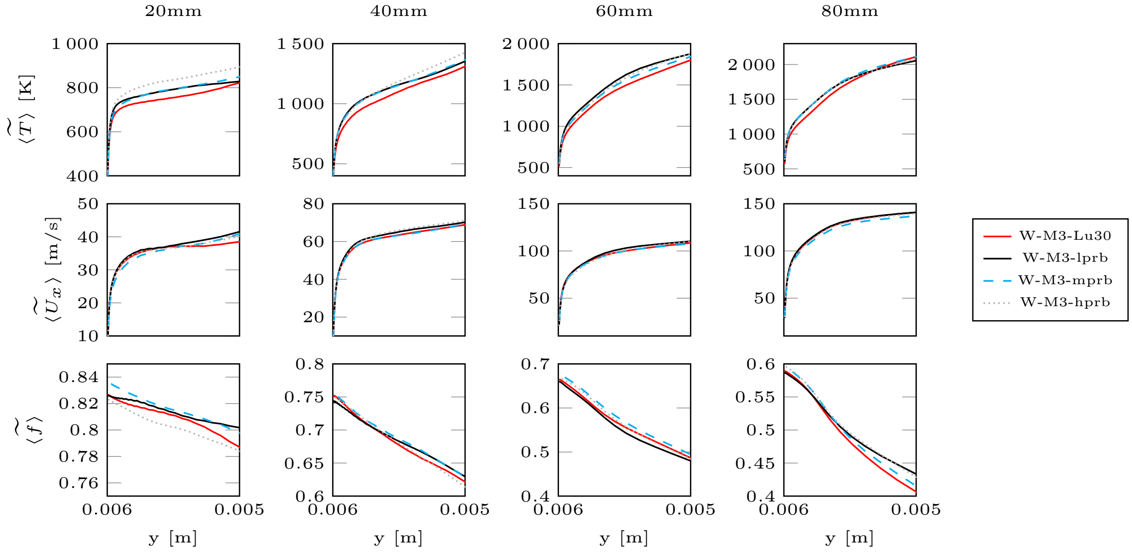

Figure 5.45.: Boundary layer development within 1 mm from the wall, taken at the centerline and sampled at x = 20, 40, 60, 80 mm. Configuration without film cooling

upwards compared to Fig. 5.38, but the development across the chamber axis is almost identical. The *lprb* shows a pressure distribution similar to Lu30. The heat loads of the new mechanisms deliver almost identical results for this configuration at 20 bar. Across the whole chamber, *hprb* and *mprb* provide almost matching results. Overall, the Lu30 chemistry seems to approximate better the wall heat flux, while the remaining chemical mechanisms predict in general higher thermal loads. This is however not surprising. The flamelet structure reported in Fig. 3.8 shows higher temperatures for reduced chemistry mechanisms in the fuel-rich zone, corresponding to the condition found in this combustion chamber of unburned CH$_4$ confined at the walls. There, the presence of endothermic fuel splitting reactions contributes to reduce the heat release, thus the wall heat flux, of Lu30.
A detailed insight of the thermal boundary layer developing at wall within the first millimeter can provide more information about the three mechanisms. The configuration without film cooling is used for this discussion, since the wall heat flux is equally distributed between

the four walls (cf. Fig. 5.42). The profiles shown in Fig. 5.45 were sampled at the upper wall along the centreline, where most of the heat release is located. The first row shows the temperature boundary layer. All reduced chemistries predict higher temperatures compared to Lu30, which results in the higher heat flux prediction observed before. The *hprb* seems to predict higher temperatures in section x= 20 mm, as confirmed by the lower values of mixture fraction f (cf. third row). The mixture fraction values show that primarily CH_4 is found close to the wall at x = 20 mm ($f \approx 0.8$), later on shifting to a fuel-rich mixture of hot gases to 0.7-0.6. In particularly, from x = 80 mm, the gradient of f at wall becomes stronger (from 0.6 to 0.4 within 1 mm), indicating the presence of combustion products closer to the wall. The stronger divergence of the profiles at x = 20 mm can be explained again analysing the counterflow diffusion flame shown in Fig. 3.8. It justifies why a richer concentration of fuel for the reduced chemistries is associated with higher temperatures, compared to Lu30. The velocity boundary layer does not seem to be strongly affected by the choice of the chemistry, although a flattened profile is predicted by Lu30 at x = 20 mm.

Overall, the results delivered by the new chemistry mechanisms are satisfactory and the validation for CH_4/O_2 combustion is considered successful. The choice of the best performing mechanism between the three candidates is the remaining topic to discuss. During the CFD simulation, the time spent in the interpolation routine is the determining factor. A quick test on OpenFOAM reveals that the interpolation time per core reduces by only 6 ms when reducing the number of species from 30 to 19 (using here 392 cores). One could directly use the Lu30 chemistry to keep the desired accuracy. However, there is a main reason why the tabulation of reduced chemical schemes is preferable to Lu30. It is linked to the memory allocation resources when parallelizing the computation. Here the tables have modest dimensions: using three table parameters a maximum size of 54 MB for the Lu30 chemistry is reached. However, if more table parameters are required to describe the thermo-chemical process (pressure, scalar dissipation rate, reaction progress variable, . . .) its size can easily grow by an order of magnitude. For instance, adding 6 grid points for a fourth table parameter would increase the storage size to about 300 MB. Increasing the number of grid points in the table or applying a grid refinement has the same effect. Under such circumstances, it could be necessary to store a reduced chemistry mechanism to prevent memory overflow, when the table is copied to each core at the beginning of the simulation. The most limiting factor becomes the computational time required by the generation of the flamelets in the pre-processing step. The left hand side of Fig. 3.1 shows that the best performance is given by *hprb*, which is therefore the preferred choice for this configuration.

5.3.4. IDDES compared to WMLES

One last topic left to discuss is the comparison with WMLES. The main objection to the use of IDDES is its strong grid dependency, which is also a common problem of WMLES [166]. When preferring WMLES however, numerous modelling of the near-wall boundary layer exists and not all of them are suitable to predict the wall heat fluxes in case of strong temperature gradients [46].

Let us consider configuration W-M3-Lu30 as reference case for this comparison, thus the half-length computational domain without film cooling and the NA-flamelets based on the Lu30 chemistry. Mesh M4 is used for the WMLES, featuring a mean $y^+ = 33$ at the walls. According to Fig. 2.5, this means that the first computational cell at wall is located (in average) at the lower boundary of the log-layer. Two different wall functions are compared.

One is the standard law from Spalding [275], leading to configuration W-M4-Lu30-WMS, the other one is the coupled temperature/velocity wall function of Cabrit [46], leading to configuration W-M4-Lu30-WMC. Both implementations were introduced in Section 2.4.

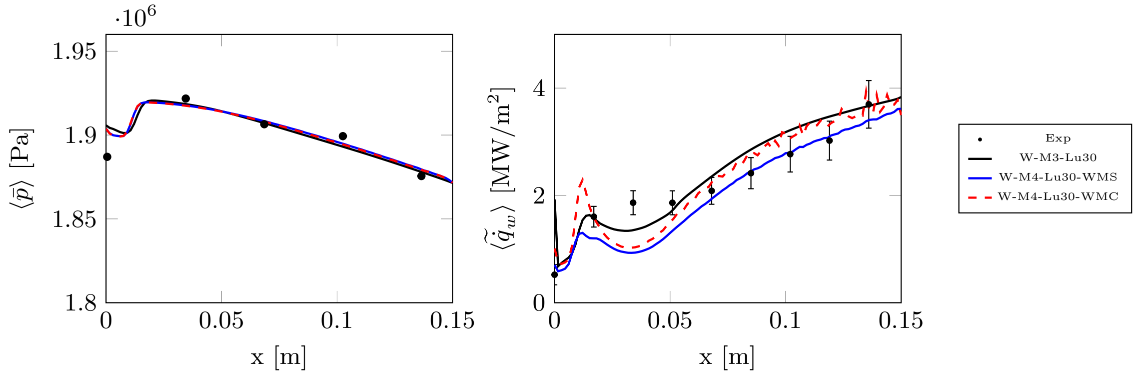

Figure 5.46.: Axial pressure and wall heat flux distribution. Comparison between IDDES and WMLES solvers on meshes M3 and M4 without film cooling

Fig. 5.46 shows again the pressure and wall heat flux distribution for the three simulations. Small differences can be seen on the axial pressure: at the faceplate, lower values are observed for WM. The recirculation zone is anticipated compared to IDDES, and the values towards the end of the domain are slightly higher than IDDES. Only the first experimental point is significantly overpredicted by all simulations. No difference is observed between WMC and WMS. The same behaviour was observed by Zips et al [333], where IDDES and WMLES simulations were compared on mesh M2, using however a frozen flamelet database.

More room of discussion is offered by $\dot{q}_w$. The conventional way of calculating the wall heat flux throughout this work is to interpolate the field $(\lambda + \lambda_{sgs})\nabla T$ at the wall patches. The OpenFOAM calculations of this work use the `alphatWallFunction` to calculate first the thermal diffusivity $\alpha_{sgs} = \frac{\nu_{sgs}\rho}{Pr_{sgs}}$, from which $\lambda_{sgs} = \alpha_{sgs}\, c_p$ is retrieved. The turbulent Prandtl number Pr_{sgs} is equal to 0.7. In W-M3-Lu30 and in all IDDES-based simulations the wall heat flux is approximately equal to $\lambda \nabla T$, since the wall refinement with $y^+ \sim 1$ guarantees that λ_{sgs} tends to zero. There could be of course a minimal influence from the RANS equation active at wall (SA), which provides the ν_{sgs} for the boundary layer. However, in W-M4-Lu30-WMS and W-M4-Lu30-WMC, it is $y^+ \sim 33$ so that the term λ_{sgs} is not negligible. The first observation for the $\dot{q}_w$ of Fig. 5.46 is that WMLES show a lower heat flux across the domain compared to the IDDES, except from the peak of W-M4-Lu30-WMC at the recirculation zone. Overall, W-M4-Lu30-WMS (using the Spalding law) represents better the distribution from $x > 75$ mm. The W-M4-Lu3-WMC instead (the Cabrit law) delivers results similar to the IDDES in the second half of the chamber. The reason for this difference can be understood by recalling Section 2.4, where it was explained that the ν_{sgs} used to calculate λ_{sgs} is evaluated differently by the two wall functions.

For the purpose of this paragraph one can see that the standard Spalding law of the wall without the temperature coupling can deliver results in the same order of accuracy of the IDDES solver.

Computational time

This final paragraph aims to compare the CPU times of the IDDES and WMLES solvers. Because the IDDES and WMLES are run on two different meshes (M3 and M4 respectively), the comparison of the CPU time is performed on two parallelized configurations, both allocating about 37000 volume cells per core. Each simulation is then run over 500 time steps of $\Delta t = 3 \cdot 10^{-8}\,\mathrm{s}$, in order to get an average of the share time required by the table interpolation, the near-wall turbulence correction and to solve the remaining transport equations. A second average of these values is then performed over three runs, in order to account for fluctuations of the network performances. Fig. 5.47 summarizes the results.

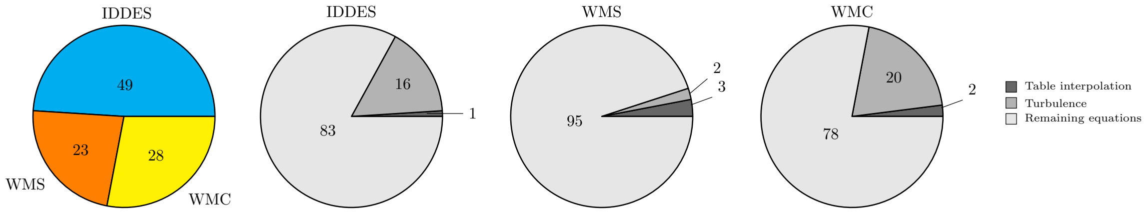

Figure 5.47.: Coloured pie chart: computational time (in %) required by IDDES, WMS and WMC for a single Δt (100% is the sum of the three solvers). Remaining charts: interpolation and turbulence share (in %) required by each solver

The coloured pie chart shows a relative comparison of the time required to advance the simulation of $3{\cdot}10^{-8}\,\mathrm{s}$, for the IDDES (blue), WMLES with Spalding function (WMS in orange) and WMLES with Cabrit function (WMC in yellow). The sum of the three times is normalized to 100% and each share is provided in the chart. The WMS is at least two times faster than IDDES. WMC is slower than WMS due to the iteration of Eq.(2.44), but still outperforms IDDES. An insight on the single solvers is provided by the gray pie charts. Within IDDES, 1% of Δt is spent to retrieve the thermo-chemical states from the table interpolation, 16% is spent to resolve the Spalart-Allmaras Eq. (2.47) and correcting the ν_{sgs}, the remaining 83% is used for the transport equations. In WMS only 3% and 2% are spent respectively for table interpolation and the evaluation of the Spalding law of the wall. Here the evaluation of the near-wall turbulence costs less than the interpolation call. In WMC the share required by the evaluation of the Cabrit wall of the law increases to 20%, with 2% required by the table interpolation. A common reference time is identified from the table interpolation routine, since the Lu30 chemistry was used for all simulations, and it is about 53 ms for all simulations.

Two important observations emerge from this analysis. First, the use of tabulated chemistry limits the evaluation of the chemistry to only less than 2% of the computation, despite the near-wall treatment used. The latter becomes therefore the limiting factor: IDDES seems to require higher computational power then WMLES because an additional equation (the SA equation) must be solved in the domain, although its value is only required at the near-wall. According to this investigation, the WMS solver with NA-flamelet chemistry could be sufficient for a satisfactory prediction of the wall heat fluxes. Nonetheless, it should be reminded that the same near-wall treatment implemented in another software rather than OpenFOAM could lead to different results.

5.4. Near−wall secondary reactions of CH_4

A final, more challenging configuration featuring autoignition is investigated in this paragraph. This serves to confirm the previous observations derived for TCI and tabulated chemistry. Here the base investigation relies on the FR-noTCI setup. The comparison with tabulated chemistry (REDIM-ESF and NA-Flamelets-β-PDF) is also discussed.

Dalshad et al [68] investigated secondary reactions in proximity of cooled walls using an effusion cooling jet configuration. In a novel test bench, the oxygen-rich hot crossflow is provided by a gas generator [67], whereas the injected gas is either CH_4, H_2 or C_3H_8. The fuel can be injected at different momentum ratios through 5 nozzles of diameter 0.4 mm, at an angle of 30° to the crossflow direction. After the reactants mix, chemical activity is observed within the test section. Because the reaction zone is located near the wall, this segment is cooled using a water manifold. An experimental configuration allowing for a stable reaction zone is chosen for the CFD validation, in order to identify where autoignition triggers. Pure CH_4 is chosen as injected fuel, with a momentum ratio of $\mathrm{I} = 10$ based on a mean jet velocity of $\bar{U}_c = 85\,\mathrm{m/s}$ and a bulk crossflow velocity $U_h = 25\,\mathrm{m/s}$ [4]. The higher the momentum I, the higher is the penetration depth of the jet into the main flow and the more stabilized appears the secondary combustion zone [68]. The hot gas composition was determined using 0D-reactor models available in Cantera [67] and it is summarized in Appendix B. Together with the autoignition length, the estimation of the wall heat flux is a key requirement for the CFD simulation. Experimental data for $\dot{q}_w$ are provided by a solution of the inverse heat transfer problem, based on 11 thermocouple readings available at the cooled wall [66]. OH chemiluminescence and OH-PLIF were used at the test bench to locate the autoignition length.

5.4.1. Numerical setup

Two middle refined meshes were generated in order to investigate the effects of the chemical mechanism, the injector/injector interaction and temperature variation at the oxidizer inlet. Being x−y−z the streamwise, spanwise and the wall normal directions, the computational domain has dimensions $82\times5\times20$ mm^3 and $0.98\cdot10^6$ (0.98M) volume cells including one injector, and dimensions $165\times15\times20$ mm^3 with 2.1M cells including three injectors. These meshes are labelled respectively as M1 and M2. The upper wall is treated as symmetry plane. The spanwise patches are treated as periodic boundary conditions. For both meshes, the maximum y^+ detected at wall is about 5.3, with an average value of 1.1. The LES is therefore well resolved. A maximum cell size of $\Delta \approx 0.61\,\mathrm{mm}$ is found at the top wall close to the outlet in M2, while it is confined below 0.3 mm where the flame is located. Similar values are retrieved from M1. In both domains, the CH_4 injection holes are located about 4 mm downstream the hot flow inlet. Uniform scalar values are applied at the CH_4 and hot inlets, taken from a precursor pipe LES. Artificial turbulence is applied at the hot inlet in one configuration, using the digital filters method [131]. The wall temperature is interpolated from the experimental values, obtained from the thermocouples' readings.
The momentum and pressure equations are coupled with a PISO loop. The time integration scheme is an implicit Euler first order, while a vanLeer second order is used for the scalar diffusion terms. A second order unbounded Gauss linear scheme is used for the velocity

---

[4] I is defined as $\frac{\rho_c U_c^2}{\rho_h U_h^2}$, where c are the injected gas and h the hot gas properties

instead, due to its low numerical viscosity. The time step is adjusted at runtime to provide a CFL of 0.6. The LES averaged fields are calculated over 5 flow-through times. Table 5.12 summarizes the investigated numerical setups.

Table 5.12.: Investigated configurations, $T_{CH4} = 570\,K$

Case	Mesh-Chemistry-Injectors	T_h [K]	Turbulent Inlet
C1	M1-Lu30-1	1500, 1550, 1600, 1620	-
C2	M2-Lu19-3	1500, 1550, 1600, 1620	-
C3	M1-Lu30-1	1620	Digital filters [131]
C4	M2-Lu19-3	1620	Digital filters [131]
C5	M1-REDIM-1	1600	-
C6	M2-NA-3	1430	Digital filters [131]

C1-C2 are based on finite rate chemistry computations without TCI modelling on the subgrid, using the mechanisms Lu30 and Lu19. In a first step, the autoignition length is investigated without the effect of a turbulent inlet. Four different T_h are investigated in the CFD, since the experimental data revealed a rather inhomogeneous temperature distribution at the hot exhaust gases coming from the burner. A peak value of 1620 K was reconstructed from the experiment, while the thermocouples located at the inlet perimeter report readings localized around 1500-1600 K [68]. The coolant inlet is assigned a mean temperature of 570 K. This evaluation derived from a previous LES of the CH_4 injector nozzle, considering the heating of the fuel from the tank (ambient temperature) to the injection plate. C3 and C4 correspond to configurations C1 and C2 with $T_h = 1620\,K$ and artificial turbulence at inlet. C5 uses the newly developed ESF-REDIM solver, with a 2D-REDIM database featuring $\{Y_{N2}, Y_{CO2}{+}0.5\,Y_{H2O}\}$ as progress variables. C6 exploits the NA-flamelet solver instead. The value $T_h = 1430\,K$ was originally included in the investigation, however, no ignition was observed within the M1-M2 domains using finite rate chemistry. This case is however retained for the flamelet simulation, because it shows a fully ignited flame where instead no ignition shall be expected.

5.4.2. Autoignition length

The location of the autoignition kernel or the lifted flame tip strongly depends on the temperature of the hot reactants. A temperature increase also increases the rate of reaction, promoting the fast chemistry process. The lifted flame of this test case establishes because the reaction/diffusion process within the ignition kernel balances the convective force, which would otherwise transport the kernel outside the domain. By further increasing the temperature, the flame anchoring point would shift further upstream until an attached flame is reached.

This effect is first investigated without a turbulent BC at the hot flow inlet. The left column of Fig. 5.48 reports an axial cut at the central plane of configurations C1-C2, coloured by the mean temperature field. The top half represents C1, the bottom half C2, unless otherwise stated. The lifted flame can be clearly recognized in the sequence, its tip moving upstream by increasing the oxidizer temperature. It is also interesting to notice the presence of a double flame branch appearing for higher inlet temperatures: the upper flame derives from the mixing and reaction of CH_4 with the hot flow, while the bottom flame is located where the CH_4-enriched mixture reacts with the oxidizer stream, the latter cooled down by the wall.

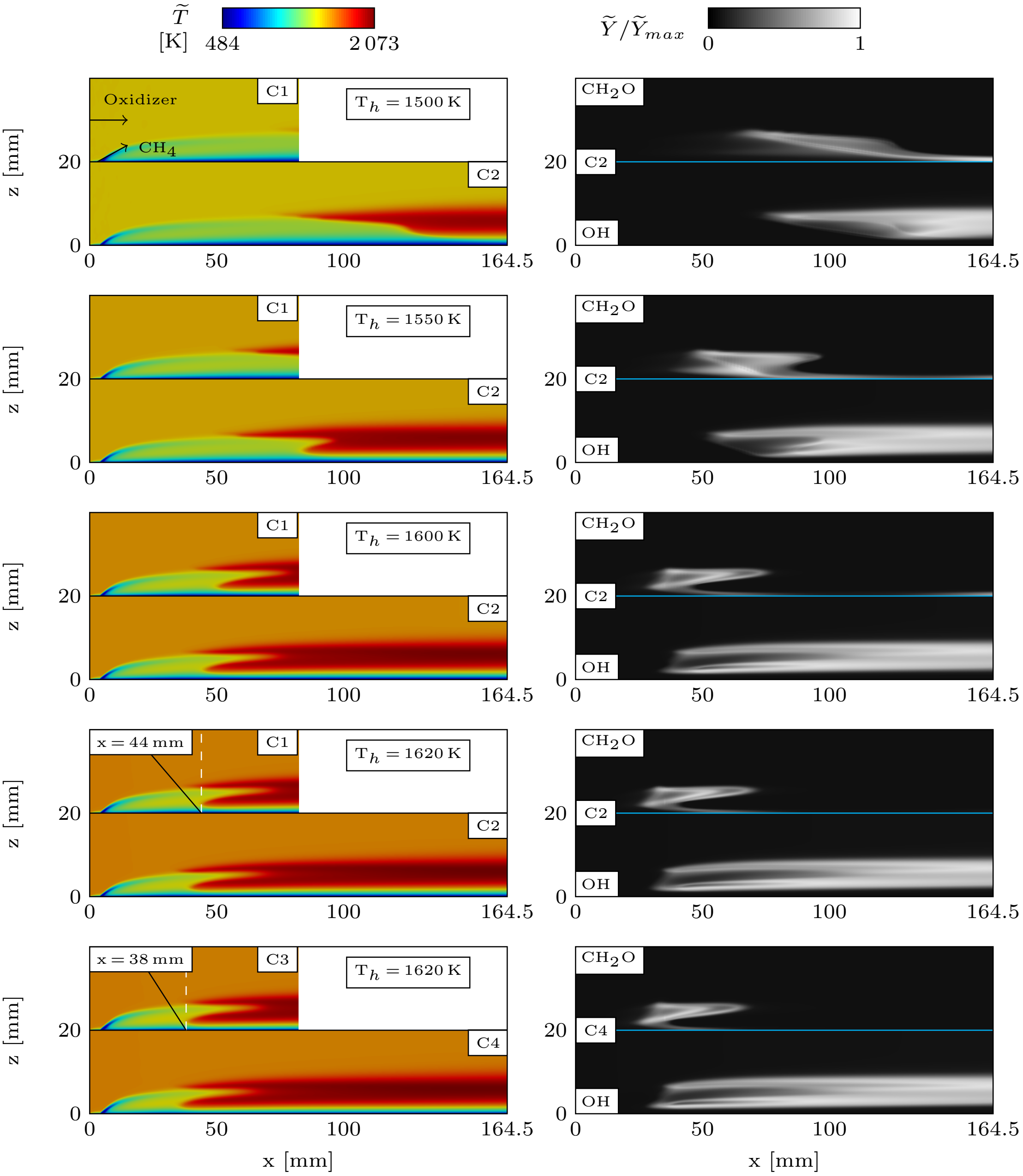

Figure 5.48.: T$_h$ = 1500, 1550, 1600, 1620 K [28]. Left column: axial cut of $\widetilde{T}$ for configurations C1-C4. Right column: line-of-sight integration of $\widetilde{CH_2O}$ and $\widetilde{OH}$ for configurations C2, C4

If artificial turbulence is provided at the hot inlet (configurations C3 and C4 on the bottom row), the flame tips shifts upstream of about 6 mm, with a stronger effect in C4 featuring the three injection nozzles. Although we see an effect of enhanced mixing created by the turbulent content, the autoignition point does not significantly move within the domain. In this configuration, the effect of chemistry appears to be stronger than turbulence. This is mainly due to the high momentum ratio (I = 10) featuring an increased jet penetration into the crossflow.

This flame structure was also observed from the post-processing images of the OH-PLIF acquisition, shown on the left side of Fig. 5.49 for a generic time t_i. An average over 300 snapshots provides the average flame position instead, as shown on the right side. OH-PLIF data acquisition and post-processing is reported in detail by Dalshad et al [68].

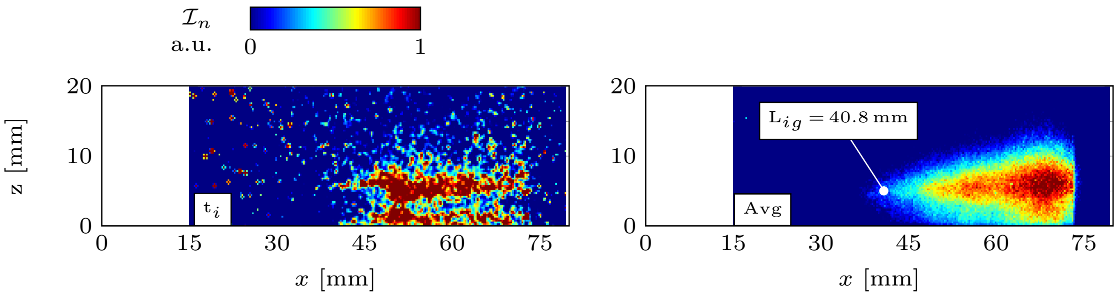

Figure 5.49.: Left: snapshot from OH-PLIF acquisition at time t_i. Right: average over 300 images [28]

To quantify the autoignition length in the CFD, one can integrate the OH concentrations over the line of sight. Since the meshes have a different depth, the OH field is sampled over 100 slices in direction y for C1 and 300 slices for C2. The integration of the obtained images is performed with a Python processing tool and normalized between 0 and 1. The same process is applied to the radical CH_2O for a further comparison of the CFD results only. The final images are shown on the right column of Fig. 5.48.

Compared to an axial cut through the CFD domain, the OH integration allows to detect the flame throughout its depth, as shown by the gray region between the two flame branches. This region also locates the pool of radicals building prior autoignition, identified by species CH_2O in the numerical simulations. It is clear to see in each image that the radical pool always initiates before the OH trace, where the temperature is still close to the fuel core temperature. The difference between the starting locations of the CH_2O and OH zones reduces by increasing T_h. This is because the chemistry is more reactive at higher temperatures, leading to a shortened induction zone. The integrated CH_2O detects the presence of the double flame, but also shows chemical activity at wall due to FWI.

Table 5.13.: Autoignition lengths of Fig. 5.50

	$L_{3\%OH}$ [mm]				$L_{10\%CH_2O}$ [mm]			
T_{hot} [K]	C1	C2	C3	C4	C1	C2	C3	C4
1500	-	73.7	-	-	-	54.5	-	-
1550	53.7	51.6	-	-	40.3	40.5	-	-
1600	36.3	34.1	-	-	28.7	27.8	-	-
1620	31.8	30.1	29.4	28.3	25.4	24.7	23.6	23.4

There are several criteria to determine the autoignition length in a CFD simulation, whose investigation on a 2D domain is left to Appendix A.1.3. Hereby two definitions are

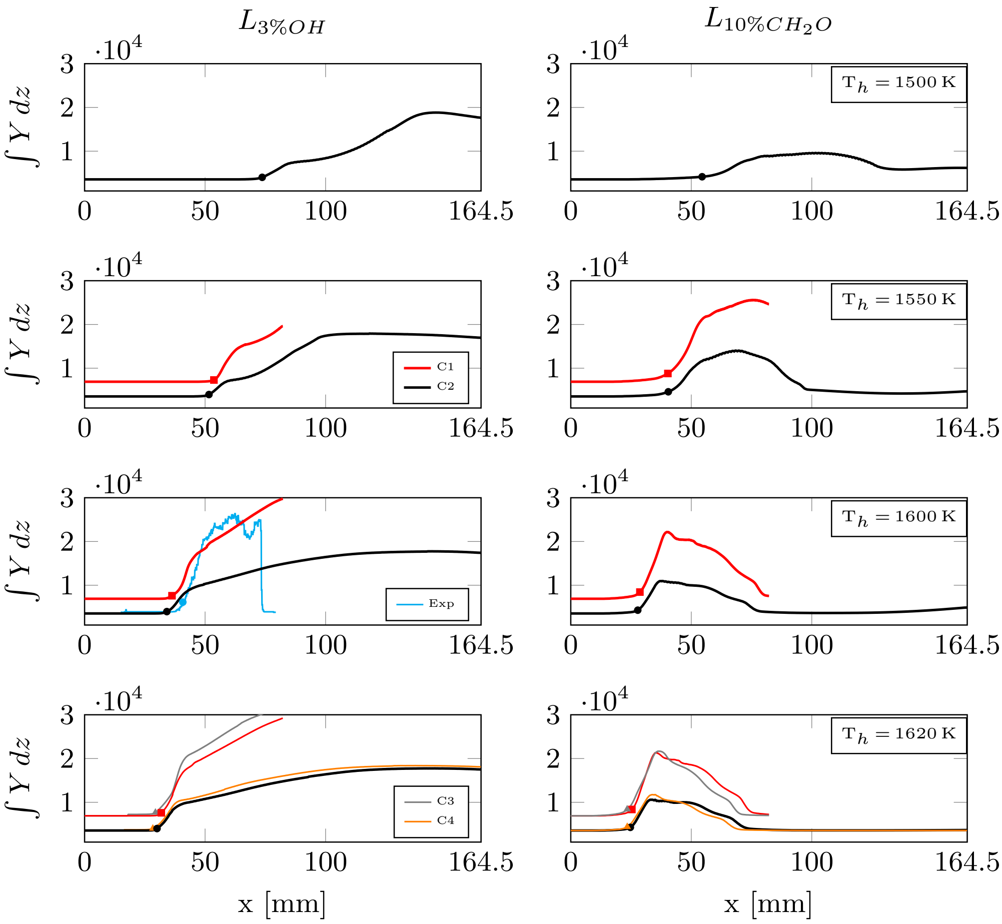

Figure 5.50.: z-integration of the OH and CH_2O pixel distributions from the black-white images of Fig. 5.48 [28]

chosen: an increase of 10 % of CH_2O in the radical pool and an increase of 3 % of OH. Only the latter can be compared with the experimental data. Before applying the criterion, the species distribution should be further integrated along the z-direction. Hereby the same method used by Dalshad et al [67] is used for consistency: the pixel intensities from the black/white images of Fig. 5.48 are added together along the z-axis, providing an unique distribution along x. The integrated quantities are labelled $\int Y\,dz$ in Fig. 5.50 and shown in red for C1 and in black for C2. On the left column the OH criterion is applied ($L_{3\%OH}$), on the right column the CH_2O one ($L_{10\%CH_2O}$). The correspondent autoignition points are marked by the symbols and reported in Table 5.13 in *mm*. When using CH_2O to detect autoignition, L_{ig} is shifted upstream compared to the OH criterion, the difference decreasing by increasing T_h. Looking at the table columns $L_{10\%CH_2O}$, a minimal difference is predicted between C1-C2, the difference becoming stronger when using $L_{3\%OH}$. When a turbulent content is provided at inlet, the ignition length is reduced by about 2 mm in the respective configurations (thus, from C1 to C3 and from C2 to C4). The integrated OH retrieved from the experimental image (Fig. 5.49 on the right) is shown by the cyan curve, giving an autoignition length of $L_{ig} = 40.8\,\text{mm}$. According to the table, the CFD simulations at $T_h = 1600\,K$ better match this value based on the OH criterion.

5.4.3. Wall heat flux

The position of the thermocouples at the wall is shown by the black dots on the bottom right of Fig. 5.51, together with the computational domains of C1 and C2 (in gray). The fuel injectors are reported for completeness. The reconstructed $\dot{q}_w$ from COMSOL [66] is interpolated at the wall patches of C1 and C2, in order to integrate on the same grid. An integration of the experimental and numerical $\dot{q}_w$ along the y-axis is necessary indeed. The integration is performed over 100 (200) equally distributed axial points x_i for mesh C1 (C2), between location $x_1 = 5.1$ mm and $x_2 = 82.3$ (164.5) mm. Note that x_1 is selected after the CH_4 injection slot. Fig. 5.51 summarizes the results for C1 (top left) and C2 (top right). The experimental curve shows a rather constant heat flux, with a peak achieved between 60 and 70 mm downstream. The peak detects the zone where ignition has triggered and combustion occurs at the wall proximity. The CFD simulations report smoother local peaks, whose location depends on the temperature of the hot gas.

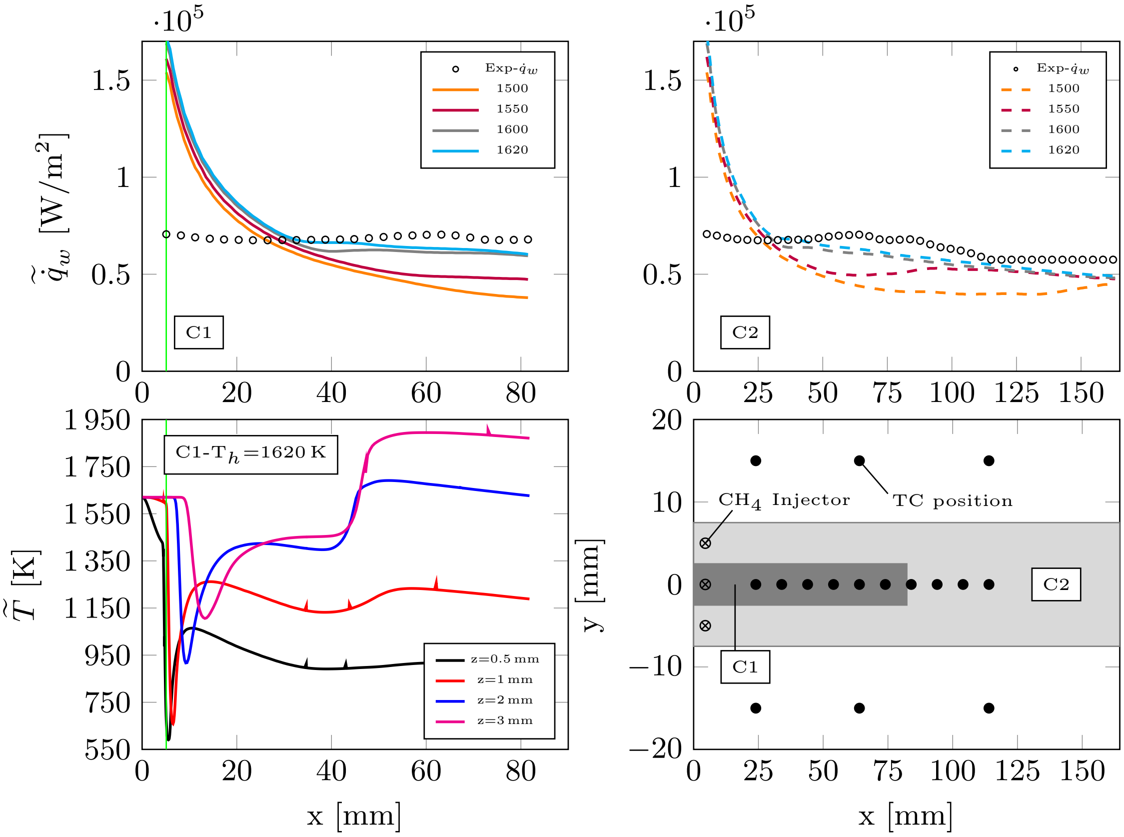

Figure 5.51.: Wall heat flux predictions for configurations C1-C2 [28]

The bottom left plot shows the thermal boundary layer developing at the center line, sampled 0.5, 1, 2 and 3 mm from the wall, for case C1 at $T_h = 1620$ K. The temperature evolution from 0.5 to 3 mm shows where the fuel core is located at the point of temperature drop. Right after the injector, a peak in wall heat flux is detected. This is effect however is not seen by the experimental data, because no thermocouple readings is available for $x < 25$ mm. As fuel and oxidizer mix, the effect of the cold flow at near the wall becomes evident and the $\dot{q}_w$ sinks. The temperature profiles detect the presence of the flame, with a steep increase located at x = 40 mm starting from z > 1 mm from the wall. This corresponds to a local maximum in $\dot{q}_w$. The minor local peaks are clearly identified for $T_h = 1500$ K and 1550 K in the second half of the domain (cfr. C2). For $T_h = 1600$ K and 1620 K instead the peaks are damped out. Overall, the inlet temperature that better approximates the wall heat flux is $T_h = 1620$ K.

The comparison of the wall heat fluxes for this experiment shows a double validation. Because the CFD simulations provide values close to the reconstructed $\dot{q}_w$, the method of Dalshad [66] as well as the FR-noTCI combustion model could both be validated.

5.4.4. Flame structure

A qualitative observation of the flame position in Fig. 5.48 shows that in C2 the flame is always shifted upstream a couple of centimetres compared to C1 (see for example $T_h = 1620$ K). This is also confirmed by the retrieved values of $L_{3\%OH}$. Three factors can influence this behaviour: the chemical mechanisms, the meshing and/or the interaction between jets.

The numerical BCs generate only minor turbulence in the chosen configuration and chemistry appears to be the driving mechanisms for autoignition. However, a 0D-reactor analysis shows that the Lu19 chemistry can correctly represent the autoignition times of Lu30 (cf. Fig. 7 in [30] based on the Sandia BC). As a consequence, the injector/injector interaction as well as the different meshing could be responsible for the slightly different ignition in C2. A cut section through the jet cores at z = 6 mm is shown for $T_h = 1550$ K in Fig. 5.52 and qualitatively confirms this observation. While the length of the central jet remains approximately the same when moving to the 3 injector configuration, a different core length is observed for the external jets. Overall the fuel jets seem to complete mixing with the crossflow earlier in the domain for the 3-injectors configuration.

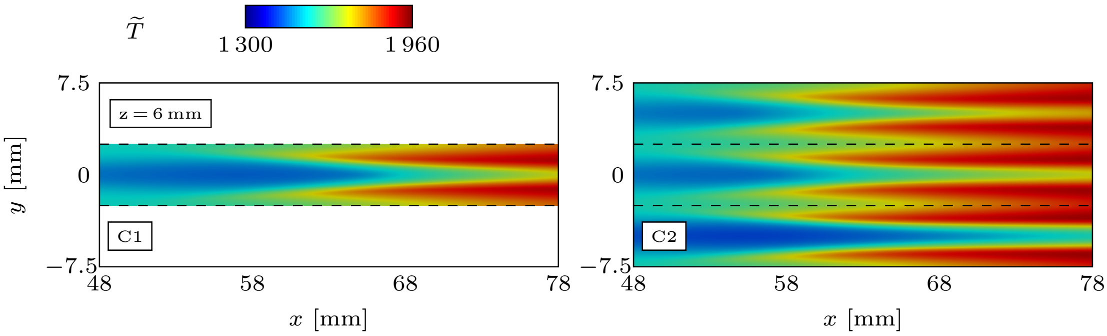

Figure 5.52.: Axial cut across the CH_4 jets at z = 6 mm for configurations C1 and C2 with $T_h = 1550$ K [28]

A better insight into the jet expansion for C1 is provided in Fig. 5.53, for sections x = 8, 28, 38, 48 and 58 mm. Similar observations apply to configuration C2. The temperature scale is the same as Fig. 5.48. For convenience, the case at $T_h = 1620$ K is shown. The scatter data provided in Fig. 5.54 are helpful to follow the discussion.

At x = 8 mm the thermal boundary layer at the wall is visible, mainly due to the hot gas cooled by the wall. Between point B and C, endothermic fuel-splitting reactions take place, where CH_4 is consumed into C_2H_x radicals (cf. $\dot{Q}$ in Fig. 5.54). Further downstream at x = 28 mm, the mixing between the jet and the cross flow has not yet completed (B-C). The production of CH_2O, the indicator of the radical pool prior ignition, increases between A and B. At x = 38 mm an ignited flame is seen between the fuel-rich core and the crossflow (B-C). CH_2O continues to form around the fuel-rich core, while OH is more localized at the hot spots (D) below the core (z ≈ 2 mm). At x = 48 mm two burning solutions are visible: the lower branch between the cooled crossflow gases and the fuel-rich core (A-B) and the upper branch between the fuel-rich core and the hot crossflow (B-C). This explains where the double flame tip originates. At x = 58 mm the temperature of the core further increases and the two flame branches become more visible at the cross-section, until they collapse into a single flame once full mixing is reached further downstream (not shown).

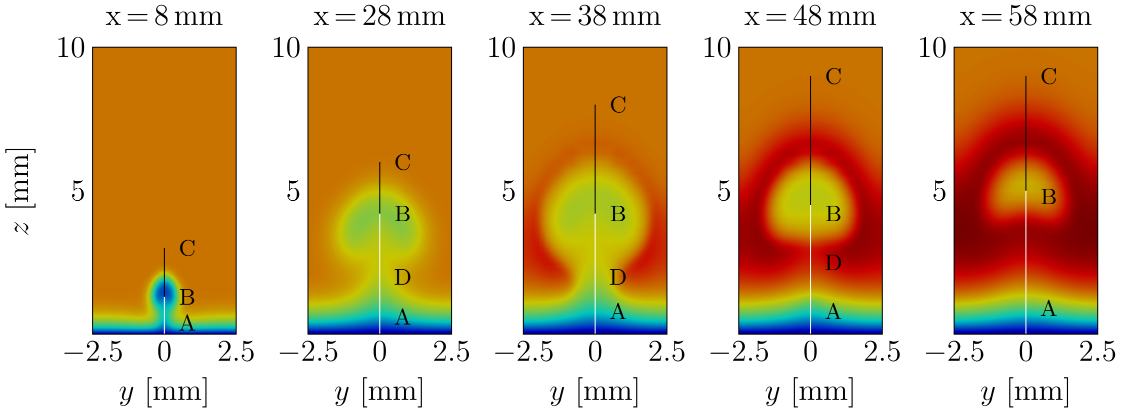

Figure 5.53.: C1: Mean $\widetilde{T}$ field for $T_h = 1620\,K$ at sections x = 8, 28, 38, 48, 58 mm

Additional information on the compositional space is obtained by the scatter data of Fig. 5.54. The chemical heat release $\dot{Q}$, the radicals OH, CH_2O and the temperature are reported for comparison and plotted against the mixture fraction f. In the temperature scatter plots the locations A-B-C identify the two flame branches discussed before. In x = 8 mm minor chemical activity is taking place: the production of CH_2O at the sides of the fuel-rich core at $f = 0.4$ (position B) together with CH_4-split reactions at the interface with the crossflow (position C). In A, the hot crossflow is cooled down by the wall. The scatter plots also show a minimal concentration of OH in the crossflow: this is a residual of the previous combustion inside the burner and does not indicate any ignition inside the investigated domain yet. At x = 28 mm a perfect mixing line is visible from the T scatter data between B and C, with a maximum fuel-rich composition of $f = 0.1$. The fuel jet expands further upwards in the domain (z ≈ 5 mm) and an entrainment of hot oxidizer is forced between the fuel-rich jet and the cold gases at wall. This entrainment is marked as D in Fig. 5.53. In D, the radical pool is forming and it is characterized by a stronger production of CH_2O while the temperature remains almost constant and close to the crossflow temperature. The reason for this entrainment is the presence of vortical structures in the fuel jet. This phenomenon is illustrated for clarity in Fig. 5.55, where the slices normal to the crossflow show the temperature field, while the two counter-rotating jets are coloured by the transversal velocity $\widetilde{U}_y$, to highlight the directions of rotation. It is clear to see that the vortical motions transport hot gases from the top to the bottom of the jets, creating the recirculation zone in D.
At x = 38 mm two ignited profiles are visible for T: one reaching higher temperatures and localized close to the entrainment D, the other localized between B and C. The value of

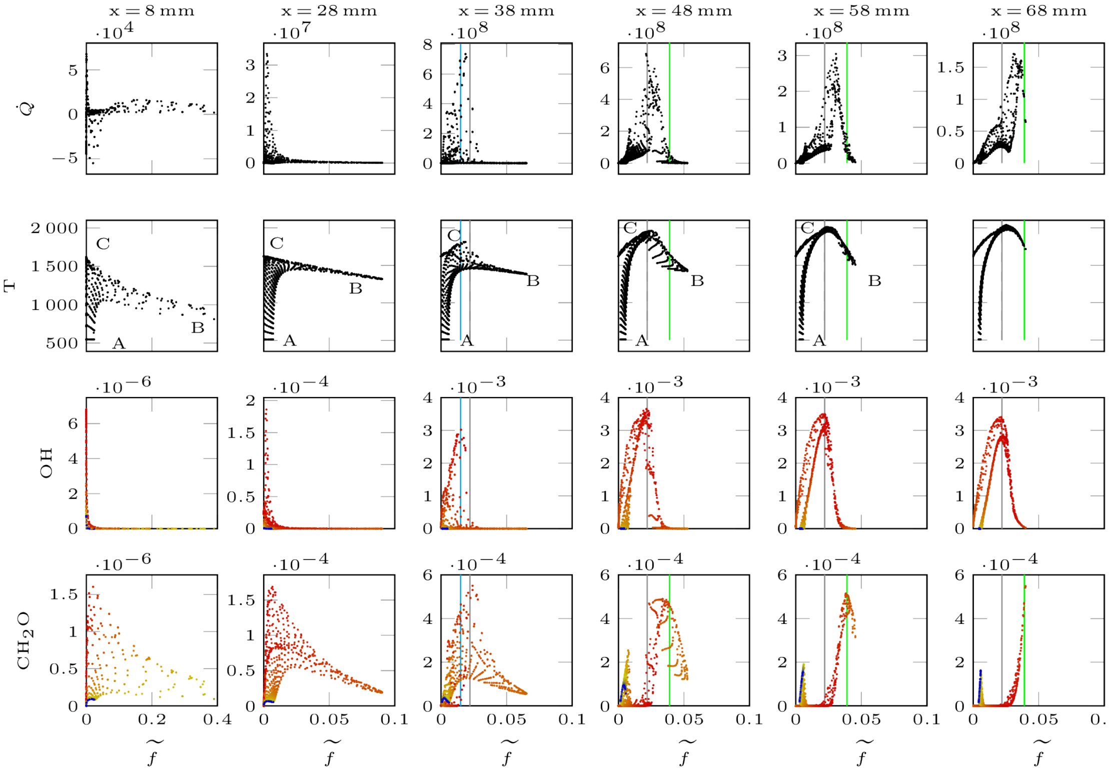

Figure 5.54.: C1: Scatter data for heat release $\dot{Q}$, temperature and radicals OH, CH_2O at sections x = 8, 28, 38, 48, 58 and 68 mm. OH and CH_2O plots coloured by temperature to localize the wall

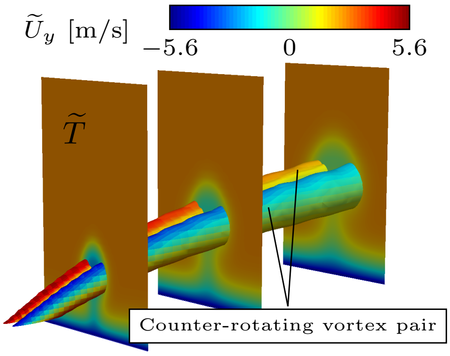

Figure 5.55.: Counter-rotating vortex structure of the cold jet [28]

$Y_{CH2O,max}$ is localized at the sides of the fuel-rich core, while $Y_{OH,max}$ occurs in zone D, right after the CH_2O reaction ring has completed. This explains the shift of the two peaks seen in the f space, the first one located at $f_{CH2O,max} \sim 0.023$ (gray line), the second one at $f_{OH,max} \sim 0.015$ (cyan line). Moving to x = 48 mm the two stable flames are visible both in the temperature and in the OH scatter clouds. The crossflow entrainment in D is not yet closed beneath the jet core, leading to a heat up of the colder fuel-rich states as seen in the temperature plot between B and C. One important thing to notice is that both OH peaks moved to the right at $f = 0.023$, which is approximately the location where the temperature peaks of both branches are located. This configuration is therefore characterized by $f_{st} = 0.023$. The $Y_{CH2O,max}$ has shifted rightwards to $f = 0.039$ (green line). A secondary CH_2O peak is located close to the wall (f approaching 0) moving from B to A: intermediate species like CH_2, CH_3O and H_2O_2 are detected at the wall proximity. This situation is rather uncommon near cooled walls, since the enthalpy losses would promote recombination reactions instead of endothermic reactions. This could mean that a secondary radical pool starts to build at this location, but the induction time is not reached due to the cooled wall which reduces the rate of reactions. The recirculation zone in D slowly vanishes when moving to locations x = 58-68 mm leading to the two fully burned profiles corresponding to counterflow diffusion flame solutions.

5.4.5. Tabulated chemistry

Simulation C5 based on REDIM tabulated chemistry was selected to assess if the REDIM is capable of capturing the autoignition phenomenon. A quantitative comparison with the experiment is not presented hereby. In fact, the investigated REDIM should include enthalpy losses to account for the cooled walls. Because the tabulated chemistry is not subjected to FWI, the location of autoignition point is also shifted upstream compared to the experiment.

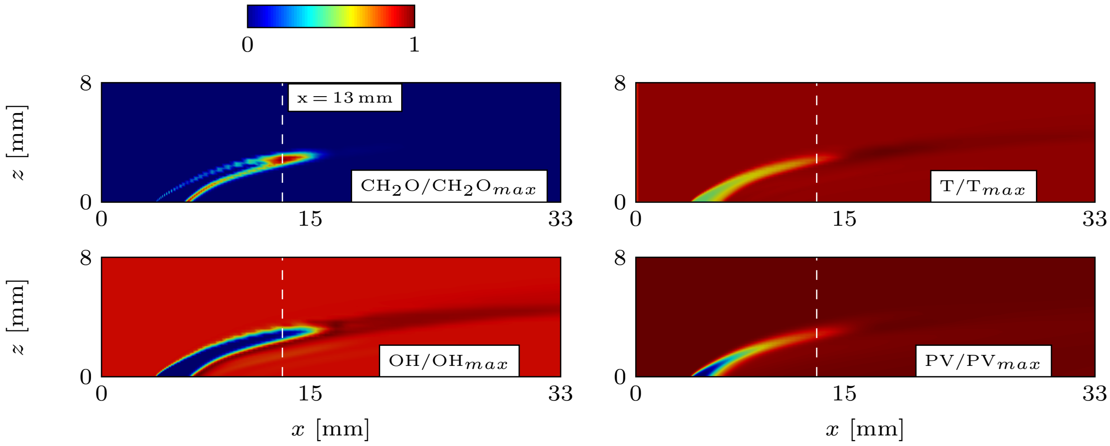

Figure 5.56.: Simulation C5 from Table 5.12 using REDIM

Fig. 5.56 shows an axial cut of the first 33 mm downstream the hot inlet, for the fields CH_2O, OH, T and PV normalized on their maximum value. When looking at T, one can see that the thermal boundary layer at the cooled wall is missing, for the reason explained before. A maximum of 1976 K is seen from x = 15 mm. The OH trace also shows a peak in correspondence of the maximum T, while the CH_2O peak is located 2 mm upstream at x = 13 mm (white dashed line). This means that the REDIM could correctly describe the generation of the radical pool prior to the autoignition point, as already observed in Fig. 5.48 for the finite rate chemistry. When looking at CH_2O and OH, a burning solution is detected on the bottom side of the core jet, typical of a flamelet database (all mixed is burned). A more accurate choice of PV could improve the predictions on this region, as well as the inclusion of multiple χ tables in proximity of the fuel inlet nozzles.

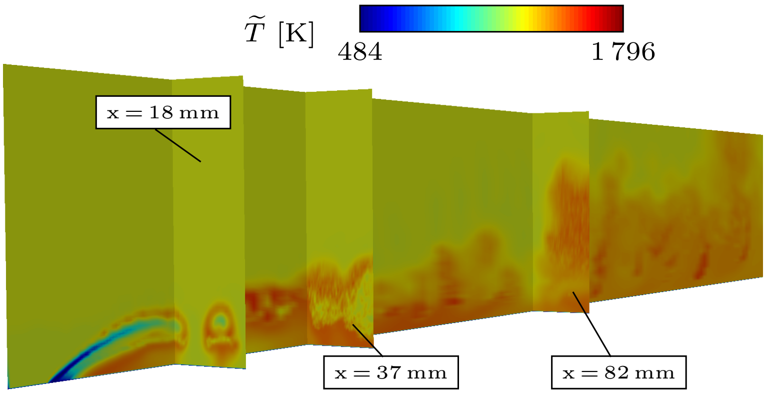

Figure 5.57.: Simulation C6 from Table 5.12 using NA flamelets

Setup C6 of Table 5.12 aims to show that although the non-adiabatic flamelet method described in Section 3.5.2 can account for enthalpy losses, it is not suitable to predict the flame autoignition length. This is expected from the flamelet theory [221], where the chemistry time scales are assumed faster than the flow time scales. The assumption does not hold when a pool of reactants is forming, during the autoignition process. Fig. 5.57 shows several cuts coloured by the instantaneous $\widetilde{T}$ for C6. An attached flame is observed directly after the fuel nozzles: below the nozzle due to FWI, above the nozzle due to the instantaneous mixing of the reactants. About 37 mm downstream, the fuel jets have almost completely mixed and reacted with the hot flow and a turbulent burning flame exists in the domain. This is likely due to the β-PDF model, since the finite rate simulations without TCI (C3, C4) do not report such a turbulent flow. Moreover, no burning solution was observed in the same domain for $T_h = 1430\,K$, when using finite rate chemistry. To correctly model the autoignition problem, the NA-Flamelets-β-PDF model should at least include a reaction progress variable as additional parameter to track the radical pool.

Although both databases could provide a reduced computational cost, they need to be extended to include at least one additional table parameter, before they can be capable to correctly predict this test case. As a consequence, finite rate chemistry simulations remained the preferred option for the first investigation of this case.

6. Conclusions

This work investigated several combustion models for LES of CH_4/air and CH_4/O_2 flames. The main target was reducing the computational cost, while maintaining a good accuracy compared to the available experimental data. All implementations and validations were performed using the software OpenFOAM. A wide spectrum of challenges was encountered in the modelling.

The solution of the stiff system of equations deriving from a detailed chemistry mechanism was avoided by means of tabulated chemistry tables. In particular, approaches based on low dimensional manifolds (ILDM and REDIM) and the flamelet theory (FPV, non-adiabatic flamelets) were considered. Because the sub-grid scales are filtered out by the LES approach, the importance of TCI was also investigated. Two transported PDF methods were selected for comparison on finite rate and tabulated chemistry computations: the Eulerian approach based on the stochastic fields and the MMC model representing a Lagrangian particle approach. Absence of TCI modelling (no-TCI) was also considered as a valid alternative to the expensive computations featuring a transported PDF. The reference test cases used for the investigation of the manifold-based tabulated chemistry and the TCI were the Sandia flames D to F featuring partially-premixed homogeneous inlets.

Strong ignition/re-ignition effects expected for Sandia flame F could not be improved by the finite rate ESF model. The micro-mixing contribution of the ESF equations was minimal compared to the stochastic term. As a matter of fact, a laminar chemistry computation (no-TCI) provided good results already, with a computational speed-up of factor 4.63 compared to a standard ESF solver with 8 fields. The necessary criterion to neglect the ESF model was identified in the LES grid requirement proposed by Pope, provided that the simulation does not involve strongly under-resolved premixed flames as they typically occur in the simulation of high-pressure combustion.

Another method to speed-up the computation was coupling the ESF with tabulated chemistry. A preliminary comparison based on ILDM, FPV and REDIM databases identified the REDIM as the best candidate to describe the thermo-chemical states. ILDM lacked in representing the diffusion process, the FPV the extinction/re-ignition events. While a 2D-REDIM based on a constant parametrization matrix was sufficient to describe flames D and E, a third variable was required for flame F. A significant improvement in the predictions of H_2 and CO was observed when including differential diffusion in the REDIM. A 2D-REDIM with differential diffusion provided better results than a 3D-REDIM with simplified transport, when simulating flame F. The ESF-REDIM solver based on 8 fields was found to be about 30% faster than a laminar flame computation (no-TCI), the gap increasing by reducing the number of transported fields.

Although the ESF-REDIM solver improved the predictions of finite rate chemistry ESF, too much extinction was foreseen upstream. A finite rate simulation of flames D-E based on MMC instead of ESF showed an excellent match with the experimental means and fluctuations, due to the more accurate mixing model. The MMC computation was found to

be about 15 % faster than the laminar case (no-TCI), outperforming ESF in both accuracy and speed-up. A MMC-REDIM solver was implemented for comparison with ESF-REDIM, obtaining a good agreement between the results. The bottleneck of both MMC solvers however was not identified in the chemistry module, but with the particle module and the density feedback, so that the use of tabulated chemistry was not particularly advantageous in this configuration.
The partially premixed flame FJ200-5GP-Lr75-57 featuring inhomogeneous inlets was retained for final validation of the ESF-REDIM solver, as it is more challenging. A 2D-REDIM could already represent the flame with a good agreement to the experimental data and previous finite rate ESF simulations. However, the scatter plots were quite different from the experiment for small x/D, thus in the premixed region.

The second part of the investigation was focused on the wall heat flux prediction and the correct modelling of FWI. The single-injector combustion chamber with gaseous CH_4/O_2 propellants at moderate pressure developed at TUM was selected as validation case for non-adiabatic flamelet databases. TCI was based on a presumed β-PDF here. Wall treatment in LES was investigated in terms of hybrid LES/RANS (i.e. IDDES) and wall-modelled LES.

Non-adiabatic flamelet databases could correctly predict the wall heat fluxes, provided that the enthalpy losses in the flamelets were based on a physical process (like the permeable wall assumption). Although known to have a strong dependence on the wall-parallel grid, the IDDES model provided good predictions on all investigated meshes. Because of the higher sub-scale turbulent content provided by IDDES on coarser meshes, higher fluctuations in mixture fraction were seen to cause an overprediction of the wall heat flux downstream in the chamber.

The investigation of the same chamber with film cooling confirmed the validity of the IDDES/non-adiabatic flamelet solver. Overall, the wall heat flux slightly increased compared to the previous configuration, due to the flame pushing closer to the lateral walls. The cooling efficiency reduced already to 25% within the first quarter of the chamber. Three new reduced chemical mechanisms (*hprb*, *mprb*, *lprb*), targeted for methane combustion at moderate pressure, could be validated on this test case. Based on the CPU time required by a finite rate chemistry computation and the accuracy delivered, *hprb* was identified as best candidate for such applications.

A comparison of IDDES with wall-modelled LES showed that a conventional law of the wall (from Spalding in this work) was sufficient to correctly capture the wall heat fluxes, at a reduced computational cost compared to IDDES, although for $y^+ > 4$ the assumption of $\dot{q} \approx \lambda(T_1 - T_w)$ is not correct. The coupled velocity/temperature law of Cabrit, implemented in OpenFOAM, provided similar results.

A final configuration featuring autoignition of CH_4 in a hot crossflow of combustion products was investigated, with secondary reactions occurring close to a cooled wall. The dependency of the autoignition length on the hot flow inlet temperature was investigated without turbulent content, using laminar chemistry. The ignition points were compared with the available experimental data based on OH-PLIF, showing a good agreement for higher inlet temperatures. Ignition based on the radical CH_2O instead occurred earlier in the domain. The choice of the chemical mechanism did not influence the autoignition length, the midstream turbulence and the injector/injector interaction showed a minor influence.

The wall heat flux was qualitatively captured by all simulations, but not the peak caused by secondary reactions. Using the non-adiabatic flamelet database for this case resulted in a wrong prediction of the flame structure, immediately igniting after the fuel inlet. Additionally, too much turbulence was predicted by the β-PDF. Using a REDIM database instead did not allow to estimate the wall heat flux, because the manifold did not include enthalpy losses. However, the REDIM showed potential to predict autoignition delays.

Summary: The computational cost of finite rate calculations could be saved by neglecting the TCI model for the investigated non-premixed, partially-premixed and autoignition flame configurations, provided that the computational grid satisfied the LES requirements. When using TCI, the REDIM reduced chemistry was capable to significantly reduce the computational cost and to correctly predict strong extinction/re-ignition events in non-premixed flames, if differential diffusion and/or a third reaction progress variable was added to the table. A 2D-REDIM table was already sufficient to describe the global behaviour of partially-premixed regimes and flames subjected to low and moderate extinction degrees with satisfactory accuracy. Although the REDIM did not account for FWI in this work, it showed potential to capture autoignition delays. On the contrary, non-adiabatic flamelet databases showed satisfactory wall heat flux predictions, but could not predict non-equilibrium phenomena like autoignition.

6.1. Outlook

The potential for major improvements has been identified while summarizing the results, which justifies the need for future investigations:

- The validation of laminar chemistry (no-TCI) for LES should be extended to more complex flames and to the premixed regime, to generalize this assumption. The identification of a more detailed criterion rather than the one based on the LES mesh would be advantageous. Alternatively to no-TCI, it shall be further investigated if the use of the MMC model is advantageous also for more complex flames and mechanisms. In both cases, one could seek to further optimize the chemistry integration using accelerated chemistry routines. The range of applicability of the ESF-REDIM and MMC-REDIM solvers should be also extended to more complex flames and chemistries.
- Several improvements are suggested for the REDIM tabulated chemistry:
    - Although computationally cheap, the use of a constant parametrization matrix $\mathbf{C}$ to project the off-manifold thermochemical states onto the REDIM surface showed some deficiencies when coupled with MMC. A more accurate projection strategy shall be investigated for REDIM, following the work of Yu et al [323] for RANS-TPDF, although the disadvantage of increasing the computational cost is tangible.
    - In wall-free flame configurations subjected to strong extinction regimes, a 4-dimensional REDIM including a second reaction progress variable (PV) shall be investigated, to improve the predictions of species CO.
    - It would be advantageous to extend the REDIM theory to describe flame SWQ and HOQ for non-premixed configurations, following the work initiated by Strassacker et al [284] for premixed regimes. The validation should cover not only

  atmospheric conditions, but also moderate pressures. This would allow a direct comparison with the non-adiabatic flamelet approach used in this work for the single-injector CH_4/O_2 combustion chamber.

  - Together with the inclusion of enthalpy losses, autoignition modelling shall be further validated for REDIM. This would allow to extend the REDIM capability of predicting autoignition phenomena and the wall heat loads in configurations featuring secondary reactions near the wall.

- Further models for wall-bounded LES applications like the single-injector CH_4/O_2 combustion chamber shall be investigated. For example, the approach of local embedded grids to solve the boundary layer via RANS, proposed by Kawai and Larsson [145], showed very good results in the modified formulation of Muto et al [207, 205], when applied to sub-scale rocket combustion chambers with H_2/O_2 and CH_4/O_2.

- The test case of Dalshad et al [68] featuring secondary reactions was validated here only for CH_4 as a fuel and for a moderate momentum ratio. The CFD investigation should be extended to cover the range of momentum ratios provided by the experiment, to further validate the implemented numerical models. Moreover, the experiment also provides data for injection of H_2 and C_3H_8 (propane). The more complex chemistry of propane would surely challenge the models developed for this work.

Appendix

A. Appendix A

A.1. Preliminary assessment on 2D flame configurations

In a preliminary step, 2D configurations are investigated first for ILDM, REDIM and flamelet-based tables using the setups of Table A.1. A third configuration is investigated for the autoignition problem of Dalshad [68] using finite rate chemistry. In particularly, the following questions are addressed:

1. Interesting for this work is the performance of ILDM for non-premixed regimes. How well does a 3D-ILDM perform in a laminar diffusion flame calculation, compared to a flamelet method?
2. When introducing the REDIM in Section 3.4 it was stated that this manifold is less dependent on the choice of the progress variable in laminar regimes [282], compared to a FPV manifold. How is this difference visible when computing a 2D-bunsen flame?
3. The literature shows numerous criteria to locate the autoignition length in CFD simulations. How do such criteria behave in a 2D simulation representative of the autoignition problem of Dalshad's experiment? Which one shall be considered for the turbulent case?

Table A.1.: 2D-flame configurations

Configuration	Table	Parameters	Grid	Size [MB]
Laminar diffusion flame	Flamelet	χ_{st}, f''^2, f	8x10x202^a	4.4
	ILDM	CO_2, H_2O, f	90x90x170^b	476
Bunsen flame	FPV	PV_n, f''^2, f	501x10x501^a	594.8
	ILDM	CO_2, H_2O, f	50x50x150^b	133.5
	REDIM	PV	100^a	0.6

[a] uniform equidistant grid

[b] non-uniform grid with expansion ratio $\delta_r = \{0.8, 0.8, 1.08\}$

A.1.1. ILDM for non-premixed laminar diffusion flames

A preliminary evaluation of the ILDM database is performed for a laminar diffusion flame parallel to an adiabatic wall and compared to a classical flamelet approach. The same geometry presented in [31] for CH_4/O_2 flames is used. A CH_4 inflow at 300 K enters the domain parallel to an adiabatic wall and a hot air inflow at 1800 K (see left side of Fig. A.1). Such boundary conditions are similar to the ones encountered in the Sandia flames [10] and in the experiment of Dalshad [68]. The Smooke mechanism was used in the finite rate

simulation and to generate the manifolds. The ILDM generated in this work requires a refinement around f_{st}, resulting in a non-uniform interpolation grid [82]. This results in a higher storage size and a slower interpolation call at run-time, compared to the flamelet database [29] (cf. Table A.1). In the framework of this investigation, it was attempted to replace the ILDM table interpolation routine with a trained Deep Neural Network (DNN), which showed about 98 % reduced memory footprint (cfr.[116] for a comparison DNN/FPV tables). In the CPU-based implementation for OpenFOAM however, the use of DNNs did not lead to a reduction of the computational time, due to the complex neural networks required to describe the chemistry database [295, 34].
Fig. A.1 shows the temperature field for the ILDM calculation on the left, the white line localizing the stoichiometric mixture. The evolution of the major species at wall are reported on the right. Both flamelets and ILDM underpredict H_2O and CO_2 across the domain compared to the finite rate simulation. The steepness of the CO production strongly depends on the database assumption, with both flamelet and ILDM diverging from the finite rate solution. The ILDM presents a spike in the CO profile at x = 0.05 m. This is associated with the discontinuity in the low temperature domain discussed for Fig. 3.4. The ILDM however performs fairly well for non-premixed configurations, compared to the previous investigation on free flames and 2D-Bunsen flames [29].

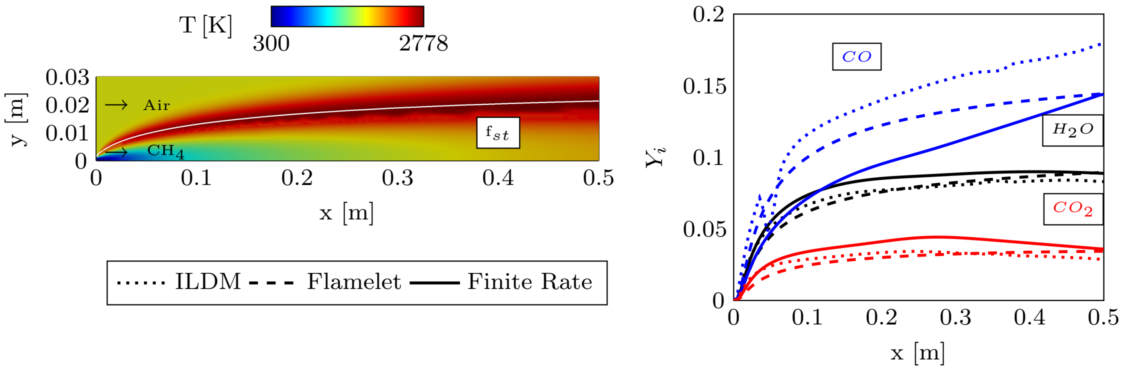

Figure A.1.: CH_4/air diffusion flame parallel to an adiabatic wall. Left: T field for ILDM computation. Right: Major species composition at wall for Finite Rate, Flamelet and ILDM computations

A.1.2. REDIM sensitivity to PV

The flame length and flame speed of premixed flame configurations calculated with ILDM or flamelet databases are seen to vary strongly in the literature, depending on the choice of the progress variable (cfr. [111]). CH_4/air 2D-Bunsen flames at $\phi = 0.8$, $T_u = 400$ K were investigated using the REDIM tabulation to extend the comparison. Although the REDIM was generated from the full GRI-3.0 mechanisms, only the 16 species from Smooke are retrieved, for a comparison with ILDM and FPV. The second block of Table A.1 summarizes the manifold topologies. The CFD domain is taken from a previous work [29]. Fig. A.2 summarizes the results. A finite rate chemistry simulation with unity Lewis numbers serves as reference case and it is reported on the bottom half of Fig. A.2a-A.2f. Fig. A.2a shows that the ILDM cannot represent the flame thickness correctly, the flame being at least 1 mm shorter than the reference case. This means that the fuel is consumed faster, thus the laminar

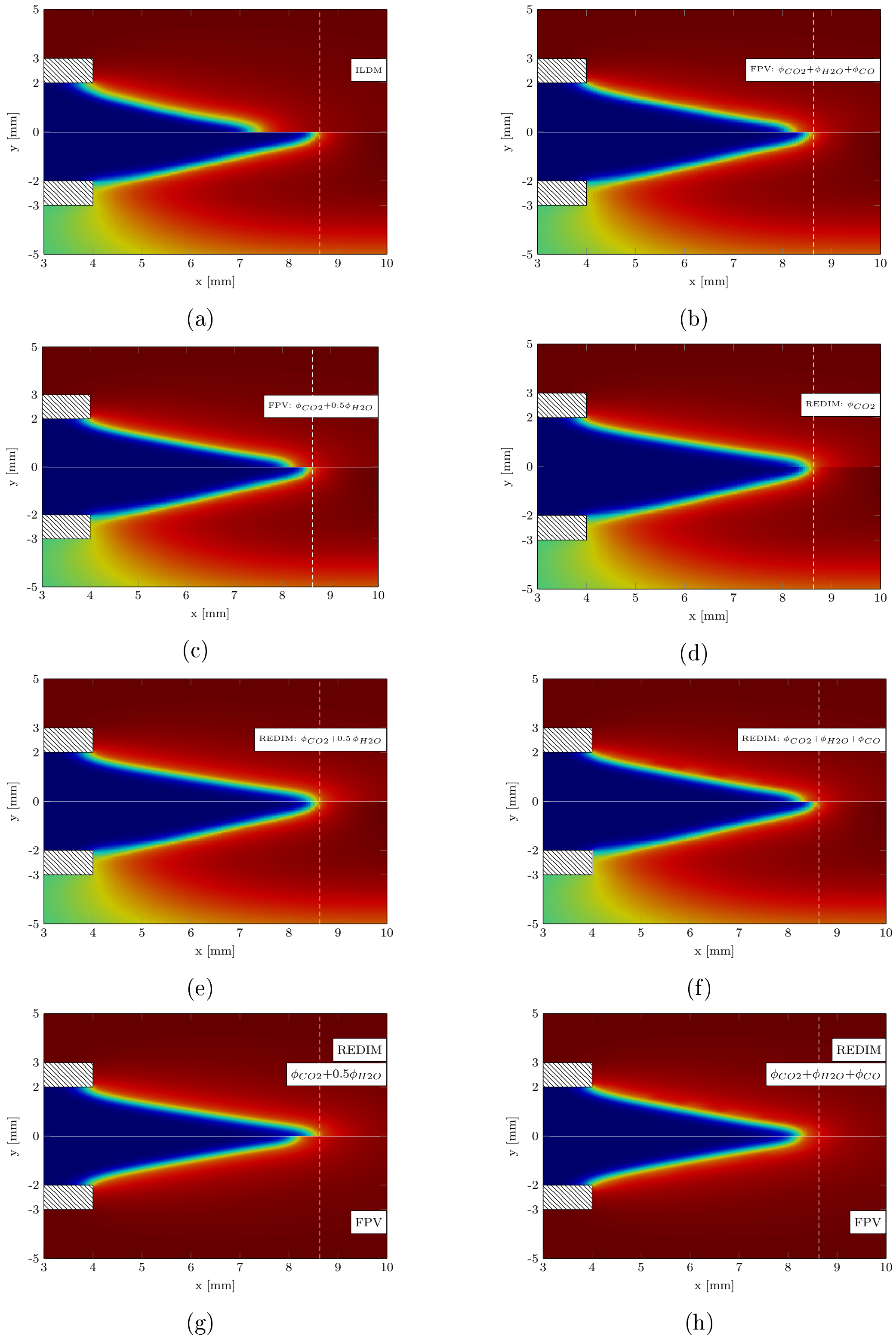

(a) (b)

(c) (d)

(e) (f)

(g) (h)

Figure A.2.: CH_4/air 2D-Bunsen flames at $\phi = 0.8$, $T_u = 400\,K$. Comparison between finite rate chemistry, FPV, REDIM and ILDM with different progress variables flame speed is higher. Literature works report that the laminar flame speed can be correctly recovered if an extra reactive progress variable is included into the ILDM. In the view of a 3D turbulent test case, increasing the table dimensions is definitely a disadvantage in terms of memory footprint and computational time. Fig.A.2b-A.2c show the same flame calculated with two FPV tables, using respectively $PV = \phi_{CO2} + 0.5\phi_{H2O}$ (suggested by Yu and Maas [324]) and $PV = \phi_{CO2} + \phi_{CO} + \phi_{H2O}$. The flame height estimation definitely improves because the manifold was built for a reaction-diffusion space, but it is still underestimated. The REDIM calculations presented in Fig.A.2d-A.2f show instead a perfect match in flame height with the reference case, when using $PV = \phi_{CO2}$ and $PV = \phi_{CO2} + 0.5\phi_{H2O}$. Interestingly, only the use of $PV = \phi_{CO2} + \phi_{CO} + \phi_{H2O}$ generates a shorter flame, as previously observed for FPV, meaning that $\phi_{CO2} + \phi_{CO} + \phi_{H2O}$ might not correctly describe the slow chemistry space. The REDIM and FPV are finally compared in Fig.A.2g-A.2h. One can finally state that the REDIM is not strongly influenced by the choice of the progress variable like the FPV is, but definitely the use of $\phi_{CO2} + 0.5\phi_{H2O}$ would lead to a better prediction of the flame structure. A second interesting observation is that in all tabulated chemistry simulations the flame curvature is stronger at the inlet tip, being anchored at the inner inlet wall instead of at the posttip as shown by the reference case.

A.1.3. Autoignition delay

A first numerical test to evaluate several autoignition criteria was run on a 2D domain with a laminar solver (no TCI) and the Lu13 chemistry. The computational mesh is shown in Fig. A.3, coloured by the temperature field, with a contraction factor of 0.5 applied along the x axis for the sake of clarity. Pure CH_4 at 373.15 K is injected through a 0.6 mm slot parallel to an isothermal wall at 800 K. The fuel interacts with the wall on one side and with the hot-gas co-flow on the other, having inlet temperature of 1611 K. The hot gas composition corresponds to $Y_{O2} = 0.0844287$, $Y_{OH} = 0.000139473$, $Y_{H2O} = 0.0790079$, $Y_{CO2} = 0.0972894$ and $Y_{N2} = 0.739134$. The inflow velocities are respectively 110 m/s for CH_4 and 25 m/s for the hot gases. The maximum flame temperature is located in the region of x = 100 m, as shown in the plot.

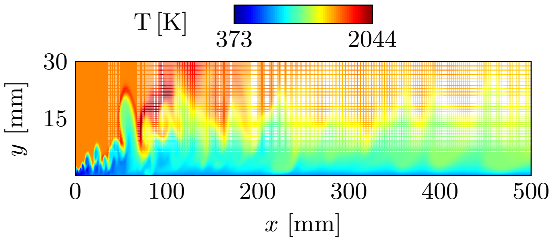

Figure A.3.: Autoignition test case: 2D computational mesh with temperature contour

In order to qualitatively estimate the autoignition length of the flame, the fields of interest were first averaged. Fig. A.4 shows six possible criteria to visually assess the autoignition length, which are respectively:

1. $\max ||\nabla(\widetilde{Y}_{CH2O})||$, where CH_2O represents the radical pool. This was seen to give a similar result to a 10 % increase in $\widetilde{Y}_{CH2O}$
2. 3-10% increase of heat of reaction $\dot{q}$

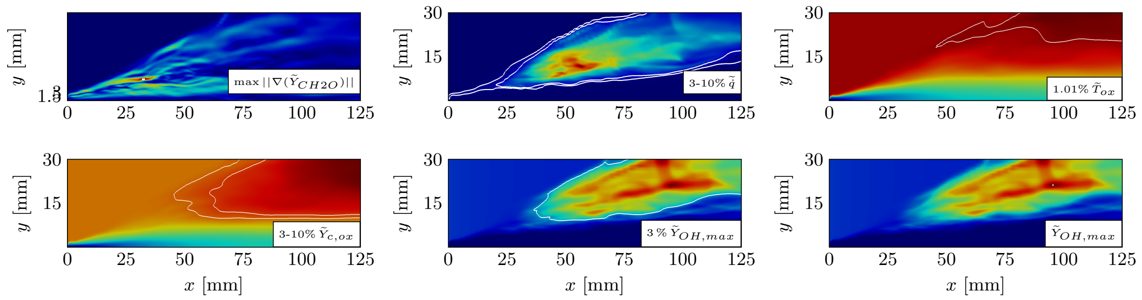

Figure A.4.: Qualitative evaluation of the autoignition length based on 6 criteria

3. 1.01% temperature increase based on the oxidizer inlet flow (therefore from 1611 to 1627.11 K)
4. 3-10% increase of progress variable Y_c=Y_{CO2}+Y_{CO}+Y_{CH2O}, starting from the value at the oxidizer inlet
5. 3 % increase of $\widetilde{Y}_{OH}$
6. mean autoignition length estimated at $\widetilde{Y}_{OH,max}$

Except from the location determined by 10 %$Y_{c,ox}$ and OH_{max}, the autoignition length seems to be located within 25 mm and 50 mm downstream. The location can be estimated more accurately if one integrates the fields over the y axis. Selected values of L_{ign} are listed in Table A.2. The selected mean fields were sampled on 250 point along the axis x, at N locations between $y = 0$ and $y = 30$ mm. The number of axial samples N was varied as 5, 10, 20 and 40, to ensure convergence of the integration routine. For each axial point x_i, the selected CFD field was integrated over the N points along the y axis using the Simpson rule. At least 20 sample lines were found necessary to guarantee convergence. The final results are shown in Fig. A.5. The top left plot shows the integrated Y_c and the autoignition length (in red) evaluated at 10 % of the interval between the local minimum and the maximum (in gray). The progress variable drops close to the injector since fresh methane is injected and $Y_c = 0$ where $CH_4 = 1$. Between the fuel and the oxidizer jet, the radical pool is activated, consuming CO_2 and H_2O in favour of CH_2O and CO (top right plot). It is easy to apply the autoignition criteria for CH_2O, since the profile increases monotonously until the peak is reached (middle left). The criteria for OH was applied from the local minimum (middle right). The bottom plots show the criterion on $\dot{q}$ and the wall heat flux prediction at wall for this configuration. From the plots one can infer that the determination of the autoignition length from the Y_{CH2O} or the $\dot{q}$ profiles is easier, since they are monotonous where the autoignition is expected and they lead to a similar prediction. The OH criterion is chosen for the 3D configuration to be compared with the experimental data of Dalshad, where OH-PLIF images are available. The criterion on CH_2O is additionally selected for a qualitative comparison.

Table A.2.: Estimated autoignition lengths

Criteria	L$_{ign}$ [mm]
10% $\int Y_{c,max}$	54.5
10% $\int Y_{CH2O,max}$	23
3% $\int Y_{OH,max}$	32.5

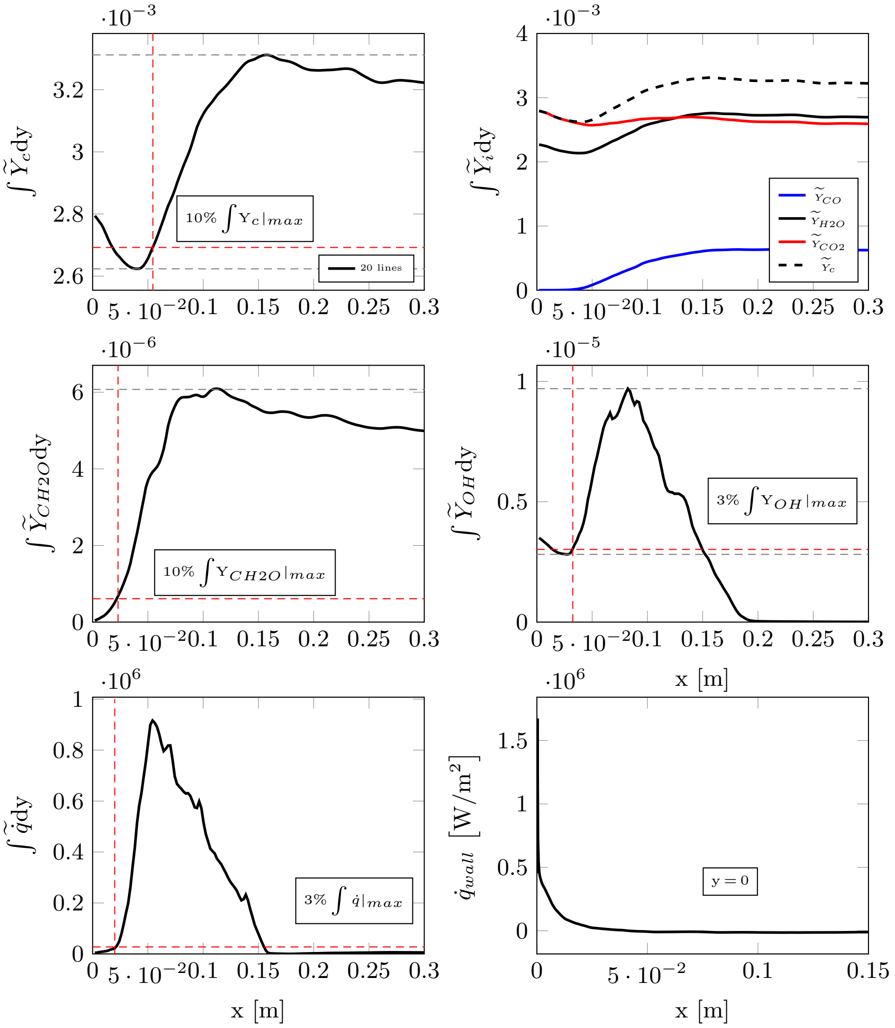

Figure A.5.: Axial distribution of mean fields, integrated over 20 lines in y

B. Appendix B

B.1. Investigated chemistry-TCI configurations

A complete list of the chemistry databases investigated in this work and their TCI coupling is summarized in Table B.1, together with the boundary conditions dictated by the experiment.

Table B.1.: Chemistry databases with correspondent boundary conditions and TCI models for the investigated test cases

Case	Fuel	Oxidizer	Stoichiometry	TCI Model
Sandia D-F [10] 1 bar	$Y_{CH4} = 0.156$ $Y_{O2} = 0.1965$ $Y_{N2} = 0.6468$ T = 294 K	$Y_{O2} = 0.2329$ $Y_{N2} = 0.7575$ T = 291 K	$f_{st}=0.351$	FPV-β-PDF ILDM-ESF REDIM-ESF REDIM-MMC FR-noTCI
Lr57-75 [11] 1 bar	$Y_{CH4} = 0.139$ $Y_{O2} = 0.2$ $Y_{N2} = 0.66$ T = 300 K	$Y_{O2} = 0.2330$ $Y_{N2} = 0.7674$ T = 300 K	$f_{st}=0.055$	REDIM-ESF
Secondary near-wall reactions [68] 1 bar	$Y_{CH4} = 1$ T = 570 K	$Y_{O2} = 0.0842$ $Y_{N2} = 0.7401$ $Y_{H2O} = 0.0789$ $Y_{CO2} = 0.0966$ T = 1620 K	$f_{st}=0.023$	NA-Flamelets-β-PDF REDIM-ESF FR-noTCI
Single-injector CC 20 bar [113]	$Y_{CH4} = 1$ T = 269 K	$Y_{O2} = 1$ T = 278 K	$f_{st}=0.2$	NA-Flamelets-β-PDF

C. Appendix C

C.1. OpenFOAM code

The software OpenFOAM was used for the CFD simulations of this work. It is based on a finite volume cell-centred discretization of the computational domain and stores the topology of meshes in an unstructured manner. A detailed overview of mesh connectivity, domain and equation discretization, as well as the implicit solvers for the resolution of the linear system of equations can be found for example in the book of Moukalled et al [199]. The OpenFOAM code is based on C++ and it is open access, allowing a flexible implementation of custom-based libraries and classes.
Throughout this work, the libraries were implemented in or imported to OpenFOAM v.6 [1] in a package named `ESFredimFoam-6`. The `mmcFoam-5.0` libraries are based on version 5.x (see [97]).

C.2. Pressure-based solvers

The methodology for solving the compressible flow equations is briefly discussed in this paragraph. The generic transport equation for the scalar field ϕ

$$\frac{\partial \phi}{\partial t} + \nabla \cdot (\mathbf{u}\phi) = \nabla \cdot (D^{\phi} \nabla \phi) + Q\phi - C \tag{C.1}$$

contains in sequence the unsteady, convection, diffusion, source and sink terms, which are integrated over the cell volume V_c (and over time, due to the unsteady term). After discretization, one obtains an algebraic equation for each cell element, centred at the centroid C

$$a_C \phi_C + \sum_{C_{nb}} a_F \phi_F = b_C \tag{C.2}$$

where the a_C and a_F are the coefficients at the element centre and at the neighbours' centres (F), while b_C contains the explicit terms. The global matrix assembled from all algebraic equations is sparse and contains the necessary information for each element (located on the diagonal), as well its mesh connectivity (neighbours located on the upper and lower diagonals). Eq. (C.1) written for the computational domain becomes a linear system $\mathbf{A}\,\phi = \mathbf{b}$ which is solved using iterative methods, since we are dealing with time dependent problems (consult [199] for a detailed overview of the OpenFOAM iterative solvers).
In compressible flows, the effect of pressure on the flow field is dual: it affects the density through the equation of state (Eq.(2.6)) and the velocity through the pressure gradient in the momentum equation (Eq.(2.29)). A pressure-based algorithm is used hereby because the applications of interest are limited to the sub-sonic regime (low Mach numbers). The

---

[1] https://openfoam.org/version/6/

libraries exploit a Pressure-Implicit Split-Operator (PISO) algorithm [132]. Further details on this algorithm can be found again in [199]. The PISO algorithm is used for transient problems and couples the equations for momentum and mass conservation, starting at each time step by solving the momentum equation (`momentumPredictor` in the OpenFOAM language). Among different settings, one can decide how many times the pressure equation and the momentum corrector are solved at each step (`nCorrectors` in Table C.1), if repeated solutions of the pressure equation are necessary for the correction of the non-orthogonal terms (`nNonOrthogonalCorrectors` usually activated for strongly non-orthogonal meshes), and how many times the entire system of equations shall be solved for each time step (`nOuterCorrectors`). In PISO it is `nOuterCorrectors`=1.

Table C.1.: Pressure-based solvers settings

Settings	`mmcFoam-5.0`	`ESFredimFoam-6`
nOuterCorrectors	1	1
nCorrectors	1-3	3-5
nNonOrthogonalCorrectors	1	0
ThermoType	`hePsiThermo`	`heRhoThermo`
Chemistry integrator	ODE-`seulex`	`canteraChemistry` [334]

The ESF and MMC solvers show two differences in the thermodynamic and chemistry classes. The `mmcFoam` library was derived from the OpenFOAM `hePsiThermo` class using enthalpy and compressibility for the model calculation, while `ESFredimFoam` is based on `heRhoThermo` using enthalpy and density instead. The use of `hePsiThermo` against `heRhoThermo` is beneficial for non-ideal gas behaviours, because it includes already the compressibility factor Z from which ρ is calculated. However, when limited to the applications of this work, both classes provide a similar behaviour because the ideal gas assumption holds (compressible equations, but at low Mach). The second difference is given by the ODE solver used for finite rate chemistry computations. In `mmcFoam` it is the standard OpenFOAM `seulex` integrator, while `ESFredimFoam` exploits the Cantera chemistry routine implemented by Zirwes et al [334].

Additionally, the low-Mach number algorithm of Lessani and Papalexandris [169] for variable density flows was implemented in the ESF solvers for the investigation of the Sandia flames. Under atmospheric conditions, the hydrodynamic pressure p_d is the only contribution entering the momentum equation, the thermodynamic pressure p is used in the Equation of State (EOS) and the term $\partial p/\partial t$ in Eq. (2.29) is removed.

C.3. Library `ESFredimFoam−6`

This library contains the low Mach pressure-based solver for laminar chemistry (no-TCI model) and ESF [118], which were adapted from a previous OpenFOAM version (4.1). The reader can refer to the work of Breda at al [35] for the schematic of the ESF solver based on finite rate chemistry. More interesting is the discussion of the new routine for ESF-REDIM.

Fig. C.1 and C.2 help to understand the code structure. A new class named `eulerianCombustionModel` was derived from the OpenFOAM standard class `rhoThermoCombustion`. On this level all stochastic fields are initialized for the progress

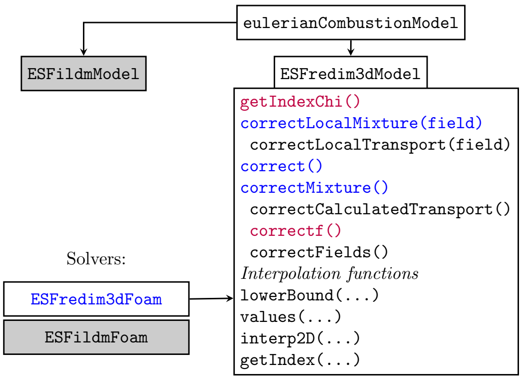

Figure C.1.: Class hierarchy and solver calls for `ESFredimFoam-6`

variables provided as input. Moreover, this class allows the use of another reduced chemistry database, the ILDM. Two classes are derived from `eulerianCombustionModel`, namely `ESFildmModel` and `ESFredim3dModel`. The former is blended out in gray because it is not the primarily focus of this work. This split is necessary, since the interpolation routine differs from ILDM to REDIM.

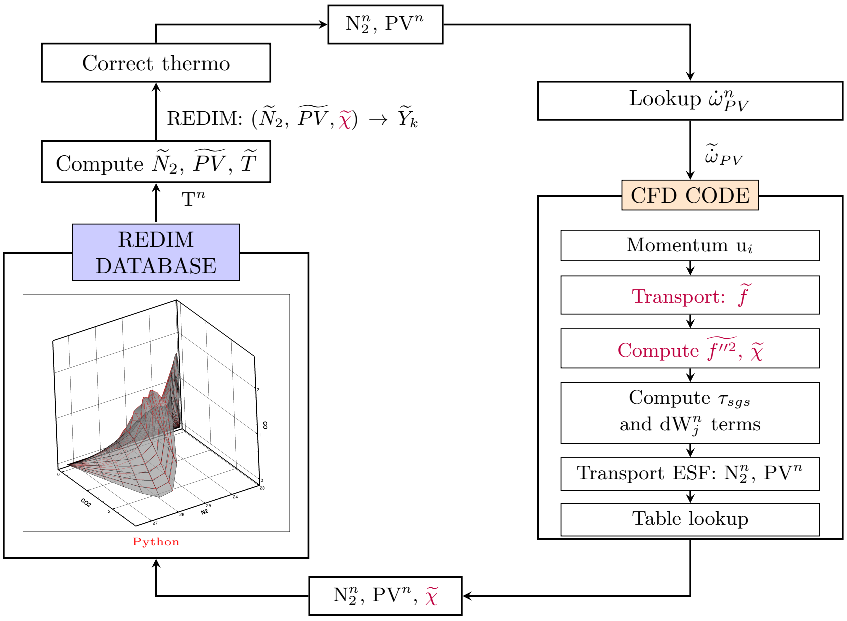

Figure C.2.: Low Mach pressure-based OpenFOAM algorithm for ESF-REDIM chemistry developed in this work

The transport equations for the ESF were directly implemented on the solver level (`ESFredim3dFoam` in blue), so that the combustion model `ESFredim3dModel` is only accessed by the solver to perform table interpolation and to update the scalar fields, via the three 'correct' functions marked in blue. The steps listed under the orange labelled box (CFD CODE) in Fig. C.2 occur at the solver level. At each time step the momentum equation is first calculated, followed by the N_f stochastic equations for the REDIM progress variables N_2 and PV. Three additional quantities are calculated in case a 3D-REDIM is used: the mixture fraction is transported, its variance is calculated algebraically and the scalar dissipation rate is updated using the definition of Domingo et al [73]. The variables or functions involved in case of a 3D-REDIM database are marked in red in the figure. The function `getIndexChi()` determines which is the 2D-REDIM table in the database closer to the local $\widetilde{\chi}$ calculated on the computational cell (remember that χ is the third table variable in the 3D-REDIM). In case of a 2D-REDIM, there is only a single-χ table and this call is obsolete.

The calculation of the local mixture properties for the n-th ESF equation as well as the interpolation of the chemical source terms $\dot{\omega}_k^n$ occurs in `ESFredim3dModel` via the `correctLocalMixture(field)` call, before the ESF equation is solved for the current time step. After the new (N_2^n, PV^n, χ) are obtained, the call `correct()` retrieves the temperature of each field n, entering the REDIM DATABASE marked in the blue box of Fig. C.2. Fig. C.1 shows the functions used for the bi-linear interpolation, under the label *Interpolation functions*. Finally, the `correctMixture()` calculates the first moments $\widetilde{N}_2$, $\widetilde{PV}$ and $\widetilde{T}$, retrieves the $\widetilde{Y}_k$ from the table and updates the mixture thermodynamic properties. The computation is then advanced to the next time step.

C.4. Library `mmcFoam−5.0`

A detailed description of the `mmcFoam-5.x` library package can be found in the paper of Galindo et al [97], which should definitely be consulted in order to understand the extension applied in this work. The code of interest is the `mmcFoam` solver for sparse Lagrangian LES, for the simulation of the Sandia flames. In this case, the templates loaded to define the derived class for the Pope particles follow the sequence `Reacting` ← `Mixing` ← `Thermo` ← `Advection` ← `particle` where the templates `Reacting` and `Thermo` contain some changes compared to the original code. Moreover, an additional reacting sub-model is created to deal with the tabulated chemistry. Instead of using the finite rate chemistry model (`finiteRateParticleChemistry`), the tabulated chemistry of REDIM is treated in `tabulatedParticleChemistry`.

Fig. C.3 shows the new algorithm. Differently from the ESF solver, there is a coupling between the Eulerian solver (orange box) and the Lagrangian solver (green box) used for the particles. The Eulerian solver is left unaltered: a PISO loop is applied on the pressure-momentum equation, the reference variable $\widetilde{f}$ is transported and the density coupling is applied. Here the equivalent species H_2, O_2, OH, H_2O, CH_4, CO, CO_2, C_2H_2 and C_2H_4 as well as the equivalent specific enthalpy $\widetilde{h}_s^E$ are transported, to guarantee mass consistency between the particles and the computational cell. Details about the density feedback can be found in [58]. The quantities $\widetilde{u}_i$, $\widetilde{f}$, D_{eff} (the sum of molecular and turbulent diffusion), $\bar{\rho}$ and $\bar{p}$ are interpolated from their values at the cell centres to the particles. With these values the Lagrangian solver is entered. New particles are inserted into the domain and are moved in space (within the `Advection` template), using the interpolated values obtained from the Eulerian solver. After controlling the number of particles in the domain, the mixing model `mmcCurl` is applied (`Mixing` template). Details related to the choice of the particle pairs are found again in [58].

The blue box shows how the new reacting sub-model treats the reaction term on each particle, based on the REDIM chemistry. Mixing and reaction are applied consequently, using a fractional step. In theory, only the progress variables (N_2 and CO_2 here) require the evaluation of the reaction term. The NOx chemistry was not included in the tables because

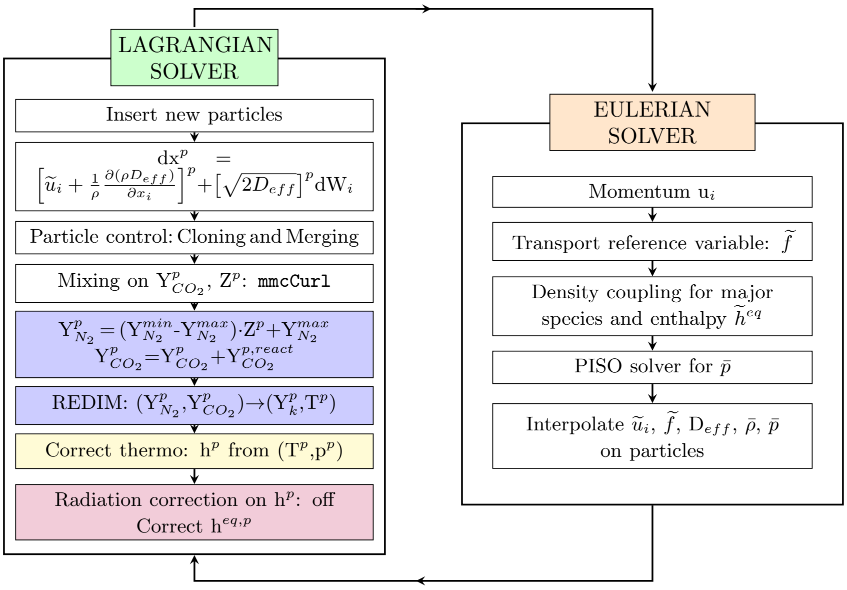

Figure C.3.: Pressure-based solver algorithm for MMC-REDIM tabulated chemistry [33]. Code extension for `mmcFoam-5.0`

not the scope of this work, so that only mixing is applied to N_2. However the code can be generalized to include source terms for N_2 when NOx chemistry is involved in the database. The reaction part for CO_2^p is obtained from the integrated $\dot{\omega}_{CO2}$ over the time step t_{CFD}. One can either use the CFD time step directly for the integration, or the minimum time step available from the REDIM integration ($5{\cdot}10^{-7}$ s) or an approximated integration based on the ratio $\mathrm{t}_{CFD}/5 \cdot 10^{-7}$. Once mixing and reaction have been applied to each particle, the values of Y_k^p and T^p are retrieved from the interpolation routine. The particle enthalpy h^p is then calculated from T_p in the template `Reacting` (yellow box), contrarily to the finite rate implementation where T_p is calculated from h^p. The enthalpy correction for radiation is disabled in the `Thermo` template (red box), as it would require the REDIM to account for enthalpy losses. Finally, the particle equivalent enthalpy $\mathrm{h}_s^{E,p}$ required for the density feedback in the Eulerian solver is updated from T_p.

C.5. NA-flamelet solver

The tabulated chemistry solver based on the non-adiabatic flamelets and used for the wall heat flux predictions of the single-injector combustion chambers was largely discussed in previous works (Frank [93], Müller [200] and Zips [330]). Because the previous routine was based on OpenFOAM v.4.1, it has been ported to v.6 in this work. Only a schematic of the NA-flamelet solver is shown in Fig. C.4, where the table parameters are ($\widetilde{f}$, $\widetilde{f''^2}$, $\widetilde{h}_n$). The discussion goes similarly to the ESF-REDIM solver, with the difference that the PDF distribution is assigned a-priori, with the filtered scalars corrected in a pre-processing step and stored in the table.

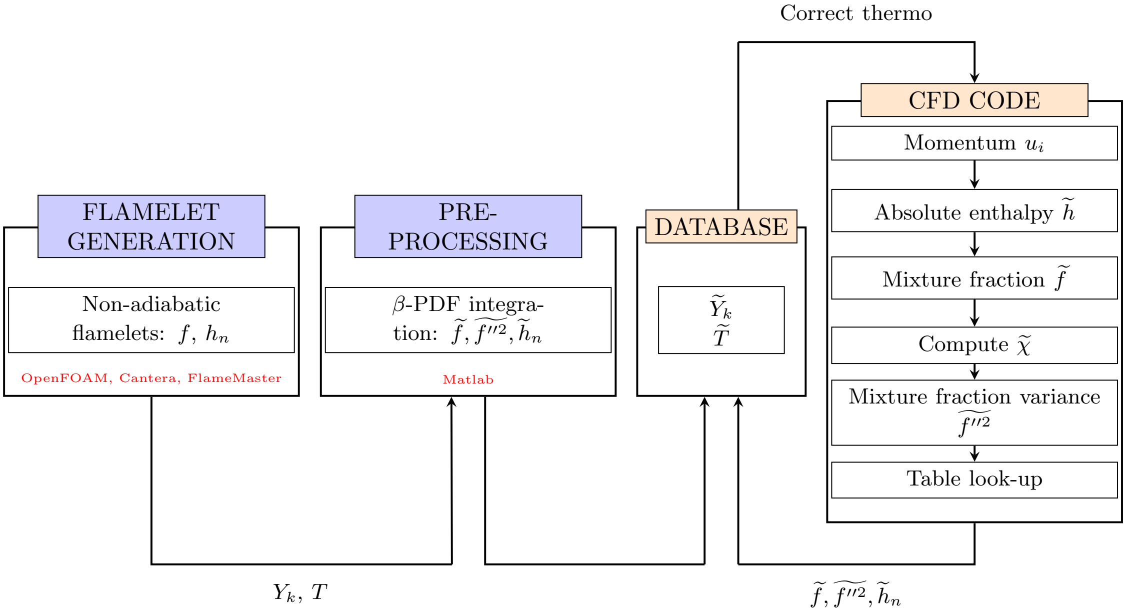

Figure C.4.: Pressure-based solver algorithm for non-adiabatic flamelets based on previous libraries [93, 200, 330]

Bibliography

[1] Al-Abdeli, Y., Masri, A., Marquez, G., and Starner, S. Time-varying behaviour of turbulent swirling nonpremixed flames. *Combust. Flame 146*, 1-2 (2006), 200–214.

[2] Alshaalan, T. M., and Rutland, C. J. Turbulence, scalar transport, and reaction rates in flame-wall interaction. *Symp. Int. Combust. Proc. 27*, 1 (1998), 793–799.

[3] An, J., He, G., Qui, F., Wei, X., and Liu, B. Dynamic adaptive chemistry with mechanisms tabulation and in situ adaptive tabulation (ISAT) for computationally efficient modeling of turbulent combustion. *Combust. Flame 206* (2019), 467–475.

[4] Arnold, R. *Experimentelle Untersuchungen zur Filmkühlung in Raketenbrennkammern.* Cuvillier, E; 1., Aufl. edition (29 Dec 2008), 2008.

[5] Arnold, R., Suslov, D. I., and Haidn, O. J. Film Cooling in a High-Pressure Subscale Combustion Chamber. *J. Propuls. Power 26*, 3 (2010), 428.

[6] Avdic, A., Kuenne, G., di Mare, F., and Janicka, J. LES combustion modeling using the Eulerian stochastic field method coupled with tabulated chemistry. *Combust. Flame 175* (January 2017), 201–219.

[7] Balaras, E., Benocci, C., and Piomelli, U. Two-layer approximate boundary conditions for large-eddy simulations. *AIAA J. 34*, 6 (1996), 1111–1119.

[8] Barlow, R. International Workshop on Measurements and Computations of Turbulent Non-Premixed Flames. https://www.sandia.gov/TNF/abstract.html.

[9] Barlow, R., and Frank, J. Effects of turbulence on species mass fractions in methane/air jet flames. *P. Combust. Inst. 27* (1998), 1087–1095.

[10] Barlow, R., and Frank, J. Piloted CH4/Air Flames C,D,E, and F - Release 2.1. Report, Sandia National Laboratories, June 2007.

[11] Barlow, R., Meares, S., Magnotti, G., Cutcher, H., and Masri, A. Local extinction and near-field structure in piloted turbulent CH4/air jet flames with inhomogeneous inlets. *Combust. Flame 162*, 10 (2015), 3516–3540.

[12] Bartz, D. A Simple Equation for Rapid Estimation of Rocket Nozzle Convective Heat Transfer Coefficients. *Jet. Propuls - Technical Notes 27* (1957), 49–51.

[13] Battista, F., Ricci, D., Natale, P., and Salvatore, V. The HYPROB Demonstrator Line: Status of the LOX/LCH4 Propulsion Activities. *8th European Conference For Aeronautics and Space Science* (Madrid, Spain, July 2019).

[14] BAUER, J., BYKOV, V., AND MAAS, U. Implementation of ILDMs based on a representation in generalized coordinates. *European Conference on Computational Fluid Dynamics* (2006), 1.

[15] BAURLE, R. A., TAM, C., EDWARDS, J. R., AND HASSAN, H. A. Hybrid Simulation Approach for Cavity Flows: Blending, Algorithm, and Boundary Treatment Issues. *AIAA J. 41*, 8 (2003), 1463–1480.

[16] BENDER, R., BLASENBREY, T., AND MAAS, U. Coupling of detailed and ILDM-reduced chemistry with turbulent mixing. *P. Combust. Inst. 28* (2000), 101–106.

[17] BETTI, B., MARTELLI, E., NASUTI, F., AND ONOFRI, M. Numerical Study of Heat Transfer in Film Cooled Thurst Chambers. *AIAA 2012-3907* (2012).

[18] BILGER, R. The Structure of Diffusion Flames. *Combust. Sci. Tech. 13* (1976), 155–170.

[19] BILGER, R. Conditional moment closure for turbulent reacting flow. *Phys. Fluids 5* (1993), 436.

[20] BLASCO, J. A., FUEYO, N., DOPAZO, C., AND BALLESTER, J. Modelling the Temporal Evolution of a Reduced Combustion Chemical System With an Artificial Neural Network. *Combust. Flame 113* (1998), 38–52.

[21] BLASCO, J. A., FUEYO, N., LARROYA, J., DOPAZO, C., AND CHEN, Y. A single-step time-integrator of a methane–air chemical system using artificial neural networks. *Computers and Chemical Engineering 23*, 9 (1999), 1127–1133.

[22] BOHAN, B., BLUNCK, D., POLANKA, M., AND STOUFFER, S. Impact of an Upstream Film-Cooling Row on Mitigation of Secondary Combustion in a Fuel Rich Environment. *J. Turbomach. 136*, 3 (2013), 031008.

[23] BOROK, S., GOLDFARB, I., AND GOL'DSHTEIN, V. Causes for 'ghost' manifolds. *Communications in Nonlinear Science and Numerical Simulation 14*, 5 (2009), 1791–1795.

[24] BOROK, S., GOLDFARB, I., AND V.GOL'DSHTEIN. On a modified version of ILDM method and its asymptotic analysis. *Int. J. Pure Appl. Math. 47*, 3 (2009).

[25] BRANDL, A. *Anwendung einer konditionierten Skalar-Transport-PDF-Methode auf die Large-Eddy-Simulation zur Beschreibung der turbulenten nicht-vorgemischten Verbrennung.* PhD thesis, Bundeswehr University of Munich, 2010.

[26] BRANDT, M., POLIFKE, W., IVANCIC, B., FLOHR, P., AND PAIKERT, B. Auto-Ignition in a Gas Turbine Burner at Elevated Temperature. *GT2003-38224* (2003), 195–205.

[27] BRAY, K., DOMINGO, P., AND VERVISCH, L. Role of the progress variable in models for partially premixed turbulent combustion. *Combust. Flame 141*, 4 (2005), 431–437.

[28] BREDA, P., FISCHER, L., DALSHAD, R., AND PFITZNER, M. Numerical investigation of autoignition length and wall heat flux for near-wall reaction of CH4. In *30. Deutscher Flammentag* (Sept. 2021).

[29] BREDA, P., HANSINGER, M., AND PFITZNER, M. Low dimensional chemistry manifolds applied to premixed methane/air flames under atmospheric conditions. In *9th European Combustion Meeting* (Apr. 2019).

[30] BREDA, P., HANSINGER, M., AND PFITZNER, M. Chemistry computation without a sub-grid PDF model in LES of turbulent non-premixed flames showing moderate local extinction. *P. Combust. Inst. 38*, 2 (2021), 2655–2663.

[31] BREDA, P., AND PFITZNER, M. Delayed Detached Eddy Simulations with Tabulated Chemistry for Thermal Loads Predictions. *J. Propuls. Power 37*, 1 (2021), 29–46.

[32] BREDA, P., PFITZNER, M., PERAKIS, N., AND HAIDN, O. Generation of Non-adiabatic Flamelet Manifolds: Comparison of two Approaches Applied on a Single-element GCH4/GO2 Combustion Chamber. In *8th European Conference For Aeronautics and Space Science* (July 2019).

[33] BREDA, P., SHARMA, E., DE, S., CLEARY, M., AND PFITZNER, M. Coupling the Multiple Mapping Conditioning Mixing Model with Reaction-diffusion Databases in LES of Methane/air Flames. *Combust. Sci. Tech.* (July 2021).

[34] BREDA, P., TRAUTNER, E., KLEIN, M., HANSINGER, M., AND PFITZNER, M. CPU-based deployment of artificial neural networks for LES of reacting flows in OpenFOAM. In *13th International ERCOFTAC Symposium* (Sept. 2021).

[35] BREDA, P., YU, C., MAAS, U., AND PFITZNER, M. Validation of an Eulerian Stochastic Fields solver coupled with reaction-diffusion manifolds on LES of methane/air non-premixed flames. *Flow Turbul. Combust. 107* (2021), 441–477.

[36] BREDA, P., ZIPS, J., AND PFITZNER, M. A Non-Adiabatic Flamelet Approach for Non-Premixed O2/CH4 Combustion. In *Proceedings of the 3rd World Congress on Momentum, Heat and Mass Transfer* (Apr. 2018).

[37] BRUNEAUX, G., AKSELVOLL, K., POINSOT, T., AND FERZIGER, J. Flame-wall interaction simulation in a turbulent channel flow. *Combust. Flame 107*, 1-2 (1996), 27–36.

[38] BUTZ, D., HARTL, S., POPP, S., WALTHER, S., BARLOW, R., HASSE, C., DREIZLER, A., AND GEYER, D. Local flame structure analysis in turbulent CH4/air flames with multi-regime characteristics. *Combust. Flame 210* (2019), 426–438.

[39] BYKOV, V., GOL'DSHTEIN, V., AND MAAS, U. Simple global reduction technique based on decomposition approach. *Combust. Theory Model.* (2008), 1–30.

[40] BYKOV, V., AND MAAS, U. The extension of the ILDM concept to reaction-diffusion manifolds. *Combust. Theory Model. 11*, 6 (Dec 2007), 839–862.

[41] BYKOV, V., AND MAAS, U. Extension of the ILDM method to the domain of slow chemistry. *P. Combust. Inst. 31*, 1 (2007), 465–472.

[42] CABOT, W., AND MOIN, P. Approximate Wall Boundary Conditions in the Large-Eddy Simulation of High Reynolds Number Flow. *Flow Turbul. Combust. 63* (2000), pages269–291.

[43] CABRA, R., CHEN, J., DIBBLE, R., KARPETIS, A., AND BARLOW, R. Lifted methane–air jet flames in a vitiated coflow. *Combust. Flame 143* (2005), 491–506.

[44] CABRA, R., MYHRVOLD, T., CHEN, J., DIBBLE, R., KARPETIS, A., AND BARLOW, R. Simultaneous laser Raman-Rayleigh-LIF measurements and numerical modeling results of a lifted turbulent H2/N2 jet flame in a vitiated coflow. *P. Combust. Instit. 29* (2002), 1881 – 1888.

[45] CABRIT, J., AND NICOUD, F. Direct Simulations for Wall Modeling of Multicomponent Reacting Compressible Turbulent Flows. *Phys. Fluids 21*, 5 (2009), 55–108.

[46] CABRIT, O. *Modelisation des flux parietaux sur les tuyeres des moteurs a propergol solid*. PhD thesis, Universite Montpellier II, Montpellier, France, 2009.

[47] CAILLER, M., DARABIHA, N., AND FIORINA, B. Development of a virtual optimized chemistry method. Application to hydrocarbon/air combustion. *Combust. Flame 211* (2020), 281–302.

[48] CAO, R., AND POPE, S. The influence of chemical mechanisms on PDF calculations of nonpremixed piloted jet flames. *Combust. Flame 143* (2005), 450–470.

[49] CELANO, M., KIRCHBERGER, C., SILVESTRI, S., SUSLOV, D., AND HAIDN, O. Model Assessment for Gaseous Film Cooling in a Subscale Single Element GCH4-GOX Combustion Chamber. In *SP2016 3124835* (2016).

[50] CELANO, M., SILVESTRI, S., KIRCHBERGER, C., SCHLIEBEN, G., SUSLOV, D., AND HAIDN, O. Gaseous Film Cooling Investigation in a Model Single Element GCH4-GOX Combustion Chamber. *Transactions of the Japan Society for Aeronautical and Space Sciences 14*, ists30 (2016), 129–137.

[51] CELANO, M., SILVESTRI, S., SCHLIEBEN, G., KIRCHBERGER, C., HAIDN, O., AND KNAB, O. Injector Characterization for a Gaseous Oxygen-Methane Single Element Combustion Chamber. *Progress in Propulsion Physics 8* (2016), 145–164.

[52] CHAPMAN, D. Computational Aerodynamics Development and Outlook. *AIAA J. 17*, 12 (1979), 1293–1313.

[53] CHEMNITZ, A., SATTELMAYER, T., ROTH, C., HAIDN, O., DAIMON, Y., KELLER, R., GERLINGER, P., ZIPS, J., AND PFITZNER, M. Numerical Investigation of Reacting Flow in a Methane Rocket Combustor: Turbulence Modeling. *J. Propuls. Power 34*, 4 (July 2018).

[54] CHEN, J., BLASCO, J., FUEYO, N., AND DOPAZO, C. An economical strategy for storage of chemical kinetics: Fitting in situ adaptive tabulation with artificial neural networks. *P. Combust. Inst. 28*, 1 (2000), 115–121.

[55] CHEN, J., KOLLMANN, W., AND DIBBLE, R. Pdf Modeling of Turbulent Nonpremixed Methane Jet Flames. *Combust. Sci. Tech. 64*, 4-6 (1989), 315–346.

[56] CHRISTO, F., MASRI, A., NEBOT, E., AND POPE, S. An integrated PDF/neural network approach for simulating turbulent reacting systems. *Symp. Int. Combust. Proc. 26*, 1 (1996), 43–48.

[57] Cleary, M., and Klimenko, A. A generalised multiple mapping conditioning approach for turbulent combustion. *Flow Turbul. Combust. 4* (2009), 477–491.

[58] Cleary, M., and Klimenko, A. A detailed quantitative analysis of sparse- Lagrangian filtered density function simulations in constant and variable density reacting jet flows. *Phys. Fluids 23*, 11 (2011), 115102.

[59] Cleary, M., Klimenko, A., Janicka, J., and Pfitzner, M. A sparse-Lagrangian multiple mapping conditioning model for turbulent diffusion flames. *Flow Turbul. Combust. 32*, 1 (2009), 1499–1507.

[60] Coelho, P., Teerling, O., and Roekaerts, D. Spectral Radiative Effects and Turbulence/radiation Interaction in a Non-luminous Turbulent Jet Diffusion Flame. *Combust. Flame 133*, 1-2 (2003), 75–91.

[61] Collonval, F. B. *Modeling of auto-ignition and NOx formation in turbulent reacting flows.* PhD thesis, Technischen Universität München, 2015.

[62] Contino, F., Jeanmart, H., Lucchini, T., and D'Errico, G. Coupling of in situ adaptive tabulation and dynamic adaptive chemistry: An effective method for solving combustion in engine simulations. *P. Combust. Inst. 33* (2011), 3057–3064.

[63] Dabireau, F., Cuenot, B., Vermorel, O., and Poinsot, T. Interaction of Flames of H2 + O2 with Inert Walls. *Combust. Flame 135*, 1-2 (2003), 123–133.

[64] Daimon, Y., Negishi, H., Silvestri, S., and Haidn, O. Conjungated Combustion and Heat Transfer Simulation for a 7 Element GOX/GCH4 Rocket Combustor. *AIAA Paper 2018–4553* (July 2018).

[65] Dally, B., Masri, A., Barlow, R., and Fiechtner, G. Instantaneous and Mean Compositional Structure of Bluff-Body Stabilized Nonpremixed Flames. *Combust. Flame 114*, 1-2 (1998), 119–148.

[66] Dalshad, R., Perakis, N., Pfitzner, M., and Haidn, O. Implementation of an Optimization Method for Inverse Heat Conduction and Sensor Position Correction. In *Comsol Conference 2020 User Presentations* (2020).

[67] Dalshad, R., Sander, T., and Pfitzner, M. Experimental investigation of auto-ignition in non-premixed gaseous CH4/hot air cross flows. In *29. Deutscher Flammentag* (2019).

[68] Dalshad, R., Sander, T., and Pfitzner, M. Characterization of a newly designed test bench for investigation of flame-wall-interaction. *Proc. of the ASME Turbo Expo 2021* (2021), GT2021–59170.

[69] Davis, M., and Skodje, R. Geometric investigation of low-dimensional manifolds in systems approaching equilibrium. *J. Chem. Phys. 111*, 3 (1999), 859–874.

[70] DeLallo, M., Polanka, M., and Blunck, D. Impact of Trench and Ramp Film Cooling Designs to Reduce Heat Release Effects in a Reacting Flow. *GT2012-68311* (2012).

[71] DeLataillade, A., Dabireau, F., Cuenot, B., and Poinsot, T. Flame/wall interaction and maximum wall heat fluxes in diffusion burners. *P. Combust. Inst. 29*, 1 (2002), 775–779.

[72] Domingo, P., Vervisch, L., and Veynante, D. Auto-ignition and flame Propagation effects in LES of burned gases diluted turbulent combustion. *Proceedings of the Summer Program* (2006), 337–348. Center for Turbulence Research.

[73] Domingo, P., Vervisch, L., and Veynante, D. Large-Eddy Simulation of a Lifted Methane Jet Flame in Vitiated Coflow. *Combust. Flame 152* (2008), 415–432.

[74] Dopazo, C., and O'Brien, E. An approach to the autoignition of a turbulent mixture. *Acta Astronaut. 1* (1974), 1239.

[75] Drake, M., and Haworth, D. Advanced gasoline engine development using optical diagnostics and numerical modeling. *P. Combust. Inst. 31*, 1 (2007), 99–124.

[76] Duan, Y., Xia, Z., Ma, L., Luo, Z., Huang, X., and Deng, X. LES of the Sandia flame series D-F using the Eulerian stochastic field method coupled with tabulated chemistry. *Chinese J. Aeronaut.* (2019), 1.

[77] Dunn, M., Masri, A., and Bilger, R. Finite Rate Chemistry Effects in Highly Sheared Turbulent Premixed Flames. *Flow Turbul. Combust. 85* (2010), 621–648.

[78] Dunn, M., Masri, A., Bilger, R., and Barlow, R. A new piloted premixed jet burner to study strong finite-rate chemistry effects. *Combust. Flame 151*, 1-2 (2007), 46–60.

[79] Eastman, E. Theory of the Soret effect. *J. Am. Chem. Soc. 50*, 2 (1928), 283–291.

[80] Echekki, T., and Chen, J. Unsteady Strain Rate and Curvature Effects in Turbulent Premixed Methane-Air Flames. *Comb.Flame 106* (1996), 184–202.

[81] Echekki, T., and Mastorakos, E. *Turbulent Combustion Modeling.* Springer, 2011.

[82] Eggels, R. *Modelling of Combustion Processes an NO Formation with Reduced Reaction Mechanisms.* PhD thesis, Technische Universiteit Eindhoven, 1996.

[83] Eggels, R., and de Goey, L. Mathematically reduced reaction mechanisms applied to adiabatic flat hydrogen/air flames. *Combust. Flame 100*, 4 (1995), 559–570.

[84] Elasrag, H., and Li, S. Investigation of Extinction and Reignition Events Using the Flamelet Generated Manifold Model. *GT2018-75420* (2018).

[85] Evans, D. S. The Impact of Heat Release in Turbine Film Cooling. Master's thesis, Wright-Patterson AirForce Base, 2008.

[86] Ezekoye, O., Greif, R., and Sawyer, R. Increased surface temperature effects on wall heat transfer during unsteady flame quenching. *P. Combust. Inst. 24* (1992), 1465–1472.

[87] FELSCH, C., GAUDING, M., HASSE, C., VOGEL, S., AND PETERS, N. An extended flamelet model for multiple injections in DI Diesel engines. *P. Combust. Inst. 32*, 2 (2009), 2775–2783.

[88] FERRARO, F., GE, Y., PFITZNER, M., AND CLEARY, M. A Fully Consistent Hybrid Les/rans Conditional Transported Pdf Method for Non-premixed Reacting Flows. *Combust. Sci. Tech.* (Aug 2019), 1–20.

[89] FIORINA, B., GICQUEL, O., VERVISCH, L., CARPENTIER, S., AND DARABIHA, N. Approximating the chemical structure of partially premixed and diffusion counterflow flames using FPI flamelet tabulation. *Combust. Flame 140* (2005), 147–160.

[90] FIORINA, B., GICQUEL, O., VERVISCH, L., CARPENTIER, S., AND DARABIHA, N. Premixed turbulent combustion modeling using tabulated detailed chemistry and PDF. *P. Combust. Inst. 30* (2005), 867–874.

[91] FLEMMING, F., SADIKI, A., AND JANICKA, J. LES using artificial neural networks for chemistry representation. *Prog. Comput. Fluid Dy. 5*, 7 (2005).

[92] FOX, R. *Computational Models for Turbulent Reacting Flows.* Cambridge University Press, Cambridge, UK, 2003.

[93] FRANK, G. *Reaktive Kühlfilme und Flamme-Wand-Interaktionen in Raketenbrennkammern.* PhD thesis, Bundeswehr University of Munich, 2018.

[94] FRANKE, L., CHATZOPOULOS, A., AND RIGOPOULOS, S. Tabulation of combustion chemistry via Artificial Neural Networks (ANNs): Methodology and application to LES-PDF simulation of Sydney flame L. *Combust. Flame 185* (2017), 245–260.

[95] FRÖHLICH, J. *Large Eddy Simulation turbulenter Strömungen.* Teubner, Wiesbaden, 2006.

[96] GALINDO-LOPEZ, S., SALEHI, F., CLEARY, M., AND MASRI, A. MMC-LES simulations of turbulent piloted flames with varying levels of inlet inhomogeneity. *P. Combust. Inst. 36*, 2 (2017), 1759–1766.

[97] GALINDO-LOPEZ, S., SALEHI, F., CLEARY, M., MASRI, A., NEUBER, G., STEIN, O., KRONENBURG, A., VARNA, A., HAWKES, E., SUNDARAM, B., KLIMENKO, A., AND GE, Y. A stochastic multiple mapping conditioning computational model in OpenFOAM for turbulent combustion. *Comput. Fluids 172* (2018), 410–425.

[98] GALPIN, J., ANGELBERGER, C., NAUDIN, A., AND VERVISCH, L. Large-eddy simulation of H2–air auto-ignition using tabulated detailed chemistry. *J. Turbul. 9* (2008).

[99] GANTER, S., HEINRICH, A., MEIER, T., KUENNE, G., JAINSKI, C., RISSMANN, M., DREIZLER, A., AND JANICKA, J. Numerical analysis of laminar methane–air side-wall-quenching. *Combust. Flame 186* (2017), 299–310.

[100] GANTER, S., STRASSACKER, C., KUENNE, G., MEIER, T., HEINRICH, A., MAAS, U., AND JANICKA, J. Laminar near-wall combustion: analysis of tabulated chemistry simulations by means of detailed kinetics. *Int. J. Heat Fluid Flow 70* (2018), 259–270.

[101] GAO, F., AND O'BRIEN, E. A large-eddy simulation scheme for turbulent reacting flows. *Phys. Fluids 5* (1993), 1282–1284.

[102] GARDINER, C. *Stochastic methods*, 4 ed. Springer, 2009.

[103] GE, Y., CLEARY, M., AND KLIMENKO, A. A comparative study of Sandia flame series (D-F) using sparse-Lagrangian MMC modelling. *P. Combust. Inst. 34* (2013), 1325–1332.

[104] GERMANO, M., PIOMELLI, U., MOIN, P., AND CABOT, W. H. A dynamic subgrid scale eddy viscosity model. *Phys. Fluids 3* (1991), 1760.

[105] GHASEMI, E., SOLEIMANI, S., AND LIN, C. Secondary reactions of turbulent reacting flows over a film-cooled surface. *International Communications in Heat and Mass Transfer 55* (2014), 93–101.

[106] GICQUEL, O., DARABIHA, N., AND THÉVENIN, D. Laminar premixed hydrogen/air counterflow flame simulations using flame prolongation of ILDM with differential diffusion. *P. Combust. Inst. 28* (2000), 1901–1908.

[107] GOLDA, P., BLATTMANN, A., NEAGOS, A., BYKOV, V., AND MAAS, U. Implementation problems of manifolds-based model reduction and their generic solution. *Combust. Theory Model. 24*, 3 (2020), 377–406.

[108] GOLUB, G., AND VAN LOAN, C. *Matrix Computation*. The Johns Hopkins University Press, 1989.

[109] GOODWIN, D., SPETH, R., MOFFAT, H., AND WEBER, B. Cantera: An Object-oriented Software Toolkit for Chemical Kinetics, Thermodynamics, and Transport Processes. https://www.cantera.org, 2018.

[110] GOUSSIS, D., AND MAAS, U. *Turbulent Combustion Modeling*. Springer, 2011, pp. 193–220.

[111] GUPTA, H., TEERLING, O., DE GOEY, L., AND VAN OIJEN, J. Effect of Progress Variable Definition on the Mass Burning Rate of Premixed Laminar Flames in Flamelet Generated Manifold Methods. *9th European Combustion Meeting* (2019).

[112] GUTHEIL, E., AND BOCKHORN, H. The Effect of More Dimensional PDFs on the Turbulent Reaction Rate in Turbulent Reacting Flows at Moderate Damköhler Numbers. *Physico Chemical Hydrodynamics 9* (1987), 525–535.

[113] HAIDN, O., CELANO, M., SILVESTRI, S., KIRCHBERGER, C., AND SCHLIEBEN, G. Test Case 1: Single Element Combustion Chamber - GCH4/GOX Transregio SFB-TR40 Test Case 1. Tech. rep., 2015.

[114] HAIRER, E., NØRSETT, S., AND WARNER, G. *Solving Ordinary Differential Equations II: Stiff and Differential-Algebraic Problems*, 2 ed. Springer-Verlag, Berlin, 1996.

[115] HAMBA, F. A Hybrid RANS/LES Simulation of Turbulent Channel Flow. *Theor. Comput. Fluid Dyn. 16* (2003), 387–403.

[116] HANSINGER, M., GE, Y., AND PFITZNER, M. Deep Residual Networks for Flamelet/progress Variable Tabulation with Application to a Piloted Flame with Inhomogeneous Inlet. *Combust. Sci. Tech.* (2020).

[117] HANSINGER, M., PFITZNER, M., AND SABELNIKOV, V. LES of oxy-fuel jet flames using the Eulerian Stochastic Fields method with differential diffusion. *P. Combust. Inst. 38*, 2 (2021), 2665–2672.

[118] HANSINGER, M., ZIRWES, T., ZIPS, J., PFITZNER, M., ZHANG, F., HABISREUTHER, P., AND BOCKHORN, H. The Eulerian Stochastic Fields method applied to Large Eddy Simulations of a piloted flame with inhomogeneous inlet. *Flow Turbul. Combust. 105* (2020), 837–867.

[119] HASSE, C., AND PETERS, N. A two mixture fraction flamelet model applied to split injections in a DI Diesel engine. *P. Combust. Inst. 30*, 2 (2005), 2755–2762.

[120] HAWORTH, D. Progress in probability density function methods for turbulent reacting flows. *Prog. Energy and Combust. Sci. 36* (2010), 168–259.

[121] HEINRICH, A., GANTER, S., KUENNE, G., JAINSKI, C., DREIZLER, A., AND JANICKA, J. 3D Numerical Simulation of a Laminar Experimental SWQ Burner with Tabulated Chemistry. *Flow Turbul. Combust. 100*, 2 (2018), 535–559.

[122] HIRSCHFELDER, J., CURTISS, C., AND BYRD, R. *Molecular theory of gases and liquids.* John Wiley & Sons, New York, 1969.

[123] HOSSAIN, M., JONES, J., AND MALALASEKERA, W. Modelling a Bluff-Body Nonpremixed Flame Using a Coupled Radiation/Flamelet Combustion Model. *Flow Turbul. Combust. 67*, 3 (2001), 217–234.

[124] HUANG, P., AND COLEMAN, G. Van Driest Transformation and Compressible Wall-Bounded Flows. *AIAA J. 32*, 10 (1993).

[125] HUNG, P. *Algorithms for reaction mechanism reduction and numerical simulation of detonations initiated by projectiles.* PhD thesis, California Institute of Technology, 2003.

[126] HUO, H., AND YANG, V. Large-Eddy Simulation of Supercritical Combustion: Model Validation Against Gaseous H2–O2 Injector. *J. Propuls. Power 33*, 5 (2017).

[127] IHME, M., AND PITSCH, H. Modeling of radiation and nitric oxide formation in turbulent nonpremixed flames using a flamelet/progress variable formulation. *Phys. Fluids 20* (2008), 055110.

[128] IHME, M., AND PITSCH, H. Prediction of extinction and re-ignition in nonpremixed turbulent flames using a flamelet/progress variable model 1. A priori study and presumed PDF closure. *Combust. Flame 155* (2008), 70–89.

[129] IHME, M., AND PITSCH, H. Prediction of extinction and reignition in nonpremixed turbulent flames using a flamelet/progress variable model 2. Application in LES of Sandia flames D and E. *Combust. Flame 155* (2008), 90–107.

[130] IHME, M., SCHMITT, C., AND PITSCH, H. Optimal artificial neural networks and tabulation methods for chemistry representation in LES of a bluff-body swirl-stabilized flame. *P. Combust. Inst. 32*, 1 (2009), 1527–1535.

[131] IMMER, M. *Time-resolved measurement and simulation of local scale turbulent urban flow.* PhD thesis, ETH Zürich, 2016.

[132] ISSA, R., AHMADI-BEFRUI, B., BESHAY, K., AND GOSMAN, A. Solution of the implicitly discretised reacting flow equations by operator-splitting. *J. Comput. Phys. 93*, 2 (1991), 388–410.

[133] IVANCIC, B., FLOHR, P., PAIKERT, B., BRANDT, M., AND POLIFKE, W. Auto-Ignition and Heat Release in a Gas Turbine Burner at Elevated Temperature. *GT2004-53339* (2004), 179–187.

[134] JABERI, F. A., COLUCCI, P., JAMES, S., GIVI, P., AND POPE, S. Filtered mass density function for large-eddy simulation of turbulent reacting flows. *J. Fluid Mech. 401* (1999), 85–121.

[135] JAINSKI, C., RISSMANN, M., BÖHM, B., AND DREIZLER, A. Experimental investigation of flame surface density and mean reaction rate during flame–wall interaction. *P. Combust. Inst. 36*, 2 (2017), 1827–1834.

[136] JAINSKI, C., RISSMANN, M., BÖHM, B., JANICKA, J., AND DREIZLER, A. Sidewall quenching of atmospheric laminar premixed flames studied by laser-based diagnostics. *Combust. Flame 183* (2017), 271–282.

[137] JAISHREE, J., AND HAWORTH, D. Comparisons of Lagrangian and Eulerian PDF methods in simulations of non-premixed turbulent jet flames with moderate-to-strong turbulence-chemistry interactions. *Combust. Theory Model. 16*, 3 (435–463 2012), 1.

[138] JANICKA, J., KOLBE, W., AND KOLLMANN, W. Closure of the Transport Equation for the Probability Density Funcfion of Turbulent Scalar Fields. *J. Non-Equil. Thermodyn. 4*, 1 (1979), 47–66.

[139] JAROSINSKI, J. A survey of recent studies on flame extinction. *Combust. Sci. Technol. 12* (1986), 81–116.

[140] JENNY, P., POPE, S., MURADOGLU, M., AND CAUGHEY, D. A hybrid algorithm for the joint PDF equation of turbulent reactive flows. *J. Comput. Phys. 166*, 2 (2001), 215–252.

[141] JONES, W., AND PRASAD, V. Large Eddy Simulation of the Sandia Flame Series (D-F) using the Eulerian stochastic field method. *Combust. Flame 157* (2010), 1621–1636.

[142] JOOS, F., BRUNNER, P., SCHULTE-WERNING, B., AND SYED, K. Auto-ignition and heat release in a gas turbine burner at elevated temperature. *Proc. of ASME Turbo Expo 2004* (1996).

[143] KADER, B. A. Temperature and concentration profiles in fully turbulent boundary layers. *Int. J. Heat Mass Transfer 24* (1981), 1541.

[144] Kalt, P., Al-Abdell, Y., Masri, A., and Barlow, R. Swirling turbulent non-premixed flames of methane: Flow field and compositional structure. *P. Combust. Inst. 29*, 2 (2002), 1912–1919.

[145] Kawai, S., and Larsson, J. Wall-modeling in large eddy simulation: Length scales, grid resolution, and accuracy. *Phys. Fluids 24* (2012), 015105.

[146] Kawai, S., and Larsson, J. Dynamic non-equilibrium wall-modeling for large eddy simulation at high Reynolds numbers. *Phys. Fluids 25* (2013), 015105.

[147] Kays, W., and Crawford, M. *Convective Heat and Mass Transfer*. McGraw Hill, 1993.

[148] Kemenov, K., Wang, H., and Pope, S. Modelling Effects of Subgrid-Scale Mixture Fraction Variance in LES of a Piloted Diffusion Flame. *Combust. Theory Model. 16*, 4 (2012), 611–638.

[149] Kempf, A., Flemming, F., and Janicka, J. Investigation of lengthscales, scalar dissipation,and flame orientation in a piloted diffusion flame by LES. *P. Combust. Inst. 30* (2005), 557–565.

[150] Kim, S., Joh, M., Choi, H., and Park, T. S. Multidisciplinary simulation of a regeneratively cooled thrust chamber of liquid rocket engine: Turbulent combustion and nozzle flow. *Int. J. Heat Mass Transfer 70* (2014), 1066–1077.

[151] Kirchberger, C., Schlieben, G., Hupfer, A., and Soller, S. Investigation on Film Cooling in a Kerosene/ GOX Combustion Chamber. In *45th AIAA Joint Propulsion Conference and Exhibit* (2009).

[152] Kirk, D. R., Guenette, G. R., Lukachko, S. P., and Waitz, I. A. Gas Turbine Engine Durability Impacts of High Fuel-Air Ratio Combustors—Part II: Near-Wall Reaction Effects on Film-Cooled Heat Transfer. *J. Eng. Gas Turbines Power 125*, 3 (2003), 751–759.

[153] Kitano, T., Iida, H., and Kurose, R. Effect of Chemical Reactions of H2/O2 Combustion Gas on Wall Heat Flux in a Turbulent Channel Flow. *J. Heat Transfer 139*, 4 (2017), 044501.

[154] Klimenko, A. Matching conditional moments in PDF modelling of non-premixed combustion. *Combust. Flame 143*, 4 (2005), 369–385.

[155] Klimenko, A., and Bilger, R. Conditional moment closure for turbulent combustion. *Prog. Energy Combust. Sci. 25*, 6 (1999), 595–687.

[156] Klimenko, A., and Pope, S. The modelling of turbulent reactive flows based on multiple mapping conditioning. *Phys. Fluids 15*, 7 (2003), 1907–1925.

[157] Knikkerr, R., Dauptain, A., Cuenot, B., and Poinsot, T. Comparison of computational methodologies for ignition of diffusion layers. *Combust. Sci. Tech. 175*, 10 (2003), 1783–1806.

[158] KOSAKA, H., ZENTGRAF, F., SCHOLTISSEK, A., HASSE, C., AND DREIZLER, A. Effect of flame–wall interaction on local heat release of methane and DME combustion in a side-wall quenching geometry. *Flow Turbul. Combust. 104* (2019), 1029–1046.

[159] KROGER, H., AND KORNEV, N. Generation of divergence free synthetic inflow turbulence with arbitrary anisotropy. *Comput. Fluids 165* (2018), 78–88.

[160] KUENNE, G., SEFFRIN, F., FUEST, F., STAHLER, T., KETELHEUN, A., GEYER, D., JANICKA, J., AND DREIZLER, A. Experimental and numerical analysis of a lean premixed stratified burner using 1D Raman/Rayleigh scattering and large eddy simulation. *Combust. Flame 159*, 8 (2012), 2669–2689.

[161] KULKARNI, R., AND POLIFKE, W. Large Eddy Simulation of Autoignition in a Turbulent Hydrogen Jet Flame Using a Progress Variable Approach. *J. Combust. 2012* (2012).

[162] KULKARNI, R., AND POLIFKE, W. LES of Delft-jet-in-hot-coflow (DJHC) with tabulated chemistry and stochastic fields combustion model. *Fuel Process Technol. 107* (2013), 138–146.

[163] LAM, S. *Recent Advances in the Aerospace Sciences.* Springer, Boston, MA, 1985, ch. Singular Perturbation for Stiff Equations Using Numerical Methods, pp. 3–19.

[164] LAMPMANN, A., HANSINGER, M., AND PFITZNER, M. LES of a turbulent CH4/air multi-regime burner configuration using an artificially thickened flame model with reduced finite-rate chemistry. In *10th European Combustion Meeting* (Apr. 2021).

[165] LAPENNA, P., AMADUZZI, R., DURIGON, D., INDELICATO, G., NASUTI, F., AND CRETA, F. Simulation of a Single-element GCH4/GOX Rocket Combustor Using a Non-adiabatic Flamelet Method. *AIAA Paper 2018-4872* (July 2018).

[166] LARSSON, J., KAWAI, S., BODART, J., AND BERMEJO-MORENO, I. Large Eddy Simulation with Modelled Wall-Stress: Recent Progress and Future Directions. *Mechanical Engineering Reviews 3*, 1 (2016), 15–00418.

[167] LAUBSCHNER, R. *Utilization of artificial neural networks to resolve chemical kinetics in turbulent fine strucutres of an advanced CFD combustion model.* PhD thesis, Stellenbosch University, 2017.

[168] LEE, D., THAKUR, S., WRIGHT, J., IHME, M., AND SHYY, W. Characterization of Flow Field Structure and Species Composition in a Shear Coaxial Rocket GH2/GO2 Injector: Modeling of Wall Heat Losses. *AIAA Paper 2011-6125* (July 2011).

[169] LESSANI, B., AND PAPALEXANDRIS, M. Time-accurate calculation of variable density flows with strong temperature gradients and combustion. *J. Comput. Phys. 212*, 1 (2006), 218–246.

[170] LIANG, L., STEVENS, J., AND FARRELL, J. A dynamic adaptive chemistry scheme for reactive flow computations. *P. Combust. Inst.*, 32 (2009), 527–34.

[171] LU, J., EZEKOYE, O., GREIF, R., AND SAWYER, R. Unsteady Heat Transfer during Side-Wall Quenching of a Laminar Flame. *P. Combust. Inst. 23* (1990), 441–446.

[172] Lu, T., and Law, C. A Directed Relation Graph Method for Mechanism Reduction. *P. Combust. Inst. 30*, 1 (2005), 1333–1341.

[173] Lu, T., and Law, C. K. A criterion based on computational singular perturbation for the identification of quasi steady state species: A reduced mechanism for methane oxidation with NO chemistry. *Combust. Flame 154*, 4 (2008), 761–774.

[174] Lu, T., Law, C. K., Yoo, C. S., and Chen, J. H. Dynamic stiffness removal for direct numerical simulations. *Combust. Flame 156*, 8 (2009), 1542–1551.

[175] Lukachko, S. P., Kirk, D. R., and Waitz, I. A. Gas Turbine Engine Durability Impacts of High Fuel-Air Ratio Combustors—Part I: Potential for Secondary Combustion of Partially Reacted Fuel. *J. Eng. Gas Turbines Power 125*, 3 (2003), 742–750.

[176] Løvås, T., Mauss, F., Hasse, C., and Peters, N. Development of adaptive kinetics for application in combustion systems. *P. Combust. Inst. 29*, 1 (2002), 1403–1410.

[177] Ma, P., Greene, M., Sick, V., and Ihme, M. Non-equilibrium wall-modeling for internal combustion engine simulations with wall heat transfer. *Int. J. Engine Res. 18*, 1-2 (Feb. 2017), 15–25.

[178] Ma, P., Wu, H., and Ihme, M. Nonadiabatic Flamelet Formulation for Predicting Wall Heat Transfer in Rocket Engines. *AIAA J. 56*, 6 (June 2018), 2336–2349.

[179] Ma, P., Wu, H., Ihme, M., and Hickey, J. A Flamelet Model with Heat-loss Effects for Predicting Wall-heat Transfer in Rocket Engines. *AIAA Paper 2017–4856* (July 2017).

[180] Maas, U., and Bykov, V. The extension of the reaction/diffusion manifold concept to systems with detailed transport models. *P. Combust. Inst. 33*, 1 (2011), 1253–1259.

[181] Maas, U., and Pope, S. Implementation of simplified chemical kinetics based on intrinsic low-dimensional manifolds. *Symp. Int. Combust. Proc. 24*, 1 (1992), 103–112.

[182] Maas, U., and Pope, S. Simplifying Chemical Kinetics: Intrinsic Low-Dimensional Manifolds in Composition Space. *Combust. Flame 88* (1992), 239–264.

[183] Maas, U., and Pope, S. Laminar flame calculations using simplified chemical kinetics based on intrinsic low-dimensional manifolds. *Symp. Int. Combust. Proc. 25*, 1 (1994), 1349–1356.

[184] Maas, U., and Thévenin, D. Correlation analysis of direct numerical simulation data of turbulent non-premixed flames. *Symp. Int. Combust. Proc. 27*, 1 (1998), 1183–1189.

[185] Maestro, D., Cuenot, B., and Selle, L. Large Eddy Simulation of Combustion and Heat Transfer in a Single Element GCH4/GOx Rocket Combustor. *Flow, Turbul. Combust. 103*, 5 (2019).

[186] Maestro, D., Cuenot, B., Selle, L., Frank, G., Pfitzner, M., Daimon, Y., Keller, R., Gerlinger, P., Chemnitz, A., Sattelmayer, T., and Haidn, O. Numerical Investigation of Flow and Combustion in a Single Element GCH4/GOX Rocket Combustor: Chemistry Modeling and Turbulence-Combustion Interaction. *AIAA Paper 2016–4996* (July 2016).

[187] Mahmoud, R., Jangi, M., Ries, F., Fiorina, B., Janicka, J., and Sadiki, A. Combustion Characteristics of a Non-Premixed Oxy-Flame Applying a Hybrid Filtered Eulerian Stochastic Field/Flamelet Progress Variable Approach. *Appl. Sci. 9* (2019), 1320.

[188] Marracino, B., and Lentini, D. Radiation Modelling in Non-Luminous Non-premixed Turbulent Flames. *Combust. Sci. Technol. 128*, 1-6 (1997), 23–48.

[189] Masri, A. Partial premixing and stratification in turbulent flames. *P. Combust. Inst. 35*, 2 (2015), 1115–1136.

[190] Masri, A., and Bilger, R. Turbulent diffusion flames of hydrocarbon fuels stabilized on a bluff body. *Symp. Int. Combust. Proc. 20*, 1 (1985), 319–326.

[191] Masri, A., Dibble, R., and Barlow, R. Raman-rayleigh measurements in bluff-body stabilised flames of hydrocarbon fuels. *Symp. Int. Combust. Proc. 24*, 1 (1992), 317–324.

[192] Masri, A., Kalt, P., and Barlow, R. The compositional structure of swirl-stabilised turbulent nonpremixed flames. *Combust. Flame 138*, 1-2 (2004), 1–37.

[193] Masri, A., Pope, S., and Dally, B. Probability density function computations of a strongly swirling nonpremixed flame stabilized on a new burner. *P. Combust. Inst. 28*, 1 (2000), 123–131.

[194] Mastorakos, E., Baritaud, T., and Poinsot, T. Numerical simulations of autoignition in turbulent mixing flows. *Combust. Flame 109*, 1–2 (1997), 198–223.

[195] McBride, B., Gordon, S., and Reno, M. Coefficients for Calculating Thermodynamic and Transport Properties of Individual Species. https://ntrs.nasa.gov/search.jsp?R=19940013151, 1993. retrieved 30 Apr. 2020.

[196] Meares, S., and Masri, A. A modified piloted burner for stabilizing turbulent flames of inhomogeneous mixtures. *Combust. Flame 161* (2014), 484–495.

[197] Minuzzi, F., Yu, C., and Maas, U. Simulation of methane/air non-premixed turbulent flames based on REDIM simplified chemistry. *Flow Turbul. Combust.* (Oct 2019), 1–22.

[198] Mitarai, S., Riley, J., and Kosaly, G. Testing of mixing models for Monte Carlo probability density function simulations. *Phys. Fluids 17* (2005).

[199] Moukalled, F., Mangani, L., and Darwish, M. *The Finite Volume Method in Computational Fluid Dynamics.* Springer, 2015.

[200] Müller, H. *Simulation turbulenter nicht-vorgemischter Verbrennung bei überkritischen Drücken.* PhD thesis, Bundeswehr University of Munich, 2016.

[201] Müller, H., Zips, J., Pfitzner, M., Maestro, D., Cuenot, B., Menon, S., Ranjan, R., Tudisco, P., and Selle, L. Numerical Investigation of Flow and Combustion in a Single-Element GCH4/GOX Rocket Combustor: A comparative LES study. *AIAA Paper 2016–4997* (July 2016).

[202] Muradoglu, M., Jenny, P., Pope, S., and Caughey, D. A consisten hybrid finite-volume/particle method for the PDF equations of turbulent reactive flows. *J. Comput. Phys. 154* (1999), 342–371.

[203] Muradoglu, M., Pope, S., and Caughey, D. The hybrid method for the PDF equations of turbulent reactive flows: Consistency conditions and correct algorithms. *J. Comput. Phys. 172*, 2 (2001), 841–878.

[204] Mustata, R., Valiño, L., Jimenez, C., Jones, W., and Bondi, S. A probability density function Eulerian Monte Carlo field method for large eddy simulations: Applications to a turbulent piloted methane/air diffusion flame (Sandia D). *Combust. Flame 145*, 1-2 (2006), 88–104.

[205] Muto, D., Daimon, Y., Negishi, H., and Shimizu, T. Wall modeling of turbulent methane/oxygen reacting flows for predicting heat transfer. *Int. J. Heat Fluid Flow 87* (2021), 108755.

[206] Muto, D., Daimon, Y., Shimizu, T., and Negishi, H. Preliminary Study on Wall-modeled Large Eddy Simulation of Turbulent Heat Transfer for Liquid Rocket Engines. *7th European Conference for Aeronautics and Space Sciences* (2017).

[207] Muto, D., Daimon, Y., Shimizu, T., and Negishi, H. An equilibrium wall model for reacting turbulent flows with heat transfer. *Int. J. Heat Mass Transfer 141* (2019), 1187–1195.

[208] Nafe, J., and Maas, U. A general algorithm for improving ILDMs. *Comb. Theory Model. 6*, 4 (2002), 697–709.

[209] Natale, P., Saccone, G., and Battista, F. CFD Kinetic Scheme Validation for Liquid Rocket Engine Fuelled by Oxygen/Methane. In *8th European Conference For Aeronautics and Space Science* (July 2019).

[210] Nguyen, P., Vervisch, L., Subramanian, V., and Domingo, P. Multidimensional flamelet-generated manifolds for partially premixed combustion. *Combust. Flame 157*, 1 (2010), 43–61.

[211] Nicoud, F., and Ducros, F. Subgrid-Scale Stress Modelling Based on the Square of the Velocity Gradient Tensor. *Flow Turbul. Combust. 62*, 3 (1999), 183–200.

[212] Nikitin, N. V., Nicoud, F., Wasistho, B., Squires, K. D., and Spalart, P. R. An approach to wall modeling in large-eddy simulations. *Phys. Fluids 12*, 7 (2000), 1629–1632.

[213] Olmeda, R., Breda, P., Stemmer, C., and Pfitzner, M. *Future Space-Transport-System Components under High Thermal and Mechanical Loads. Notes on Numerical Fluid Mechanics and Multidisciplinary Design.* Springer, Cham., 2021,

ch. Large-Eddy Simulations for the Wall Heat Flux Prediction of a Film-Cooled Single-Element Combustion Chamber, pp. 223–234.

[214] Oran, E., and Boris, J. *Numerical Simulation of Reactive Flow.* Cambridge University Press, 2001.

[215] Pera, C., Colin, O., and Jay, S. Development of a FPI Detailed Chemistry Tabulation Methodology for Internal Combustion Engines. *Oil Gas Sci. Technol. 64*, 3 (2009), 243 – 258.

[216] Perakis, N., and Haidn, O. Inverse heat transfer method applied to capacitively cooled rocket thrust chambers. *Int. J. Heat Mass Transfer 131* (2019), 150–166.

[217] Perakis, N., and Haidn, O. Wall heat transfer prediction in CH4/O2 and H2/O2 rocket thrust chambers using a non-adiabatic flamelet model. *A. Astronaut. 174* (2020), 254–269.

[218] Perakis, N., Haidn, O., Rahn, D., Eiringhaus, D., Zhang, S., Daimon, Y., Karl, S., and Horchler, T. Qualitative and Quantitative Comparison of RANS Simulation Results for a 7 element GOx-GCH4 Rocket Combustor. *AIAA Paper 2018-4556* (July 2018).

[219] Perakis, N., Rahn, D., Haidn, H., and Eiringhaus, D. Heat Transfer and Combustion Simulation of a 7-element GOX/GCH4 Rocket Combustor. *AIAA Paper 2018-4554* (July 2018).

[220] Perakis, N., Roth, C., and Haidn, O. Development of a Non-adiabatic Flamelet Model for Reacting Flows with Heat Loss. *Space Propulsion Conference SP2018-00171* (Sevilla, Spain, May 2018).

[221] Peters, N. Laminar diffusion flamelet models in non-premixed turbulent combustion. *Prog. Energy Combust. Sci. 10* (1984), 319–339.

[222] Petersen, E., Davidson, D., and Hanson, R. Kinetics Modeling of Shock-Induced Ignition in Low-Dilution CH4/O2 Mixtures at High Pressure and Intermediate Temperatures. *Combust. Flame 117* (1999), 272–290.

[223] Pfitzner, M., and Breda, P. An analytic probability density function for partially premixed flames with detailed chemistry. *Phys. Fluids 33*, 3 (2021), 035117.

[224] Pierce, C., and Monin, P. Progress-variable approach for large-eddy simulation of non-premixed turbulent combustion. *J. Fluid Mech. 504* (2004), 73–97.

[225] Pitsch, H., and Ihme, M. An Unsteady/Flamelet Progress Variable Method for LES of Nonpremixed Turbulent Combustion. *AIAA Paper 2005-557* (2005).

[226] Pohl, S. *Numerische Untersuchung von Verbrennungsprozessen in Raketenbrennkammern und Gasturbinen.* PhD thesis, Univierstität der Bundeswehr of Munich, 2016.

[227] Pohl, S., Frank, G., and Pfitzner, M. Heat Transfer In Reacting Cooling Films, Part I: Influence and Validation of Combustion Modelling in CFD Simulations. *Proceedings of ASME Turbo Expo 2014: Turbine Technical Conference and Exposition* (2014).

[228] Poinsot, T., Haworth, D., and Bruneaux, G. Direct simulation and modeling of flame-wall interaction for premixed turbulent combustion. *Combust. Flame 95* (1993), 118–132.

[229] Poinsot, T., and Veynante, D. *Theoretical and Numerical Combustion*, 3 ed. Aquaprint, Bordeaux, 2005, pp. 87–129.

[230] Polanka, M., Zelina, J., Anderson, W., Sekar, B., Evans, D., Lin, C., and Stouffer, S. Heat Release in Turbine Cooling I: Experimental and Computational Comparison of Three Geometries. *J. Propuls. Power 27*, 2 (2011), 257–268.

[231] Polifke, W., Geng, W., and Döbbeling, K. Optimization of Rate Coefficients for Simplified Reaction Mechanisms with Genetic Algorithms. *Combust. Flame 113*, 1-2 (1998), 119–134.

[232] Poling, B., Prausnitz, J., and O'Connell, J. *The Properties of Gases and Liquids.* McGraw−Hill, New York, 2000.

[233] Pope, S. A Monte Carlo Method for the PDF Equations of Turbulent Reactive Flow. *Combust. Sci. Tech. 25* (1981), 159–174.

[234] Pope, S. PDF methods for turbulent reactive flows. *Prog. Energy Combust. Sci. 11*, 2 (1985), 119–192.

[235] Pope, S. Computations of turbulent combustion: progress and challenges. *23rd Symp. Int. Combust. Proc.* (1990), 591–612.

[236] Pope, S. Computationally efficient implementation of combustion chemistry using in situ adaptive tabulation. *Combust. Theory Model. 1*, 1 (1997), 41–63.

[237] Pope, S. *Turbulent Flows.* Cambridge University Press, Cambridge, 2000.

[238] Pope, S. Ten questions concerning the large-eddy simulation of turbulent flows. *New J. Phys. 6*, 35 (Mar 2004), 1.

[239] Pope, S., and Maas, U. Simplified chemical kinetics: Trajectory-generated low-dimensional manifolds. Internal report, Cornell University, 1993.

[240] Popp, P., and Baum, M. Analysis of wall heat fluxes, reaction mechanisms and unburned hydrocarbons during the head-on quenching of a laminar methane flame. *Combust. Flame 108* (1997), 327–348.

[241] Porumbel, I., Petcu, A., Gabriel, F., and Hritcu, E. Artificial Neural Networks for Modeling of Chemical Source Terms in CFD Simulations of Turbulent Reactive Flows. *Appl. Mech. Mater. 555* (2014), 395–400.

[242] Press, W. H., Teukolsky, S. A., Vetterling, W. T., and Flannery, B. P. *Numerical Recipes - The Art of Scientific Computing.* Cambridge University Press, 2007.

[243] Rahn, D., Haidn, O., and Riedmann, H. Conjungate Heat Transfer Simulation of a Subscale Rocket Thrust Chamber Using a Timescale Based Frozen Non-Adiabatic Flamelet Combustion Model. *AIAA Paper 2019–3864* (July 2019).

[244] Rahn, D., Haidn, O., Riedmann, H., and Behr, R. Non-Adiabatic Flamelet Modeling for the Numerical Simulation of Methane Combustion in Rocket Thrust Chambers. *AIAA Paper 2018–4869* (July 2018).

[245] Ramaekers, W., van Oijen, J., and de Goey, L. A Priori Testing of Flamelet Generated Manifolds for Turbulent Partially Premixed Methane/Air Flames. *Flow Turbul. Combust. 84* (2010), 439–458.

[246] Raman, V., and Pitsch, H. A consistent LES/filtered-density function formulation for the simulation of turbulent flames with detailed chemistry. *P. Combust. Inst. 31* (2007), 1711–1719.

[247] Ranjan, R., Panchal, A., and Menon, S. On the Effects of Chemical Kinetics and Thermal Conditions on the Flow and Flame Features in a Single-Element GCH4/GOX Rocket Combustor. *AIAA Paper 2016–4999* (July 2016).

[248] Ren, Z., and Pope, S. The geometry of reaction trajectories and attracting manifolds in composition space. *Comb. Theory Model. 10*, 3 (2006), 361–388.

[249] Ritchie, H. Fossil Fuels. *Our World in Data* (2017). https://ourworldindata.org/fossil-fuels.

[250] Roth, C., Haidn, O., Chemnitz, A., Sattelmayer, T., Frank, G., Müller, H., Zips, J., Keller, R., Gerlinger, P., Maestro, D., Cuenot, B., Riedmann, H., and Selle, L. Numerical Investigation of Flow and Combustion in a Single-Element GCH4/GOX Rocket Combustor. *AIAA Paper 2016–4995* (July 2016).

[251] Sabel'nikov, V., and Soulard, O. Rapidly decorrelating velocity-field model as a tool for solving one-point Fokker-Planck equations for probability density functions of turbulent reactive scalars. *Physical Review E 72* (2005), 16301–163022.

[252] Saccone, G., Natale, P., and Battista, F. Reduced Kinetic Scheme of Methane/Oxygen Combustion for Liquid Rocket Engines Applications. In *Proceedings of the 3rd World Congress on Momentum, Heat and Mass Transfer* (Apr. 2018).

[253] Saccone, G., Natale, P., Battista, F., Breda, P., and Pfitzner, M. Methane / Oxygen Combustion Kinetic Scheme Optimization for Liquid Rocket Engine CFD Applications. In *Proceedings of the 4th World Congress on Momentum, Heat and Mass Transfer* (Apr. 2019).

[254] Sagaut, P. *Large Eddy Simulation for Incompressible Flows.* Springer, 2001.

[255] Sakellarakis, V. D. *Mixing and Autoignition of Underexpanded Methane Jets at High Pressure Conditions.* PhD thesis, ETH Zürich, 2020.

[256] Sankaran, R., Hawkes, E., Chen, J., Lu, T., and Law, C. Structure of a spatially developing turbulent lean methane/air Bunsen flame. *P. Combust. Inst. 31*, 1 (Jan 2007), 1291–1298.

[257] Schlichting, H. *Boundary layer theory.* McGraw–Hill, New York, 1955.

[258] Schmidt, D., Blasenbrey, T., and Maas, U. Intrinsic low-dimensional manifolds of strained and unstrained flames. *Comb. Theory Model. 2*, 2 (1998), 135–152.

[259] SCHMIDT, D., SEGATZ, J., RIEDER, U., WARNATZ, J., AND MAAS, U. Simulation of Laminar Methane-Air Flames using Automatically Simplified Chemical Kinetics. *Combust. Sci. Tech. 113*, 1 (1996), 3–16.

[260] SCHNEIDER, C., DREIZLER, A., AND JANIKA, J. Flow Field Measurements of Stable and Locally Extinguishing Hydrocarbon-Fuelled Jet Flames. *Combust. Flame 135* (2003), 185–190.

[261] SHENVI, N., GEREMIA, J., AND RABITZ, H. Efficient chemical kinetic modelling through neural network maps. *J. Chem. Phys. 120*, 21 (2004), 9942–51.

[262] SHROTRIYA, P., WANG, P., JIANG, L., AND MURUGESAN, M. REDIM-PFDF modelling of turbulent partially-premixed flame with inhomogeneous inlets using a top-hat function for multi-stream mixing problem. *Aerosp. Sci. Technol. 107* (2020), 106258.

[263] SHROTRIYA, P., WANG, P., JIANG, L., AND MURUGESAN, M. REDIM-PFDF Subgrid Scale Combustion Modeling for Turbulent Partially-premixed Flame: Assessment of Combustion Modes. *Combust. Sci. Tech.* (2020).

[264] SHUR, M., SPALART, P., STRELETS, M., AND TRAVIN, A. A hybrid RANS-LES approach with delayed-DES and wall-modelled LES capabilities. *Int. J. Heat Fluid Fl. 29*, 6 (2008), 1638–1649.

[265] SILVESTRI, S., CELANO, M., SCHLIEBEN, G., AND HAIDN, H. Characterization of a Multi-Injector GOX-GCH4 Combustion Chamber. *AIAA Paper 2016–4071* (July 2016).

[266] SIMONTACCHI, P., EDELINE, E., BLASI, R., SAGNIER, S., RAVIER, N., ESPINOSA-RAMOS, A., AND BREREAU, J. Prometheus: Precursor of New Low-Cost Rocket Engine Family. *8th European Conference For Aeronautics and Space Science* (July 2019).

[267] SINGLA, G., SCOUFLAIRE, P., ROLON, C., AND CANDEL, S. Transcritical oxygen/transcritical or supercritical methane combustion. *P. Combust. Inst. 30*, 2 (2005), 2921–2928.

[268] SMAGORINSKY, J. General Circulation Experiments with the Primitive Equations: I. The Basic Experiment. *Monthly weather review 91*, 3 (1963), 99–164.

[269] SMITH, G., GOLDEN, D., FRENKLACH, M., MORIARTY, N., EITENEER, B., GOLDENBERG, M., BOWMAN, C., HANSON, R., SONG, S., GARDINER, W., LISSIANSKI, V., AND QIN, Z. GRI-Mech—An Optimized Detailed Chemical Reaction Mechanism for Methane Combustion. Report GRI-95/0058, Nov 1995.

[270] SMOOKE, M., PURI, I., AND SESHADRI, K. A comparison between numerical calculations and experimental measurements of the structure of a counterflow diffusion flame burning diluited methane in diluited air. *Symp. Combust. 21*, 1 (1998), 1783–1792.

[271] SOULARD, O. *Prise en compte d'un spectre d'échelles turbulentes dans la modélisation du micromélange et élaboration d'une méthode de Monte Carlo Eulérienne.* PhD thesis, University of Rouen, 2005.

[272] SPALART, P., AND ALLMARAS, S. A One-equation Turbulence Model for Aerodynamic Flows. *AIAA Paper 1992-439* (January 1992).

[273] SPALART, P., DECK, S., SHUR, M., SQUIRES, K., STRELETS, M. K., AND TRAVIN, A. A New Version of Detached-eddy Simulation, Resistant to Ambiguous Densities. *Theor. Comput. Fluid Dyn. 20*, 3 (2006), 181–195.

[274] SPALART, P., JOU, W., STRELETS, M., AND ALLMARAS, S. Comments on the Feasibility of LES for Wings, and on a Hybrid RANS/LES. *Advances in DNS/LES, First AFOSR International Conference on DNS/LES* (Ruston, LA, January 1997), 137–147.

[275] SPALDING, D. A single formula for the law of the wall. *J. Appl. Mech. 28*, 3 (1961), 455–459.

[276] SREENIVASAN, K. Fractals and Multifractals in Fluid Turbulence. *Annual Review of Fluid Mechanics 23* (1991), 539–600.

[277] STEINHAUSEN, M., LUO, Y., POPP, S., STRASSACKER, C., ZIRWES, T., KOSAKA, H., ZENTGRAF, F., MAAS, U., SADIKI, A., DREIZLER, A., AND HASSE, C. Numerical Investigation of Local Heat-Release Rates and Thermo-Chemical States in Side-Wall Quenching of Laminar Methane and Dimethyl Ether Flames. *Flow, Turbul. Comb. 106* (2021), 681–700.

[278] STEINHILBER, G. *Numerische Simulation turbulenter Verbrennungsprozesse mittels statistischer Verfahren und REDIM reduzierter Kinetik.* PhD thesis, Karlsruhe Institut für Technologie, 2015.

[279] STERNIN, A., PERAKIS, N., CELANO, M., TAJMAR, M., AND HAIDN, O. CFD-analysis of the Effect of a Cooling Film on Flow and Heat Transfer Characteristics in a GCH4/GOX Rocket Combustion Chamber. In *Space Propulsion Conference SP2018-00275* (Sevilla, Spain, May 2018).

[280] STONE, C., AND BISETTI, F. Comparison of ODE Solver for Chemical Kinetics and Reactive CFD Applications. *AIAA Paper 2014-0822* (2014).

[281] STRASSACKER, C., BYKOV, V., AND MAAS, U. REDIM reduced modeling of quenching at a cold wall including heterogeneous wall reactions. *Int. J. Heat Fluid Fl. 69* (2018), 185–193.

[282] STRASSACKER, C., BYKOV, V., AND MAAS, U. Parametrization and projection strategies for manifold based reduced kinetic models. *P. Combust. Inst. 37*, 1 (2019), 763–770.

[283] STRASSACKER, C., BYKOV, V., AND MAAS, U. REDIM reduced modeling of flame quenching at a cold wall – The influence of detailed transport models and detailed mechanisms. *Combust. Sci. Technol. 191*, 2 (2019), 208–222.

[284] STRASSACKER, C., BYKOV, V., AND MAAS, U. Comparative analysis of Reaction-Diffusion Manifold based reduced models for Head-On- and Side-Wall-Quenching flames. *P. Combust. Inst. 38*, 1 (2021), 1025–1032.

[285] STRAUB, C., DE, S., KRONENBURG, A., AND VOGIATZAKI, K. The effect of timescale variation in multiple mapping conditioning mixing of PDF calculations for Sandia Flame series D–F. *Comb. Theory Model. 20*, 5 (2016), 894–912.

[286] STRAUB, C., KRONENBURG, A., STEIN, O., KUENNE, G., JANICKA, J., BARLOW, R., AND GEYER, D. Multiple mapping conditioning coupled with an artificially thickened flame model for turbulent premixed combustion. *Combust. Flame 196* (2018), 325–336.

[287] SUBRAMANIAM, S., AND POPE, S. B. A mixing model for turbulent reactive flows based on Euclidean minimum spanning trees. *Combust. Flame 115* (1998), 487.

[288] SUSLOV, D., BETTI, B., AICHNER, T., SOLLER, S., NASUTI, F., AND HAIDN, O. Experimental Investigation and CFD-Simulation of the Film Cooling in an O2/CH4 subscale Combustion Chamber. *Proceedings. Space Propulsion 2012, 7. - 10. Mai 2012, Bordeaux, France* (2012).

[289] SUTHERLAND, W. The Viscosity of Gases and Molecular Force. *The London, Edinburgh, and Dublin Philosophical Magazine and Journal of Science 36*, 223 (1893), 507–531.

[290] SUTTON, J., AND BIBLARZ, O. *Rocket Propulsion Elements.* John Wiley and Sons, 2010.

[291] TANG, Y., HASSANALY, M., RAMAN, V., SFORZO, B., WEI, S., AND SEITZMAN, J. Simulation of Gas Turbine Ignition Using Large Eddy Simulation Approach. *GT2018-76216* (2018).

[292] TCHOU-KIEN, D., IANNETTI, A., GIRARD, N., BONHOMME, C., RAVIER, N., AND EDELINE, E. Prometheus, A Low Cost LOX/LCH4 Engine Prototype. *AIAA Paper 2017-4750* (July 2017).

[293] TEMMERMAN, L., HADŽIABDIĆ, M., LESCHZINER, M., AND HANJALIĆ, K. A hybrid two-layer URANS–LES approach for large eddy simulation at high Reynolds numbers. *Int. J. Heat Fluid Fl. 26*, 2 (2005), 173–190.

[294] TOMITA, T., UEDA, S., KAWASHIMA, H., ONODEA, T., KANO, Y., KUBOTA, I., AND MUNENAGA, T. Status of Experimental Research on High Performance Methane-Fueled Rocket Thrust Chamber. *AIAA Paper 2011-5936* (July 2011).

[295] TRAUTNER, E. Deep Neural Networks for Combustion Modeling: Optimizing CPU-based Inference for OpenFOAM. Master's thesis, Ostbayerische Technische Hochschule Regensburg, Sept. 2019.

[296] VAJDA, S., VALKO, P., AND TURÁNYI, T. Principal component analysis of kinetic models. *Int. J. Chem. Kin. 17*, 1 (1985), 55–81.

[297] VALIÑO, L. A Field Monte Carlo Formulation for Calculating the Probability Density Function of a Single Scalar in a Turbulent Flow. *Flow Turbul. Combust. 60*, 2 (June 1998), 157–172.

[298] VALIÑO, L., MUSTATA, R., AND LATAIEF, K. Consistent Behavior of Eulerian Monte Carlo fields at Low Reynolds Numbers. *Flow Turbul. Combust. 96* (2016), 503–512.

[299] VAN OIJEN, J., AND DE GOEY, L. Modelling of premixed counterflow flames using the flamelet-generated manifold method. *Combust. Theory Model. 6*, 3 (2002), 463–478.

[300] VAN OIJEN, J., LAMMERS, F., AND DE GOEY, L. Modelling of complex premixed burner systems by using flamelet-generated manifolds. *Combust. Flame 127*, 3 (2001), 2124–2134.

[301] VILLERMAUX, J., AND DEVILLON, J. Representation de la coalescence et de la redispersion des domains de segregation dans un fluide per modele d'interaction phenomenologique. *Proc. of the Second International Symposia on Chemical Reaction Engineering* (1972), B1.

[302] VO, S., STEIN, O., KRONENBURG, A., AND CLEARY, M. Assessment of mixing time scales for a sparse particle method. *Combust. Flame 179* (2017), 280–299.

[303] VON KARMAN, T., AND MILLAN, G. Thermal theory of laminar flame front near cold wall. *Fourth Symp. (Int.) on Combustion* (1953), 173–177.

[304] WANDEL, A., AND KLIMENKO, A. Y. Testing multiple mapping conditioning mixing for Monte Carlo probability density function simulations. *Phys. Fluids 17* (2005), 128105.

[305] WANDEL, A. P., AND LINDSTEDT, R. P. Hybrid multiple mapping conditioning modeling of local extinction. *P. Combust. Inst. 34*, 1 (2013), 1365–1372.

[306] WANG, M., FRISQUE, A., HUANG, J., AND BUSHE, W. Trajectory generated low-dimensional manifolds generated using the stochastic particle model. *Combust. Theory Model. 12*, 2 (2008), 249–267.

[307] WANG, M., AND MOIN, P. Dynamic wall modeling for large-eddy simulation of complex turbulent flows. *Phys. Fluids 14* (2002), 2043.

[308] WANG, Y., AND TROUVE, A. Direct Numerical Simulation of Nonpremixed Flame-wall Interactions. *Combust. Flame 144*, 3 (2006), 461–475.

[309] WEI, J., YE, M., ZHANG, S., QIN, J., AND HAIDN, O. Modeling of a 7-Elements GOX/GCH4 Combustion Chamber using RANS with Eddy-Dissipation Concept Model. *Aerosp. Sci. Technol. 29* (Apr 2020).

[310] WEISE, S., AND HASSE, C. Reducing the memory footprint in Large Eddy Simulations of reactive flows. *Parallel Comput. 49* (2015), 50–65.

[311] WEISE, S., POPP, S., MESSIG, D., AND HASSE, C. A Computationally Efficient Implementation of Tabulated Combustion Chemistry based on Polynomials and Automatic Source Code Generation. *Flow Turbul. Combust. 100*, 1 (2018), 119–146.

[312] WELLER, H., TABOR, G., JASAK, H., AND FUREBY, C. A tensorial approach to computational continuum mechanics using object-oriented techniques. *Comput. Phys. 12*, 6 (Nov/Dec 1998).

[313] WICHMAN, I. On the Quenching of a Diffusion Flame Near a Cold Wall. *Combust. Sci. Technol. 64*, 4-6 (1989), 295–313.

[314] WICHMAN, I., AND BRUNEAUX, G. Head-on quenching of a premixed flame by a cold wall. *Combust. Flame 103* (1995), 296–310.

[315] WILLIAMS, F. *Combustion Theory.* Benjamin Cummings, Menlo Parks, CA, 1985.

[316] WINTER, F., PERAKIS, N., AND HAIDN, O. Emission Imaging and CFD Simulation of a Coaxial Single-element GOX/GCH4 Rocket Combustor. *AIAA Paper 2018–4764* (July 2018).

[317] WU, H., AND IHME, M. Modeling of Wall Heat Transfer and Flame/Wall Interaction A Flamelet Model with Heat-Loss Effects. Conference paper, 9th U.S. National Combustion Meeting, May 2015.

[318] XU, J., AND POPE, S. PDF Calculations of Turbulent Nonpremixed Flames with Local Extinction. *Combust. Flame 123* (2000), 281–307.

[319] YAMASHITA, H., SHIMADA, M., AND TAKENO, T. A numerical study on flame stability at the transition point of jet diffusion flames. *Symp. Int. Combust. Proc. 26*, 1 (1996), 27–34.

[320] YANG, Y., DEC, J., DRONNIOU, N., AND SJÖBERG, M. Tailoring HCCI heat-release rates with partial fuel stratification: Comparison of two-stage and single-stage-ignition fuels. *P. Combust. Inst. 33*, 2 (2011), 3047–3055.

[321] YU, C. *Numerical Simulation of Turbulent Flames based on Reaction-Diffusion Manifolds (REDIM) reduced chemistry.* PhD thesis, Karlsruher Institut für Technologie, 2020.

[322] YU, C., BREDA, P., MINUZZI, F., PFITZNER, M., AND MAAS, U. A novel model for incorporation of differential diffusion effects in PDF simulations of non-premixed turbulent flames based on Reaction-Diffusion Manifolds (REDIM). *Phys. Fluids 33*, 2 (2021), 025110.

[323] YU, C., BREDA, P., PFITZNER, M., AND MAAS, U. Coupling of mixing models with manifold based simplified chemistry in PDF modeling of turbulent reacting flows. *P. Combust. Inst. 38*, 2 (2021), 2645–2653.

[324] YU, C., BYKOV, V., AND MAAS, U. Coupling of simplified chemistry with mixing processes in PDF simulations of turbulent flames. *P. Combust. Inst. 37*, 2 (2019), 2183–2190.

[325] YU, C., AND MAAS, U. Numerical Study of turbulent reacting flows with local extinction and re-ignition effects based on a statistical method and REDIM reduced reaction kinetics. In *28. Deutscher Flammentag* (2017).

[326] YU, C., MINUZZI, F., AND MAAS, U. Numerical Simulation of Turbulent Flames based on a Hybrid RANS/Transported-PDF Method and REDIM Method. *Eurasian Chem.-Technol. J. 20* (2018), 23–31.

[327] ZHANG, Y. F., VICQUELIN, R., GICQUEL, O., AND TAINE, J. Physical study of radiation effects on the boundary layer structure in a turbulent channel flow. *Int. J. Heat Mass Transfer 61* (2013), 654–666.

[328] ZHANG, Y. F., VICQUELIN, R., GICQUEL, O., AND TAINE, J. A wall model for LES accounting for radiation effects. *Int. J. Heat Mass Transfer 67* (2013), 712–723.

[329] ZHOU, D., AND YANG, W. A Bundled Dynamic Adaptive Chemistry Method toward Accelerating Combustion Chemistry Integration. *Energy Procedia 142* (2017), 1034–1039.

[330] ZIPS, J. *Simulation turbulenter Verbrennung von Methan und Sauerstoff in Raketenbrennkammern.* PhD thesis, Bundeswehr University of Munich, 2019.

[331] ZIPS, J., MÜLLER, H., AND PFITZNER, M. Non-Adiabatic Tabulation Methods to Predict Wall-Heat Loads in Rocket Combustion. Conference Paper 2017-1469, AIAA SciTech Forum, Jan 2017.

[332] ZIPS, J., TRAXINGER, C., BREDA, P., AND PFITZNER, M. Assessment of Presumed / Transported Probability Density Function Methods for Rocket Combustion Simulations. *J. Propuls. Power 35*, 4 (2019), 1–18.

[333] ZIPS, J., TRAXINGER, C., AND PFITZNER, M. Time-resolved Flow Field and Thermal Loads in a Single-element GOx/GCH4 Rocket Combustor. *Int. J. Heat Mass Transfer 143* (2019).

[334] ZIRWES, T., ZHANG, F., DENEV, J., HABISREUTHER, P., AND BOCKHORN, H. *High Performance Computing in Science and Engineering '17.* Springer, Cham, 2018, ch. Automated Code Generation for Maximizing Performance of Detailed Chemistry Calculations in OpenFOAM, pp. 189–204.

[335] ZIRWES, T., ZHANG, F., HABISREUTHER, P., HANSINGER, M., BOCKHORN, H., PFITZNER, M., AND TRIMIS, D. Quasi-DNS Dataset of a Piloted Flame with Inhomogeneous Inlet Conditions. *Flow Turb. Combust. 104* (2020), 997–1027.

[336] ZIRWES, T., ZHANG, F., HABISREUTHER, P., HANSINGER, M., BOCKHORN, H., PFITZNER, M., AND TRIMIS, D. Identification of Flame Regimes in Partially Premixed Combustion from a Quasi-DNS Dataset. *Flow Turbul. Combust. 106* (2021), 373–404.